Crystal growth and anisotropic magnetic properties of Ce and Pr based binary intermetallic compounds

A Thesis

Submitted to the
Tata Institute of Fundamental Research, Mumbai
for the degree of Doctor of Philosophy
in Physics

by

Pranab Kumar Das

Department of Condensed Matter Physics and Materials Science
Tata Institute of Fundamental Research
Mumbai
January, 2015

DECLARATION

This thesis is a presentation of my original research work. Wherever contributions of others are involved, every effort is made to indicate this clearly, with due reference to the literature, and acknowledgment of collaborative research and discussions.

The work was done under the guidance of Prof. Arumugum Thamizhavel at the Tata Institute of Fundamental Research, Mumbai.

Pranab Kumar Das

[Candidate's name and signature]

In my capacity as supervisor of the candidate's thesis, I certify that the above statements are true to the best of my knowledge.

Prof. Arumugum Thamizhavel

[Supervisor name and signature]

Date: 12-Jan-2015

To my parents

Acknowledgments

It has been a wonderful experience both personally and professionally during the course of last five years while perusing PhD at TIFR which houses a stimulating environment with many great people. Here I take this opportunity to say "Thank you" to some of the people without whom it would not have been possible to arrive at this point.

First of all I would like to thank my Ph.D. advisor Prof. Arumugam Thamizhavel for his guidance and support. I have learned, and still learning, a lot from him about many interesting physics and techniques, especially about the crystal growth. I am equally thankful to Prof. Sudesh Kumar Dhar for his support and invaluable advices.

I would like to thank Prof. S. Ramakrishnan for various help, and allowing me to perform some of the experiments in his lab. I am thankful to our collaborators: Prof. Bauer, Dr. Soma Banik, Dr. Ivana Vobornik, Dr. Azzedine Bendaunan.

I am thankful my lab members Ruta Kulkarni, Neeraj, Arvind, Darje, Amitava, Ramesh, Devang, Sangeetha, Manjusha, Bhanu, Om Prakash, Anil, Sannabhatti, Palash for making this journey friendly and more enjoyable. I have received professional helps form all of them in various occasions. Ruta helped me in various measurements; also she invests lot of time and effort in maintaining various setups in the lab. Darjee helped me to design and build crucibles, and various other experimental setups.

Synopsis

Executive Summary

This synopsis presents a summary of the experimental results obtained on the anisotropic physical properties of some Ce and Pr based intermetallic binary compounds. In all cases single crystalline samples were prepared using either of the two different crystal growth methods (viz., Bridgman and Czochralski), depending upon the compound. Well oriented single crystals were used for the anisotropic physical property measurements. Powder X-ray diffraction and Rietveld refinement were performed in order to confirm the phase purity and to estimate the lattice parameters. To check the stoichiometry and homogeneity of the samples Energy Dispersive Analysis by X-ray (EDAX) was performed. Magnetic properties were studied by measuring magnetic susceptibility, magnetization, heat capacity and electrical transport on well oriented single crystals. Crystal electric field (CEF) calculations were performed on the magnetic susceptibility and heat capacity data to determine the level splitting of the $(2J + 1)$ fold degenerate state of the Ce^{3+} or Pr^{3+} ions in these systems. Magnetocaloric effect (MCE) was investigated on PrSi and PrGe compounds from magnetization data. Angle resolved photoemission spectroscopy (ARPES) was performed in PrGe in order to understand the electronic structure of this system.

A general introduction to strongly correlated electron systems and crystal electric field is given in Chapter 1 of the thesis. Chapter 2 presents various crystal growth methods and experimental techniques used. Chapter 3 describes the results obtained on the Kondo lattice compound $CeMg_3$, and magnesium rich binary $CeMg_{12}$. The anisotropic magnetic properties and superzone gap formation in CeGe are described in Chapter 4. A comparison with the results obtained on CeSi is also given in this

chapter. The anisotropic magnetic properties and magnetocaloric effect of PrGe and PrSi are described in Chapter 5. Experimental photoemission results on PrGe are discussed in chapter 6.

Introduction

The rare earth intermetallic compounds can be visualized as a lattice of localized $4f$ moments immersed in a sea of conduction electrons. The $4f$ moments in intermetallic compounds interact with each other via the conduction electron mediated Ruderman-Kittel-Kasuya-Yosida (RKKY) exchange interaction, which drives the local moments to a magnetically ordered state. On the other hand there also exists the local Kondo-exchange interaction between the $4f$ moment and the conduction electrons in some compounds (mainly Ce and Yb based), which is antiferromagnetic. Below a characteristic temperature (called the Kondo temperature, T_K) the conduction electrons screen the $4f$ derived local moments and yield a non-magnetic ground state. In some compounds of Ce and Yb the $4f$-level lies close to Fermi-level, which enhances the hybridization between the $4f$ level and the band states resulting in an antiferromagnetic local $s - f$ exchange interaction, which is a prerequisite for Kondo effect. The relative strengths of these two competing exchange interactions give rise to various ground states with interesting physical properties, e.g., normal behavior with typically magnetic ordering at low temperature, heavy fermion Kondo lattice without any long range magnetic order (example, CeAl$_3$ [1], CeCu$_6$ [2]); Kondo lattice compounds that order magnetically at low temperature with reduced magnetic moments (example, cubic CeAl$_2$ [3], CeB$_6$ [4], YbRh$_2$Si$_2$ [5], YbAlB$_4$ [6]). Some more examples of heavy fermion compounds are: CeCu$_2$Si$_2$ [7], CeCoIn$_5$ [8], where charge carriers have enormous effective mass, as high as thousand times that of the free electron mass. Some of these heavy fermion compounds show anomalous superconductivity. CeCu$_2$Si$_2$ [7] shows superconductivity at ambient pressure, while CeCu$_2$Ge$_2$ [9], CeRh$_2$Si$_2$ [10], CeIn$_3$ [11] and CePd$_2$Si$_2$ [12] show superconductivity under hydrostatic pressure. These compounds are Kondo lattice antiferromagnets at ambient pressure. The application of external pressure is an excellent way to control the ground state of these heavy fermion compounds, where the Kondo interaction depends sensitively on lattice volume (and hence external pressure). One can attain

quantum critical point in these systems ($T_N \rightarrow 0$) by chemical doping, magnetic field, or pressure [13]. The field of quantum criticality is intensively studied these days. It is therefore of interest to explore new Ce and Yb based compounds for probable anomalous behavior. In view of the above mentioned interesting phenomena, we have grown the single crystals of CeMg$_3$, CeMg$_{12}$, CeGe, and CeSi binary compounds and investigated their physical properties.

In a crystal environment, the rare earth ions are surrounded by other ions, which produce an inhomogeneous electric field in the lattice. The crystal electric filed (CEF) plays an important role in modifying many properties of the rare earth system. It is able to lift, at least partially, the ($2J + 1$) fold degeneracy of the free-rare earth ion, where J is the total angular momentum of the rare earth ion. The effect of this level splitting can be observed on various physical properties, like the magnetic susceptibility and isothermal magnetization; the thermal variation of the electrical resistivity and Schottky heat capacity. In case of Pr (which is a non-Kramers ion) based systems, the degeneracy can be totally lifted due to CEF and a non-magnetic singlet ground state is possible (example, PrNi$_5$ [14]). Also some Pr compounds (example PrAg [15]) show interesting quadrupolar effect. The interaction between the quadrupole moment of Pr^{3+} ions and conduction electrons may give rise to quadrupolar Kondo effect similar to the conventional magnetic Kondo effect discussed above. The heavy fermion state with quadrupolar Kondo effect is observed in a number of compounds e.g., PrInAg$_2$ [16] and PrOs$_4$Sb$_{12}$ [17] which shows superconductivity as well.

It is therefore of interest to study Pr based compounds. Besides the binary Ce compounds we have also investigated binary PrSi and PrGe compounds in this thesis. We observed a first order like magnetic transition reflecting large change of entropy across the transition. Thus we attempted to study the anisotropic mangnetocaloric properties of these two compounds.

The surface of a crystal is interesting from many points of view. Especially, at the surface the three dimensional translational symmetry of the bulk is not present. In a crystal having inversion symmetry, the splitting of the states due to the spin-orbit interaction is not allowed. But the lack of translational symmetry along the surface normal may lead to spin-orbit splitting [18]; the so-called Rashba effect. But it is

found that Rashba interaction at such crystal surfaces becomes significant only when it couples to the large intra-atomic spin-orbit interaction. It is expected that in the rare-earth compounds which have high Z (atomic number) rare earth ions, the Rashba interaction should contribute significantly to their surface electronic structures [19, 20]. Thus PrGe single crystal which exhibits a large electronic density of Pr $4f$ states that are localized on the surface is therefore a natural choice for the investigation of Rashba spin-orbit interaction. Also to understand the complex magnetism in PrGe, electronic band structure and Fermi surface measurements have been performed in the paramagnetic, antiferro and ferromagnetic states using high resolution (10 meV) angle resolved photo emission spectroscopy (ARPES).

Experimental methods

Crystal growth

Single crystals can be grown by a variety of methods depending on the melting behavior of the compound. Here in this thesis, we have employed two different techniques to grow the single crystals viz., the Bridgman and Czochralski methods. From the binary phase diagram of Ce-Mg and La-Mg [21], it is found that the $CeMg_3$ and $LaMg_3$ phases melt congruently near 800 °C. Thus in principle, these two compounds can be grown directly from the melt. Due to the high vapor pressure of Mg above 600 °C, we employed the Bridgman method to grow the single crystal of $CeMg_3$ and its non-magnetic analogue $LaMg_3$. Pure Ce and Mg metals were taken in 1 : 3.1 stoichiometric proportion in a sharp tip alumina crucible. A little excess of Mg was taken to compensate the weight loss due to evaporation. Due to the very high vapor pressure of magnesium, the crucible was first sealed inside a molybdenum crucible in argon atmosphere, and subsequently inside a quartz ampule in a vacuum of 10^{-6} mbar. A box type resistive heating furnace was used to heat the crucible up to 850 °C, well above the congruent melting temperature of $CeMg_3$ and the temperature was maintained there for 1 day for proper homogenization of the melt; then the furnace was slowly cooled down at a rate of 1 °C/hr to 750 °C and finally switched off to cool down to room temperature. Shiny pieces of single crystals were obtained by gently tapping the alumina crucible. Identical procedure was employed to grow

the single crystal of LaMg$_3$. The Mg-rich, binary CeMg$_{12}$ also melts congruently and a similar procedure was used to grow its single crystal.

In the case of CeGe it is reported that CeGe phase forms peritectically at 1433 °C, but increasing the Ge concentration slightly leads to a nearly congruent melting [22]. For CeGe, the crystal growth was started with a little excess of Ge by taking Ce and Ge in the stoichiometric proportion of 1 : 1.05. First the individual metals were melted in a tetra arc furnace and the resulting button re-melted several times to form the polycrystalline sample. Later a tungsten rod was used as a seed to pull the crystal. A pulling rate of 10 mm/hr was employed. About 5 cm long and 3-4 mm diameter single crystal rod was grown by this method. The crystal has a cleavage plane along the growth direction, which is found to be [010] crystallographic direction from Laue diffraction.

LaGe, PrGe, CeSi and PrSi phases melt congruently at the exact 1 : 1 stoichiometric proportion. Thus they can also be grown directly from the melt. In all cases pure elements were taken in the exact 1 : 1 stoichiometric proportion. First the polycrystalline button was prepared by arc melting the charge several times as described above. Similar to CeGe, a clean tungsten rod was used as seed to pull the crystals. The pulling speed was 10 mm/hr in all cases. Polycrystalline sample of YGe, which was used as a non-magnetic analogue compound of PrGe, was prepared using arc melting.

Measurement techniques

Powder X-ray diffraction of the samples was performed in a PANalytical X-ray diffractometer using monochromatic Cu Kα radiation to check for the phase purity and to determine the lattice parameters. EDAX was also used as an additional probe for sample characterization. Crystals were oriented along the desired crystallographic directions by using back reflection Laue diffraction method. Representative Laue patterns of CeGe and PrGe single crystals are shown in Fig. 1. Crystals were cut along the desired crystallographic directions by using a spark erosion cutting machine. The magnetic susceptibility and isothermal magnetization measurements were performed in Quantum Design (QD) Superconducting Quantum Interference Device
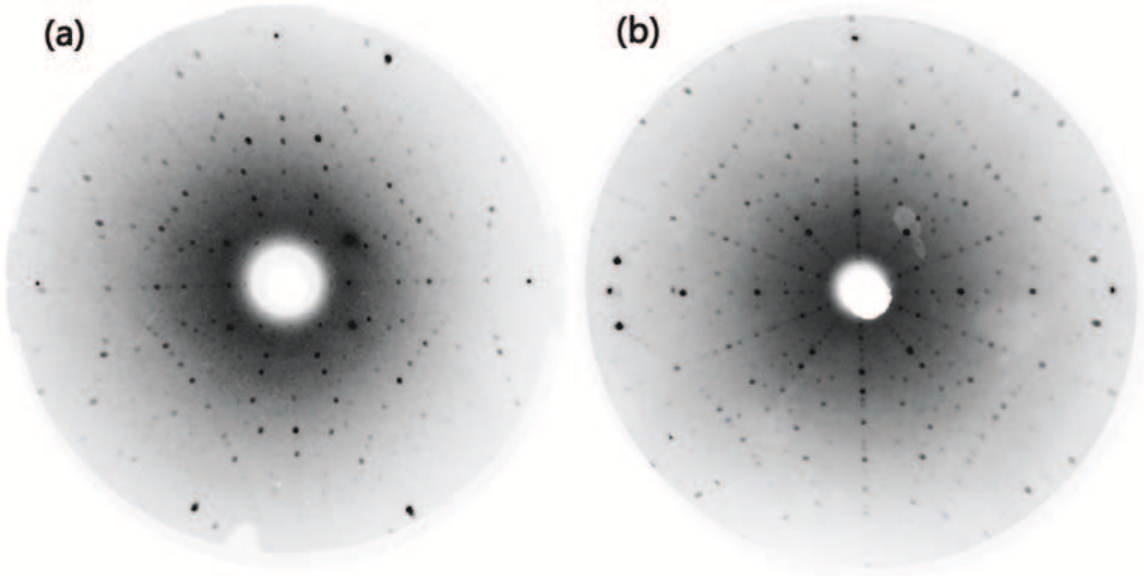
Figure 1: Representative Laue pattern of (a) (010)-plane of CeGe and (b) (001)-plane of PrGe single crystals.

(SQUID) and Vibration Sample Magnetometer (VSM), respectively. Resistivity in zero magnetic field was measured in a home made setup using conventional four probe method. Heat capacity and electrical resistivity with applied magnetic field were measured using a QD Physical Property Measurement System (PPMS).

The pressure studies on $CeMg_3$ were performed in collaboration with Prof. Bauer, Vienna. Initial measurements at lower pressure were performed on our home built setup. Photoemission (ARPES) measurements on PrGe were carried out at APE beamline, Elettra Sincrotrone Trieste.

Magnetic properties of the Kondo lattice antiferromagnet $CeMg_3$, and $CeMg_{12}$

Magnetic properties of $CeMg_3$ and $NdMg_3$ have been studied by Buschow [23] on a polycrystalline sample, and he reported no magnetic ordering down to 4.2 K. On the other hand, Pierre et al. [24] and Galera et al. [25] reported $CeMg_3$ orders antiferromagnetically with $T_N = 3.4$ K, while $NdMg_3$ orders antiferromagnetically below

6 K [25]. Recently, Tanida et al. [26] have performed detailed magnetic measurements on $PrMg_3$ single crystal and found it exhibits a nonmagnetic Γ_3 doublet ground state. A detailed study on the single crystalline sample of $CeMg_3$ has not been reported so far in the literature.

Here we have made a detailed investigation on the magnetic properties of $CeMg_3$ first time on a single crystalline sample. $CeMg_3$ crystallizes in the cubic structure with space group $Fm\bar{3}m$. A Rietveld analysis on powder X-ray pattern obtained by crushing a small piece of single crystal to powder was performed using FULLPROF [27] software package to obtain the lattice parameters. The crystal was oriented along the principal crystallographic direction, namely [100] by means of back reflection Laue diffraction method, and then the sample was cropped in rectangular bar form using a spark erosion cutting machine. Well oriented crystals were used for all anisotropic measurements.

Magnetic susceptibility (χ) of $CeMg_3$ shows a cusp at 2.6 K which is identified as the Néel temperature (T_N), where the Ce moments order antiferromagnetically. Our T_N is different from the reported polycrystalline value [24, 25]. The χ^{-1} varies linearly with temperature (T) at high temperatures (200 to 300 K) in accordance with the Curie-Weiss law (Fig. 2a). The effective paramagnetic moment of 2.6 μ_B/Ce is obtained from fitting the high temperature data to the Curie-Weiss law, which is close to the theoretical value of 2.54 μ_B/Ce for Ce^{3+} free ion. Below 200 K a deviation from the linearity in $\chi^{-1}(T)$ is observed (Fig. 2a), which is attributed to the CEF effect. The isothermal magnetization at 1.8 K reaches a value of 0.5 μ_B/Ce in an applied magnetic field of 12 T, while the saturation moment of a free Ce^{3+} ion $g_J J$ is 2.14 μ_B. This reduction in magnetization value is attributed to Kondo effect and crystal electric field. Electrical resistivity of $CeMg_3$ and $LaMg_3$ was measured in the temperature interval from 1.9 to 300 K. The resistivity of $LaMg_3$ is typical of a metallic sample following Bloch-Gruneisen behavior. On the other hand the resistivity of $CeMg_3$ shows a broad hump around 150 K. The magnetic ordering at 2.6 K is not very clearly seen as the data are collected only down to 1.9 K. The magnetic part of electrical resistivity (ρ_{mag}) was estimated by subtracting the resistivity of $LaMg_3$ from that of $CeMg_3$. ρ_{mag} shows two broad humps centered around 6 K and 100 K, respectively and $\rho_{mag}(T)$ varies linearly with $-ln(T)$ at low and high temperatures. According to Cornut and Coqblin [28], this type of behavior is expected in Kondo compounds

in the presence of strong crystal field splitting and arises due to the interplay of the Kondo interaction and the CEF splitting (Δ_{CEF}). The low temperature peak occurs on an energy scale of the order of Kondo temperature. While the high temperature peak is attributed to the CEF effect.

The heat capacity of CeMg$_3$ was measured in the temperature interval 0.5 to 200 K. The heat capacity data show a sharp peak at 2.6 K confirming the bulk nature of magnetic ordering of the sample. Sommerfield coefficient (γ) was estimated by fitting the low temperature heat capacity data (below 1 K) to: $C/T = \gamma + \beta T^2$, and is thus inferred to be 370 $mJ/molK^2$. The high temperature γ value estimated in the paramagnetic phase (12 K <T <17 K) is estimated to be 41 $mJ/molK^2$. This implies that the enhanced low temperature γ value is due to the Kondo interaction. Since the Sommerfield coefficient γ is proportional to the effective electron mass, the large value of low temperature γ indicates that CeMg$_3$ is a moderate heavy fermion compound. The magnetic part of entropy (S_{mag}) is calculated by integrating C_{mag}/T vs. T plot. At T_N the S_{mag} reaches only a value of $0.5Rln2$ with respect to the value of $Rln2$ anticipated for doublet ground state, inferred from the CEF calculation discussed later.

The reduced value of the magnetization, the reduction in magnetic entropy, and the double peak structure in the electrical resistivity are signature of Kondo interaction in this compound. An estimate of T_K was made from the magnetic part of entropy and from the jump in the magnetic part of the heat capacity at T_N. T_K is found to be of the order of T_N. The $4f$ contribution to the heat capacity was obtained by subtracting the heat capacity of LaMg$_3$ from that of CeMg$_3$, assuming their phonon spectra are identical. A broad hump is observed in C$_{4f}$ centered around 80 K, which is attributed to Schottky anomaly arising from the CEF level splitting. A CEF analysis was performed on the heat capacity and magnetic susceptibility data.

For the Ce atom in cubic point symmetry, the CEF Hamiltonian is given by,

$$\mathcal{H}_{\text{CEF}} = B_4^0 \left(O_4^0 + 5O_4^4 \right) \tag{1}$$

.

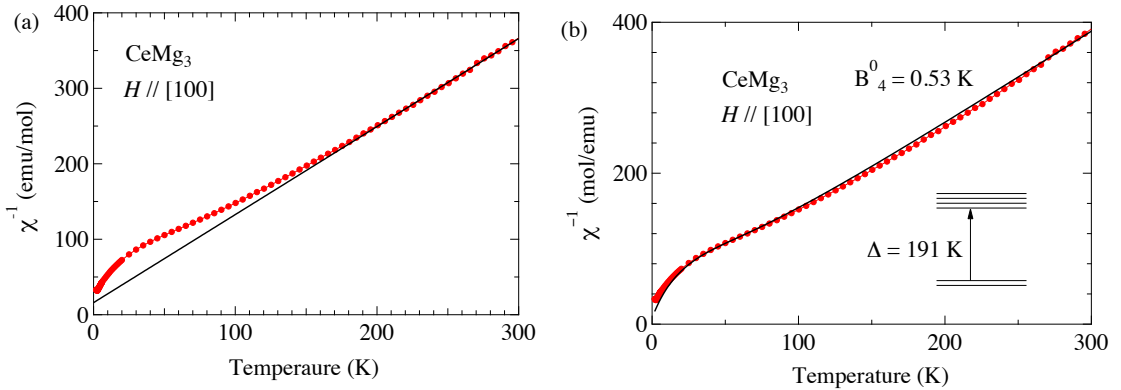where B_l^m and O_l^m are the crystal field parameters and the Steven's operators

Figure 2: Temperature dependence of inverse susceptibility of $CeMg_3$. The solid line shows the fit based on (a) Curie-Weiss law and (b) the CEF calculation.

respectively [29, 30]. From the CEF analysis, it found that the $J = 5/2$ multiplet of Ce^{3+} splits into a doublet and a quartet state with an energy splitting of 191 K. The calculated inverse susceptibility matches well with the experimental data as shown in Fig. 2b.

The reduction in the magnetization and a reduced jump in the heat capacity at the magnetic transition, double peak structure in electrical resistivity along with a Kondo temperature T_K which is of the order of T_N, indicate the properties of $CeMg_3$ are similar to other heavy fermion antiferromagnetic compounds like, $CeIn_3$ [11, 13], $CePd_2Si_2$ [11] and $CeCu_2Ge_2$ [9], to mention a few. As mentioned in the introduction, the magnetic state of such compounds is very sensitive to external pressure, so we explored any possible changes in the magnetic behavior by measuring the electrical resistivity of $CeMg_3$ under hydrostatic pressure up to 12 kbar in collaboration with Prof. Bauer's group at Vienna. Initial measurements at lower pressure were performed on our home made set up. It was found that T_N increases slightly with the application of pressure. Most likely higher pressures may decrease T_N leading eventually to a quantum critical point, as expected on the basis of Doniach's phase diagram.

As a continuation of our work on binary Ce-Mg phases, we have studied and reported for the first time the magnetic properties of magnesium rich compound $CeMg_{12}$ compound on a single crystalline sample. $CeMg_{12}$ crystallizes in the tetragonal struc-

ture with space group $I4/mmm$ (no. 139). Magnetic susceptibility and electrical transport were measured in the temperature range 1.8 to 300 K. Heat capacity was measured down to 0.05 K, and the data revealed that $CeMg_{12}$ undergoes a magnetic transition at 1.2 K. With the application of magnetic field the transition shifts to lower temperature, typical of antiferromagnetic ordering. A crystal field analysis was performed on the magnetic susceptibility and magnetization data. From the CEF fitting it is estimated that J = 5/2 multiplet splits into three doublets, with an energy splitting of 30 K and 126 K respectively for the first and second excited state from the ground state.

Anisotropic magnetic properties of equiatomic CeGe and CeSi

CeGe and CeSi compounds crystallize in the orthorhombic FeB-type structure with space group $Pnma$ (no. 62). Polycrystalline CeSi has been investigated by Shaheen [31] and it was found to order magnetically with $T_N = 5.6$ K. From the heat capacity data Shaheen concluded that the ground state is quartet, which is unusual for a Ce atom occupying a monoclinic site symmetry. For Ce^{3+} ion placed in such a low symmetry site, the $(2J + 1)$ degenerate state would split into three doublets. More recent work by Noguchi et.al. [32] on single crystalline CeSi reported a doublet ground state. On the other hand, polycrystalline CeGe was investigated [33, 34, 35], and found to order antiferromagnetically below $T_N = 10.8$ K. Marcano et. al. [35] observed an upturn in the electrical resistivity at T_N, indicating the onset of a magnetic superzone gap. Due to the low crystal symmetry of CeGe, it is expected to exhibit anisotropic magnetic properties. We were, therefore, motivated to grow a single crystal of CeGe to explore its anisotropic magnetic properties, including the superzone gap.

Since the single crystal of CeGe was grown by taking slightly excess of Ge, the phase purity was checked by means of powder X-ray diffraction. We have performed a Rietveld analysis on the powder XRD pattern using the software package FULL-PROF [27]. A good fit to the experimental pattern confirmed that the grown crystal is single phase with the symmetry of the orthorhombic space group $Pnma$. The stoi-

chiometry of the sample was further confirmed by EDAX where the composition of the sample was probed at various locations. The magnetic susceptibility was measured along the three crystallographic directions in an applied magnetic field of 1 kOe. It was found that CeGe orders antiferromagnetically below 10.5 K, in good agreement with the previous reports on polycrystalline samples. Electrical transport and magnetization data revealed large anisotropy arising from the orthorhombic crystal structure. The isothermal magnetization data measured at 1.8 K show metamagnetic transitions at 4.8 and 6.4 T along [010] direction, and at 10.7 T along [100] direction, while the magnetization along [001] direction increases linearly without any anomaly up to a field of 16 T. Thus from the magnetic susceptibility and magnetization data [010] was found to be the easy axis of magnetization. Isothermal magnetization was measured at various temperatures and a magnetic phase diagram constructed from the differential plot $(dM/dH vs. H)$. The electrical resistivity exhibits an upturn at the onset of magnetic ordering at 10.5 K along all the three principal crystallographic directions, due to the supezone gap effect, shown in Fig. 3. This type of behavior is well documented in the heavier rare-earth metals where it is usually observed along the hexagonal c-axis [36, 37]. The spiral spin structures in these heavier rare-earth metals have a different periodicity than the lattice, which gives rise to new Brillouin zone boundaries and creates discontinuities in the Fermi surface. The behavior of resistivity in CeGe below T_N is similar to the orthorhombic UCu_2Sn [38], where the superzone gap is observed along all three principal crystallographic directions. Magnetic part of resistivity (ρ_{mag}) is obtained by subtracting the LaGe resistivity values from that of the CeGe. ρ_{mag} shows a broad hump centered around 80 K which is attributed to the incoherent Kondo scattering of the charge carriers and the CEF level splitting. However, we do not observe any evidence of Kondo effect in the low temperature region above T_N. We have performed a crystal electric field analysis on the susceptibility and heat capacity data. It was found that the J = 5/2 multiplet splits into three doublets, with an energy splitting of 39 K and 111 K for the first and second excited states, respectively.

The magnetic properties of single crystalline CeSi have already been studied by Noguchi et. al. [32]. We have also grown the single crystal of CeSi and studied its magnetic properties in detail. The lattice constants were obtained from the powder X-ray data and found to match with the previously reported values. A large
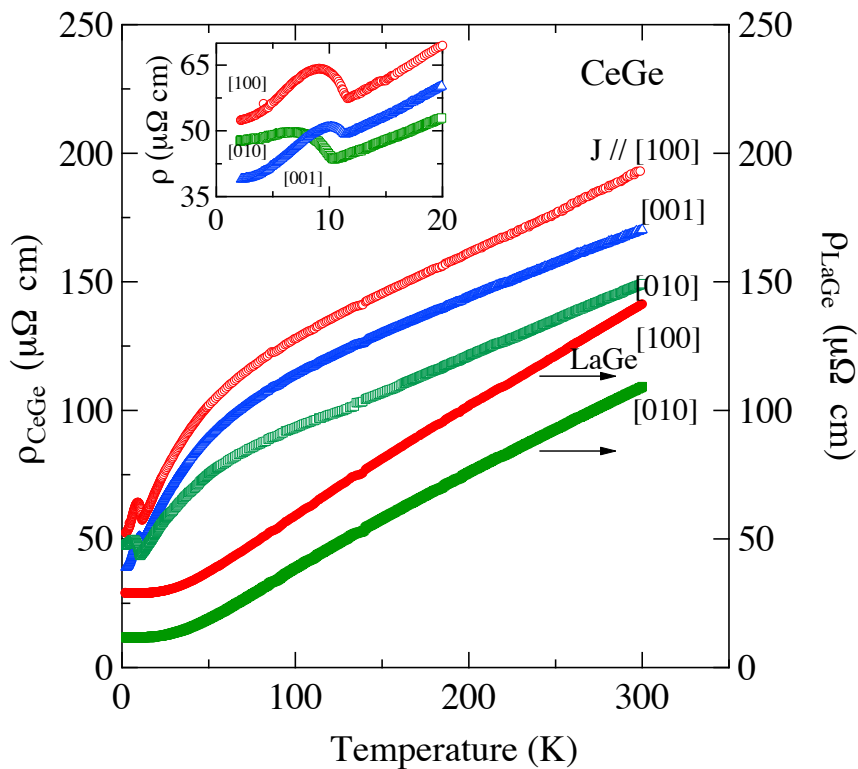
Figure 3: Temperature dependence of the electrical resistivity for CeGe and LaGe for current parallel to the three principal crystallographic directions, respectively. The inset shows the low temperature resistivity of CeGe.

anisotropy is observed in the electrical resistivity and susceptibility measurement. CeSi was found to order antiferromagnetically with $T_N = 6$ K corroborating the previous reports [32, 39]. [010] crystallographic direction is found to be the easy axis of magnetization similar to CeGe. In addition to previous work, we measured the magnetization at various temperatures, and constructed magnetic phase diagrams along the three principle directions. From the CEF fit to susceptibility and heat capacity data, it was found that the $(2J+1)$ degenerate state of Ce^{3+} splits into three doublets with the first excited state at 30 K and the second excited state at 112 K. The crystal field split energy levels are of the same order as observed in CeGe system.

Anisotropic magnetic properties and the magnetocaloric effect of PrSi and PrGe

Pr-based intermetallic compounds show many interesting ground state properties because of the critical role of CEF and in some cases the quadrupolar interaction. The heavy fermion mechanism in Pr-based compounds is quite different from the usual (magnetic) Kondo route to heavy fermions in the Ce-based compounds. In addition to our work on Ce-binary compounds, we have also investigated in this thesis two binary Pr-based compounds, single crystalline PrSi and PrGe.

Anisotropic magnetic properties of PrSi have been studied in single crystalline sample by measuring the magnetic susceptibility, isothermal magnetization, heat capacity and electrical transport. From the Rietveld refinement of powder X-ray pattern it is found that the PrSi crystallizes in the orthorhombic FeB-type structure with space group $Pnma$ (no. 62).

Electrical resistivity data show a large anisotropy which is associated with the orthorhombic crystal structure. Resistivity decreases with decrease in temperature, and shows a broad curvature, which is due to the thermal depopulation of CEF split levels. Resistivity falls sharply below 52 K, due to the reduction in the spin disorder scattering of conduction electrons below the magnetic ordering temperature, T_C. Corresponding anomalies in the magnetization and heat capacity confirm the transition from the paramagnetic to a magnetically ordered state at 52 K. The residual resistivity ratio (RRR) is found to be 23, 22, and 23 for current parallel to [100], [010], and [001], respectively reflecting good quality of the single crystals. The low temperature resistivity behavior, in the ferromagnetic state (inferred from magnetization) can be described by spin-wave gap model. For energy $k_{\mathrm{B}}T \ll \Delta$, where Δ is the gap, the resistivity is given by,

$$\rho(T) = \rho_0 + aT^2 + bT\Delta \left(1 + \frac{2T}{\Delta}\right) \exp\left(\frac{-\Delta}{T}\right). \tag{2}$$

The first term in the above expression is the residual resistivity, the second term is the usual Fermi liquid term, and the third term is due to the magnon contribution.

	ρ_0 ($\mu\Omega$ cm)	a ($\mu\Omega$ cm/K^2)	b ($\mu\Omega$ cm/K^2)	Δ (K)
$\rho_{[100]}$	4.721	1.91×10^{-3}	2.88×10^{-2}	128
$\rho_{[010]}$	2.477	9.188×10^{-4}	9.53×10^{-3}	124
$\rho_{[001]}$	0.525	2.242×10^{-4}	2.58×10^{-3}	132

Table 1: Fitting parameters of the resistivity data in PrSi along the three principal directions described in Eqn. 2.

Here the coefficient a determines the degree of electron-electron scattering and b is a constant for the given material and depends on the spin wave stiffness. The resistivity data are fitted to the above expression and the obtained parameters are listed in Table 1.

The magnetic susceptibility shows a sharp increase at 52 K when the field is applied along the [010] crystallographic direction indicating ferromagnetic ordering. Anomalies at 52 K are also seen for $H \mid\mid$ [100] and [001] directions but the susceptibility is relatively smaller and the temperature dependence below T_C is relatively complex. [010] crystallographic direction is found to be the easy axis of magnetization. In the high temperature range (100 to 300 K), the susceptibility follows the Currie-Weiss law with an effective moment of 3.58 μ_B for Pr^{3+} ion, indicating the trivalent nature of Pr in this system.

Isothermal magnetization vs. field at 2 K shows hysteresis behavior along all the three crystallographic directions confirming the ferromagnetic ground state. Along [010] direction the magnetization reaches saturation in a low applied field of just 3 kOe, and attains a value which is an order of magnitude larger compared to other two directions, thus confirming [010] as the easy axis of magnetization and also reflecting the strong anisotropy in this compound. From the field dependence of isothermal magnetization at selected temperatures the Arrott plots of PrSi were obtained.

The heat capacity of PrSi shows a huge jump (about 40 J/K mol) at 52 K confirming the bulk nature of magnetic ordering. At low temperature (below 5 K), the heat

capacity increases with decreasing temperature, which is attributed to the nuclear Schottky contribution arising from the hyperfine splitting of Pr nuclear levels. The low temperature ($T \leq 4$ K) heat capacity data were fitted to following expression:

$$C_{\mathrm{p}} = \gamma T + \beta T^3 + \left(\frac{C_{\mathrm{N}}}{T^2}\right), \tag{3}$$

where the first term is the electronic contribution, second term is the lattice contribution, while the third term is the contribution from the nuclear Schottky heat capacity. We obtain $\gamma = 7.4$ mJ/K^{2}mol, $\beta = 0.115$ mJ/K^4 mol and the nuclear Schottky term $C_{\mathrm{N}} = 850.2$ mJK/mol from the fitting. The magnetic part of the heat capacity (C_{mag}) was estimated by the usual method of subtracting LaSi heat capacity from that of PrSi.

A crystal field analysis is performed on the magnetic susceptibility and heat capacity data, and it was found that J = 4 multiplet splits into a nine singlet states with an overall splitting energy of 284 K.

The huge jump in heat capacity at the magnetic transition and the shape of Arrott plot suggest a possible first order like magnetic transition. Magnetocaloric properties have been investigated along all three principal crystallographic directions from the magnetization data. The magnetic entropy change (ΔS_M) is calculated from M vs. H isotherms using Maxwell's relation [40]: $\Delta S_M(0 \to H) = \int_0^H \frac{dM}{dT} dH$. Large value of magnetic entropy change $-\Delta S_M = 22.2$ J/Kg K, and the relative cooling power RCP = 460 J/Kg are observed near the transition temperature ($T_C = 52$ K) for a field change of $H = 70$ kOe along the easy axis of magnetization. These values of $-\Delta S_M$ are comparable to that of well known giant magnetocaloric material Gd$_5$Si$_2$Ge$_2$ [41, 42]. For $H \parallel [100]$ the magnetic entropy is positive in the magnetically ordered state for fields as high as 70 kOe and for $H \parallel [001]$ direction the $-\Delta S_M$ values is about 10 times smaller compared to $H \parallel [001]$ direction. Thus PrSi exhibits a giant magnetocaloric anisotropy. It is interesting to note that this type of giant magnetocaloric effect and large RCP is generally observed in compounds of heavier rare-earth elements which have higher magnetic moments [42, 43].

In contrast to PrSi, PrGe is known to exhibit dimorphism by crystallizing in both orthorhombic CrB and FeB-type structures. From the powder X-ray diffraction and

Laue diffraction at room temperature (300 K) we found that our Czochralski-grown single crystal is orthorhombic CrB-type with space group $Cmcm$ (no. 63). PrGe was found to exhibit two consecutive magnetic transitions; first from paramagnetic to antiferromagnetic at 44 K, then from antiferro to ferromagnetic phase at 41.5 K upon further cooling. The magnetic susceptibility at low applied magnetic field (100 Oe) shows a cusp like behavior at 44 K, and a ferromagnetic like increase at 41.5 K. The isothermal magnetization data at 1.8 K show hysteresis along all the three crystallographic directions confirming the ferromagnetic nature of the ground state. Electrical resistivity is measured in the temperature range 1.8 to 300 K with current parallel to the three principal crystallographic directions. The antiferromagnetic transition at 44 K is indicated by a small change of slope. The ferromagnetic ordering at $T_C = 41.5$ K brings a sharp drop in the electrical resistivity along all three crystallographic directions. The low temperature part of resistivity (ferromagnetic phase) data are fitted to the spin-wave gap expression 2, and a nearly isotropic spin-wave gap (about 150 K) is inferred.

The heat capacity of PrGe shows two clear anomalies at 44 K and 41.5 K confirming the bulk nature of magnetic transitions at respective temperatures. A polycrystalline sample of YGe was used as a non-magnetic reference compound, as the crystal structure of LaGe is different from that of PrGe. The magnetic part of the heat capacity is obtained by subtracting the heat capacity of YGe from that of PrGe after applying the mass renormalization (due to the different atomic masses of Y and Pr) as mentioned in [44]. In the ferromagnetic state, the magnetic contribution to the heat capacity can be fitted to the spin-wave gap expression [45], which is given by

$$C_{4\mathrm{f}} = \gamma T + C_{\mathrm{SW}}, \tag{4}$$

$$C_{\mathrm{SW}} = \alpha \left(\frac{\Delta^2}{\sqrt{T}} + 3\Delta\sqrt{T} + 5\sqrt{T^3} \right) e^{\frac{-\Delta}{T}}. \tag{5}$$

where γ is the electronic term and C_{SW} is the contribution to the ferromagnetic spin-wave excitation spectrum with an energy gap Δ and α is a constant. The above expression (5) fits well with the C_{4f} data up to 40 K, obtained values of the fitting

parameters are $\gamma = 45.9$ mJ/K^2 mol, $\alpha = 0.105$ J/(K$^{5/2}$ mol) and $\Delta = 140$ K. The spin-wave gap parameter Δ is in close agreement with the values obtained from the electrical resistivity data.

Photoemission study on PrGe single crystal

PrGe crystallizes in orthorhombic crystal structure having inversion symmetry. At the surface of a crystal, the three dimensional translational symmetry is broken. This enables the possibility of a Rashba-type spin-orbit splitting of the electronic bands at the surface [18], although this splitting may be vanishingly small. The potential gradient of the surface by itself is not sufficient to cause a directly observable splitting of the surface electronic bands into spin sub-bands [46]. It is found that the Rashba interaction at a crystal surface becomes significant only when it couples to the large intra-atomic spin-orbit coupling [47]. The intra-atomic spin-orbit coupling is significant in the high Z rare earth systems; therefore the Rashba interaction may contribute significantly to their surface electronic structure [19, 20]. The single crystal surface of PrGe exhibits a large surface localized electronic density of Pr $4f$ states (vide infra) and offers therefore a natural choices for the investigation of Rashba spin-orbit interaction.

A high resolution (10 meV) Angle Resolved Photo Emission Spectroscopy (ARPES) measurement was performed on PrGe single crystal in APE beamline at Elettra Sincrotrone Trieste, Italy [48]. The band structure and Fermi surface measurements were performed at different temperatures. Resonant photoemission (RPES) across the Pr $4d$ - $4f$ resonance shows a large enhancement of the Pr $4f$ states near the Fermi level. The band structure of PrGe [010] surface in the paramagnetic and the ferromagnetic phase is shown in Fig 4. It is found that the energy bands are symmetric with respect to Γ point. The most explicit feature here is the Rashba-type band splitting in the paramagnetic phase which is not so evident in the ferromagnetic phase. The changes in the band between paramagnetic and ferromagnetic phases are mostly observed in the binding energy range between E_F to 0.5 eV. The bands at higher binding energy show similar behavior indicating that they are of bulk origin and localized in nature.
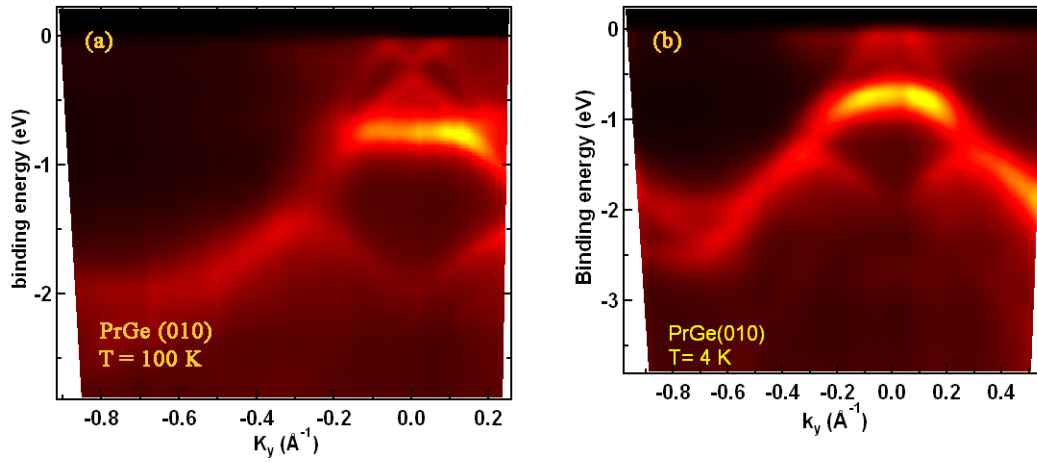
Figure 4: Band structure of PrGe [010] surface along the K_y direction in the (a) paramagnetic phase at 100 K showing clearly the split band near the Fermi surface, (b) ferromagnetic phase at 4 K showing a band structure different form that of the paramagnetic phase.

Bibliography

[1] K. Andres, J. E. Graebner and H. R. Ott, Phys. Rev. Lett **35**, 1779 (1975).

[2] Y. Ōnuki, Y. Shimizu and T. Komatsubara, J. Phys. Soc. Japan **53**, 1210 (1984).

[3] B. Barbara, J. X. Boucherle et al., Solid State Commun. **24**, 481 (1977).

[4] K. Winzer, Solid State Commun. **16**, 521 (1975).

[5] O. Trovarelli, C. Geibel, S. Mederle, C. Langhammer, F. M. Grosche, P. Gegen-wart, M. Lang, G. Sparn, and F. Steglich, Phys. Rev. Lett. **85**, 626 (2000).

[6] M. Okawa, M. Matsunami, K. Ishizaka, R. Eguchi, M. Taguchi, A. Chainani, Y. Takata, M. Yabashi, K. Tamasaku, Y. Nishino, T. Ishikawa, K. Kuga, N. Horie, S. Nakatsuji, and S. Shin, Phys. Rev. Lett. **104**, 247201 (2010).

[7] F. Steglich, J. Aarts, C. D. Bredl, W. Lieke, D. Meschede, W. Franz, and H. Schafer, Phys. Rev. Lett. **43**, 1892 (1979).

[8] V. A. Sidorov, M. Nicklas, P. G. Pagliuso, J. L. Sarrao, Y. Bang, A. V. Balatsky, and J. D. Thompson, Phys. Rev. Lett. **89**, 157004 (2002).

[9] D. Jaccard, K. Behnia, and J. Sierro, Phys. Lett. A **163**, 475 (1992).

[10] R. Movshovich, T. Graf, D. Mandrus, J. D. Thompson, J. L. Smith, and Z. Fisk, Phys. Rev. B **53**, 8241 (1996).

[11] F. M. Grosche, I. R. Walker, S. R. Julian, N. D. Mathur, D. M. Freye, M. J. Steiner and G. G. Lonzarich, J. Phys. Condens. Matter **13**, 2845 (2001).

[12] F.M Grosche, S.R Julian, N.D Mathur, G.G Lonzarich, Physica B: Condens. Matt., **223-224**, 50 (1996).

[13] G. Knebel, D. Braithwaite, P. C. Canfield, G. Lapertot, and J. Flouquet, Phys. Rev. B **65**, 024425 (2001).

[14] K. Andres and S. Darack, Phys. Rev. B **19**, 5475 (1979).

[15] P. Morin and D. Schmitt, Phys. Rev. B **26**, 3891 (1982).

[16] A. Yatskar, W. P. Beyermann, R. Movshovich, and P. C. Canfield, Phys. Rev. Lett. **77**, 3637 (1996).

[17] Masahumi Kohgi, Kazuaki Iwasa, Motoki Nakajima, Naoto Metoki, Shingo Araki, Nick Bernhoeft, Jean-Michel Mignot, Arsen Gukasov, Hideyuki Sato, Yuji Aoki, and Hitoshi Sugawara, J. Phys. Soc. Jpn. **72**, 1002 (2003).

[18] L. Petersen, P. Hedegard, Surface Science **459**, 49 (2000).

[19] O. Krupin, G. Bihlmayer, K. Starke, S. Gorovikov, J. E. Prieto, K. Dobrich, S. Blugel and G. Kainds, Phys Rev B **71**, 201403 (R) (2005).

[20] O. Krupin, G. Bihlmayer, K. M. Dbrich, J. E. Prieto, K. Starke, S. Gorovikov, S. Blgel, S. Kevan and G. Kaindl, New Journal of Physics **11**, 013035 (2009).

[21] B. Nayeb-hashemi and J. Clark, Bull. Alloy Phase Diagrams **9**, 916 (1988).

[22] A. B. Gokhale and G. J. Abbaschian, Bull. Alloy Phase Diagr. **10**, 142 (1989).

[23] K. H. J. BUschow, J. Less-Common Met., **44**, 301 (1976).

[24] J. Pierre, A. P. Murani, R. M. Galera, J. Phys. F: Et. Phys., **11**, 679 (1981).

[25] R. M. Galera, J. Pierre, and J. Pannetier, J. Phys. F: Met. Physs, **12**, 993 (1982).

[26] H. Tanida, H. S. Suzuki, S. Takagi, H. Onodera, and K. Tanigaki, J. Phys. Soc. Jpn., **75**, 073705 (2006).

[27] J. Rodrguez-Carvajal, Physica B: Condens. Matt. **192**, 55 (1993).

[28] B. Cornut and B. Coqblin Phys. Rev. B **5**, 4541 (1972).

[29] K. W. H. Stevens, Proc. Phys. Soc. London, Sect. A **65**, 209 (1952).

[30] M. T. Hutchings, Solid State Physics: Advanced in Research and Applications, edited by F. Seitz and B. Turnbull (Academic Press, New York, 1965), Vol. 16, p. 227.

[31] S. A. Shaheen, Phys. Rev. B, **36**, 5472 (1987).

[32] Satoru Noguchi, Kiichi Okuda, Hiroyuki Nojiri, Mitsuhiro Motokawa, J. Magn. Magn. Mater. 177181, 403 (1998).

[33] K. H. Bushchow, J. F. Fast, Phys. Status Solidi, **16**, 467 (1966).

[34] N. Marcano, J. I. Espeso, D. R. Noakes, G.M. Kalvius, J. C. Gomez Sal, Physica B, **359**, 269 (2005).

[35] N. Marcano, J. I. Espeso, J. C. Gomez Sal, J. Magn. Magn.. Mater., **310**, e35 (2007).

[36] Mark Ellerby, Keith A. McEwen, Jens Jensen, Phys. Rev. B, **57**, 8416 (1998).

[37] M. D. Wilding, E. W. Lee, Proc. Phys. Soc., **85**, 995 (1965).

[38] T. Takabatake, M. Shirase, K. Katoh, Y. Echizen, K. Sugiyama, T. Osakabe, J. Magn. Magn. Mater., **177-181**, 53 (1998).

[39] S. A. Shaheen, J. Appl. Phys. **63**, 3411 (1988).

[40] K. A. Gschneidner, Jr., V. K. Pecharsky, A. O. Tsokol, Rep. Prog. Phys. **68**, 1479 (2005).

[41] V. K. Pecharsky and K. A. Gschneidner Jr., Phys. Rev. Lett. **89**, 222512 (2006).

[42] A. M. Tishin and Y. I. Spichkin, The magneto caloric effect and its applications, Bristol: Institute of Physics Publishing (2003).

[43] K. A. Gschneidner, Jr., and V. K. Pecharsky, Annu. Rev. Mater. Sci. **30**, 387 (2000).

[44] M. Bouvier, P. Lethuillier and D. Schmitt, Phys. Rev. B **43**, 13137 (1991).

[45] B. Coqblin, The Electronic Structure of Rare-Earth Metals and Alloys: The Magnetic Heavy Rare-Earths (New York: Academic) p 211 (1977).

[46] H. Nakamura, T. Koga, and T. Kimura, Phys. Rev. Lett. **108**, 206601 (2012).

[47] S. LaShell, B. A. McDougall, and E. Jensen, Phys. Rev. Lett **77**, 3419 (1996).

[48] G. Panaccione, I. Vobornik, J. Fujii, D. Krizmancic, E. Annese, L. Giovanelli, F. Maccherozzi et. al., Rev. Sci. Instrum. **80**, 043105 (2009).

List of Publications

Publications arising from work related to this thesis

1. Magnetic properties of the heavy-fermion antiferromagnet $CeMg_3$
   Pranab Kumar Das, Neeraj Kumar, R. Kulkarni, and A. Thamizhavel
   Phys. Rev. B **83**, 134416 (2011).

2. Crystal growth and magnetic properties of RMg_3 (R= La, Ce and Nd)
   Pranab Kumar Das, Neeraj Kumar, R Kulkarni, and A Thamizhavel
   Journal of Physics: Conference Series **391** 012009 (2012)

3. Magnetic properties of single crystalline $CeMg_{12}$
   Pranab Kumar Das, and A Thamizhavel
   Accepted for SCES 2013 Proceeding : Journal of the Physical Society of Japan
   (JPSJ)
   arXiv:1311.4379

4. Anisotropic magnetic properties and superzone gap formation in CeGe single
   crystal
   Pranab Kumar Das, Neeraj Kumar, R Kulkarni, S K Dhar and A Thamizhavel
   J. Phys.: Condens. Matter **24** 146003 (2012)

5. Anisotropic magnetic properties and giant magnetocaloric effect of single-crystal
   PrSi
   Pranab Kumar Das, Amitava Bhattacharyya, Ruta Kulkarni, S. K. Dhar, and
   A. Thamizhavel
   Phys. Rev. B **89**, 134418 (2014)

6. Antiferro- and ferromagnetic ordering in a PrGe single crystal
   Pranab Kumar Das, K Ramesh Kumar, R Kulkarni, S K Dhar and A Thamizhavel
   J. Phys.: Condens. Matter **24** 476001 (2012)

7. Anisotropic magnetocaloric properties of PrGe
   Pranab Kumar Das, Amitava Bhattacharyya, Ruta Kulkarni, S. K. Dhar, and A. Thamizhavel
   Manuscript under preparation

8. Rashba spin-orbit anisotropy at the surface of PrGe single crystal
   Soma Banik, Pranab Kumar Das, Azzedine Bendounan, Ivana Vobornik, A. Thamizhavel, P. Sastry, A. K. Sinha, D. M. Phase, S. K. Dhar, S. K. Deb
   Manuscript under preparation

Other publications

1. Antiferromagnetic ordering in $EuPtGe_3$
   Neeraj Kumar, Pranab Kumar Das, R Kulkarni, A Thamizhavel, S K Dhar and P Bonville
   J. Phys.: Condens. Matter **24** 036005 (2012)

2. Strongly correlated electron behavior in single crystalline $U_2Os_3Al_9$
   Neeraj Kumar, Pranab Kumar Das, Ruta Kulkarni, A Thamizhavel and S K Dhar
   J. Phys.: Conf. Series**391**,012033 (2012).

3. Crystal growth and magnetic properties of equiatomic CeAl
   Pranab Kumar Das and A. Thamizhavel
   Submitted to SCES -2014 Conference Proceedings (IoP conference series).

Contents

List of Figures

Chapter 1

Introduction

The interest in the studies on rare-earth intermetallic compounds stems from their unusual magnetic and electronic properties. The magnetic properties of rare earths arise from the partially filled $4f$-shell which is localized even in a metallic environment. The $4f$-derived local moments are exchange coupled via the indirect Ruderman-Kittel-Kasuya-Yosida (RKKY) [1, 2, 3] interaction, which leads to magnetic ordering. In some compounds of Ce and Yb there is a competition between the RKKY and the Kondo [4] interaction. The local Kondo interaction arises when an appreciable hybridization between the localized rare earth $4f$ orbital and the conduction electrons leads to a net antiferromagnetic $s - f$ exchange interaction between the rare earth spins S and the conduction electrons. The relative strengths of these two interactions give rise to various interesting phenomena in some Ce and Yb based compounds such as magnetic ordering, intermediate valence behavior, Kondo lattice, heavy fermion, unconventional superconductivity etc. [5, 6, 7, 8, 9, 10, 11, 12, 13, 14]. Along with these interesting physical properties, some heavy fermion compounds provide the cleanest evidence of quantum phase transition [15, 16]. The characteristic energy scale of heavy fermion compounds is several order of magnitude smaller than that of normal metals due to their high effective mass, $\epsilon(k) = \hbar^2 k^2 / 2m^*$, and this characteristic low energy scale can be controlled by some non-thermal control parameters like external magnetic field, hydrostatic pressure and chemical doping. It is therefore of interest to explore the magnetic behavior of Ce compounds. The primary motivation of this thesis is to explore the rich physical properties of Ce based binary

intermetallic compounds by growing good quality single crystals. In some cases we have also studied the physical properties of the analogous Pr based compounds. The anisotropic physical properties of the crystals are studied by measuring the magnetic susceptibility, magnetization, heat capacity, electrical transport etc. The outline of this thesis is as follows:

In this chapter an introduction to magnetism, rare earths, exchange interactions, crystal electric field, superzone gap and some theoretical concepts are presented. Chapter 2 presents the description of various crystal growth methods and experimental methods used in this study. The experimental results are presented in Chapter 3, 4, 5, and 6. Chapter 3 presents the results of heavy fermion Kondo lattice compound $CeMg_3$ and magnesium rich $CeMg_{12}$. Chapter 4 focuses on the anisotropic magnetic properties of binary compounds CeGe and CeSi. Chapter 5 presents the anisotropic magnetic properties and magnetocaloric effect of PrGe and PrSi. Finally the Chapter 6 presents the electronic band structure study of PrGe using Angle Resolved Photo Emission Spectroscopy (ARPES).

1.1 Magnetism

The magnetism in a free atom arises due to its electronic spin and orbital angular momentum. The magnetic moment (μ) and the total angular momentum $\mathbf{J}$ of a free atom are related by $\mu = g_J \mu_B \mathbf{J}$, where $\mathbf{J}(= \mathbf{L} + \mathbf{S})$; $\mathbf{L}$ and $\mathbf{S}$ are the total orbital and spin angular momentum of the free atom, respectively, μ_B is the Bohr magneton and g_J is the Lande g factor and given by, $g_J = 1 + \frac{J(J+1)+S(S+1)-L(L+1)}{2J(J+1)}$.

The orbital and the spin quantum numbers of the ground state are given by the Hund's rule:

- The combination of $\vec{s}_i$ that gives the lowest energy consistent with the Pauli exclusion principle is that with the highest value of $(2S + 1)$.

- When the first rule is satisfied, if there are several possible l values having same $(2S + 1)$, that with the largest l will be the most stable.

- For an electronic shell that is less than half-filled, J is given by $J = |L - S|$,

and for an electronic shell that is more than half-filled, $J = |L + S|$, and $J = S$ for the half filled state.

Now in the absence of any external magnetic field, all the atoms with equal magnetic moments have the same energy. But if an external magnetic field $\vec{B}$ is applied, the degeneracy of the $(2J + 1)$ state is lifted. If the magnetic field is applied along the z-axis, then the different eigenstates are characterized by the magnetic quantum number m_j, and the corresponding energies are:

$$E_{m_j} = - < lsjm_j|\vec{\mu}|lsjm_j > \cdot\vec{B} = -g\mu_B m_j B \tag{1.1}$$

Here the total energy of the system depends on the thermal occupation of the $(2J + 1)$ sub-levels, and the thermal occupation of the levels are given by the law of statistical mechanics:

$$P(m_j) = \frac{exp(-E_{m_j}/k_B T)}{\sum exp(-E_{m_j}/k_B T)} \tag{1.2}$$

The free energy of the system is given by the following expression:

$$F = -Nk_B T \sum_{n=1}^{2J+1} exp(-\frac{E_{m_j}(B)}{k_B T}) \tag{1.3}$$

where N is the total number of magnetic atoms in the system. The magnetization (M) of the system can be obtained from the free energy of the system:

$$M = -\frac{1}{V}\frac{\partial F}{\partial H} = -\frac{N}{V}g_J\mu_B J B_J(\frac{g_J\mu_B JH}{k_B T}) \tag{1.4}$$

where V is the volume of the system, and $B_J(x)$ is the Brillouin function. At high temperature, $k_B T >> g_J\mu_B B$, the susceptibility can be approximated to

$$\chi = \frac{\partial M}{\partial H} = N_A\frac{(g_J\mu_B)^2}{3}\frac{J(J + 1)}{k_B T} = N_A\frac{\mu_{eff}^2\mu_B^2}{3k_B}\frac{1}{T} \tag{1.5}$$

3

where $\mu_{eff} = g_J \mu_B \sqrt{J(J+1)}$. Thus within this approximation the susceptibility varies as inverse of temperature. This is the Curie law of paramagnetism.

1.2   Rare earths and their intermetallic compounds

The rare earth atoms have the common electronic configuration: $[Xe]4f^n5d^16s^2$; inert Xe core, incompletely filled $4f$ shell and outer $5d$ and $6s$ electronic shells. La metal is the first member of the so-called Lanthanide series, with no $4f$ electron in its trivalent state; while from Ce onwards, the $4f$ shell begins to fill up with electrons, with one electron in the $4f$ shell of Cerium metal and two $4f$ electrons in the Pr and so on. The number of $4f$ electrons gradually increases up to Lu, where there is completely filled $4f$ shell (14 electrons). Because of the incompletely filled $4f$ shell, the rare earth elements (Ce - Yb) posses permanent magnetic moment. The $4f$ electronic shell, responsible for the magnetic moment, is well localized in rare earth atoms. A schematic of the radial wave function of various orbitals of Ce is shown in Fig. 1.1. As we see in the figure, the $4f$ shell is well localized inside the atom, and shielded by the $5s$, $5p$, $5d$, and $6s$ orbitals. The radius of $4f$-shell is about 0.3 Å, which is an order of magnitude less than the typical inter-atomic distances in a solid. So there is hardly any overlap between the $4f$ orbitals of neighboring rare earth atoms in a solid. In a crystalline environment the atoms are arranged in a regular ordered pattern to form the crystalline solid. In the solid the $4f$ shell still remains well localized, while the outer $5d$ and $6s$ electrons become delocalized into *Bloch states*, extending throughout the solid, and form the conduction band. Therefore, one can consider the rare earth intermetallic compounds as a lattice of localized $4f$ derived moments embedded in a sea of conduction electrons. The conduction electrons play an important role in the magnetic properties of rare earth intermetallic compound by mediating the indirect magnetic interaction between the $4f$ electrons.

The primary interaction between these localized moments of rare earth atoms is mediated via the conduction electrons, the so-called Ruderman-Kittel-Kasuya-Yosida (RKKY) interaction, which leads to magnetic ordering in these local moment systems.
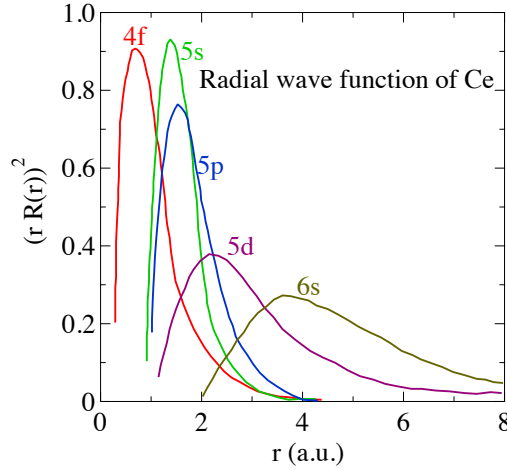
Figure 1.1: Schematic representation of the radial wave function of different electronic orbitals of Ce atom.

1.3 RKKY interaction

In the case of rare-earth atoms, due to the highly localized nature of the $4f$ electrons, the interaction between magnetic ions is generally mediated by the conduction electrons. A localized magnetic moment spin-polarizes the conduction electrons and this polarization in turn couples to a neighboring localized magnetic moment at a distance r away. The exchange interaction between the localized magnetic moments is thus indirect and this type of interaction is knowns as the RKKY interaction. The RKKY interaction has the following form [17]:

$$\mathcal{J} = J_0 \frac{2k_{\mathrm{F}}r cos(2k_{\mathrm{F}}r) - sin(2k_{\mathrm{F}}r)}{(2k_{\mathrm{F}}r)^4}, \tag{1.6}$$

where $\mathcal{J}$ is the RKKY exchange coefficient, k_{F} is the Fermi wave vector, r = $|\mathbf{R}_{\mathrm{i}} - \mathbf{R}_{\mathrm{j}}|$ is the distance between the two interacting magnetic ions and J_0 is the strength of the interaction. This indirect interaction extends to far distances and damps with a sinusoidal $2k_{\mathrm{F}}r$ oscillation also called Friedel oscillation as shown in Fig. 1.2. It is evident from the figure that the RKKY interaction is oscillatory over the distance. Depending upon the strength of exchange constant $(\mathcal{J})$, the ground state could be ferro or antiferromagnetic. The magnetic ordering temperature in the mean

5
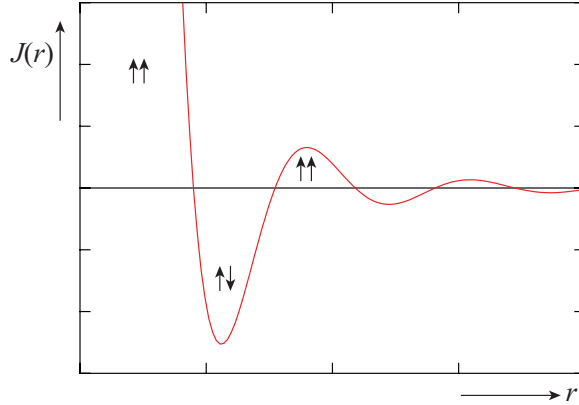
Figure 1.2: Distance dependence of the RKKY exchange $\mathcal{J}(r)$.

field approximation is roughly proportional to the de Gennes factor, $(g_J - 1)^2 J(J+1)$. Here g_J is the Landé g-factor and J is the total angular momentum.

1.4 Kondo effect and heavy fermions

There also exists an additional local Kondo-exchange interaction between the $4f$ moment and the conduction electrons in some compounds (mainly Ce and Yb based), which is antiferromagnetic. Below a characteristic temperature (called the Kondo temperature, T_K) the conduction electrons screen the $4f$ derived local moments and yield a non-magnetic ground state. In some compounds of Ce and Yb the $4f$-level lies close to Fermi-level, which enhances the hybridization between the $4f$ level and the band states resulting in an antiferromagnetic local $s - f$ exchange interaction, which is a prerequisite for Kondo effect.

The study of Kondo effect dates back to several decades when a low temperature resistivity minimum was observed in alloys where dilute magnetic impurities, like Fe, Co, Mn (about 1 atomic %) were dissolved in a non-magnetic host like Au, Cu etc. Kondo showed theoretically that the negative logarithmic increase in the electrical resistivity at low temperatures is due to the spin-flop scattering of the conduction electrons by localized magnetic moment of impurity atoms [4]. In the case of transition metal $3d$ alloys, the Kondo effect can be observed only at very low concentration of $3d$ magnetic impurities. This is because the degeneracy of the

localized spins is very important for the Kondo effect. When the concentration of $3d$ magnetic impurities increases, the $3d$ atoms would come near each other and thus the overlapping or interaction between the $3d$ shells would occur, which would in principle lift the degeneracy of the impurity spin and suppress the Kondo spin-flop process.

Since the observation of Kondo effect in the non-magnetic CeAl$_3$ compound [18], several rare-earth compounds, in particular Ce based intermetallic compounds were found to show anomalous behavior in the electrical resistivity reminiscent of impurity Kondo effect. In the case of Cerium based intermetallic compounds, the concentration of $4f$ ions are so high that they form a crystalline lattice which cannot be considered as impurities and hence the appearance of Kondo-like behavior has been named as dense Kondo lattice. The Kondo effect has been very intensively studied in Ce$_x$La$_{1-x}$Cu$_6$ single crystalline samples by Ōnuki's research group [19], and several other systems. The Kondo effect can be understood as follows: at temperature much higher than the Kondo temperature T_K, the localized spin $\mathbf{S}(\uparrow)$ and the conduction electron $\mathbf{s}(\downarrow)$ do not interact, for temperature just above T_K the conduction electron and the f electron interacts weakly and for $T < T_K$, the localized spin $\mathbf{S}(\uparrow)$ is coupled antiferromagnetically with the conduction electron $\mathbf{s}(\downarrow)$ resulting in the singlet state $\mathbf{S}(\uparrow) \cdot \mathbf{s}(\downarrow) \pm \mathbf{S}(\downarrow) \cdot \mathbf{s}(\uparrow)$, thereby screening the local f electron and hence results in a non-magnetic ground state. Here the Kondo temperature T_K is the single energy scale. In other words, non-magnetic ground state is thought to be due to the formation of a spin-compensating cloud of the conductions electrons around the local moment, as shown schematically in Fig. 1.3. There are several consequences of the Kondo effect; the system goes from a state with existence of local moments at $T >> T_K$ to a non-magnetic state at $T < T_K$. A logarithmic increase in the electrical resistivity is observed upon cooling, due to the scattering of conduction electrons by the local magnetic moments. A reduction in the saturation value of magnetization, and a reduction in the heat capacity jump at the magnetic ordering of the system compared to its mean field value are often seen in those compounds where the Kondo interaction is a weak perturbation on the more stronger RKKY interaction.

The heavy fermion state in cerium compounds can be roughly understood as follows. At high temperatures the magnetic susceptibility obeys the Curie-Weiss law with an effective magnetic moment of Ce^{3+}, namely 2.54 μ_B/Ce. As the temperature decreases, the electronic states changes. At low temperature, the magnetic entropy
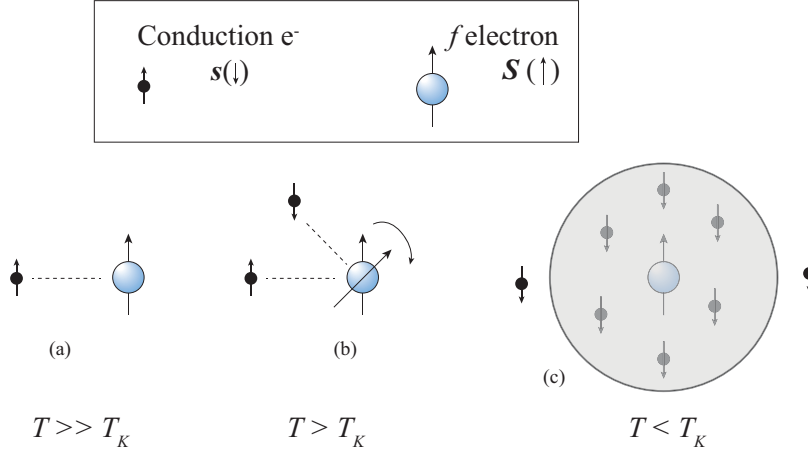
Figure 1.3: Cartoon diagram of Kondo effect: (a) for $T \gg T_K$ the conduction electron and the f electron do not interact, (b) for $T > T_K$ there is a weak interaction and (c) for $T < T_K$ the conduction electrons screen the local magnetic moments of f electrons.

of doublet ground state of $4f$ levels, $R \ln 2$, is obtained by integrating the magnetic specific heat C_m in the form of C_m/T over the temperature. The magnetic part of the heat capacity can be converted to electronic specific heat γT via the many-body Kondo effect by following expression:

$$R \ln 2 = \int_0^{T_K} \frac{C_{m}}{T} dT, \tag{1.7}$$

$$C_m = \gamma T, \tag{1.8}$$

thus

$$\gamma = \frac{R \ln 2}{T_K} = \frac{5.8 \times 10^3}{T_K} (\text{mJ/K}^2 \cdot \text{mol}). \tag{1.9}$$

For example, the γ value of the dense Kondo lattice compound $CeCu_6$, is of the order 1600 mJ/K^2·mol and 350 mJ/K^2·mol in another Kondo compound $CeRu_2Si_2$. The localized electronic state is thus changed into an f-derived band with a flat energy vs momentum dispersion possessing an extremely large effective mass. Therefore, the Kondo lattice system with large γ value are often referred to as heavy fermion or heavy electron system [14].

1.5 Competition between RKKY and Kondo interactions

The magnetism exhibited by Kondo lattice compounds arises as a competition between the indirect RKKY interaction and the on-site Kondo effect. The two energy scales T_K and T_{RKKY} are given by the expressions:

$$T_{RKKY} \propto D(\epsilon_F)|J_{cf}^2|, \qquad (1.10)$$

and

$$T_K \propto \exp\left(\frac{-1}{D(\epsilon_F)|J_{cf}^2|}\right) \qquad (1.11)$$

where $D(\epsilon_F)$ is the electronic density of states at the Fermi energy ϵ_F, J_{cf} is the exchange interaction term between the conduction electron and the local moment. J_{cf} is related to the hybridization potential V_{sf}, the $4f$ level position with respect to the Fermi level E_F, and to the Hubbard intra-site Coulomb repulsion U of two electrons with opposite spins in the same magnetic $4f$ atom. For V_{sf}, $E_F - E_{4f} \ll U$, the J_{cf} is given by the following expression:

$$J_{cf} \approx \frac{V_{sf}^2}{E_F - E_{4f}}. \qquad (1.12)$$

In most of the rare-earth intermetallic compounds, the $4f$ levels lie deep inside the Fermi sea and hence the J_{cf} is small. For small J_{cf} the energy scale T_K which depends exponentially on J_{cf} is negligible with respect to T_{RKKY} and the system orders magnetically [20]. This competing interaction between the RKKY interaction and the Kondo effect is very well explained by the famous Doniach diagram which was conceptualized by Doniach [21] as shown in Fig. 1.4. For small values of J_{cf} the system undergoes magnetic ordering due to the dominance of RKKY interaction and for larger values of J_{cf}, T_K becomes stronger and the system does not show magnetic ordering. For a particular value of J_{cf} both T_{RKKY} and T_K are equal and this point
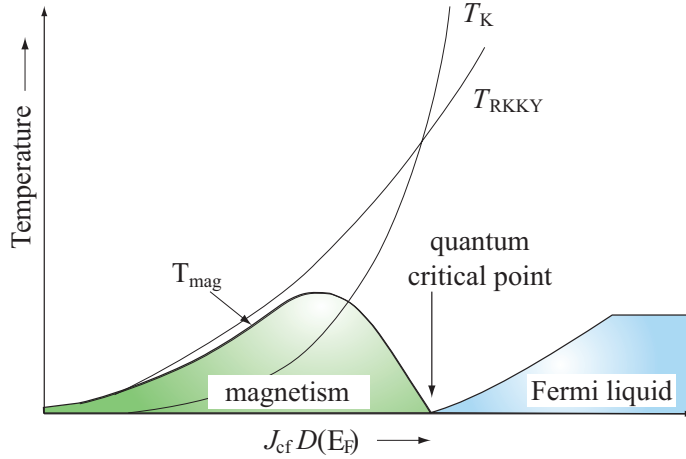
Figure 1.4: Doniach phase diagram depicting the competition between the RKKY interaction and the Kondo effect.

is termed as the quantum critical point (QCP). Above QCP, Kondo-lattice paramagnetism is realized (a non-magnetic ground state) and consequently the valency of the f electron becomes unstable, leading to a heavy fermion system. In the heavy fermion systems, the electrical resistivity varies as $\rho = \rho_0 + AT^2$, where ρ_0 is the residual resistivity. The coefficient $\sqrt{A}$ correlates with an enhanced Pauli susceptibility $\chi (T \rightarrow 0) \simeq \chi_0$ and with large electronic specific heat coefficient $C/T (T \rightarrow 0) \simeq \gamma$.

Experimentally, the J_{cf} can be controlled by pressure, magnetic field or the composition. In general hydrostatic pressure is usually employed to tune J_{cf}. The magnetic ordering decreases with increasing pressure and essentially becomes zero for a critical pressure P_c which is the quantum critical point regime. Around QCP, the heavy fermion state is realized as mentioned above, together with non-Fermi liquid behavior and occasionally appearance of superconductivity [22]. The non-Fermi liquid (nFL) behavior around the QCP is one of the recent topics of interest in the f electron system. The nFL regime has the following characteristics: The electrical resistivity varies as T^n with $n < 2$ and the specific heat C/T shows a $-\log(T)$ behavior at low temperature.

Because of these two competing interactions, RKKY and Kondo, depending upon their relative strengths, there is a diversity of ground states among the Kondo lattice intermetallic compounds with interesting physical properties, e. g., heavy fermion Kondo lattice without any long range order, heavy fermion Kondo lattice that orders

magnetically at low temperature, pressure induced superconductivity etc. This is our main motivation to explore the Ce based compounds for probable interesting physical properties. In view of these, we have grown single crystals of $CeMg_3$, $CeMg_{12}$, $CeGe$ and $CeSi$ binary compounds and investigated their physical properties.

Apart from their rich and interesting physical properties, rare earth intermetallic compounds are important from various technological application point of view. For example, rare earth intermetallic $SmCo_5$ is used as permanent magnet. $Gd_5Si_2Ge_2$ is a giant magnetocaloric material, used for magnetic refrigeration. In this thesis investigations on some Pr-based intermetallic compounds have been performed which exhibit reasonably large magnetocaloric effect. They can be used for magnetic refrigeration at low temperatures.

Besides the RKKY and Kondo exchange interaction, an additional prominent interaction that exists in the rare-earth intermetallic system is the crystal electric field (CEF). In an intermetallic system the rare earth atoms are no longer isolated free atoms, rather they are surrounded by other ions, which produce inhomogeneous electric field in the lattice. This inhomogeneous electric field, similarly as magnetic field (Zeeman effect), can lift the degeneracy of $(2J + 1)$ degenerate ground state of rare earth atoms. CEF can modify various physical properties, like magnetic susceptibility, isothermal magnetization, electrical transport, heat capacity etc. In the next section the CEF effect is discussed.

Non-magnetic analog compounds: Sometime we need to estimate only the $4f$ magnetic contribution of rare earth atom in an intermetallic system. In order to do that, we prepare isostructural compound of the system, with non-magnetic La or Lu or Y ions in place of corresponding magnetic rare earth (Ce - Yb) atom of the system. Because of the chemical similarity of rare earths (La - Lu), generally they form an isostructural series of compounds at some specific stoichiometry. In the case of La, Lu or Y, the compounds are non-magnetic because La, Lu and Y do not have any unpaired $4f$ electrons. These compounds are then taken as the non-magnetic reference compounds for a magnetic rare earth compound with same structure and stoichiometry. For example, one often assumes that the phonon contribution to the heat capacity and electrical resistivity of magnetic rare earth intermetallic compound is same as in the non-magnetic analog compound. In our study, we prepared La or

Y analog compounds of our magnetic systems in order to extract the magnetic $4f$ contribution alone.

1.6   Crystal Electric Field

An electric field may lift the degeneracy of the atom's ground state, similar to magnetic field (Zeeman effect). Such an electric field originates from the ions positioned regularly in a crystal. The rare earth atoms in an intermetallic compound are no longer isolated atoms, rather they are surrounded by other ions. These surrounding ions produce inhomogeneous electric field in the crystalline environment. This electric field is named as crystal electric field (CEF) which lifts, at least partially, the degeneracy of rare earth's $(2J+1)$-fold degenerate ground state. This will modify the magnetic properties of a rare earth intermetallic compound. The symmetry of the nearest-neighbor coordination is determined by the crystal structure. According to Kramer's theorem, there remains a minimum degeneracy in some systems. Kramer's theorem states that:

- If the total angular momentum of an ion is half integer, there remains a degeneracy of at least 2 (doublet state) which cannot be removed by the CEF. These systems are called *Kramer's ions.*

- If the total angular momentum of an ion is integer, the degeneracy maybe fully lifted. But in practice, there might be a mixture of singlet, doublet, triplet states. Such a system is known as so-called *non-Kramer's ion.*

The number of CEF split energy levels of a system depends on the crystal symmetry of the system; a lower symmetry of the system produces more number of the non-degenerate energy levels. For example, a quartet level can be found only in a system having cubic symmetry. A representative level scheme of the $4f$ electron in Ce^{3+} is shown in Fig.1.5. The spin orbit coupling splits the 14-fold degenerate Ce^{3+} into $J = 5/2$ and $J = 7/2$ multiplets. The energy separation of the $J = 7/2$ multiplet is of the order of 3000 K and hence can be ignored as our measurements are limited to a maximum temperature of 300 K (room temperature). The crystal electric field
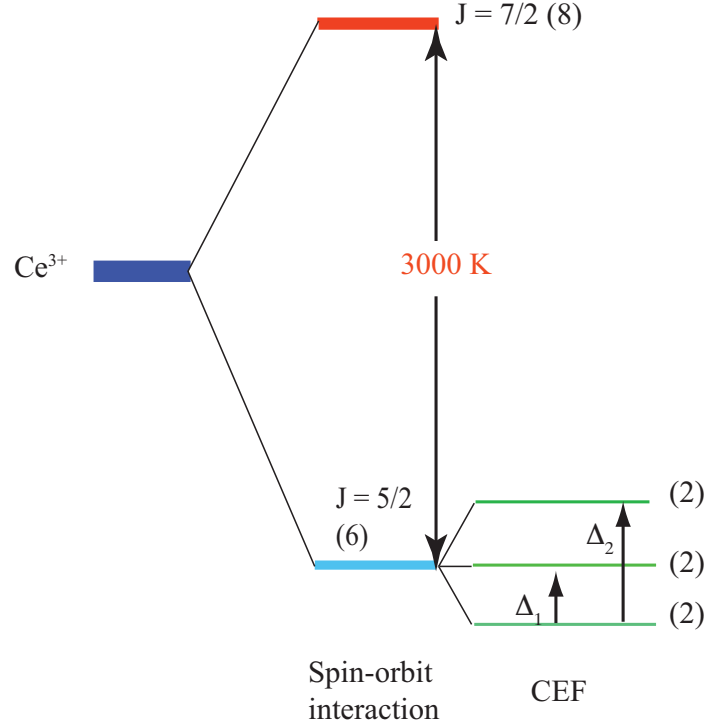
Figure 1.5: Energy level scheme of Ce^{3+} ion.

produced by the surrounding ions in a non-cubic site symmetry splits the $2J + 1$ degenerate $J = 5/2$ level, into a maximum of three doublets. The CEF level splitting however depends very much on the site symmetry of the rare-earth atom in the crystal. If the Ce atom occupies the high symmetry Cubic site, then CEF splitting may lead to a quartet ground state and an excited doublet state and also there is a possibility of ground state doublet and excited quartet depending on the charge distribution of the $4f$ ions.

We need to solve the crystal field Hamiltonian in order to calculate the magnetic properties. As we have already discussed that the charge distribution of $4f$ shell is very localized, the wave function of one ion does not overlap with the neighboring ions, thus the charge distribution satisfies the Laplace's equation. Therefore the electrostatic potential is given by the following expression:

$$V_c(\vec{r}) = \frac{1}{4\pi\epsilon_0} \sum_i \frac{q_i}{|\vec{r} - \vec{R_i}|} \tag{1.13}$$

13

where q_i are electrical charge of neighboring ions i where $\vec{r}$ is the position vector of the $4f$ electron in Ce^{3+} and $\vec{R}_i$ is the position vector of the neighboring ions.

Considering the charge distribution of the f electron $\rho(r)$, the static potential energy is expressed as:

$$\int \rho(r) V_c(r) d^3 r. \tag{1.14}$$

The CEF Hamiltonian corresponding to Eqn. 1.13 and Eqn. 1.14 can be represented in simpler form by using the Wigner-Eckart's theorem and using Steven's operator as follows:

$$H_{CEF} = \sum_{n,m} B_n^m O_n^m \tag{1.15}$$

where B_n^m are the CEF parameters and O_n^m are the Stevens' operators [23]. B_n^m can be calculated from the different models or can be determined from fitting the experimental data. It can be shown that for rare earths, the summation can not exceed $n > 6$. Furthermore, n must be even owing to inversion symmetry of the crystal field potential, i.e., the above summation for f electrons is only over $n = 2, 4, 6$. The details of the Stevens' operators method is given by Hutchings [24].

As an example, let us consider the case of Ce^{3+} ion in a cubic crystal field environment. The CEF Hamiltonian for a cubic site symmetry is given by,

$$\mathcal{H}_{CEF} = B_4^0 (O_4^0 + 5O_4^4) + B_6^0 (O_6^0 - 21O_6^4). \tag{1.16}$$

For Ce^{3+}-ion, $L = 3, S = 1/2, J = 5/2$. The 6-fold degenerate $2J + 1$ multiplet splits by the CEF effect. For $J = 5/2$, O_6 terms are zero. The Stevens operators O_4^0 and O_4^4 are given by

$$O_4^0 = 35J_z^4 - 30J(J+1)J_z^2 + 25J_z^2 - 6J(J+1) + 3J^2(J+1)^2 \tag{1.17}$$

$$O_4^4 = \frac{1}{2}(J_+^4 + J_-^4) \tag{1.18}$$

where $J_\pm = J_x \pm iJ_y$. The Stevens operator can be represented by (6×6) matrix. The CEF Hamiltonian now can be expressed as:

$$\mathcal{H}_{\mathrm{CEF}} = \begin{pmatrix} 60B_4^0 & 0 & 0 & 0 & 60\sqrt{5}B_4^0 & 0 \\ 0 & -180B_4^0 & 0 & 0 & 0 & -60\sqrt{5}B_4^0 \\ 0 & 0 & 120B_4^0 & 0 & 0 & 0 \\ 0 & 0 & 0 & 120B_4^0 & 0 & 0 \\ 60\sqrt{5}B_4^0 & 0 & 0 & 0 & -180B_4^0 & 0 \\ 0 & 60\sqrt{5}B_4^0 & 0 & 0 & 0 & 60B_4^0 \end{pmatrix}$$

The crystal field split energy levels are obtained by the following expression

$$\mathcal{H}_{\mathrm{CEF}}|i\rangle = E_i|i\rangle. \tag{1.19}$$

For the cubic crystal field, the following wave functions and energies are obtained by diagonalizing the above matrix.

$$\left.\begin{aligned} |\Gamma_7^\alpha\rangle &= \tfrac{1}{\sqrt{6}}|\tfrac{5}{2}\rangle - \sqrt{\tfrac{5}{6}}|\tfrac{-3}{2}\rangle \\ |\Gamma_7^\beta\rangle &= \tfrac{1}{\sqrt{6}}|\tfrac{-5}{2}\rangle - \sqrt{\tfrac{5}{6}}|\tfrac{3}{2}\rangle \end{aligned}\right\} E_{\Gamma_7} = -240B_4^0 \tag{1.20}$$

$$\left.\begin{aligned} |\Gamma_8^\nu\rangle &= \sqrt{\tfrac{5}{6}}|\tfrac{5}{2}\rangle + \sqrt{\tfrac{1}{6}}|\tfrac{-3}{2}\rangle \\ |\Gamma_7^\kappa\rangle &= \sqrt{\tfrac{5}{6}}|\tfrac{-5}{2}\rangle + \sqrt{\tfrac{1}{6}}|\tfrac{3}{2}\rangle \\ |\Gamma_8^\lambda\rangle &= |\tfrac{1}{2}\rangle \\ |\Gamma_8^\mu\rangle &= |\tfrac{-1}{2}\rangle \end{aligned}\right\} E_{\Gamma_8} = 120B_4^0 \tag{1.21}$$

The ground state with the energy level $-240B_4^0$ is named as Γ_7 and the energy level $120B_4^0$ is named as Γ_8. Figure 1.6 shows the spatial charge distribution of the
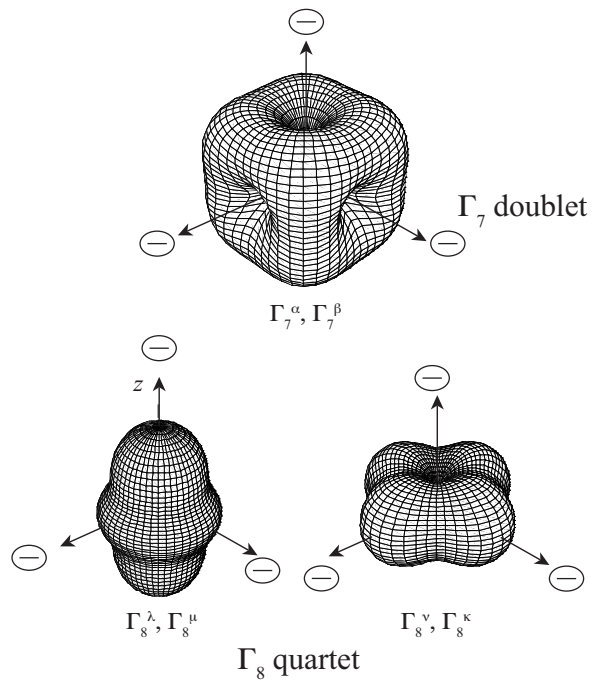
Figure 1.6: The $4f$ charge cloud of Ce^{3+} ion in a cubic crystal field. The $4f$ electron cloud will repel the negative crystal field charges and hence in this case Γ_7 will be the ground state and the Γ_8 will be the excited state.

Γ_7 and Γ_8 states. The quartet Γ_8 charge cloud extends along the x, y, z directions. On the other hand, the doublet Γ_7 extends along the $< 111 >$ direction. Since the negative $4f$ charges and the negative crystal-field charges repel each other, the most preferred ground state in this case will be Γ_7 while Γ_8 will be the excited state. This repulsion of the charge cloud and the negative crystal field charges are the source of magnetocrystalline anisotropy.

The sign of the crystal field parameter B_4^0 determines the ground state degeneracy of the rare earth system. If B_4^0 is positive, the ground state is a doublet; on the other hand if B_4^0 is negative, the ground state will be a quartet. Similarly, for the rare-earth atom occupying a tetragonal site symmetry, the sign of crystal field parameter B_2^0 determines if the compound will have an easy plane or easy direction. For example, in the case of CeT_2Ge_2 (T = Au, Cu and Ru) the B_2^0 parameter is negative and the easy axis of magnetization is along the [001] direction [25]. On the other hand, in $CeAg_2Ge_2$ the B_2^0 parameter is positive where easy axis of magnetization is along [100] direction [26], and ab-plane is the easy plane.

As mentioned earlier, if the number of f electron is odd, the total angular momentum J is half-integer, which is the case for Ce^{3+}, Nd^{3+}, Sm^{3+}, Dy^{3+}, Er^{3+} and Yb^{3+}, the crystal field split degenerate $4f$ energy level always possesses a doublet ground state, these ions are called Kramer's ions and the doublet is often referred to as Kramer's doublet. Irrespective the site symmetry of the rare-earth ions, the ground state for half integral J will always be a doublet ground state. Runciman [27] has considered the general problem of calculating the number of levels a state of a given J will be split into for each of the thirty-two crystallographic point groups and has shown that the point groups may be classified under four headings as follows:

1. Cubic: O_h, O, T_d, T_h, T.

2. Hexagonal: $D_{6h}, D_6, C_{6v}, C_{6h}, C_6, D_{3h}, C_{3h}, D_{3d}, D_3, C_{3v}, S_6, C_3$.

3. Tetragonal: $D_{4h}, D_4, C_{4v}, C_{4h}, C_4, D_{2d}, S_4$.

4. Lower symmetry: $D_{2h}, D_2, C_{2v}, C_{2h}, C_2, C_s, S_2, C_1$.

A calculation of the splitting for integral J has shown that all point groups within one of these four categories produce the same splitting, and the number of splittings

Table 1.1: Number of splittings of the degenerate levels for half integral J

J	0	1	2	3	4	5	6	7	8
Cubic	1	1	2	3	4	4	6	6	7
(n_3, n_2, n_1)	(001)	(100)	(110)	(201)	(211)	(301)	(312)	(411)	(421)
Hexagonal	1	2	3	5	6	7	9	10	11
Tetragonal	1	2	4	5	7	8	10	11	13
Lower Symmetry	1	3	5	7	9	11	13	15	17

Table 1.2: Number of splittings of the degenerate levels for integral J

J	$\left(\frac{1}{2}\right)$	$\left(\frac{3}{2}\right)$	$\left(\frac{5}{2}\right)$	$\left(\frac{7}{2}\right)$	$\left(\frac{9}{2}\right)$	$\left(\frac{11}{2}\right)$	$\left(\frac{13}{2}\right)$	$\left(\frac{15}{2}\right)$
Cubic	1	1	2	3	3	4	5	5
All other symmetries	1	2	3	4	5	6	7	8

for given J is listed in Table 1.1. The number of triply (n_3), doubly (n_2) and singly(n_1) degenerate are mentioned below the total number of levels for the cubic symmetry. For example, the total angular moment $J = 4$, for Pr atom and there are $(2J+1) = 9$ degenerate levels. In a crystalline lattice, if the site symmetry of Pr is cubic then the CEF will lead to 4 splittings of the 9 degenerate levels, with two triplets, one doublet and a singlet; where as in the case of lower site symmetries like orthorhombic site symmetry, there will be 9 splittings, which means each level will be a singlet. For the half integral spin of J, the splittings are given in Table 1.2. For example, $J = 5/2$ for Ce and if Ce atom possesses a cubic site symmetry the crystal field levels will spit into two levels a ground state and an excited state. On the other hand, if the Ce atom possesses non-cubic site symmetry, then the degenerate levels will split into 3, leading to a ground state, first excited state and a second excited state.

There are number of physical properties which get modified due to the crystal electric field. Some of the properties depend solely on the degeneracy of the energy levels, while some depends on the degeneracy and the matrix element between the energy levels. In following sections we will discuss various physical properties that get modified because of the crystal electric field level splitting.

1.6.1   Schottky heat capacity

Schottky heat capacity arises due to the discreteness of the energy levels in the system. This discreteness of the energy levels occurs due the crystal electric field. When we change the temperature of a system due to the varying thermal population of various crystal field levels, the free energy of the system changes. The energy and hence the heat capacity of a system can be calculated in the following way. Let us consider that due to crystal electric field a system splits into N levels having energy of E_i and degeneracy g_i for the ith state. The partition function of the system is given by

$$Z = \sum_{i=1}^{N} g_i exp(-E_i/k_B T) \tag{1.22}$$

the energy of the system can be obtained from the following expression:

$$\bar{E} = -\frac{\partial}{\partial \beta}[ln(Z)] = \frac{\sum_{i=1}^{N} g_i E_i exp(-E_i/k_B T)}{\sum_{i=1}^{N} g_i exp(-E_i/k_B T)} \tag{1.23}$$

where $\beta = 1/k_B T$. Next, the heat capacity of the system can be calculated by taking temperature derivative of energy.

$$C = \frac{1}{k_B T^2} \frac{(\sum_{i=1}^{N} g_i exp(-E_i/k_B T))(\sum_{i=1}^{N} g_i E_i^2 exp(-E_i/k_B T)) - (\sum_{i=1}^{N} g_i E_i exp(-E_i/k_B T))^2}{(\sum_{i=1}^{N} g_i exp(-E_i/k_B T))^2}$$
$$\tag{1.24}$$

1.6.2   Magnetization and magnetic susceptibility

Two main changes in the magnetic susceptibility due to CEF effect are (a) the anisotropy in the high temperature (paramagnetic phase) range, and (b) the deviation of inverse susceptibility at low temperature from its linear behavior. In the magnetically ordered state the anisotropy manifests itself as easy-axis or easy-plane of magnetization. The crystal field changes the charge distribution of $4f$ electronic

cloud substantially, which causes anisotropy in the magnetic susceptibility. And because of the CEF the $(2J+1)$ degeneracy is lifted, thus with temperature the thermal population of these levels changes causing the deviation of liner behavior of inverse susceptibility with temperature.

In order to calculate the magnetic susceptibility and isothermal magnetization subjected to both crystal electric field and external magnetic field, The CEF Hamiltonian together with the Zeeman term has to be diagonalized:

$$H = B_l^m O_l^m(\mathbf{J_i}) - gJ_i\mu_B\mathbf{J_i}H_i^e \tag{1.25}$$

Then the expectation value of angular momentum $\langle\mathbf{J_i}\rangle$ can be calculated:

$$\langle\mathbf{J_i}\rangle = \sum_\Gamma n_\Gamma\langle\Gamma|\mathbf{J_i}|\Gamma\rangle \tag{1.26}$$

where

$$n_\Gamma = \frac{exp(-E_\Gamma/kT)}{z} \tag{1.27}$$

$$z = \sum_\Gamma exp(-E_\Gamma/kT) \tag{1.28}$$

Here z is the partition function, and $|\Gamma\rangle$ is the eigenstate corresponding to the eigenvalue E_Γ of the Hamiltonian 1.25.

Once the eigenvalues and eigenfunctions of the Hamiltonian 1.25 are obtained, the magnetic susceptibility can be calculated using the following expression:

$$\chi_{\text{CEF}i} = N(g_J\mu_\text{B})^2\frac{1}{Z}\left(\sum_{m\neq n}|\langle m \mid J_i \mid n\rangle|^2\frac{1-e^{-\beta\Delta_{m,n}}}{\Delta_{m,n}}e^{-\beta E_n} + \sum_n|\langle n \mid J_i \mid n\rangle|^2\beta e^{-\beta E_n}\right), \tag{1.29}$$

While the isothermal magnetization of the system is given by the following expression:

$$M_i = g_J \mu_{\mathrm{B}} \sum_n |\langle n|J_i|n\rangle| \frac{\exp(-\beta E_n)}{Z}, \quad (i = x, y, z) \tag{1.30}$$

Because the scattering of conduction electrons depend on the degeneracy and splitting of energy levels, the electrical resistivity of a system also gets modified by the crystal field. We will discuss qualitatively about the effect of CEF on the electrical resistivity in the context of our data.

1.7 Superzone gap

A gap in the energy dispersion of the conduction electrons may occur due to the change in lattice periodicity below the antiferromagnetic ordering temperature. Because of this gap at the Fermi energy of the system, the electrical resistivity of the system shows anomalous behavior below the Néel temperature (T_{N}) by showing an upturn. Generally, a decrease in the resistivity is expected below the ordering temperature due to the decrease in the spin disorder scattering of conduction electrons. The partially filled $4f$ shell of a rare-earth atom is well localized and isolated from that of the $4f$ shells of adjacent atoms. The indirect interaction mediated by conduction electrons through the so-called $s - f$ exchange interaction is most important interaction between the $4f$ spins. If we assume an oscillatory arrangement of $4f$ spins, the conduction electrons experience a periodic potential through the $s - f$ exchange interaction whose period is incommensurate with that of the crystal lattice. This periodic potential, together with the lattice potential, produces gaps in the energy dispersion of the conduction electrons. One of most interesting consequences of this energy gaps is an anomalous increase in the electrical resistivity below T_N. When the gap appear in the conduction band, the effective number of conduction electrons is reduced.

Below T_N, the superzone gap causes a resistivity increase as $(T_N - T)^{1/2}$, whereas the decrease in spin disorder scattering is proportional to $(T_N - T)$. Therefore, we

observe a sharp increase in resistivity below T_N. The theory of superzone was first proposed by Mackintosh [28]. The relation between the resistivity and the superzone gap is described by Elliot and Wedgwood [29]. When an external magnetic field is applied to the $4f$ spins, the the magnitude of the principal gap is reduced [30], it reduces the resistivity upturn. Superzone gap has been widely studied in the pure rare earth metals, where the gap appears only along the hexagonal c-axis. [31]. As we will see in Chapter 3, the gap appears along all the crystallographic directions in case of orthorhombic CeGe.

Chapter 2

Experimental methods

2.1 Introduction

Physical properties of rare earth intermetallic compounds, as well as any other compounds, can be sensitive to the phase distribution, presence of impurity and crystallinity of the material. So in order to study and understand the fundamental physical properties of a material, especially to gain the knowledge on its anisotropic properties, a single crystalline sample is very much inevitable. In the present thesis investigations on the anisotropic physical properties of binary rare-earth intermetallic compounds are made on single crystals. The details of various growth methods that have been employed to grow the single crystals are presented in this chapter. Also the characterization techniques used to study the anisotropic physical properties are discussed. Although there are a number of methods available to grow the single crystals, the method to adopt a particular crystal growth technique mainly depends on the melting behavior and the constituent elements. To grow the single crystals of the materials used in this thesis work, two different melt growth techniques namely, Bridgman method and Czochralski crystal growth method have been employed. The grown crystals were subjected to x-ray diffraction studies namely, powder x-ray diffraction and Laue diffraction to check the phase purity and to orient the single crystal along the principal crystallographic directions. The powder x-ray diffraction pattern was analyzed by means of Rietveld analysis using the Fullprof [32] software to estimate

the lattice constants and to determine the positional co-ordinates of the atoms in the unit cell. Energy dispersive analysis by x-ray (EDAX) was done on the samples to check the overall stoichiometry of the samples. Magnetic susceptibility and isothermal magnetization measurements were performed in a Quantum Design (QD) built Superconducting Quantum Interference Device (SQUID) magnetometer and Vibration Sample Magnetometer (VSM), respectively. The zero field electrical transport measurements were carried out in a home built resistivity set-up, while the resistivity in applied magnetic field was measured using QD Physical Property Measurement System (PPMS). Heat capacity was measured using PPMS. In some cases, for the non-magnetic reference compound, we have used polycrystalline samples prepared by arc melting method. Some of the experiments were performed in collaboration with other groups and facilities. The electrical transport measurement under pressure on $CeMg_3$ single crystal was done in collaboration with Prof. Bauer's group in Vienna. The angle resolved photo emission (ARPES) measurement on PrGe was performed at Elettra Sincrotrone facility in Trieste.

2.2 Crystal Growth

In order to understand the basic physical properties of any compound, it is imperative that the measurements be performed on high quality single crystalline samples. Particularly in the case of magnetic compounds the studies on single crystalline samples are most preferred as it can provide information about the magnetocrystalline anisotropy, the direction of easy axis of magnetization etc. Although, some of the preliminary information about a system can be obtained from a polycrystalline sample, the single crystals have a number of advantages over the polycrystalline sample. There are no grain boundaries, relatively lower impurities which essentially will result in good quality data. Single crystals generally possess stoichiometric composition, and therefore additional impurity phases which may be present in the polycrystalline material are generally precluded. The physical properties of a compound can be sensitive to the presence of impurity, phase distribution, grain boundaries, and crystallinity of the samples. Thus to study the intrinsic physical properties of a compound, especially for properties which show anisotropic behavior, single crystalline sample is necessary. These anisotropy applies to any measurement that involves application of magnetic

field or electrical current. Some of the experiments, like the electronic Fermi surface construction using angle resolved photoemission spectroscopy (ARPES) and dHvA effect, are only possible with good quality single crystalline sample.

The choice of crystal growth method depends on the physical and chemical properties of constituent elements and the compound. Here we have used two crystal growth methods, namely Bridgman and Czochralski pulling method, to grow the single crystals. The single crystals of $CeMg_3$, $LaMg_3$ and $CeMg_{12}$ are grown by Bridgman method; while the single crystals of CeGe, LaGe, CeSi, LaSi, PrGe, PrSi are grown by Czochralski pulling method. In some cases polycrystalline samples are prepared by arc melting. We prepared the polycrystalline sample of YGe, the non-magnetic analog compound of PrGe, by arc melting method. In the following sections we will discuss the details of crystal growth methods.

2.2.1 Bridgman method

The Bridgman method is named after P.W. Bridgman who designed a method to grow the single crystals of metals in the year 1925 [33]. The schematic diagram of a typical Bridgman growth process is shown in Fig. 2.1. The general principal is that of slow solidification from the melt. The material to be crystallized is placed in a very sharp tipped crucible and the temperature of the furnace is maintained above the melting point of the material. The material in the molten condition is slowly lowered through the bottom of the furnace to a lower temperature side. Solidification thus starts at the sharp tip of the crucible and proceeds slowly along its axis, keeping pace with the lowering. If the lowering speed is at a speed less than the velocity of crystallization and also slow enough so that the latent heat of solidification may be dissipated by conduction, then the material will usually crystallize as one grain, provided that only one nucleation happens in the crucible [33]. The sharp tip of the ampoule ensures that there is only one nucleation that occurs during the lowering of the crucible. Perhaps Bridgman method is the easiest and cleanest way to grow single crystals. But this method is most suitable to the congruently melting compounds, i.e., the compounds which solidify from the liquid phase maintaining its stoichiometry. Several of the strongly correlated electron systems including the non-centrosymmetric $CePt_3Si$ [34], and the pressure induced superconductor $CePd_5Al_2$ [35] crystals have been grown by
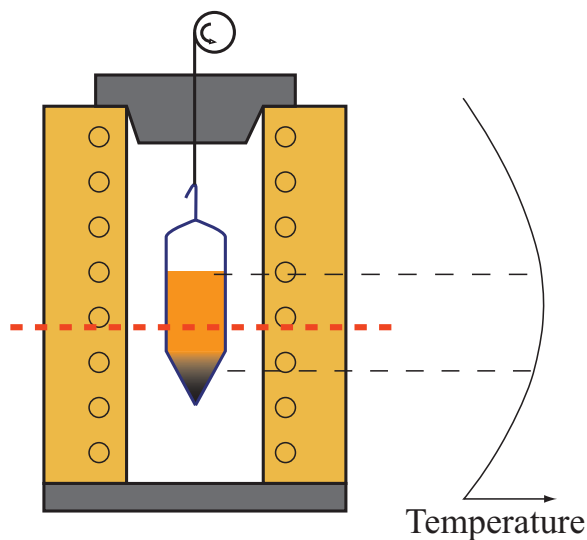
Figure 2.1: Schematic representation of Bridgman growth process

modified Bridgman method.

Here in the present thesis modified Bridgman method has been adapted to grow the single crystals of CeMg$_3$ and CeMg$_{12}$. From the binary phase diagram of Ce-Mg [36] shown in fig. 2.2, it is obvious that CeMg$_3$ phase melts congruently at 796 °C and hence the single crystal of this compound can be grown directly from the melt. Owing to the high vapor pressure of magnesium at elevated temperature, the single crystal of CeMg$_3$ has been grown by modified Bridgman method. High purity elements of Ce and Mg after removing the surface oxide layers by etching with dilute nitric acid were taken in the ratio 1:3.1 inside a sharp tipped alumina crucible and subsequently sealed in a molybdenum crucible as shown in Fig. 2.3. The molybdenum crucible is then sealed inside a quartz ampoule evacuated to a pressure of about $10^{-6} mbar$ to protect the molybdenum tube from oxidation during the process of crystal growth at elevated temperature. The quartz ampoule is introduced in a box type furnace which has a gradient such that the bottom of the furnace remains slightly lower in temperature compared to the top. The temperature of the furnace was raised at a rate of 15 °C/hr to 850 °C, well above the melting temperature of CeMg$_3$ phase and held there for 24 hours for proper homogenization. Then the temperature was lowered at rate of 1 °C/hr down to 750 °C well below the melting point of CeMg$_3$. The gradient in the box type furnace enabled the crystal growth to occur from the sharp tip of the alumina crucible where the nucleation starts and the crystal grows as the
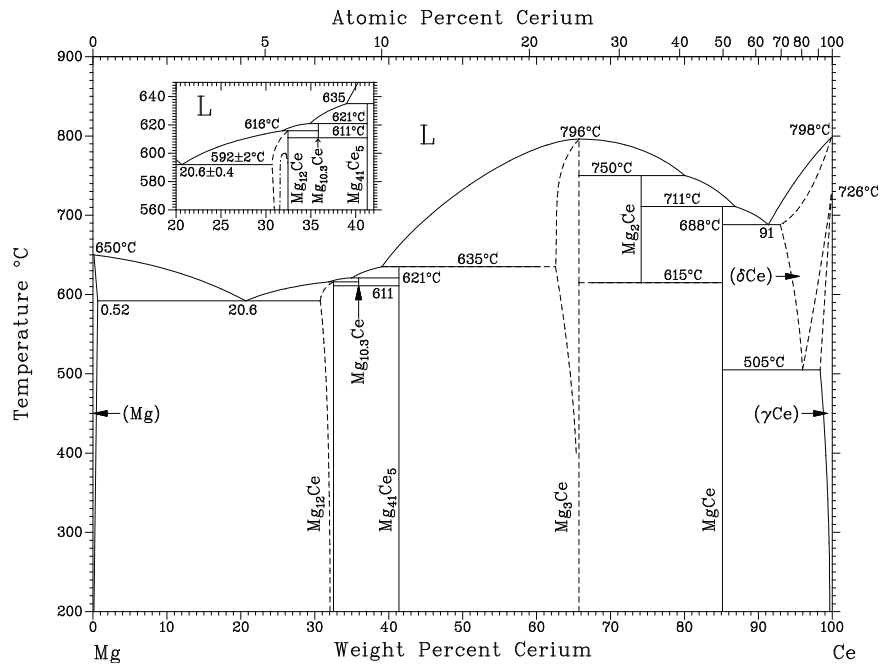
Figure 2.2: Binary phase diagram of Ce-Mg
.
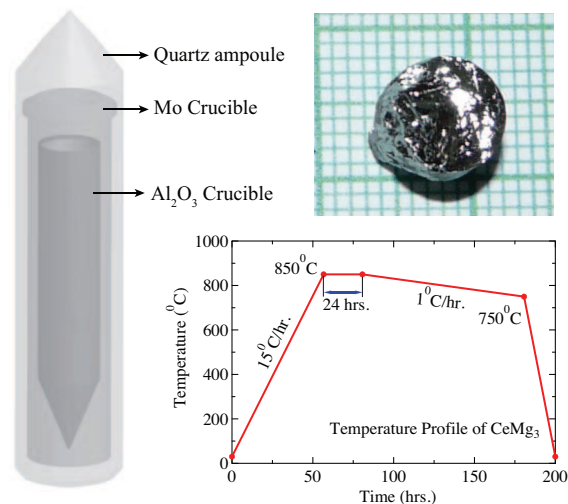
Figure 2.3: Schematic representation of the alumina crucible, sealed inside a molybdenum crucible which is subsequently sealed inside a quartz ampoule. The temperature profile adopted to grow the single crystal of CeMg$_3$. A large single grain of the CeMg$_3$ single crystal is also shown.

temperature is lowered. The grown crystal of $CeMg_3$ was removed by gently tapping the alumina crucible. The as grown single crystal of $CeMg_3$ is shown in Fig. 2.3. A similar procedure was adopted to grow the single crystals of the non-magnetic reference compound $LaMg_3$ and $CeMg_{12}$.

2.2.2 Czochralski method

When a material melts congruently and does not possess any low temperature phase transformations on cooling, the single crystal of the material can be grown directly from the molten solution. Many times, seed crystals are used to control the orientation along a particular crystallographic direction. This method of crystal growth was invented by J. Czochralski [37], when he was studying the rapid solidification of low melting metals like Sn, Bi etc. In principle, the Czochralski growth system consists of a crucible which contains the charge of the material to be crystallized in the molten form. A seed crystal with the desired crystallographic orientation is attached to a pulling rod or seed rod. The seed rod is lowered until the end of the seed crystal is dipped into the melt. The temperature of the melt should be maintained such that the solidifications happens near the seed and once the thermal steady state is achieved the seed rod is pulled at a desired rate. The Czochralski crystal pulling method has undergone many modifications over the years and resulted in the state of the art crystal pullers to grow very large size single crystals of semiconductors for technological applications.

In the present thesis work, single crystals of RX (R = La, Ce and Pr; X = Si and Ge) have been grown by Czochralski method using a tetra-arc furnace. The tetra-arc furnace employs four tungsten electrodes through which a high current of the order of $10 - 20$ A is passed to maintain a stable melt of 10 g of source material. The material to be crystallized is held in a copper hearth which is water cooled. The schematic representation of the tetra-arc and the copper hearth is shown in Fig. 2.4. To start with, a tungsten rod or a polycrystalline seed of the material that is to be grown is generally used as a seed crystal. When a polycrystalline material is used as a seed, a necking process is initially done as shown in Fig. 2.4(b) so that only one grain grows into a large single crystal.
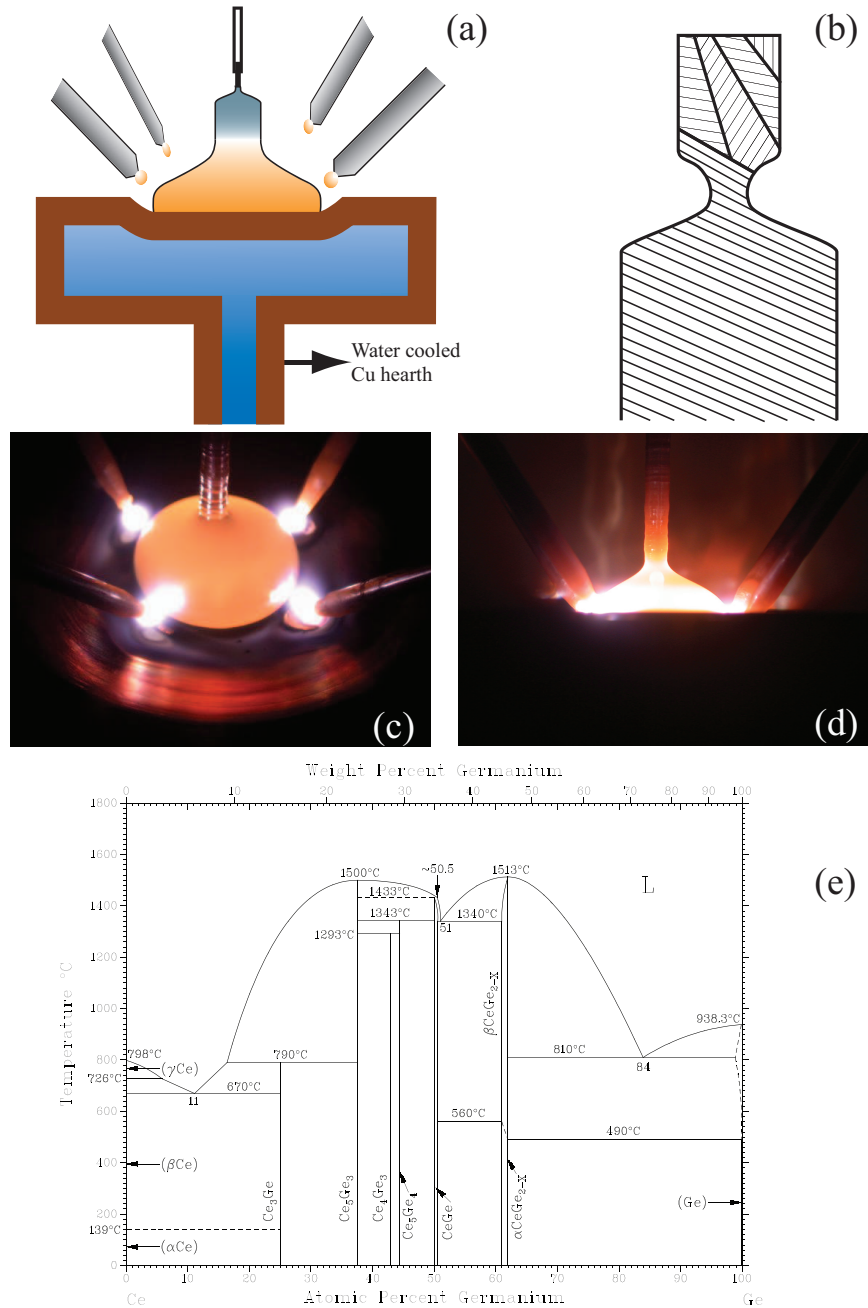
Figure 2.4: (a) Schematic representation of a tetra-arc furnace. (b) necking process to select a single crystalline seed, (c) and (d) photograph of CeGe single crystal during pulling and (e) binary phase diagram of CeGe

.

The binary phase diagram of Ce-Ge system is shown in Fig. 2.4(e). It is evident from the phase diagram that the 50:50 composition of Ce:Ge is at the verge of congruent melting. In order to grow the single crystal of CeGe, we started with a little excess of Ge with the starting composition of Ce and Ge in the ratio 1:1.05. A polycrystalline sample weighing a total of 10 g was melted in the tetra-arc furnace several times to ensure homogeneity of the sample. A tungsten rod was used as a seed crystal for the first crystal growth attempt of CeGe. As soon as the tungsten rod was inserted into the melt, it was pulled at a speed of 40 mm/hr for about 10-15 min. Then after making the necking process, the crystal was pulled at a steady speed of 10 mm/hr for about 6 hours. The cleavage plane for CeGe single crystal was perpendicular to the growth of pulling direction and hence the crystal broke by its own weight when pulled for very long duration. The cleaved plane was identified as (010) plane later by performing the Laue diffraction. In subsequent attempts we have used the previously grown single crystals as seed and pulled a good quality single crystalline sample. Similarly, the single crystals of CeSi, PrSi, PrGe and LaSi were grown by Czochralski method as all of these binary compounds melt congruently at temperature close to 1500 °C.

2.3 Powder x-ray diffraction

Powder x-ray diffraction is a standard method to determine the phase purity of a sample and to estimate the lattice parameters. Basically the x-ray diffraction is based on the Bragg's law which establishes certain relationships among the diffraction angle or the so called Bragg angle (θ), the incident wavelength (λ) and the interplanar spacing (d_{hkl}). According to the Braggs, diffraction from a crystalline sample can be explained and visualized by using a simple notion of mirror reflection of the incident x-ray beam from a series of crystallographic planes as shown schematically in Fig. 2.5. Each plane in a set (hkl) may be considered as a separate scattering object. The set is periodic in the direction perpendicular to the planes and the repeat distance in this direction is equal to the interplanar distance d_{hkl} as shown in Fig. 2.5. With the incident monochromatic beam of x-ray λ, diffraction from a set of equally spaced objects is only possible at specific angles θ and the constructive interference will take place when the Bragg condition $2d_{hkl} \sin\theta = n\lambda$ is satisfied. A peak in the x-ray
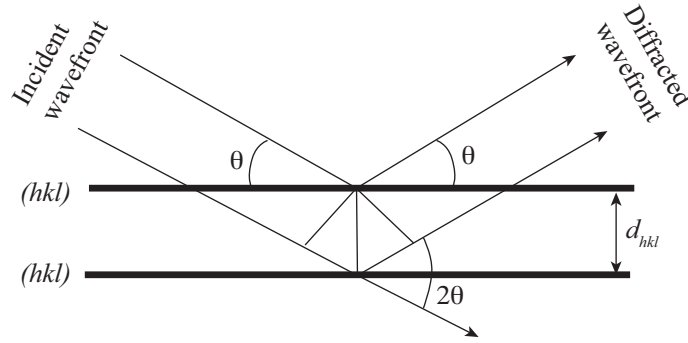
Bragg's law : $2d_{hkl}\,sin\theta = n\lambda$

Figure 2.5: Geometrical illustration of the Bragg's law.

spectrum is observed when Bragg condition is satisfied. The peak positions mainly depend on the unit cell lattice parameters and the symmetry of the unit cell.

In order to check the phase purity, the grown crystals were subjected to powder x-ray diffraction analysis by grinding the single crystals to fine powders and placed in the PANalytical x-ray diffractometer with a monochromatic Cu K_α radiation ($\lambda =$ 1.5406 Å). Due to the fine powdering, the planes of the tiny crystallites are oriented in random directions and constructive interference of the incident x-ray beam takes place only when the Bragg condition is satisfied at which point a peak in the x-ray spectrum is observed. The lattice constants and the atomic co-ordinates of the atoms (or the so called Wyckoff's position) present in the sample can be obtained from the powder x-ray diffraction pattern. In order to get the lattice constants and the atomic co-ordinates, Rietveld analysis has been performed on the powder x-ray pattern using the FULLPROF software package [32]. The powder pattern of all the samples studied in this thesis were collected at room temperature. Additionally the stoichiometric homogeneity of the samples have been analysed by Energy Dispersive Analysis by X-ray (EDAX).

2.4 Laue x-ray diffraction

One of the main objectives to grow the single crystals is to study the anisotropic physical properties. For which, the crystals have to be oriented along the desired
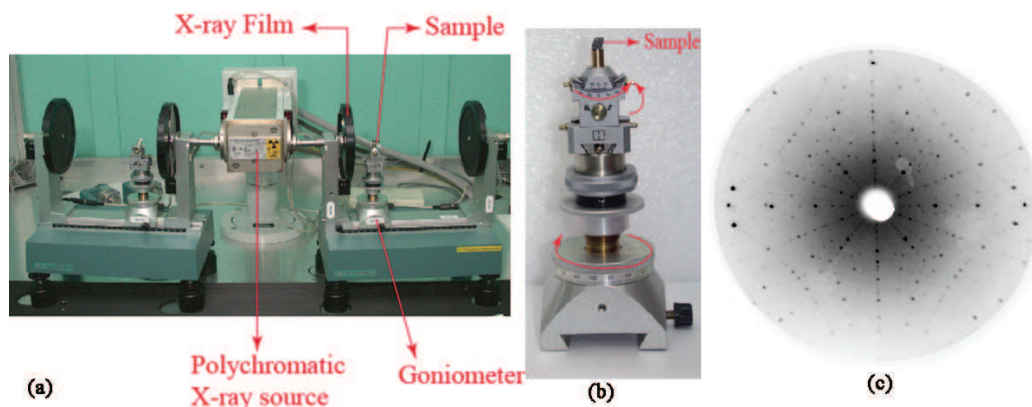
Figure 2.6: (a) Laue set up (b) a triple axis goniometer which can be rotated along three mutually perpendicular directions, and (c) Laue pattern of PrGe corresponding to (001) plane.

crystallographic directions. This is achieved by performing Laue diffraction of the grown crystals. Similar to powder x-ray diffraction analysis, Laue diffraction experiments are also based on the Bragg's law. The Laue method employs a polychromatic source of x-ray with wavelength (λ) ranging from 0.5 Å to 3.0 Å. The angle (θ) of incidence of the x-ray beam is fixed. The crystal to be oriented is mounted on a triple axis goniometer which can rotate in three mutually perpendicular directions. The main difference between the powder x-ray diffraction and the Laue diffraction method is: λ is fixed and θ is varying in the powder x-ray; while λ is varying (polychromatic x-ray) and θ is fixed in the Laue diffraction. For various λ, the planes in the single crystal satisfy the Bragg condition and a spot is observed and is recorded in the image plate or in an x-ray film. Since the grown crystals for the present thesis are metallic, the back reflection geometry has been used to orient the single crystals. A typical Laue pattern is shown in Fig. 2.6(c). The quality of the Laue pattern determines the quality of single crystals also; clear spherical Laue spots indicate a good quality of single crystal while diffused, elongated Laue spots indicate poor crystallinity of the sample. We generally orient our crystals along the principal crystallographic directions. Once the crystallographic direction is found from the Laue pattern, the crystals are cut using a spark erosion cutting machine.

2.5   Energy Dispersive Analysis by X-ray

In order to know the exact stoichiometry, the grown crystals were subjected to energy dispersive analysis by x-ray (EDX). EDX measurements were performed in a commercial INCA EDX system from Oxford instruments. The basic principle is that high energy (several kV) electrons are bombarded on a finely polished surface of the sample, which knock out the core electrons of the constituent elements. Since the sample is grounded the electrons from the higher levels make transition to the core levels, and give the characteristic x-ray radiation of the particular sample and particular orbital. Now analyzing the x-ray peak positions and the relative intensity of the peaks, with the standards, the stoichiometry of the constituent elements of the crystal can be known.

2.6   Magnetic susceptibility

The magnetic susceptibility data presented in this thesis are acquired using a Quantum Design (QD) built Superconducting Quantum Interference Device (SQUID) magnetometer. The basic design of a DC SQUID magnetometer is shown in Fig. 2.7. The SQUID magnetometer works on the principle of Josephson junction. It is a thin insulating layer, or a narrow constriction, between two superconductors. The current (must be less than the critical current) through a *weak link* (of distance less than the coherence length) can penetrate without any voltage drop. One important property of superconductors is that the flux through a superconducting loop is quantized ($\Phi_0 = 2.068 \times 10^{-15} Tm^2$). If the bias current is maintained at slightly higher than the critical current, when an external magnetic field is coupled to the Josephson loop, the voltage drop across the Josephosn junction will change. When the external flux changes, the voltage will change in a periodic manner with the period being that of the flux quantum (Φ_0). Now counting the oscillation in the voltage, we can determine the magnetic flux coupled to the SQUID loop. The details of SQUID can be found in the literature [38, 39, 40].

To measure the magnetic susceptibility measurement using a SQUID magnetometer, we fix the oriented single crystals in an over head projector (OHP) sheet using GE
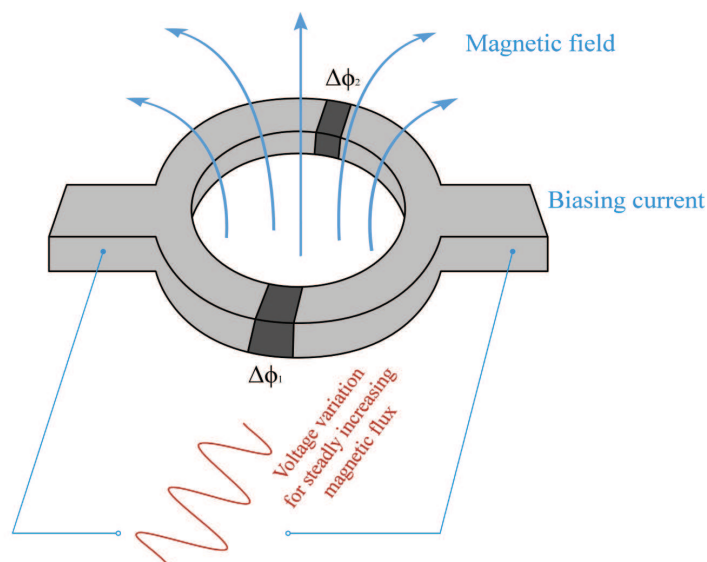
Figure 2.7: A block diagram of a DC SQUID magnetometer.

varnish. Then this OHP sheet is inserted in a straw which is subsequently suspended in the SQUID sample holder. The magnetic moments of these materials and the OHP sheet are very low compared to our compounds of interest and hence the background can be ignored. The anisotropic magnetic susceptibility has been measured in the SQUID magnetometer in the temperature range from 1.8 to 300 K and in magnetic fields up to 7 T.

2.7   Isothermal magnetization

Isothermal magnetization measurements were performed using a QD Vibration Sample Magnetometer (VSM). The magnetic field is applied along the desired crystallographic direction and the magnetization is measured by varying the magnetic field for a selected temperature. The VSM is based on the Faraday's principle which reads that if there is a change in flux linked to a coil, an electromagnetic force is generated in the coil. We can measure the induced current in the loop, calculate the change in magnetic flux through the loop, and hence the magnetization of the sample. In VSM, a magnetic sample is vibrated (sinusoidally) in the proximity of two/four pickup coils.
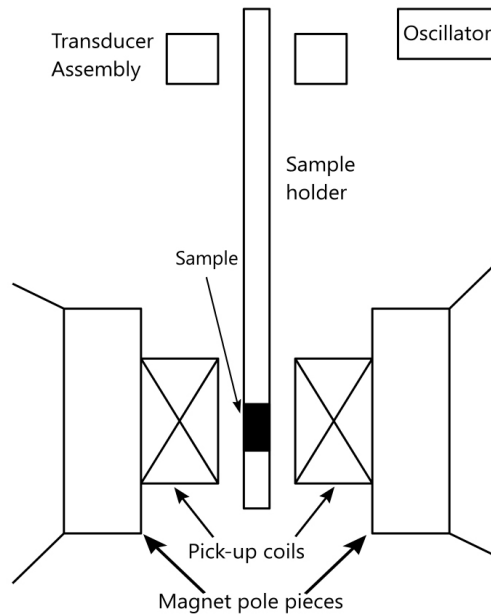
Figure 2.8: A schematic drawing of vibration sample magnetometer (VSM).

The sample is placed between the pole pieces of an electromagnet that generates a homogeneous magnetic field where we place our sample. The QD VSM used for our measurements can produce a field up to 16 T. This applied magnetic field magnetizes the sample (magnetic) and when the sample is moved, a change in flux is observed in the pick up coils, which induces a current in the coils. The induced current can be increased by increasing the number of windings in the pick up coils, and thus the instrument can detect very low magnetic moments.

2.8 Electrical transport

The zero field electrical resistivity measurements were performed in a home built set-up in the temperature range from 1.8 to 300 K, using a glass cryostat. The standard four probe method has been used to measure the electrical resistivity. The electrical

resistivity measurements with applied magnetic field were performed using physical property measurement system, which provides a maximum field of 14 T. Typical cross section of our samples are (0.5 mm × 1.0 mm) and 3 mm long. The electrical contacts were made using 20 μm gold wire with sliver paste.

2.9 Heat capacity

The heat capacity of the grown single crystals was measured using the Quantum Design Physical Property Measurement System (PPMS) in the temperature range 1.8 to 300 K and fields as high as 14 T. For temperatures below 1.8 K we used a dilution refrigeration insert. The heat capacity is measured using the thermal relaxation technique which controls the heat added to and removed from the sample while monitoring the resulting change in temperature. A known amount of heat is applied at constant power for a fixed time and then this heating period is followed by cooling period for the same amount of time. The PPMS has a small microcalorimeter platform for mounting the sample. Samples are mounted to this platform using Apiezon N grease for the low temperature measurement. The sample platform is suspended from a puck by eight thin wires that serve as the electrical leads for an embedded heater and a thermometer connected to the bottom of the platform. To ensure that heat is not lost via exchange gas, the chamber pressure is maintained at 0.01 μbar. A single heat capacity measurement consists of several distinct stages. First, the sample platform and puck temperatures are stabilized at some initial temperature. Power is then applied to the sample platform heater for a predetermined length of time, causing the sample platform temperature to rise. When the power is terminated, the temperature of the sample platform relaxes towards the puck temperature. The sample platform temperature is monitored throughout both heating and cooling, providing the raw data of the heat capacity calculation. The raw data is analyzed by the two-tau model [41] which assumes that the sample is not in good thermal contact with the sample platform. In the two-tau model, the first time constant τ_1 represents the relaxation time between the sample platform and the puck, and the second time constant (τ_2) represents the relaxation time between the sample platform and the sample. A second analysis is also performed using a simpler model that assumes perfect thermal coupling between the sample and the platform. The heat capacity

software determines which model fits best to the measured data. The heat capacity of the sample is determined by subtracting the addenda from the total heat capacity. The addenda is the heat capacity of the empty puck without the sample mounted. In the present work the heat capacity was also in various applied magnetic fields. The mass of the sample used was in the range 10-20 mg.

2.10 Angle Resolved Photoemission Spectroscopy (ARPES)

The important components of ARPES experiments are the light source and the electron analyzer. In the past, the limitations of the intensity of light source and resolution of electron analyzers significantly restricted the ARPES studies. The recent advancements in the synchrotron radiation light source and the state of the art electron analyzers allow for a high resolution Fermi surface mapping at very fast speed say in few hours. The ARPES measurements were performed in collaboration with APE beamline at Elettra Sincrotrone, Trieste, Italy. The electron energy in the storage ring at Elettra is 2 GeV. In order to enhance the output photon flux, many insertion devices, wigglers or undulators, are installed along the storage ring. The intention is to create alternating magnetic fields along the electron path and force the electrons to undergo oscillations and radiate more photons. The photons coming out from each insertion device will then go through focusing mirrors and grating chambers to reach the user's chamber. A beamline in a synchrotron facility refers to the combination of the insertion device, mirrors, slits, monochromatic grating etc. A schematic of the APE beamline used for ARPES experiments is shown in Fig. 2.9. The focusing mirrors are used to focus the beam spot typically to ¡1 mm. The slits are generally chosen so that the energy resolution of incoming photons matches the energy resolution of the electron analyzer. We have performed measurements using energy 20-70 eV and measurements are performed down to liquid helium temperature (the sample temperature reaches about 20 K). The spectra are collected using SIENTA detector having a resolution of 15-20 meV.
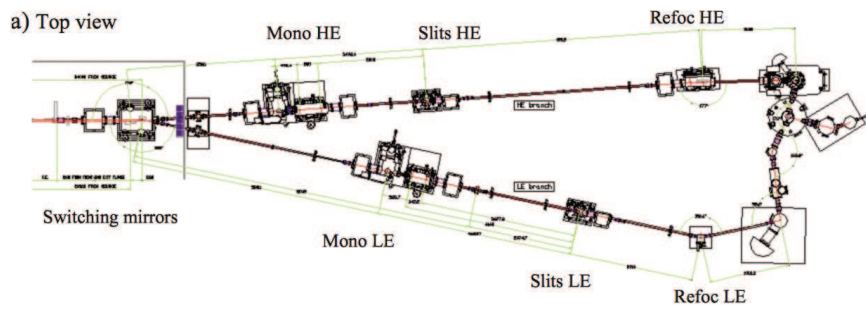
Figure 2.9: A schematic mechanical layout of the APE Beamline showing both low energy and high energy lines.

Chapter 3

Magnetic properties of a Kondo lattice antiferromagnet CeMg$_3$ and CeMg$_{12}$

3.1 Introduction

As mentioned in the introduction chapter, among the rare earth intermetallic compounds Ce and Yb based compounds are particularly interesting and extensively studied as some of them exhibit novel magnetic behavior due to the close proximity of $4f$ level to the Fermi energy. This proximity enhances the hybridization between the $4f$ level and the band states resulting in an antiferromagnetic $s - f$ exchange interaction between the conduction electron and the $4f$-derived local moment. The negative $s - f$ exchange interaction leads to Kondo effect. Depending upon the relative strengths of the Kondo exchange interaction and the conduction electron mediated RKKY interaction, some compounds of Ce and Yb show a variety of anomalous behavior. For example, CeAl$_3$ [9] and CeCu$_6$ [5] show heavy fermion Kondo lattice behavior without any long range magnetic order; cubic compounds CeAl$_2$ [10] and CeB$_6$ [11], YbRh$_2$Si$_2$ [12] and YbAlB$_4$ [13] are Kondo lattice compounds that order magnetically at low temperature; heavy fermion compounds CeIn$_3$ [42], CeCu$_2$Ge$_2$ [43], CeRh$_2$Si$_2$ [44], and CePd$_2$Si$_2$ [45] exhibit pressure in-

duced superconductivity; while the heavy fermion compound CeCu$_2$Si$_2$ [46] shows superconductivity at ambient pressure. Many of these compounds are Kondo lattice antiferromagnets at ambient pressure, upon application of external pressure [47] or magnetic field or chemical doping, these compounds exhibit quantum critical point ($T_N \to 0$), where for a particular value of the exchange constant (J_{cf}) the Kondo and the RKKY exchange interactions are equal and opposite, and the magnetically ordered and the non-magnetic ground states become degenerate. The field of quantum criticality is extensively studied these days. The application of external hydrostatic pressure is an excellent tool to control the ground state of these compounds where the Kondo interaction depends sensitively on the lattice volume, and hence on the external pressure. In view of these interesting physical properties exhibited by Ce and Yb based intermetallic compounds, an investigation on the magnetic properties of CeMg$_3$ and CeMg$_{12}$ binary compounds in single crystalline form is reported in this chapter.

RMg$_3$ compounds crystallize in cubic BiF$_3$-type structure. Prior to this work, there are no single crystalline reports on both CeMg$_3$ and CeMg$_{12}$. In one of the early works on RMg$_3$ (R = La, Ce, Pr, Nd, Sm, Gd, Tb) compounds, Buschow [48] reported the structural and magnetic properties on polycrystalline samples; it was found that CeMg$_3$, NdMg$_3$, and PrMg$_3$ do not order magnetically down to 4.2 K. The magnetic susceptibility of these three compounds showed Curie-Weiss behavior consistent with a negative value of paramagnetic Curie temperature, indicating an antiferromagnetic ordering at low temperature. SmMg$_3$ was found to order magnetically with $T_N = 6.5$ K. A low value of saturation magnetization observed in all the four lighter rare earth compounds, was attributed to the possible complex magnetic structure of these compounds. The higher rare earth compounds GdMg$_3$ and TbMg$_3$ order ferromagnetically with $T_C = 117$ K and 108 K, respectively. In a later report by Pierre *et al.* [49] it was found that CeMg$_3$ orders magnetically with $T_N = 3.4$ K, the presence of Kondo interaction indicated by the magnetic part of electrical resistivity which increases with decreasing temperature over certain temperature range. Furthermore, from inelastic neutron scattering data they estimated the crystal electric field (CEF) split level scheme. In another neutron diffraction report, Galera *et al.* [50] have reported that CeMg$_3$ orders antiferromagnetically with $T_N = 4$ K, while NdMg$_3$ orders magnetically at 6 K. From the neutron diffraction, the ordered moment in

CeMg$_3$ was found to be small, which the authors attributed to the presence of Kondo effect. Earlier, Galera *et al.* [51], and recently Chatterji *et al.* [52] have done the neutron diffraction on NdMg$_3$, and reported antiferromagnetic ordering at $T_N = 6$ K with the propagation vector **k** = (0.5, 0.5, 0.5); the magnetic structure of NdMg$_3$ possesses ferromagnetic layers of (111) which are stacked in opposite directions leading to an antiferromagnetic alignment along the [111] axis. There is a recent report by Tanida *et al.* [53], where they have studied the magnetic properties of PrMg$_3$ in detail on a single crystalline sample and found that the ground state of this compound is a non-magnetic Γ_3 doublet.

In order to remove the ambiguity over the exact magnetic ordering temperature of CeMg$_3$, and to study the Kondo behavior along with other possible interesting physical properties, single crystals of CeMg$_3$ and its non-magnetic analog compound LaMg$_3$ have been grown by Bridgman method. The magnetic properties were studied in detail by measuring magnetic susceptibility, magnetization, electrical transport, and heat capacity measurements. Crystal electric field (CEF) analysis has been performed on the magnetic susceptibility and heat capacity data and we find that our results corroborates the conclusions of previous neutron diffraction experiment performed on polycrystalline samples [49]. We have also explored the effect of external pressure on electrical resistivity up to 12 kbar; these experiments were done in collaboration with Prof. Bauer at Vienna.

Apart from CeMg$_3$, the magnetic properties of magnesium rich CeMg$_{12}$ have also been studied. The single crystal of CeMg$_{12}$ has been grown for the first time. Unlike CeMg$_3$, CeMg$_{12}$ crystallizes in tetragonal structure with space group $I4/mmm$ (no. 139); and orders below 1.2 K. CEF analysis has been performed on the magnetic susceptibility data and the CEF split level scheme has been estimated.

3.2 Crystal Growth

From the binary phase diagram of Ce-Mg [36], we found that both CeMg$_3$ and CeMg$_{12}$ phases melt congruently at 796 °C and 611 °C, respectively. Since magnesium has a high vapor pressure, Bridgman method was employed to grow the single crystal in a protective environment by sealing it in a molybdenum crucible. Good quality single

crystals of CeMg$_3$ and CeMg$_{12}$ have been obtained by this method. The details of crystal growth method are described in Chapter 2. The anisotropic properties have been investigated on well oriented single crystalline samples.

3.3 CeMg$_3$

3.3.1 Powder x-ray and Laue diffraction and EDAX

In the crystal growth of CeMg$_3$, slight excess of magnesium was taken due to the volatile nature of Mg at high temperatures. Hence the phase purity of the grown crystals was checked by means of powder x-ray diffraction (XRD). A few small pieces of the single crystals CeMg$_3$ was ground into fine powders and the powder x-ray diffraction pattern was recorded using a PANalytical x-ray diffractometer with Cu Kα ($\lambda = 1.5406$ Å) monochromatic radiation. No traces of any impurity peaks were obtained in both CeMg$_3$ and LaMg$_3$ powder pattern. The samples were phase pure and the compounds found to crystallize in the cubic crystal structure with space group $Fm\bar{3}m$ (no. 225). Rietveld analysis was performed on the powder pattern in order to estimate the lattice parameters using the FULLProf software package [54, 55]. The representative powder pattern of CeMg$_3$ along with the Rietveld fitting is shown in Fig. 3.1. The estimated lattice constants for LaMg$_3$ and CeMg$_3$ were 7.468 Å and 7.422 Å, respectively; which are in agreement with the previous reports [48]. It is worth mentioning here that the nearest Ce-Ce distance is 5.248 Å. Hence CeMg$_3$ is a good system to study the competing RKKY interaction and Kondo screening. The stoichiometry of the samples was further confirmed by the Energy Dispersive X-ray Analysis (EDX) where the stoichiometry of the crystals was examined at different regions and found to be highly homogeneous. The grown crystals were oriented along the principal crystallographic direction by Laue back reflection method. A representative back reflection Laue pattern of CeMg$_3$ corresponding to (100) plane is shown in Fig. 3.2. Clear four fold symmetry in the Laue pattern corroborates the cubic symmetry of the crystal structure and the well defined spherical spots indicate a good quality of the grown single crystal. The crystals were then cut in rectangular bar form using a spark erosion cutting machine.
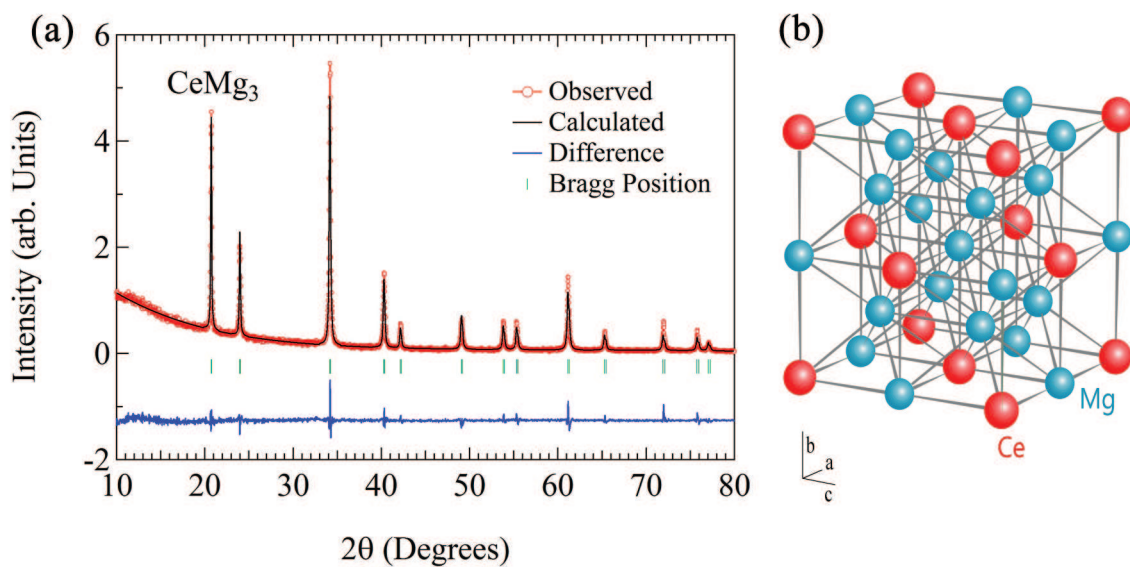
Figure 3.1: (a) Powder x-ray diffraction pattern of CeMg₃ along with the Rietveld fitting (black line), Bragg positions (green markers), and the difference between observed and calculated pattern, and (b) crystal structure of CeMg₃.
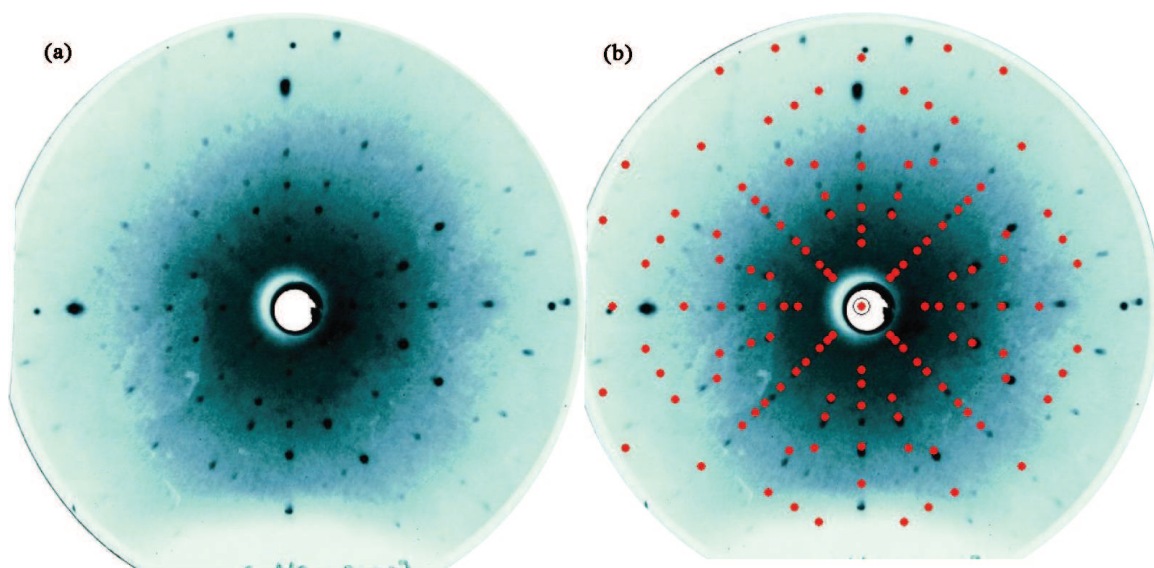
Figure 3.2: (a) Laue pattern of CeMg₃ (100) crystallographic plane, (b) a simulated pattern corresponding to (100) plane is superimposed over the experimental pattern.

3.3.2   Magnetization

The temperature dependence of magnetic susceptibility measured using a SQUID magnetometer in the temperature interval from 1.8 to 300 K in an applied magnetic field of 1 kOe for H parallel to [100] crystallographic direction is shown in Fig. 3.3(a). At 2.6 K a cusp in the magnetic susceptibility is observed as shown in the inset of Fig. 3.3(a). Below 2.6 K, the magnetic susceptibility decreases with decreasing temperature indicating an antiferromagnetic nature of the magnetic ordering. This cusp at 2.6 K in the magnetic susceptibility is the Néel temperature of CeMg$_3$, where Ce moments order antiferromagnetically. The heat capacity data, to be discussed in the following section, confirmed the bulk magnetic ordering of the system at this temperature. Inverse susceptibility vs. temperature plot is shown in Fig. 3.3(b). At high temperature (above 200 K), the inverse susceptibility varies linearly with temperature and follows the Curie-Weiss law. The high temperature inverse susceptibility data in the range 200 to 300 K is fitted to the Curie-Weiss expression:

$$\chi = \frac{C}{T - \theta_{\mathrm{p}}}, \tag{3.1}$$

where C is the Curie constant and θ_{p} is the paramagnetic Curie temperature. The Curie constant C is expressed in terms of the effective magnetic moment as:

$$C = \frac{N_{\mathrm{A}} \mu_{\mathrm{B}}^2 \mu_{\mathrm{eff}}^2 x}{3 k_{\mathrm{B}}}, \tag{3.2}$$

where N_{A} is Avagadro number, μ_{B} is the Bohr magneton and k_{B} is the Boltzmann constant, μ_{eff} is the effective magnetic moment and x is the number of magnetic rare-earth ions per formula unit. Substituting the constant values in Eqn. 3.2, Eqn. 3.1 reduces to

$$\chi = \frac{\mu_{\mathrm{eff}}^2 x}{8(T - \theta_{\mathrm{p}})}. \tag{3.3}$$

The solid line in Fig. 3.3(b) is the Curie-Weiss fit. From the fitting, the Curie temperature (θ_{p}) and the effective moment value (μ_{eff}) were found to be -12 K and

44
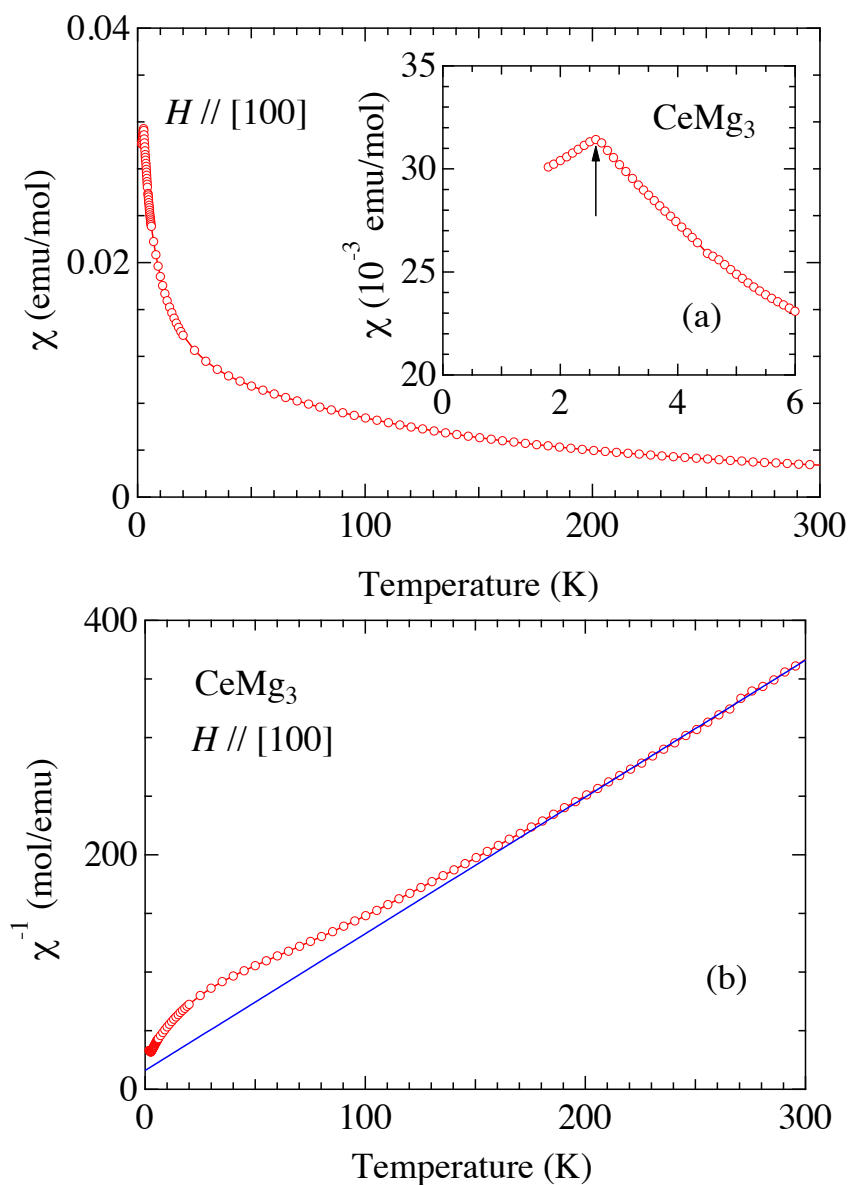
Figure 3.3: (a) Temperature dependence of magnetic susceptibility in the temperature range from 1.8 to 300 K along [100] crystallographic direction with an applied magnetic field of 1 kOe, (b) inverse susceptibility is plotted against temperature, the solid line is the Curie-Weiss fit to the experimental data.
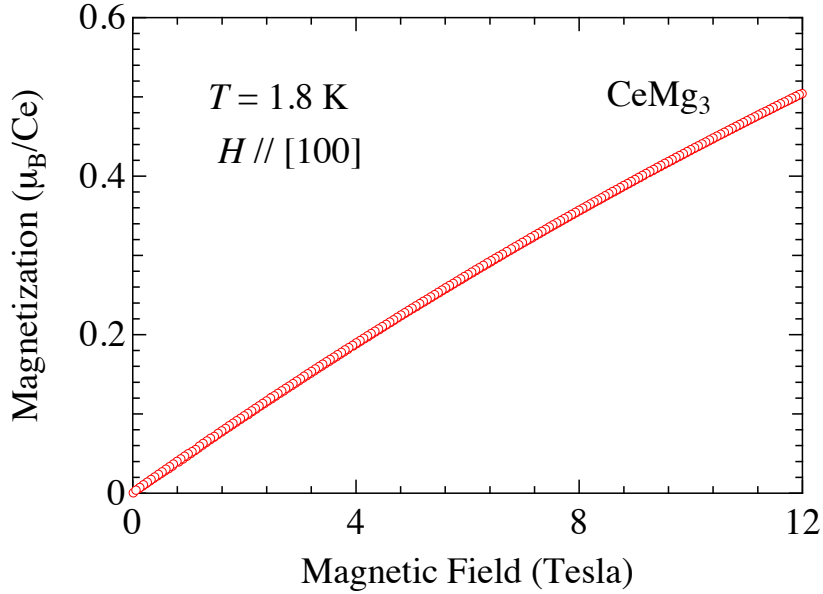
Figure 3.4: Field dependence of isothermal magnetization measured at 1.8 K with field along the [100] crystallographic direction.

2.61 μ_B/Ce, respectively. The estimated effective moment is close to the free ion value of Ce, 2.54 μ_B/Ce, thus indicating the trivalent nature of Ce ion in this compound. The negative sign of θ_p is in conformity with the antiferromagnetic ordering in this compound. The inverse susceptibility deviates from the linear behavior below 150 K, which is due to the thermal depopulation of crystal electric field (CEF) split levels, which is discussed later.

The field dependence of magnetization $M(H)$ measured in a vibration sample magnetometer (VSM), for H parallel to [100]-direction, at a constant temperature $T = 1.8$ K is shown in Fig. 3.4. The magnetization varies nearly linearly without any sign of saturation up to a magnetic field of 12 T. This type of linear behavior of magnetization is typical for an antiferromagnetic system. The magnetization reaches a value of only 0.5 μ_B/Ce at a magnetic field as high as 12 T. This low value of magnetization corroborates the previous neutron diffraction report by Galera et al. [50] where an order moment of 0.59 μ_B/Ce was observed. The saturation magnetization of Ce moment is ($g_J \times J = \frac{6}{7} \times \frac{5}{2}$) 2.14 μ_B/Ce. This reduction in the magnetization value is attributed to the combined influence of Kondo and CEF effects.

3.3.3 Electrical resistivity

The electrical resistivity of CeMg$_3$ and its non-magnetic analog LaMg$_3$ measured in the temperature range from 1.9 to 300 K for current along [100] direction is shown in Fig. 3.5. Here the magnetic transition is not clearly observed from the resistivity plot as the resistivity was measured down to 1.9 K only. But we see a drop in the resistivity below 2.6 K due the reduction in spin disorder scattering below the ordering temperature. Resistivity of LaMg$_3$ decreases with decreasing temperature, and the temperature dependence is typical of a metallic compound without any anomaly at low temperature. On the other hand the electrical resistivity of CeMg$_3$ shows a broad hump centered around 150 K followed by a minimum around 30 K. Below 30 K, the resistivity shows a weak increase and then decreases. A large value of the residual resistivity for both CeMg$_3$ and LaMg$_3$ may be attributed to slight magnesium vacancy in the crystal due to the volatile nature of molten magnesium during the crystal growth.

The magnetic part of electrical resistivity (ρ_{mag}) was obtained by subtracting the resistivity value of LaMg$_3$ from that of CeMg$_3$. The ρ_{mag} is plotted in a semi-logarithmic scale and is shown in the inset of Fig. 3.5. ρ_{mag} increases with the decreasing temperature below 300 K, and shows two broad hump centered around 100 and 6 K. The $\rho_{\mathrm{mag}}(T)$ varies linearly as $-ln(T)$ at low and high temperatures. This kind of double peak structure is often observed in the Kondo lattice compounds that exhibit magnetic ordering at low temperature. The broad hump at 100 K is attributed to the combined influence of the crystal electric field and the Kondo effect. Hence, CeMg$_3$ can be termed as a Kondo lattice compound. According to Cornut and Coqblin [56], this type of behavior is expected for Kondo-type interaction in presence of strong crystal field splitting with the Kondo temperature T_{K} much less than the overall crystal field splitting Δ_{CEF}. The low temperature peak in $\rho_{mag}(T)$ maybe attributed to the Kondo scattering of the conduction electrons with an energy scale of the order of Kondo temperature T_{K}, while the high temperature peak is due to the thermal population of the CEF split levels.
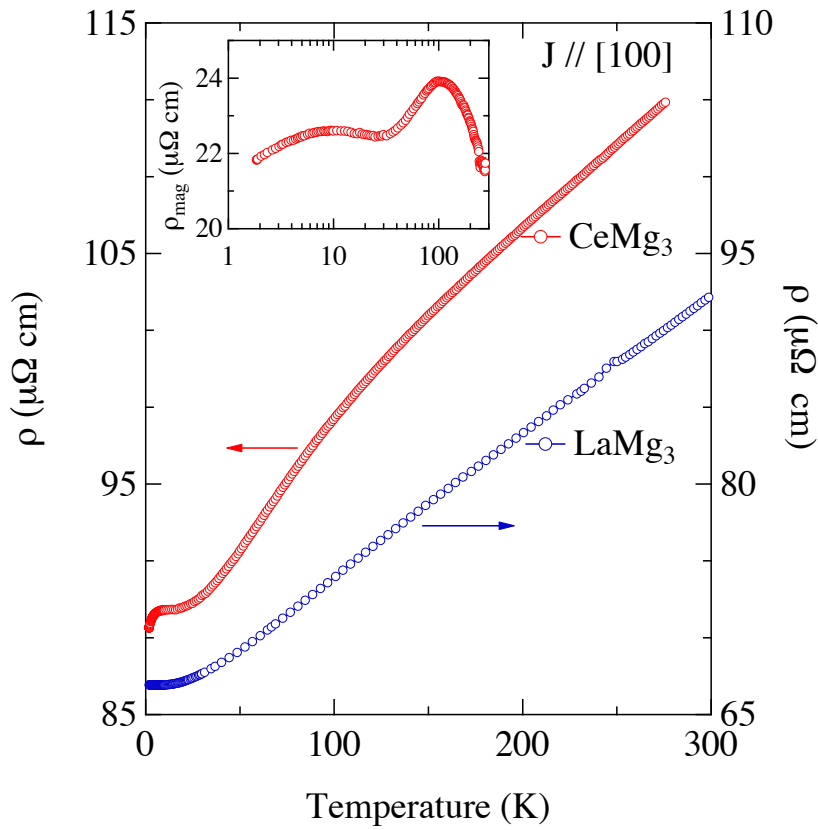
Figure 3.5: Temperature dependence of electrical resistivity of CeMg$_3$ and LaMg$_3$ for current density J parallel to [100] crystallographic direction. The inset shows the magnetic part of resistivity on a semi-logarithmic scale.
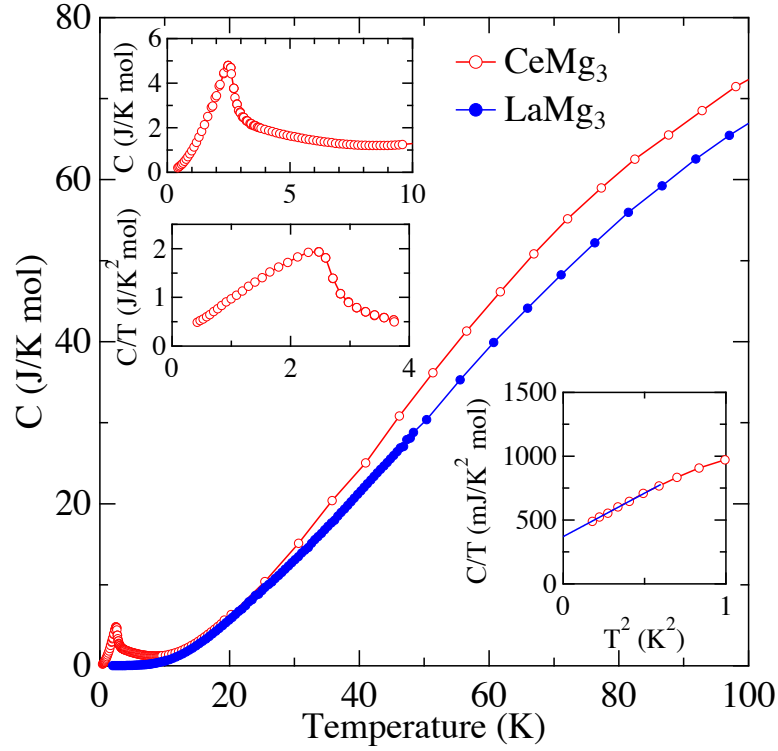
Figure 3.6: Temperature dependence of heat capacity in CeMg$_3$ and LaMg$_3$. The top inset shows the low temperature parts of C vs T and C/T vs T of CeMg$_3$. The bottom inset shows the C/T vs T^2 plot.

3.3.4   Heat capacity

The heat capacity of LaMg$_3$ was measured in the temperature range from 1.8 to 200 K, while the heat capacity of CeMg$_3$ was measured down to 0.5 K using a Quantum Design PPMS. The temperature dependence of the specific heat capacity of CeMg$_3$ and LaMg$_3$ are shown in Fig. 3.6. The heat capacity of LaMg$_3$ does not show any anomaly, and its temperature dependence is typical for a non-magnetic reference compound. The low-temperature part of the heat capacity of CeMg$_3$ is shown in the top inset of Fig. 3.6. A clear jump at T_{N} = 2.6 K, confirms the bulk magnetic ordering in this compound. It is to be mentioned here that no anomaly is seen either at 3.5 or 4 K as reported by Galera et al. [50] in the earlier studies on polycrystalline samples. The antiferromagnetic ordering of CeMg$_3$ is confirmed to be at 2.6 K, from our studies on single crystalline sample.

49
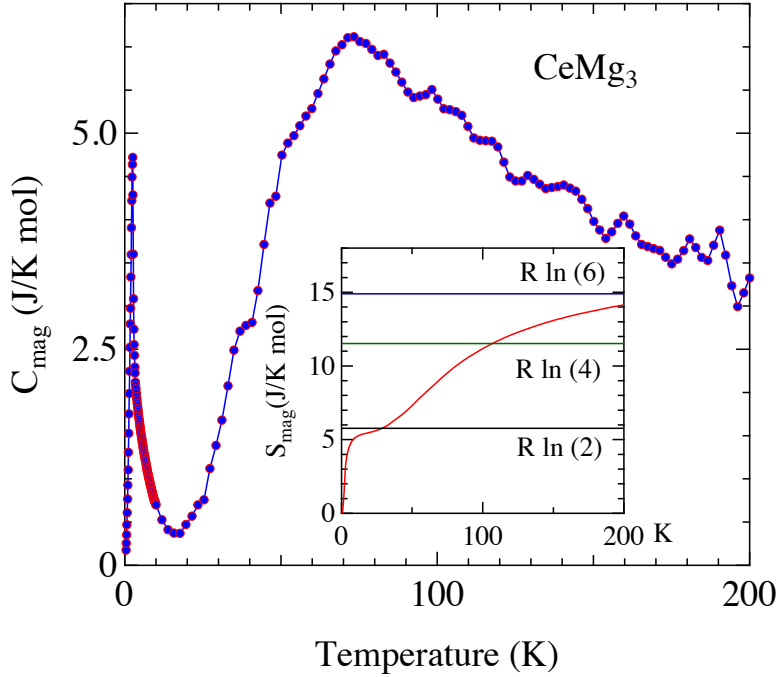
Figure 3.7: (a) Magnetic part of the heat capacity of CeMg$_3$. The inset shows the magnetic entropy.

The low temperature part of the C/T *vs.* T^2 plot is shown in the bottom inset of Fig. 3.6(a) and an estimate of the magnitude of Sommerfeld coefficient γ is obtained by extrapolating the low temperature data and fitting to the expression $C/T = \gamma + \beta T^2$. The γ value thus obtained is estimated to be 370 mJ/K^2 mol, and the β value is estimated to be 608 mJ/K^4 mol. This implies that the enhanced low-temperature γ value is due to the strong Kondo interaction. The large value of γ in the low temperature region indicates that CeMg$_3$ is a heavy-fermion compound, while the obtained high β value implies the expected contribution from magnons in the magnetic phase. The large value of the γ at the low temperature also signals the enhanced density of quasiparticle states at the Fermi level.

The magnetic part of heat capacity, obtained by subtracting the heat capacity of LaMg$_3$ from that of CeMg$_3$, is shown in Fig. 3.7. The jump in the magnetic part of the heat capacity amounts to 4.35 J/K mol which is considerably reduced compared to the mean field model prediction of 12.5 J/K mol for $S = 1/2$ system. The reduced value of the jump in heat capacity at the magnetic transition temperature supports

the presence of Kondo effect in CeMg$_3$. C_{mag} shows a broad hump centered around 80 K. This feature is attributed to the Schottky excitations among the CEF levels of the Ce^{3+} ions which is discussed in the next section. The temperature variation of C_{mag}/T is shown in the inset of Fig. 3.7. At T_{N} (= 2.6 K) the entropy amounts to only 0.5 R ln(2) in comparison to the value of R ln(2) anticipated for a doublet ground state. The reduced value of R ln(2) further confirms the presence of Kondo effect in this compound.

An estimation of the Kondo temperature T_{K} was made by the method described by Bredl et al., [57] where in the mean field approach, the jump in the heat capacity ΔC_{mag} of a Kondo system is related to the Kondo temperature. Besnus *et al.* [58] have found that the estimation of T_{K} by this model agrees well with the experimental data on various Ce and Yb based compounds. Fig. 3.8 shows the plot of Kondo temperature of various compounds and the jump in heat capacity, where the Kondo temperature is determined independently from other methods. The data plotted in Fig. 3.8 is extracted from the paper by Besnus *et al.* [58]. Based on the model described in Ref. [57], Blanco et al. [59] have given the expression for ΔC_{mag} at the magnetic ordering temperature as

$$\Delta C_{\mathrm{mag}} = \frac{6N_{\mathrm{A}}k_{\mathrm{B}}}{\psi''' \left(\frac{1}{2}+x\right)} \left[\psi'\left(\frac{1}{2}+x\right) + x\psi''\left(\frac{1}{2}+x\right)\right]^2, \qquad (3.4)$$

where $x = (T_{\mathrm{K}}/T_{\mathrm{N}})/2\pi$ and ψ', ψ'' and ψ''' are the first, second and third derivative of the polygamma function and the other terms have the usual meaning. A plot of this function is shown in Fig. 3.8(a).

The jump in the magnetic part of heat capacity was found to be 4.35 J/K mol, which results in a T_{K} value of 3.5 K. Desgranges and Schotte [60] have theoretically explained that the entropy of a Kondo system at the characteristic temperature T_{K} amounts to 0.68 R ln 2 (= 3.92 J/K mol). According to this description, in case of CeMg$_3$, at 3.8 K the entropy reaches 0.68 R ln 2, which indicates that the Kondo temperature is in close agreement with the one estimated from Eq. 3.4. Furthermore, as mentioned by Gruner and Zawadowski [61], the Kondo temperature can be estimated from the paramagnetic Curie-Weiss temperature, $|\theta_{\mathrm{p}/4}|$ (12/4 = 3 K). These estimation of the Kondo temperatures (T_{K}) by various methods give a value of 3 - 4 K,
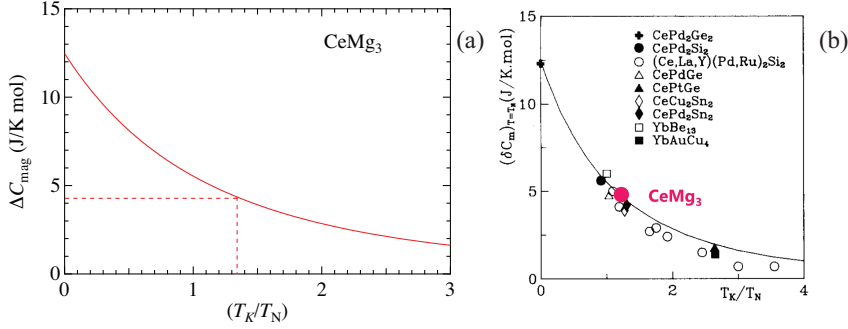
Figure 3.8: (a)An estimation of Kondo temperature made from the jump in heat capacity. The solid line is the plot of the Eq. 3.4. (b) The plot of Kondo temperature vs. the jump in heat capacity for various Ce and Yb based Kondo lattice compounds. The data is extracted from the paper by Besnus *et al.* (see text).

which is close to the magnetic ordering temperature of CeMg$_3$. However, a detailed neutron diffraction experiment has to be performed to substantiate our estimation of Kondo temperature.

Figure 3.9 shows the C/T versus T plot of CeMg$_3$ measured in applied fields of 0, 1 and 5 T. There is no appreciable change in the ordering temperature in an applied field of 1 T while in a 5 T field the Néel temperature shifts to a lower temperature and the jump in the heat capacity also decreases as it is usually observed in antiferromagnetic compounds. The low temperature part of C/T versus T^2 plot is shown in the inset of Fig. 3.9. An estimation of the γ value by linear extrapolation of the C/T versus T^2 plot of the heat capacity data measured in 1 T and 5 T field results in intercepts of 300 and 200 mJ/K^2·mol, respectively. The reduction in the γ value implies that the application of magnetic field tends to break the Kondo coupling between the localized Ce-4f electron and the conduction electrons.

3.3.5 Crystal field analysis

The deviation of the inverse magnetic susceptibility from the Curie-Weiss behavior below 150 K, the double peak structure in the electrical resistivity and the Schottky anomaly in the magnetic part of the heat capacity all reveal the substantial crystal electric field effect in CeMg$_3$. To gain more insight into the CEF we have performed the crystalline electric field analysis on the magnetic susceptibility and the heat ca-
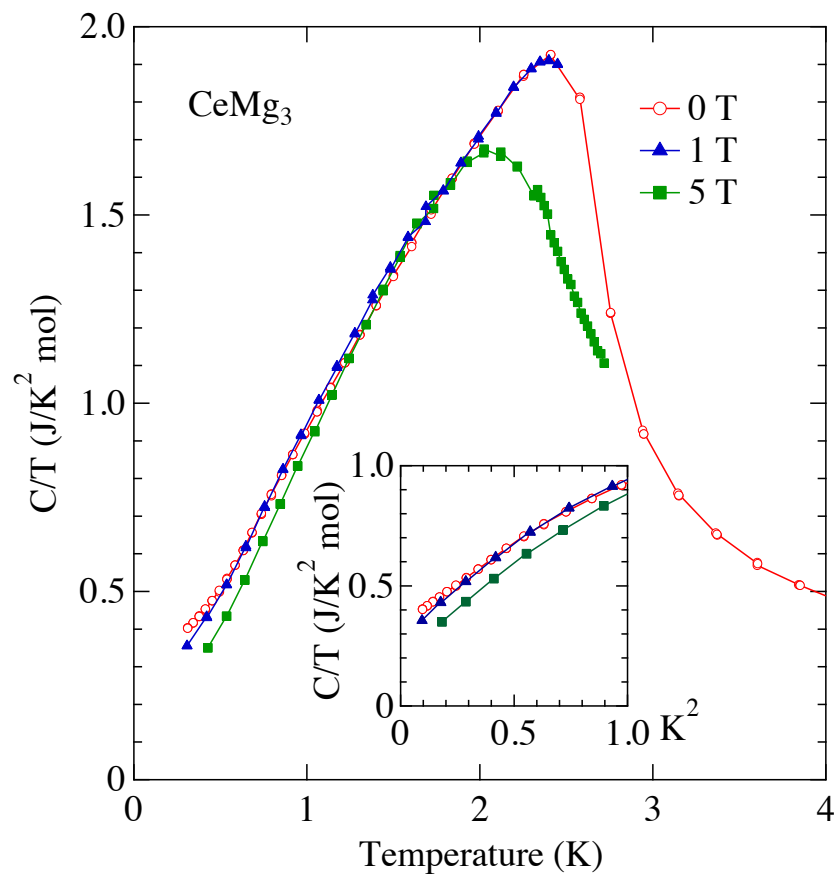
Figure 3.9: C/T versus T plot of CeMg$_3$ in applied magnetic fields, in the temperature range 0.5 to 4 K. The inset shows the low temperature part of C/T versus T^2 plot.

pacity data. The Ce atom in CeMg$_3$ occupies $4a$ Wyckoff's position, which has the $(m - 3m)$ cubic point symmetry. For a cubic point symmetry, the CEF Hamiltonian is given by

$$\mathcal{H}_{\text{CEF}} = B_4^0 \left(O_4^0 + 5O_4^4 \right) + B_6^0 \left(O_6^0 - 21O_6^4 \right), \tag{3.5}$$

where B_l^m and O_l^m are the crystal field parameters and the Steven's operators respectively [23, 24]. For Ce atom, the sixth order terms O_6^0 and O_6^4 are zero and hence the CEF Hamiltonian reduces to

$$\mathcal{H}_{\text{CEF}} = B_4^0 \left(O_4^0 + 5O_4^4 \right). \tag{3.6}$$

The magnetic susceptibility including the molecular field contribution λ_i is given by

$$\chi_i^{-1} = \chi_{\text{CEF}i}^{-1} - \lambda_i, \tag{3.7}$$

where the expression for χ_{CEF} is given in Chapter 1. The CEF parameter B_4^0 was estimated by using the Eqns. 3.6, and 3.7. The solid line Fig. 3.10(a) is the calculated CEF curve and the value of B_4^0 thus obtained is 0.53 K and the molecular field contribution λ was -8 mol/emu. For Ce atom, in the case of cubic site symmetry, depending on the sign of the crystalline electric field parameter the ground state will be a doublet or a quartet. The ground state will be a doublet if the sign of the crystal field parameter is positive, while it will be a quartet if the sign is negative. From the CEF calculations, it has been found that the sign of the B_4^0 parameter is positive, which clearly indicates that the ground state is a Γ_7 doublet. Diagonalizing the Hamiltonian of Eq. 3.6 gives the eigenvalues and the eigenfunctions. The eigenvalues are the energies of the crystal field split levels. From the eigenvalues of the crystal field Hamiltonian the crystal field splitting energy was found to be 191 K. The crystal field level scheme thus obtained from the magnetic susceptibility and the heat capacity data are in accordance with the previous neutron diffraction results on polycrystalline samples [49, 51]. The magnitude of the ordered moment of a Γ_7 doublet ground state based on the CEF calculation ($g_J J_x = 6/7 \times 0.833$) should be 0.714 μ_{B}/Ce. The observed magnetization value at 1.8 K is only 0.56 μ_{B}/Ce, this confirms that the
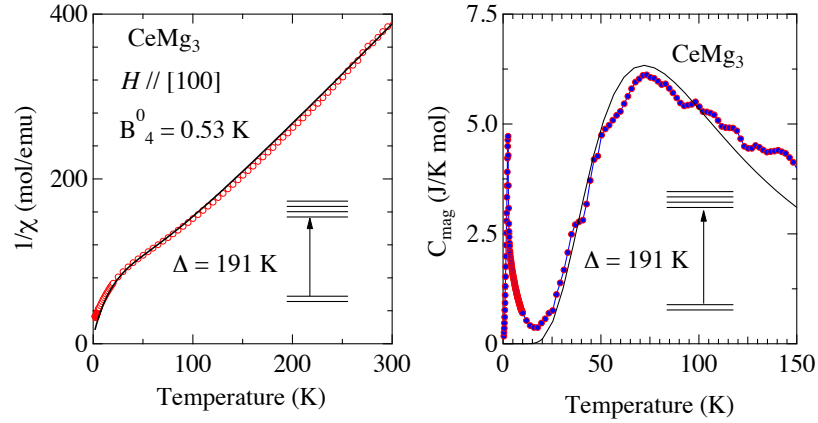
Figure 3.10: (a) CEF fit to the inverse susceptibility data. The CEF calculations exactly reproduce the experimentally observed susceptibility data. (b) The Schottky fit to the heat capacity data.

moment reduction in this compound is due to the combined effect of Kondo and crystal field effects.

As discussed earlier, the magnetic part of the heat capacity C_{mag} of CeMg$_3$ shows a broad peak at high temperature as shown in Fig. 3.10(b). This feature is attributed to the Schottky excitations between the CEF levels of the Ce^{3+} ions. An analysis of the heat capacity data has been performed on the basis of CEF model. The Schottky contribution to heat capacity is given by the following expression,

$$C_{Sch}\left(T\right) = R\left[\frac{\sum_i g_i e^{-E_i/T} \sum_i g_i E_i^2 e^{-E_i/T} - \left[\sum_i g_i E_i e^{-E_i/T}\right]^2}{T^2\left[\sum_i g_i e^{-E_i/T}\right]^2}\right], \qquad (3.8)$$

where R is the gas constant, E_i are the CEF energy levels in the units of temperature and g_i are the corresponding degeneracy of the levels. From the entropy calculations discussed above, it is obvious that the ground state of CeMg$_3$ should be a doublet ground state. Considering a degeneracy of doublet ground state and a quartet excited state, we found that the CEF levels are separated by an energy of 191 K
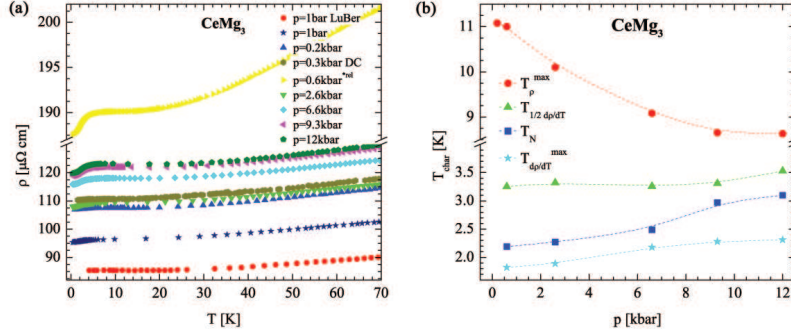
Figure 3.11: (a) Temperature vs. electrical resistivity of CeMg$_3$ with $J \parallel [100]$ at various applied hydrostatic pressures, and (b) The pressure dependence of T_ρ^{max}, $T_{1/2\ d\rho/dT}$, $T_{d\rho/dT}^{max}$, and a tentative T_N are shown.

apart. The solid line in Fig. 3.10(b) is based on the Eq. 3.8, which indicates that the calculated Schottky heat capacity matches well with the experimental data, which also supports the energy level obtained from the CEF analysis of the susceptibility data.

3.3.6   Pressure studies

From the physical properties of CeMg$_3$ discussed so far, it is obvious that this compound undergoes an antiferromagnetic ordering at sufficiently low temperature. CeMg$_3$ exhibits a double peak structure in the electrical resistivity, a reduced magnetic moment in the ordered state and a large Sommerfeld coefficient. Furthermore, it was found that the Kondo temperature (T_K) is close to the Néel temperature (T_N). All these indicate that CeMg$_3$ is similar to the other well known heavy fermion antiferromagnetic compounds like CeIn$_3$ [42, 47], CePd$_2$Si$_2$ [42], and CeCu$_2$Ge$_2$ [43], to mention a few, which show pressure induced superconductivity. As we have discussed in the introduction (Chapter 1), the magnetic state of these compounds are very sensitive to the external pressure, so we explored the effect of external hydrostatic pressure on CeMg$_3$ up to a pressure of 12 kbar. This work was done in collaboration with Prof. Bauer's group at Vienna. Some of the initial pressure measurements were performed in our home-made resistivity set-up as well.

The electrical resistivity of CeMg$_3$ has been investigated in the temperature inter-

val from 350 mK to 290 K in a piston cylinder type pressure cell up to a pressure of 12 kbar. The current was applied along the crystallographic [100] direction. Fig. 3.11 shows the results of pressure dependent resistivity. A clear tendency of higher residual resistivity values with increasing hydrostatic pressure is observed. With increasing hydrostatic pressure, the maximum at low temperature becomes more distinct and the broad hump around 100 K at ambient condition gets shifted to slightly lower temperatures (not shown in Fig. 3.11. The higher values for the resistivity curve for 0.6 kbar pressure, has been obtained after the high pressure study with 12 kbar applied pressure and a partial relief of that. It is likely that a contact problem of the voltage leads accounts to the shift by a factor of two, though the general behaviour is comparable.

The maximum in the resistivity (T_ρ^{max}) at low temperatures was determined directly form the maximum in the measurement data. Identification of the Néel temperature is done in different ways found in the literature: (a) a tentative T_{N} is proposed by two line fits intersecting in the vicinity of the transition peak, (b) taking temperature ($T_{1/2\ d\rho/dT}$) at half value of the derivative with respect to temperature $d\rho/dT$. Fig. 3.11(b) shows the characteristic temperatures. The general trend is an increase in the magnetic ordering temperature with applied hydrostatic pressure, thus stabilizing the ordered ground state. One of the reasons for the increase of T_{N} with application of pressure might be due to the large separation of Ce-Ce distance (≈ 5.2 Å) in CeMg$_3$. It is likely that we need higher pressures to decrease T_{N} and eventually reach the quantum critical point, as expected on the basis of Doniach's phase diagram.

3.4 CeMg$_{12}$

3.4.1 Crystal Structure

Like CeMg$_3$, the single crystal of magnesium rich CeMg$_{12}$ has also been grown by Bridgman method, where we used little excess of magnesium in order to compensate the weight loss due to its volatile nature. The phase purity of the sample was checked by means of powder x-ray diffraction (XRD) using monochromatic Cu-K$_\alpha$ radiation with wavelength 1.5406 Å. The XRD pattern showed that the sample is phase pure
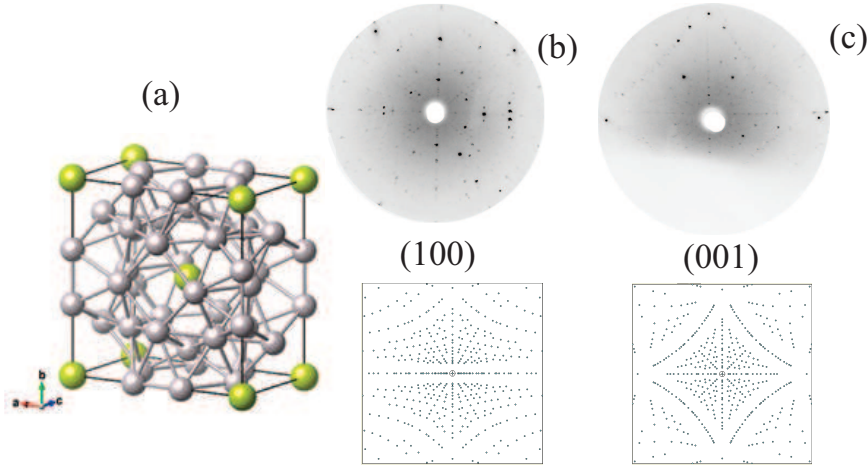
Figure 3.12: (a) Crystal structure of the tetragonal CeMg$_{12}$, (b) and (c) Experimental and theoretical Laue patterns of CeMg$_{12}$ corresponding to (100) and (001) planes.

and possesses the space group *I4/mmm*. The lattice constants were estimated to be $a = 10.332$ Å and $c = 5.961$ Å which matches well with the previous structural report [62]. The Ce-atoms are lying at the corners of the tetragonal unit cell and one at the body center. The unit cell volume is 636.35 Å^3 and the nearest Ce − Ce distance is 5.961 Å along the *c*-axis. The crystal structure of CeMg$_{12}$ is shown in Fig. 3.12(a). The crystal was oriented along the two principal crystallographic directions viz., along [100] and [001] directions by means of Laue diffraction. Well defined Laue diffraction spots together with the four fold symmetry confirmed the tetragonal crystal structure and the good quality of the sample. The experimental Laue pattern for the (100) and the (001) planes together with the simulated patterns are shown in Fig. 3.12(b) & (c).

3.4.2   Magnetic measurements

The temperature dependence of the magnetic susceptibility was studied in the temperature range from 1.8 to 300 K using a SQUID magnetometer with an applied magnetic field of 1 kOe along crystallographic [100] and [001] directions. The temperature dependence of susceptibility is plotted in Fig. 3.13(a) on a semi-logarithmic scale. We see a large magnetic anisotropy in CeMg$_{12}$ reflecting the tetragonal crystal symmetry.
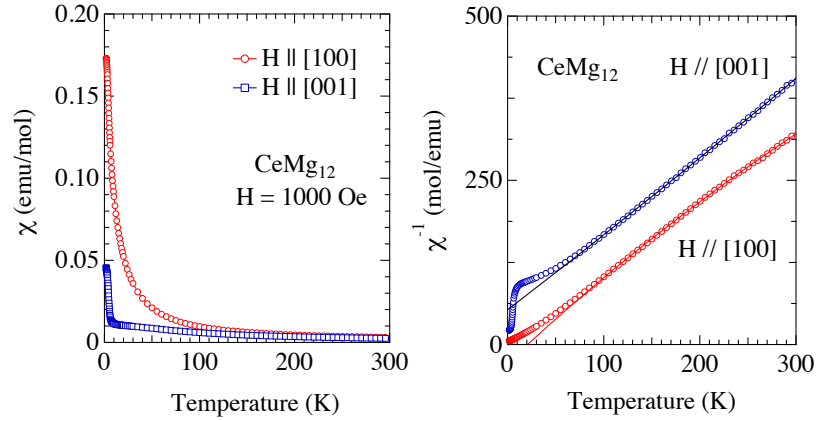
Figure 3.13: (a) Temperature dependence of magnetic susceptibility of CeMg$_{12}$ with an applied magnetic filed of 1 kOe along the crystallographic a and c directions, (b) inverse susceptibility vs. temperature plot. The solid lines are fits to the modified Curie-Weiss law.

The magnetic susceptibility along the [100] direction is larger than along the [001] direction, thus indicating that the [100] crystallographic direction is the easy axis of magnetization. Inverse susceptibility vs. temperature is plotted in Fig. 3.13(b). At high temperature range, from 100 to 300 K, inverse susceptibility varies linearly with temperature, and follows the modified Curie-Weiss law:

$$\chi(T) = \chi_{\text{para}} + \chi_0, \tag{3.9}$$

with

$$\chi_0 = \chi_{\text{Pauli}} + \chi_{\text{Landau}} + \chi_{Dia}. \tag{3.10}$$

χ_{Para} is given by the Eq. 3.1. As it is evident from Eq. 3.10, the contributions to χ_0 come from the diamagnetic susceptibility which arises due to the presence of ion cores and the Landau and Pauli spin susceptibilities of the conduction electrons. From the modified Curie-Weiss fitting we obtained $\chi_0 = 4.561 \times 10^{-4}$ emu/mol, $\theta_{\text{p}} = 20.86$ K and $\mu_{\text{eff}} = 2.44$ μ_{B}/Ce along $H \parallel [100]$ and $\chi_0 = $ -1.289 $\times 10^{-4}$ emu/mol, $\theta_{\text{p}} = -47.5$ K and $\mu_{\text{eff}} = 2.68$ μ_{B}/Ce along $H \parallel [001]$ direction. The deviation from the linear behavior in the inverse magnetic susceptibility below 100 K is mainly attributed to the crystal electric field effect.
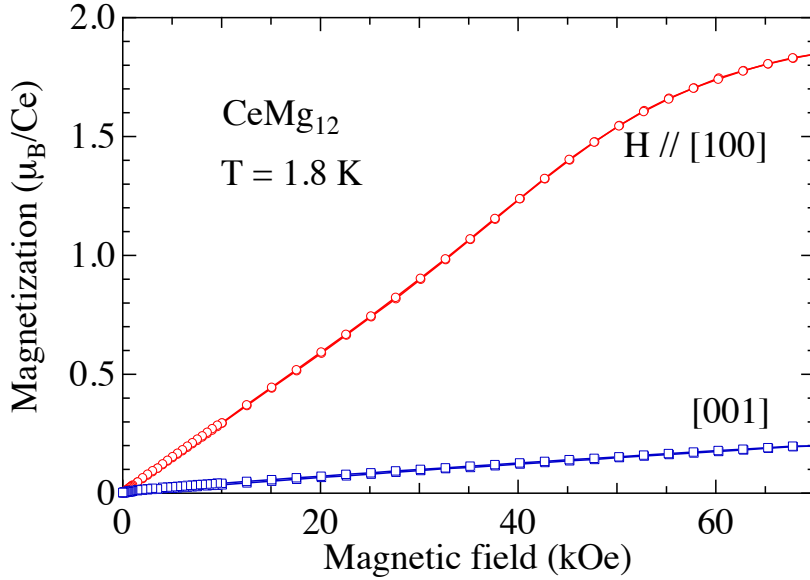
Figure 3.14: Isothermal magnetization measured at $T = 1.8$ K of CeMg$_{12}$ for applied magnetic field along the two principal crystallographic directions.

Isothermal magnetization is measured at 1.8 K up to a magnetic field of 70 kOe along both the crystallographic directions as shown in Fig. 3.14. The magnetization for $H \parallel$ [100] increases more rapidly than along the [001] direction, confirming that [100] direction is the easy axis of magnetization. For fields greater than 35 kOe, the magnetization along [100] direction shows some spin re-orientation, in spite of the fact that the magnetization is measured at 1.8 K, which is 0.6 K above the $T_{\mathrm{ord}} = 1.2$ K. This indicates some short range magnetic ordering above T_{ord}. Furthermore, the magnetization shows a saturation behavior for fields around 7 T. The magnetization reaches a value of 1.85 μ_{B}/Ce, which is close to the free ion value of Ce^{3+} ($g_J J = \frac{6}{7} \times \frac{5}{2} = 2.14$). The magnetization for $H \parallel$ [001] increases linearly and reaches only 0.2 μ_{B}/Ce at 70 kOe, indicating that [001] is the hard axis of magnetization.

Crystal electric field analysis on the magnetic susceptibility data, as well as on the isothermal magnetization data was performed in order to estimate the crystal field split energy levels of the degenerate $(2J + 1)$ states. The Ce atom in CeMg$_{12}$ occupies the $2a$ Wyckoff's position in the space group $I4/mmm$ and hence possesses the tetragonal site symmetry $4/mmm$. For the tetragonal site symmetry, the sixfold-

degenerate levels of the $J = 5/2$ multiplet will split into three doublets. The crystal electric field Hamiltonian for the Ce-atom in tetragonal site symmetry is given by,

$$\mathcal{H}_{\text{CEF}} = B_2^0 O_2^0 + B_4^0 O_4^0 + B_4^4 O_4^4, \tag{3.11}$$

where B_l^m and O_l^m are the CEF parameters and the Stevens operators, respectively [24, 23]. The magnetic susceptibility including the molecular field contribution λ_i, which represents the exchange interaction among Ce magnetic moments, is given by Eq. 3.7.

For calculating the magnetization we have used the following Hamiltonian which includes the Zeeman term and molecular field term,

$$\mathcal{H} = \mathcal{H}_{\text{CEF}} - g_{\text{J}}\mu_{\text{B}}J_i(H_i + \lambda_i M_i), \tag{3.12}$$

where,

$$M_i = g_{\text{J}}\mu_{\text{B}} \sum_n |\langle n \mid J_i \mid n\rangle \frac{e^{-E_n/k_{\text{B}}T}}{Z} \quad (i = x, y, \text{and } z). \tag{3.13}$$

For the purpose of crystal field analysis, we have plotted the experimental results on susceptibility in the form of $1/(\chi - \chi_0)$. An estimate of the crystal field energy levels are obtained by diagonalizing the Hamiltonian. The crystal field parameters thus obtained correspond to $B_2^0 = 6.8$ K, $B_4^0 = 0.022$ K and $B_4^4 = -0.75$ K and the molecular exchange field constant $\lambda_{100} = 0$ and $\lambda_{001} = 30$ mol/emu. The positive value of λ along the [001] direction suggests a ferromagnetic ordering in CeMg$_{12}$, the calculated susceptibility diverges at low temperature along this direction also supports the evidence of ferromagnetic ordering. However, further low temperature measurements are necessary to confirm the nature of magnetic ordering in CeMg$_{12}$. The difference in the molecular field contributions for [100] and [001] directions, clearly indicate the anisotropic magnetic interaction between the Ce moments. The sign of the B_2^0 parameter in general determines if the system possesses an easy plane or easy axis anisotropy [25]. Since B_2^0 is positive in CeMg$_{12}$ it suggests an easy plane magnetization. The obtained energy levels are $\Delta_1 = 30$ K and $\Delta_2 = 126$ K. A detailed neutron diffraction study and the high temperature heat capacity measurements are
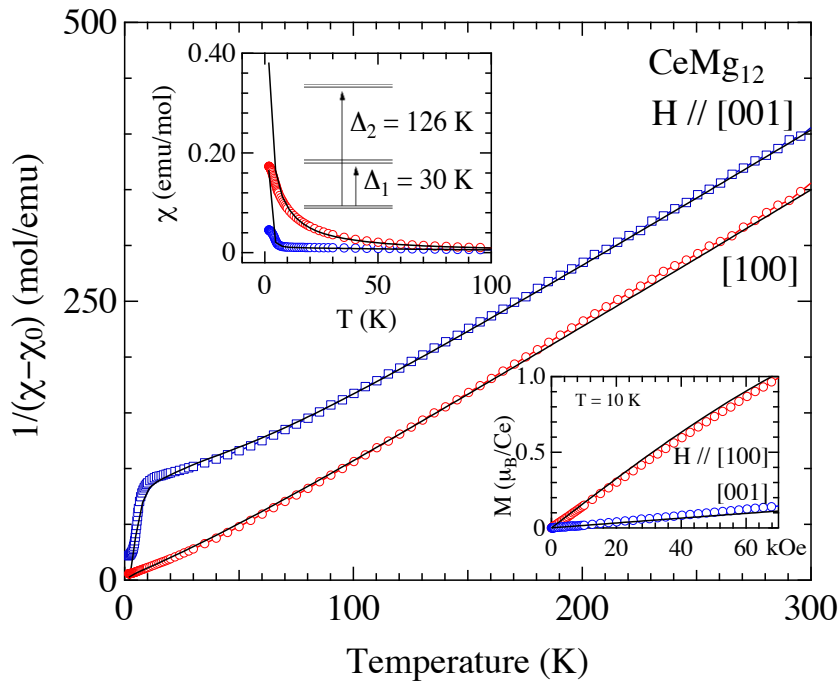
Figure 3.15: Inverse magnetic susceptibility of CeMg$_{12}$, the black solid lines are the calculated curves based on the crystal electric field calculations. The obtained energy levels are shown in the inset of the figure. The calculated CEF susceptibility is shown in the top inset. The bottom inset shows the magnetization data measured at T = 10 K, and the solid lines are the calculated CEF magnetization curves along the two principal crystallographic directions.
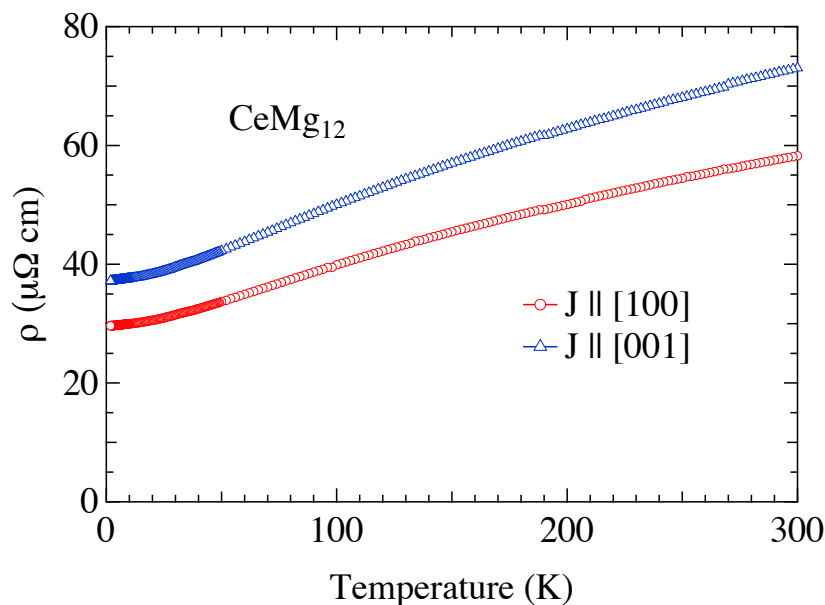
Figure 3.16: Temperature dependence of electrical resistivity of CeMg$_{12}$ along the two principal crystallographic directions.

necessary to clarify this estimated crystal field split level schemes.

3.4.3 Electrical Resistivity

The temperature dependence of electrical resistivity, measured in the temperature range from 1.8 to 300 K is shown in Fig. 3.16. As it is evident from the figure, there is a large anisotropy in the resistivity when the current is passed along the [100] and [001] directions. Since the resistivity was measured down only to 1.8 K, the magnetic ordering could not be traced. From the low temperature heat capacity measurement, to be discussed later, it is clear that this compound orders magnetically at 1.2 K. The electrical resistivity decreases with decreasing temperature showing a metallic behavior. A broad hump centered around 100 K is seen in the electrical resistivity, indicating the thermal population of the excited levels of the $2J + 1$ crystal field levels, which substantiates the crystal field calculations. Unlike the case of CeMg$_3$ no signature of Kondo effect is observed at low temperature.
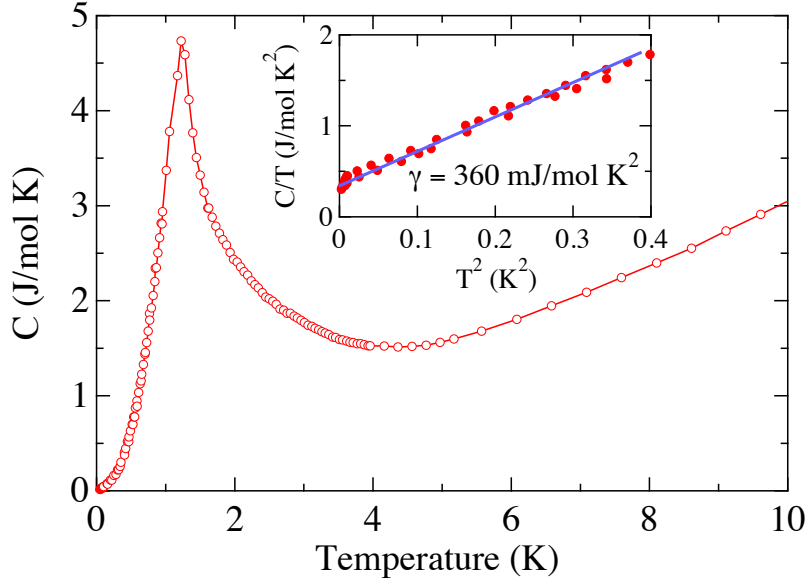
Figure 3.17: Temperature dependence of heat capacity of CeMg$_{12}$. The inset shows the low temperature part of the C/T versus T^2 plot.

3.4.4   Heat Capacity

The temperature dependence of specific heat capacity measured in a Quantum Design physical property measurement system (PPMS), in the temperature range from 0.05 to 10 K is shown in Fig. 3.17. It is evident from the figure that a huge jump in the specific heat is observed at 1.2 K suggesting a bulk magnetic ordering T_{ord} in CeMg$_{12}$. The jump in the specific heat is broad thus signalling a short range magnetic order above the T_{ord}. The inset shows the low temperature part of the C/T versus T^2 plot. An estimation of the Sommerfeld coefficient γ was made by the linear extrapolation of the C/T versus T^2 plot. The obtained γ value is 360 mJ/K^2 mol. Although the apparent γ value is large, since the magnetic ordering temperature is at 1.2 K and the crystal field split first excited state is at 30 K, one cannot claim this compound to be a heavy fermion compound. An estimate of the magnetic entropy could not be performed as the non-magnetic analog of CeMg$_{12}$ was not available.

3.5   Summary

Single crystals of CeMg$_3$, LaMg$_3$, and CeMg$_{12}$ have been grown by Bridgman method in sealed molybdenum tubes, which were then sealed in quartz ampoules. X-ray and EDAX analysis of the samples confirm that the samples are phase pure. The magnetic susceptibility and heat capacity data clearly indicated that the CeMg$_3$ orders antiferromagnetically with $T_N = 2.6$ K. The heavy fermion nature of CeMg$_3$ is concluded from the high value of Sommerfield coefficient $\gamma = 370$ mJ/K^2 mol. The reduced value of the magnetization, the reduced jump in the heat capacity at the magnetic transition temperature, and the $-ln(T)$ behavior in the electrical resistivity confirmed the presence of Kondo effect in this compound. The estimated Kondo temperature was found to of the order of the Néel temperature, around 3-4 K, suggesting a delicate competition between the Kondo interaction and the RKKY exchange interaction in this compound. From the pressure dependence of electrical resistivity, we have found that the Néel temperature (T_{N}) increases with increasing external hydrostatic pressure up to a pressure of 12 kbar. It will be interesting to observe the effect of even higher pressure in this compound, which may eventually bring down the Néel temperature and tune the system to quantum criticality. From the CEF analysis of heat capacity and magnetic susceptibility data we have found that the $J = 5/2$ six fold state splits into a doublet ground state and quartet excited state separated by an energy of 191 K.

The anisotropic physical properties have been investigated for the first time on CeMg$_{12}$. From the heat capacity measurement, it was found that CeMg$_{12}$ undergoes a magnetic ordering at 1.2 K. The low value of the magnetic ordering temperature may presumably be attributed to the long Ce-Ce distance in the unit cell. The magnetic susceptibility and the electrical resistivity are highly anisotropic reflecting the tetragonal nature of the crystal structure. The effective moment of Ce atom is close to the free ion value indicating that the Ce atom exhibits local moment behavior. The magnetization reaches 1.8 μ_B/Ce at a field of 70 kOe. The crystal electric field analysis of magnetic susceptibility data reveals that the $(2J + 1)$ degenerate level of Ce^{3+} ion split into three doublets, and first and the second excited doublets are at energy 30 K and 126 K, respectively from the ground state. From the negative value of the polycrystalline average of the paramagnetic Weiss temperature the magnetic

ordering can be supposed to be of antiferromagnetic in nature. However, a positive value of the molecular field exchange constant λ_z for H parallel to [001] direction in the CEF calculations indicates that the magnetic ordering is ferromagnetic. Neutron diffraction experiments on CeMg$_{12}$ at sufficiently low temperature is necessary to know the exact nature of magnetic ordering and to know about the magnetic structure of this compound.

Chapter 4

Anisotropic magnetic properties of equiatomic CeGe and CeSi

4.1 Introduction

In continuation of our studies on Ce based binary compounds, we have grown the single crystals of CeGe and CeSi, and investigated their anisotropic magnetic properties in detail. The RX (R = rare earth, X = Ge, Si) compounds crystallize either in FeB-type or CrB-type orthorhombic crystal structure depending upon R and heat treatment during the crystal growth. It is interesting to mention here that some compounds in the RX series exhibit polymorphism [63], by crystallizing in both the structure types. CeX (X = Ge, Si) compounds crystallize in the FeB-type orthorhombic crystal structure with space group $Pnma$ (no. 62). CeSi has been previously studied on a polycrystalline sample by Shaheen [64] and it was reported that it orders antiferromagnetically with T_{N} = 5.6 K. Furthermore, from the heat capacity data, Shaheen concluded that the ground state is a quartet, which is unusual for a system in which the Ce site symmetry is orthorhombic. In such cases a doublet ground state is usually expected, while quartet ground state is observed only when the Ce atom is located at a high site symmetry such as cubic site symmetry. In another report Noguchi et $al.$ [65] have studied the magnetic properties of CeSi single crystalline sample. They reported a doublet ground state in this system, and

found a saturation moment of 1.75 μ_B/Ce along the [010] direction, which is the easy axis of magnetization. Polycrystalline CeGe was investigated by Buschow [66] long ago, and very recently by Marcano *et al.* [67, 68]. All the previous reports on polycrystalline CeGe confirmed an antiferromagnetic ordering at around 10 K. From the heat capacity data Marcano *et al.* [68] concluded that the Kondo interaction is present in CeGe. This is interesting as Shaheen [64] did not report any evidence of Kondo interaction in isostructural CeSi which has a lower unit cell volume compared to CeGe. The μSR studies on polycrystalline CeGe revealed a complex antiferromagnetic spin structure [69]. The magnetization measurements also exhibited a strong irreversibility between the field-cooled (FC) and zero-field-cooled (ZFC) plots at low temperatures and a very broad metamagnetic transition [68] in the *M vs H* plot. Furthermore, Marcano *et al.* [68] found that the electrical resistivity in CeGe at the transition temperature (T_N) increases with decrease in the temperature indicating the signature of magnetic superzone gap opening in this compound. Due to the relatively low crystal symmetry of CeX compounds, we thought that it will be worthwhile to grow the single crystals of CeX (X = Ge and Si) and investigate their anisotropic magnetic behavior using the techniques of magnetization, electrical transport, and heat capacity, as well as studying the superzone gap in detail. In addition it was felt that a crystal electric field analysis of the anisotropic magnetic susceptibility and heat capacity of CeX single crystals would enable us to find the CEF level scheme in these two compounds.

4.2   Crystal Growth

CeGe phase melts peritectically at 1433 °C [70], but increasing Ge concentration slightly results in a near congruent melting. We took Ce and Ge in the ratio 1 : 1.05, and melted the charge several times in a tetra-arc furnace to prepare a homogeneous polycrystalline sample. Later a tungsten seed rod was used to pull the single crystal out of the melt by Czochralski method. It is interesting to mention here that the crystal has a cleavage plane perpendicular to the growth direction and because of that the crystal cleaved during the growth and its lower portion fell down due to its own weight. The cleaved surface of the crystal was later found to be crystallographic [010] direction from the Laue diffraction studies. In case of LaGe, CeSi, and LaSi,

the phases melt congruently around 1400 °C. Single crystals of LaGe, and CeSi were grown by similar method as CeGe. We prepared the polycrystalline sample of non-magnetic reference compound LaSi by arc-melting. The details of crystal growth are given in Chapter 2.

4.3 Results of CeGe

4.3.1 Structural properties

The shiny cleaved surface of CeGe crystal indicated that the grown crystal was of good quality. As the crystal was pulled from a slightly off-stoichiometric melt, the phase purity of the sample was checked by means of powder x-ray diffraction. A small piece of the single crystal was ground and the powder x-ray diffraction measurement was done using a PANalytical x-ray diffractometer with a monochromatic Cu Kα radiation. It was found that the crystal was phase pure as there were no impurity peaks in the powder diffraction pattern. From the x-ray diffractogram it was inferred that CeGe crystallizes in the orthorhombic crystal structure with the space group *Pnma* (no. 62). A Rietveld analysis was performed on the powder pattern using FULLPROF [32] software package to estimate the lattice constants. A reasonably good fit to the experimental pattern was observed which is shown in Fig. 4.1. In the inset of Fig. 4.1 the crystal structure of CeGe is shown. The estimated lattice parameters are $a = 8.355(4)$ Å, $b = 4.078(9)$ Å, and $c = 6.023(5)$ Å. From the Rietveld refinement it was found that the Ce and Ge atoms occupy the $4c$ site with positions at (0.1788, 0.25, 0.6172) and (0.0424, 0.25, 0.1366), respectively. These lattice parameter values are in good agreement with the previous reports [66, 67, 63]. The composition of the grown crystal was confirmed by means of Energy Dispersive Analysis by X-ray (EDAX) at various regions of the crystal. The grown crystal was found to be homogeneous and the stoichiometry was uniform throughout the sample. The crystal was oriented along the principal crystallographic directions by means of back reflection Laue diffraction method, and cropped out in a rectangular bar form using a spark erosion cutting machine. All the measurements were performed on well oriented single crystalline samples.
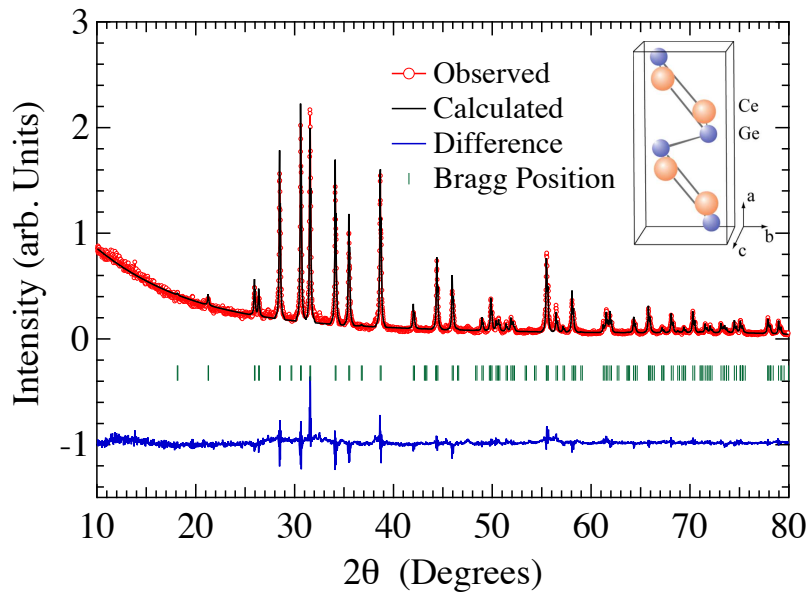
Figure 4.1: Powder x-ray diffraction pattern of CeGe along with the Rietveld refinement (black line), Bragg positions (green markers), and the difference between experimental and calculated pattern. A unit cell of CeGe crystal is shown in the inset.

4.3.2 Magnetic susceptibility and magnetization

The magnetic susceptibility of CeGe was measured in the temperature interval from 1.8 to 300 K, along the three principal crystallographic directions, namely, [100], [010], and [001] using a (Quantum Design) SQUID magnetometer in an applied field of 1 kOe. The temperature dependence of magnetic susceptibility along the three principal crystallographic directions is shown in Fig. 4.2. A large anisotropy in the susceptibility is clearly visible in both magnetically ordered and paramagnetic phases. In the inset of Fig. 4.2 the low temperature part of magnetic susceptibility is shown, where a clear drop in magnetic susceptibility is seen at 10.5 K with decreasing temperature for H ∥ [010]. Relatively small peaks were observed for H ∥ [100], and H ∥ [001] directions, indicating the onset of antiferromagnetic ordering of this compound at 10.5 K. It is clear that the [010] direction is the easy axis of magnetization, which is further confirmed from the isothermal magnetization measurements discussed next. For a collinear bipartite antiferromagnet, the magnetic susceptibility along the easy axis of magnetization ($\chi_\parallel$) should decrease to zero as the temperature is lowered to zero kelvin, while the susceptibility along the hard axes ($\chi_\perp$) are expected to be almost temperature independent. At low temperature below the Néel temperature, the susceptibility along the hard axes show an upturn with decreasing temperature, which indicates that the antiferromagnetic ordering in CeGe is not a simple collinear two-sublattice antiferromagnetism. At high temperature, in the range 150 to 300 K, the inverse susceptibility varies linearly with temperature, and follows Curie-Weiss law. The high temperature data were fitted to Curie-Weiss law and an estimate of the paramagnetic Curie temperature (θ_p), and effective moment value (μ_eff) of Ce were obtained. The effective moment values μ_eff and the paramagnetic Curie temperature θ_p were found to be 2.57 μ_B/Ce and -25 K, 2.61 μ_B/Ce and 16 K, and 2.57 μ_B/Ce and -43 K, respectively for H ∥ [100], [010], and [001] directions. The obtained experimental values of μ_eff are close to the free ion value of Ce^{3+}, 2.54 μ_B, which indicates that the Ce atom in this compound is in trivalent state. The Curie-Weiss temperature θ_p is positive along H ∥ [010], while for the other two principal directions it is negative. However,the polycrystalline average of θ_p is negative (-17 K), which is consistent with the antiferromagnetic nature of magnetic ordering of this compound.

The field dependence of isothermal magnetization $M(H)$ measured at 1.8 K is
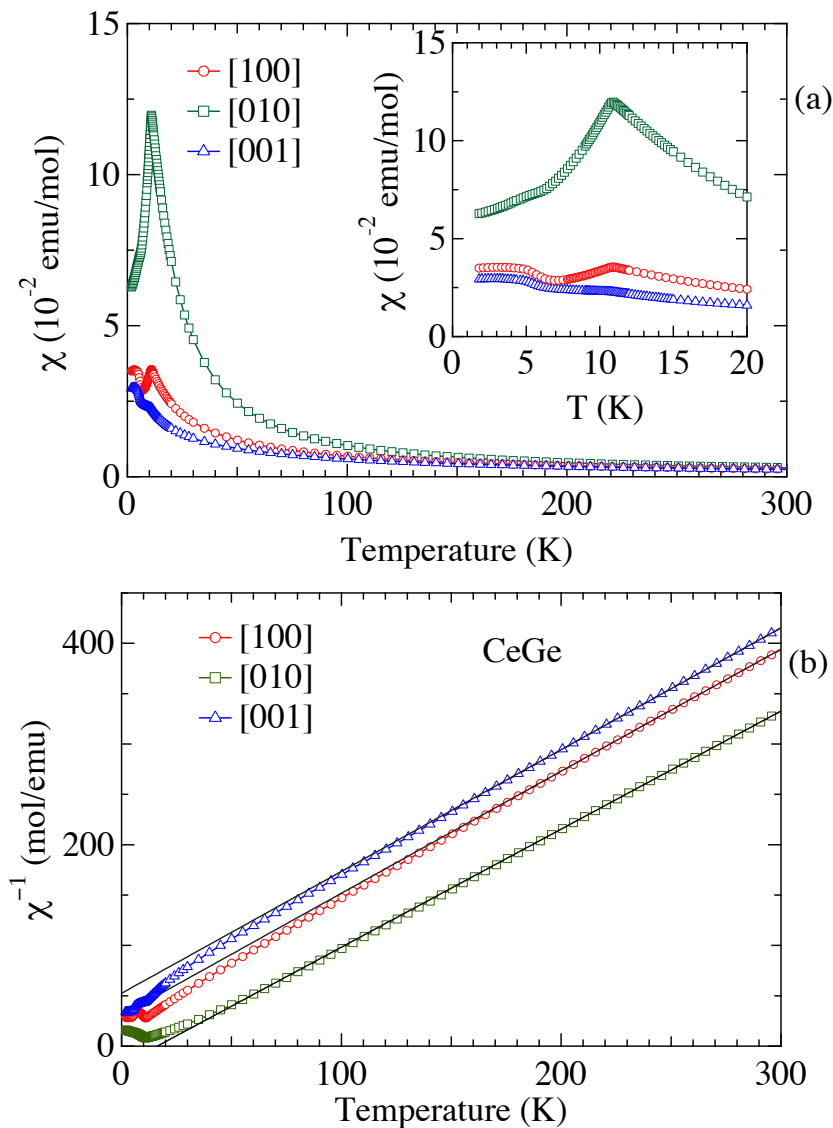
Figure 4.2: (a)Temperature dependence of magnetic susceptibility of CeGe with magnetic field along crystallographic [100], [010] and [001] directions. The inset shows the low temperature part of the magnetic susceptibility. (b) Inverse magnetic susceptibility of CeGe, the solid lines are fit to Curie-Weiss law.

shown in Fig. 4.3(a). At low applied magnetic fields, the magnetization along H ∥ [010] direction is almost linear, and exhibits an upward curvature as the field is increased. At a critical field of 4.8 T, the magnetization shows a metamagnetic like transition, the magnetization shows a more prominent metamagnetic jump at a field of 6.4 T, and then increases gradually with increasing magnetic fields. The magnetization value obtained at 12 T is about 1.5 μ_{B}/Ce which is well below the saturation magnetic moment of free Ce^{3+} ion ($g_J J \mu_B = 2.14$ μ_{B}/Ce). An estimate of the ordered moment was obtained from the Arrott plot [71]. The Arrott plot is shown in the inset of Fig. 4.3(a) for H ∥ [010], and the magnetization data measured at temperature 1.8 K. The high field data were fitted to the following expression:

$$M^2 = a \left(\frac{H}{M} \right) - b\epsilon \tag{4.1}$$

where a and b are constants and $\epsilon = (1 - T_{\mathrm{N}}/T)$. The ordered moment was found to be 0.86 μ_{B}/Ce from the fitting, which corroborates with the previous neutron diffraction result on a polycrystalline sample by Schobinger-Papamantellos *et al.* [69], where the authors estimated an ordered moment of 1.0 μ_{B}/Ce. The authors attributed the moment reduction to the presence of Kondo effect in this compound. Our resistivity measurements, to be discussed later, show a clear signature of Kondo effect in the high temperature range, from 80 to 300 K in this compound, however no signature of Kondo effect is observed in the low temperature range.

The magnetization along the [100] crystallographic direction increases linearly with field up to 10.6 T, where the magnetization exhibits a sharp metamagnetic transition and then shows a nearly saturation behavior. While the magnetization along [001] direction increases linearly without anomaly or any sign of saturation up to a field of 16 T. The magnetization reaches a value of 0.54 μ_B/Ce at a field of 16 T for [001] direction, indicating it as the hard axis of magnetization. From Fig. 4.3, it is clear that [010] direction is the easy axis of magnetization. The field dependence of magnetization at various fixed temperatures along the [100] and [010] directions are measured and is shown in Fig. 4.3(b) and (c). It is evident from the figure that with increasing temperature, the metamagnetic transition along the [100] direction shifts towards left (lower magnetic field) and vanishes at magnetic transition temperature. While along [010] crystallographic direction, the metamagnetic transition at lower
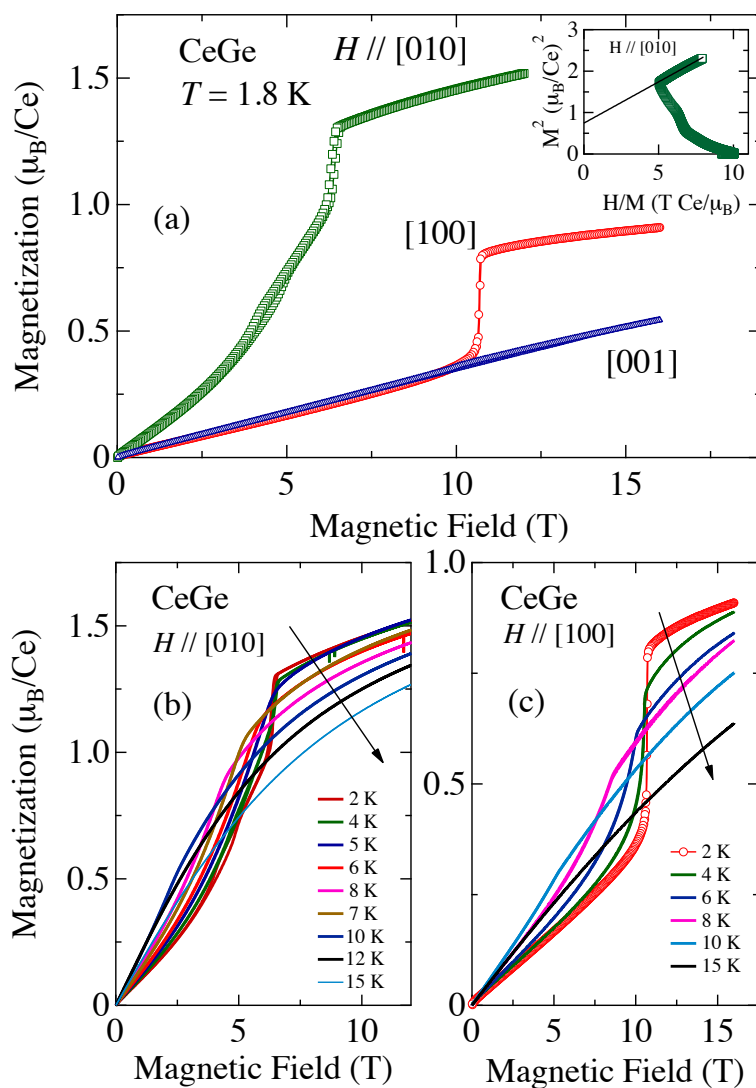
Figure 4.3: (a) Magnetization plots of CeGe along the three principal crystallographic directions measured at $T = 1.8$ K. The inset shows the Arrot plot for $H \parallel [010]$ magnetization data measured at $T = 1.8$ K (b) Isothermal magnetization of CeGe measured at various fixed temperatures for $H \parallel [010]$ and (c) for $H \parallel [100]$ direction.
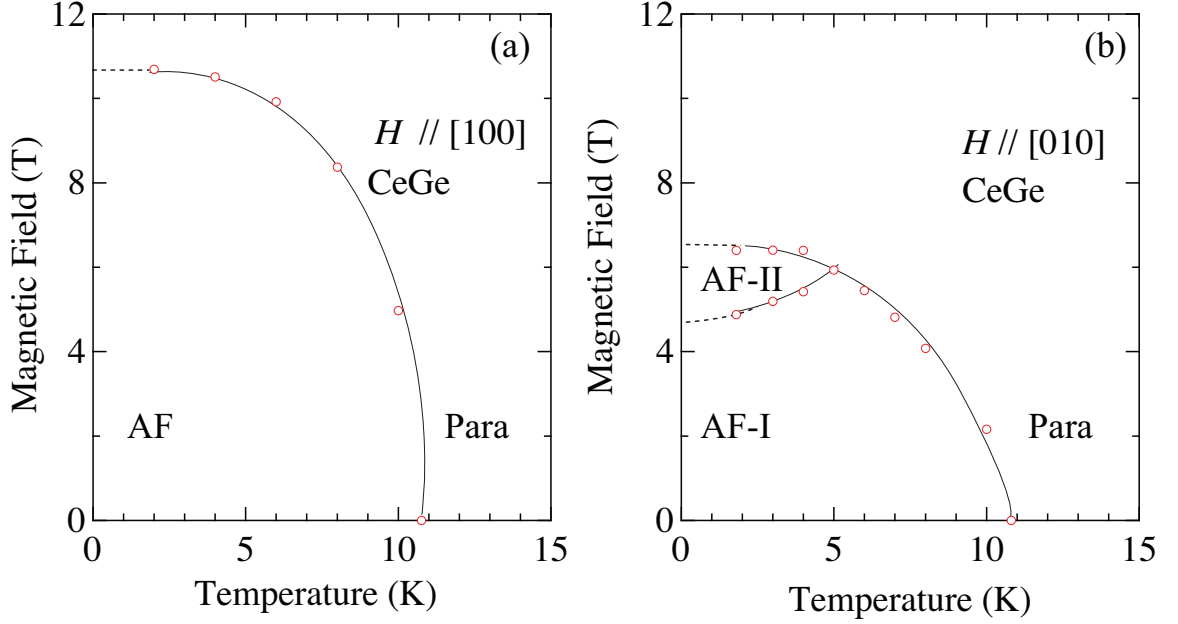
Figure 4.4: Magnetic phase diagram of CeGe for field parallel to (a) [100] and (b) [010] directions. The solid lines are guide to eyes.

field shifts toward higher field and the metamagnetic transition at the higher filed shifts toward lower field with increasing temperature, and merges at 5 K. A magnetic phase diagram has been constructed from the differential plot (dM/dH $vs.$ H) of isothermal magnetization as shown in Fig. 4.4.

For H ∥ [100] direction, above the Néel temperature (T_N) the compound is paramagnetic, while below T_N it is in antiferromagnetic state. At low temperature for magnetic field greater than 10.7 T where the magnetization exhibits a near saturation, the compound is in a field induced ferromagnetic state. In case of [010] crystallographic direction, for fields 4.5 < H 6.5 T and temperature up to 5 K the system is in a complex antiferromagnetic state as defined by AF-II in the phase diagram.

4.3.3 Electrical resistivity

The temperature dependence of electrical resistivity for current along the three principal crystallographic directions, in the temperature range from 1.9 to 300 K is shown in Fig. 4.5. The anisotropic electrical resistivity of the non-magnetic reference

compound LaGe is also shown in the Fig. 4.5.

The electrical resistivity of LaGe is typical of a metallic system, the resistivity decreases with decreasing temperature from 300 K to about 15 K, below this temperature the resistivity is almost temperature independent with a residual resistivity of 11.7 $\mu\Omega$ cm and 29.1 $\mu\Omega$ cm for $J \parallel$ [100] and [010] crystallographic directions, respectively, indicating a significant anisotropy in the compound. The electrical resistivity of CeGe also decreases with decreasing temperature, but exhibits a broad hump centered around 75 K for current parallel to all three principal crystallographic directions. The residual resistivity (at T = 2 K) of CeGe along the three principal crystallographic direction is 52 $\mu\Omega$ cm, 47.7 $\mu\Omega$ cm, and 38.96 $\mu\Omega$ cm for $J \parallel$ [100], [010], and [001]. Below 75 K the resistivity drops more rapidly down to the Néel temperature at 10.5 K, where the resistivity increases in all three directions, then shows a broad maximum centered around 9 K, and again decreases with decreasing temperature along [100] and [001] directions, while along the [010] direction the electrical resistivity levels off after passing through the broad maximum at 9 K. The magnetic part of electrical resistivity $\rho_{\text{mag}}(T)$ was calculated by subtracting the resistivity values of homologous LaGe from that of CeGe as shown in Fig. 4.5(b), where the temperature dependence of $\rho_{\text{mag}}(T)$ is plotted on a semi-logarithmic scale. We observe a negative temperature coefficient of electrical resistivity below 300 K with a broad peak at 80 K, which can be rationalized on the basis of incoherent Kondo scattering of conduction electrons and the crystal electric field split levels. However, at low temperature immediately above T_{N}, we do not see any evidence of Kondo effect in our electrical resistivity data.

The electrical resistivity of CeGe at $T_{\text{N}}(= 10.5~K)$ shows an upturn. This type of behavior is usually attributed to the magnetic superzone gap effect, which appears when the magnetic periodicity is different from the lattice periodicity. The theoretical investigation of this type of anomaly appearing at the paramagnetic to antiferromagnetic transition in rare-earth metals has been made by several authors [28, 72] and can simply be understood as shown in the cartoon diagram Fig. 4.6. In normal metals, the electron states in which the conduction electrons exist are surrounded by Brillouin zone boundaries and the Fermi sphere is completely within a Brillouin zone 4.6(a). The conduction electrons are at the Fermi surface and the surface area of the sphere governs the conductivity. Now in the case of a simple two sub-lattice antiferromagnet,
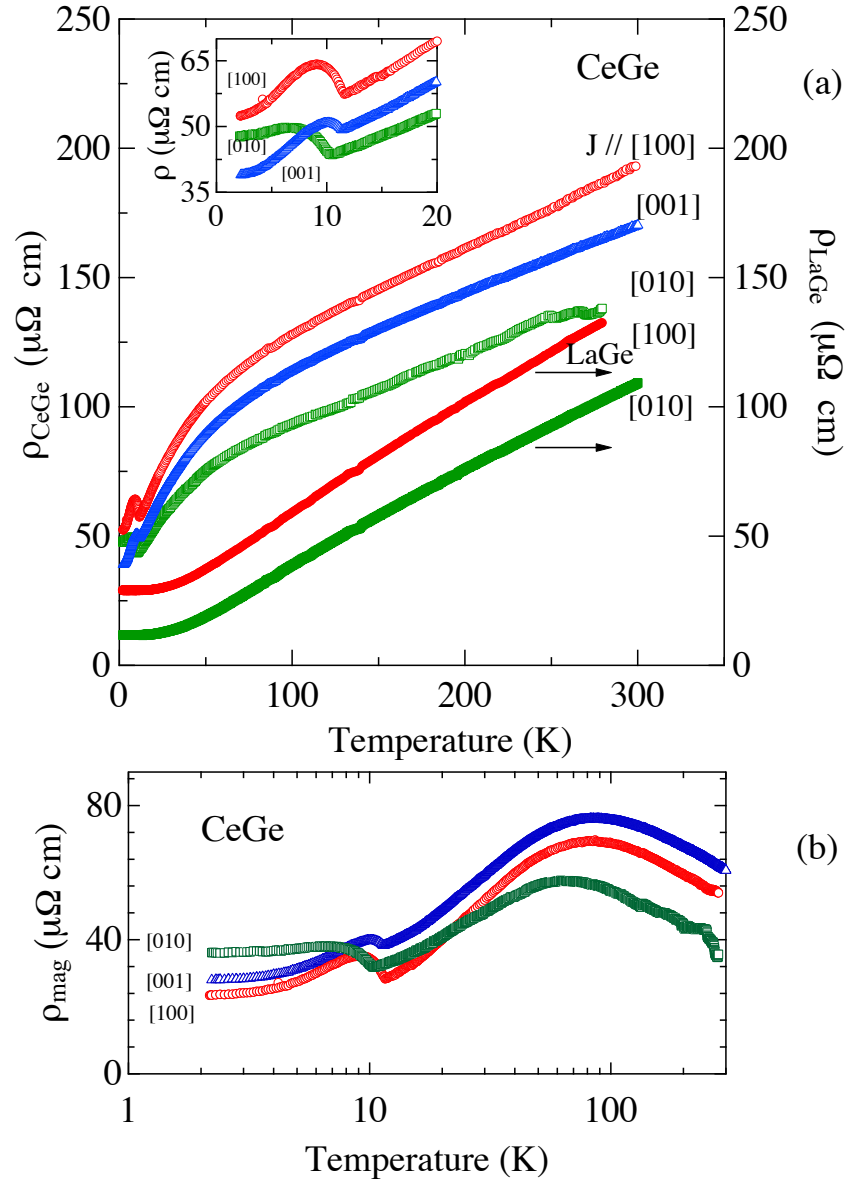
Figure 4.5: (a) Temperature dependence of electrical resistivity of CeGe and LaGe for current parallel to the three principal crystallographic directions. The inset shows the low temperature resistivity of CeGe. (b) The magnetic part of the resistivity ρ_{mag} as a function of temperature in a semi-logarithmic scale.

Crystal lattice

AF sub-lattice

a

$2a$

(a)

(b)

$\frac{2\pi}{a}$

AF - Super
zone $\frac{\pi}{a}$
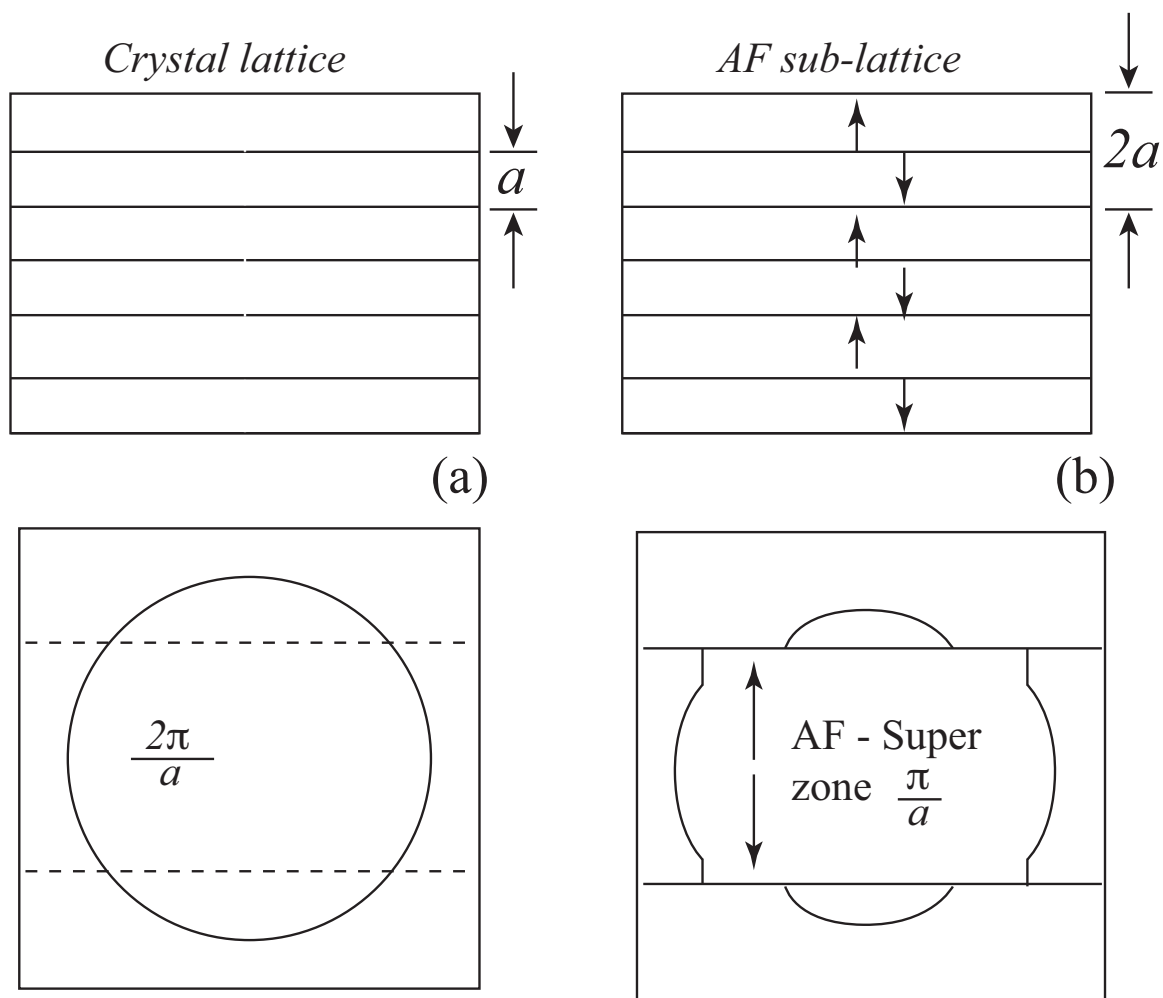
Figure 4.6: (a) Crystal lattice of a normal metal, the Fermi surface lies within the Brillouin zone. (b) Spin-up and spin-down sub-lattice due to antiferromagnetic ordering. The magnetic unit cell is doubled which causes new zone boundaries and results in antiferromagnetic superzone.

each sub-lattice has a spin up and spin-down configuration. When the sub-lattice periodicity is greater than the crystal lattice periodicity new zone boundaries will occur. These new zone boundaries may intersect the Fermi surface and a gap opens up in the Fermi surface. The effective surface area of the Fermi sphere in Fig. 4.6(b) is less than that in the Fig. 4.6(a) and consequently this gap reduces the effective number of conduction electrons below T_N and in addition to this, the thermal fluctuations in the spin system cause scattering of the conduction electrons which give rise to an increase in the resistivity. Since the fluctuations are reduced below the Néel temperature, the resistivity decreases after passing through a maximum. This type of superzone gap is usually observed in the pure heavy rare-earth metals like Tm, Er which crystallize in the hexagonal crystal structure [28, 73, 29]. The electrical resistivity shows an upturn at the magnetic ordering temperature in these heavy rare-earth metals, only along the hexagonal c-axis while no such anomaly is observed along the perpendicular direction *viz.*, a-axis.

In CeGe the superzone gap is observed along all three crystallographic directions, which is in contrast to the heavy rare-earth metals where the gap formation is only along the hexagonal c-axis [29]. The present scenario is very similar to that observed for hexagonal UCu_2Sn [74] where the superzone gap opens up along all three principal crystallographic directions. By comparing the ratio of the resistivity at the lowest temperature to the resistivity at just above the ordering temperature, we give a qualitative comparison of the gaps along different directions. The resistivity ratio $\rho(T = 2\ K)/\rho(T = 15\ K)$ is found to be 0.85, 1, and 0.71, respectively for J parallel to the [100], [010], and [001] directions. This gives an indication that the superzone gap is larger in the ab-plane than along the [001] direction.

As it is seen from the resistivity data, the superzone gap is large in the ab-plane, and an analysis of the electrical resistivity of CeGe for current parallel to [100] and [010] direction is performed based on the simple model of Elliot and Wedgwood [29]. The expression for the electrical resistivity along the magnetic modulation direction as

$$\rho = \frac{\alpha + \beta T + \gamma \left(1 - \frac{1}{2}M^2\right)}{1 - \Gamma M^2},\tag{4.2}$$

where α, β and γ are normally taken as the fitting parameters. α represents the impurity scattering, the contribution of the electron-phonon scattering is represented
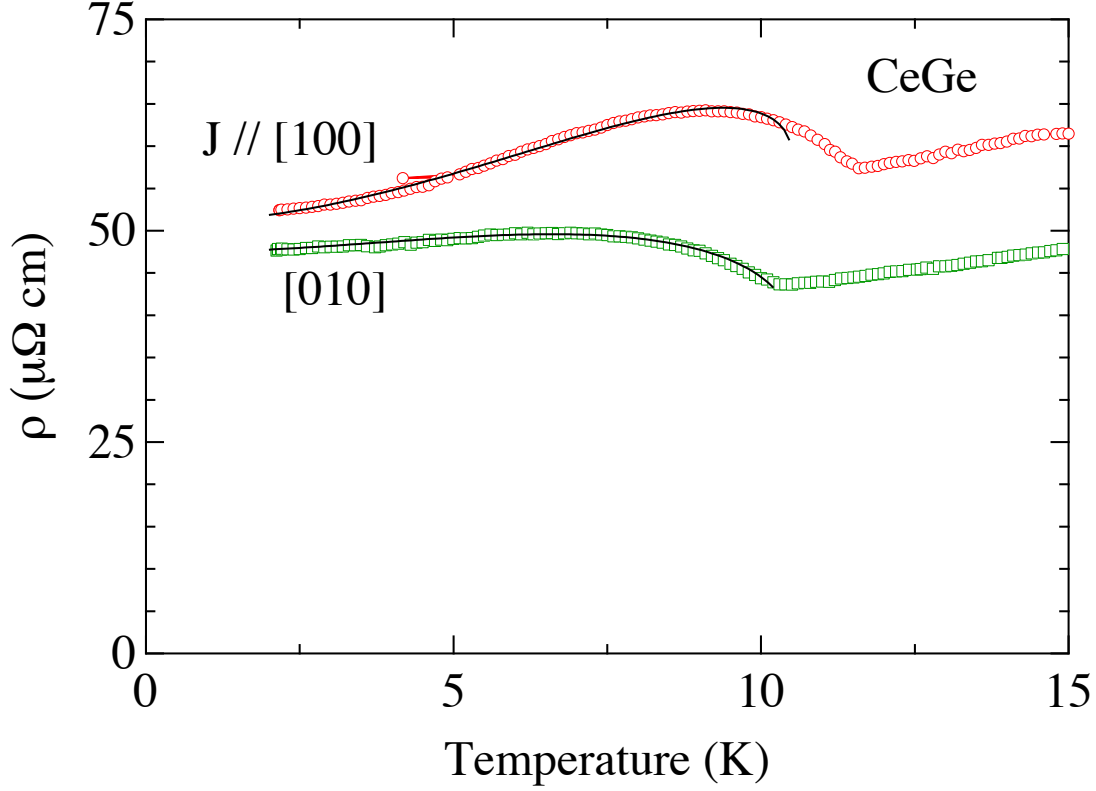
Figure 4.7: (Color online) Low temperature electrical resistivity of CeGe for current parallel to [100] and [010] direction. The solid line is the plot of Eq. 4.2. See text for details.

by β and γ represents the spin disorder scattering. Γ in the above expression defines the superzone-boundary effect and M is the sublattice magnetization usually obtained from the neutron diffraction experiment. Figure 4.7 shows the low temperature electrical resistivity of CeGe for $J \parallel [100]$ and $[010]$ directions. The solid line is fit to the Eqn. 4.2. While fitting the experimental data to Eqn. 4.2 the sublattice magnetization in the ordered state is taken as $M = [1 - (T/T_N)^2]^{0.5}$ similar to BCS-gap, where the superzone gap should open as the temperature decreases [75]. It is evident from the figure that we could get a reasonably good fit for both the directions and the estimated values of the parameter are, $\alpha = 3.42$ $\mu\Omega\cdot$cm, $\gamma = 55.51$ $\mu\Omega\cdot$cm and $\Gamma = 0.38$ for $J \parallel [100]$ and $\alpha = 1.0$ $\mu\Omega\cdot$cm, $\gamma = 37.31$ $\mu\Omega\cdot$cm and $\Gamma = 0.58$ for $J \parallel [010]$, in the above fitting process for the βT term the respective resistivity
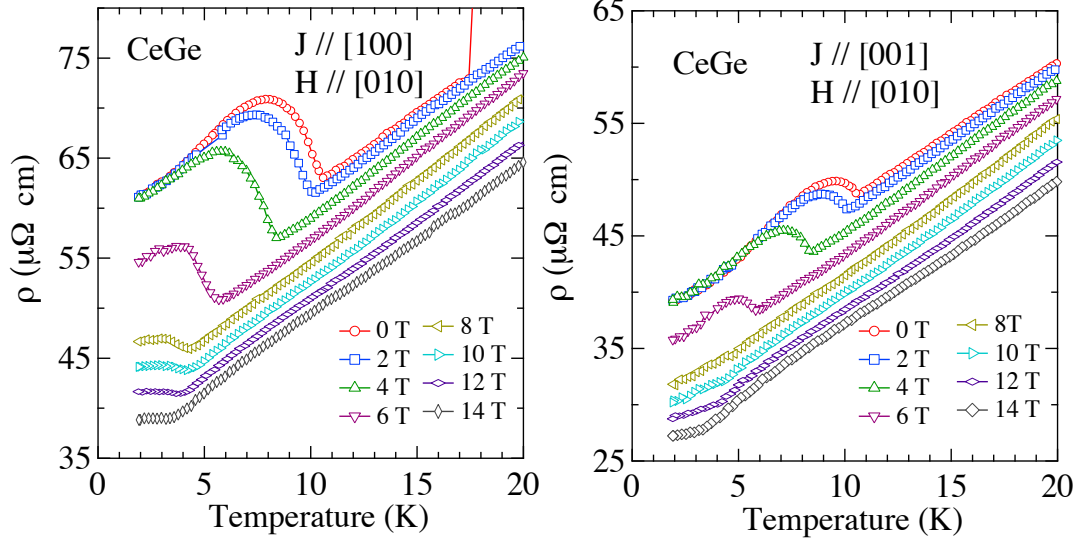
Figure 4.8: Electrical resistivity of CeGe measured in applied magnetic fields. The magnetic field is parallel to [010].

of LaGe has been used. The Γ values thus obtained for CeGe for [100] and [010] directions are of the same order as obtained for the heavy rare-earth metals [29]. The large value of Γ for [010] direction indicates that the superzone gap is larger along [010] direction compared to [100] direction.

The electrical resistivity of CeGe measured in applied magnetic fields is shown in Fig. 4.8. Since the easy axis of magnetization is the [010] direction, the magnetic field was applied parallel to [010] direction while the current was passed along the [100] and [001] direction. It is evident from the figure that as the magnetic field increases, the peak associated with the magnetic superzone gets suppressed and T_N shifts towards low temperatures.

4.3.4   Heat capacity

The specific heat of single crystalline CeGe and LaGe was measured in the temperature range from 1.8 to 200 K using a Quantum Design PPMS. The temperature dependence of heat capacity is shown in the main panel of Fig. 4.9(a).
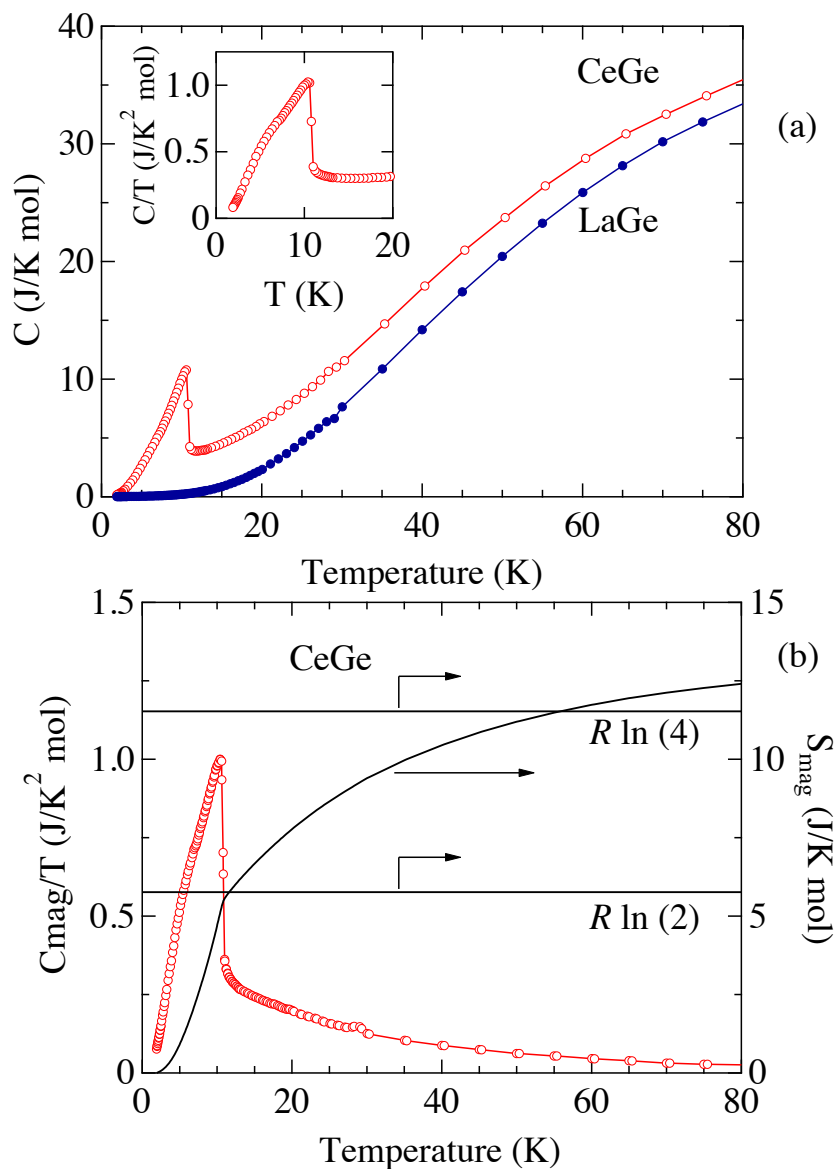
Figure 4.9: (a) Temperature dependence of the specific heat capacity in CeGe and LaGe. The inset shows the low temperature plot C/T vs. T of CeGe. (b) C_{mag}/T vs. T of CeGe. The calculated entropy is plotted on the right axis.

A sharp transition in the heat capacity data of CeGe at 10.5 K, confirms the bulk nature of the magnetic ordering. The heat capacity values of CeGe are significantly larger than that of LaGe in both magnetically ordered and paramagnetic states. The jump in the heat capacity of CeGe at the magnetic transition temperature (T_{N}) amounts to 6.9 J K^{-1} mol^{-1} which is significantly reduced compared to the mean field value of 12.5J K^{-1} mol^{-1} for spin S = 1/2, but compares well with the value of 6.5 J K^{-1} mol^{-1} observed by Marcano *et al.* [68]. The reduction in the heat capacity jump at the transition temperature often arises due to the Kondo effect. However, neither the magnetization data nor low temperature electrical resistivity data showed any evidence of Kondo effect in CeGe. Hence, it maybe concluded that the reduction in heat capacity jump in CeGe arises either due to the short range order in the paramagnetic phase or due to the presence of a background Schottky heat capacity due to the thermal depopulation of the crystal field split levels with decreasing temperature. The plot of C/T versus T^2 is shown in the inset of Fig. 4.9(a), and by extrapolating the data below 4 K to T = 0 we obtained the γ value of 13 mJ K^{-2} mol^{-1}. In case of LaGe we get a Sommerfield coefficient γ of 5 mJ K^{-2} mol^{-1}. The low value of γ indicates that there is no mass enhancement in CeGe compound. The magnetic part of heat capacity C_{mag} is obtained by subtracting the heat capacity of LaGe from that of CeGe, and the magnetic entropy S_{mag} is obtained by integrating C_{mag}/T data. C_{mag}/T versus T along with the magnetic entropy S_{mag} is shown in Fig. 4.9(b). The entropy reaches about $R\,ln2$ (=5.78 J K^{-1} mol^{-1}) at the transition temperature in conformity with a doublet ground state. Above T_{N} the entropy increases gradually and reaches $Rln4$ around 56 K, which gives a rough estimate of the first excited doublet state of the crystal field split levels. The magnetic field dependence of the heat capacity with the applied magnetic field parallel to the easy of magnetization namely [010]-direction is shown in Fig. 4.10. We observe that with increasing magnetic field the heat capacity peak shifts towards lower temperature, which is typical of antiferromagnetic compounds.

The magnetic part of heat capacity after subtracting the heat capacity of homologous LaGe from that of CeGe, is shown in Fig. 4.9. A broad peak in the paramagnetic region is mainly attributed to the Schottky-type excitations between the CEF levels of the Ce^{3+} ions. For a three level system, the Schottky heat capacity is given by the following expression:
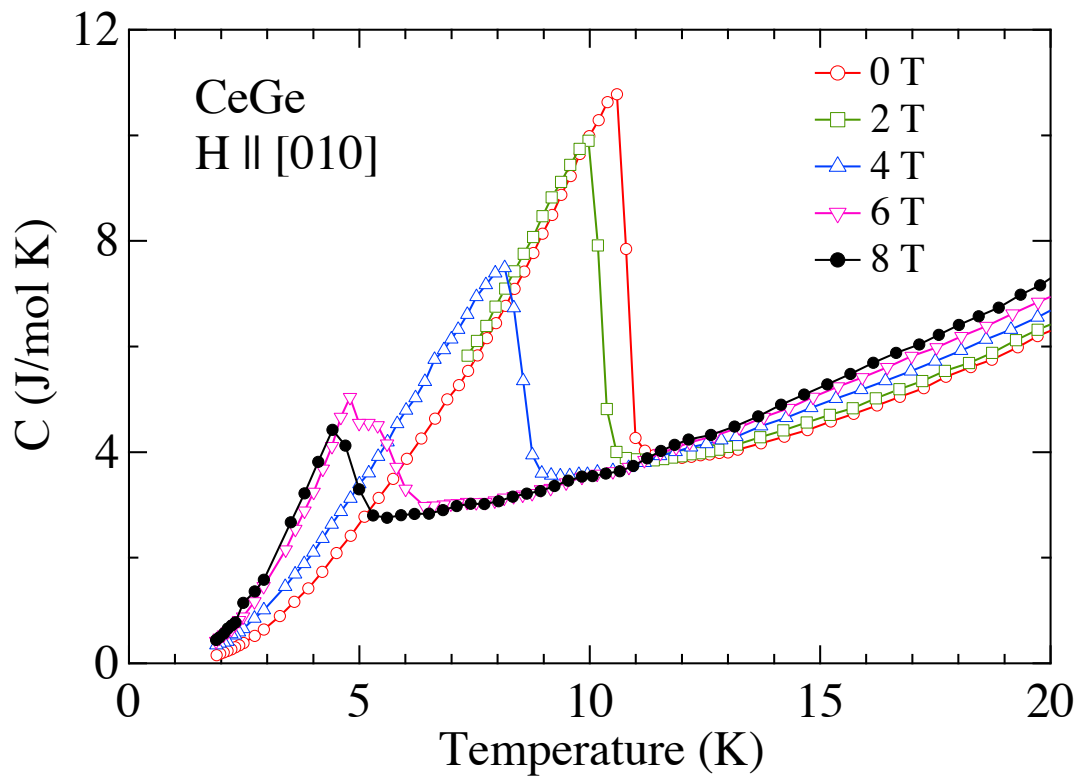
Figure 4.10: Heat capacity of CeGe in various applied magnetic fields for $H \parallel$ [010], the magnetic easy axis direction.
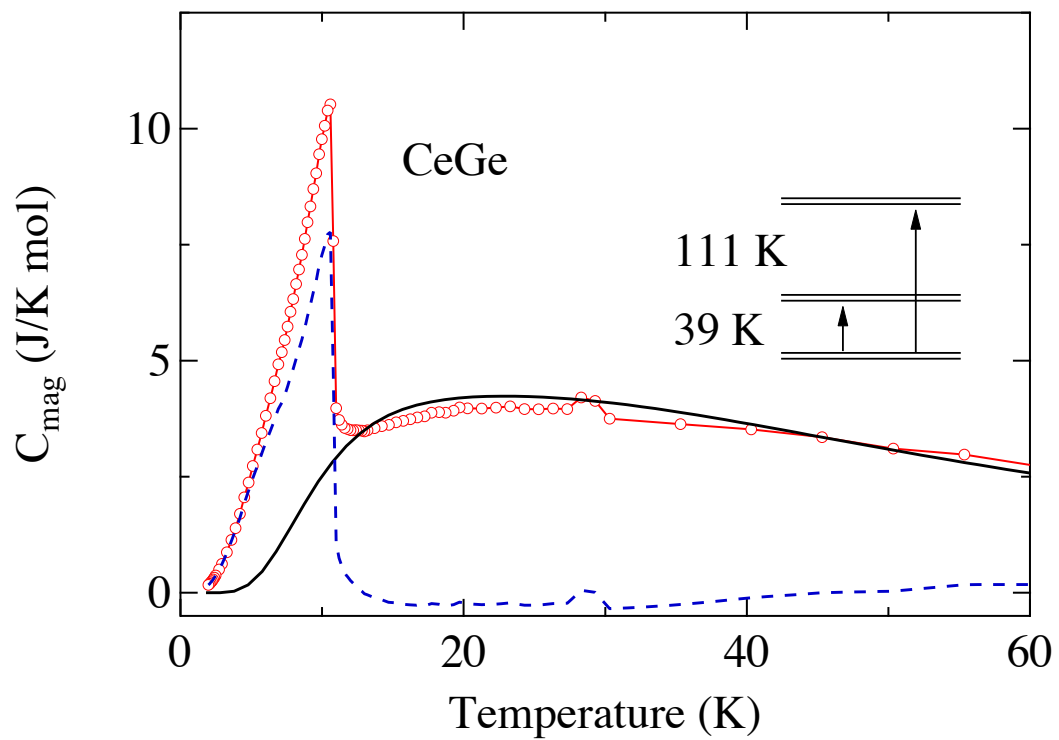
Figure 4.11: Magnetic part of the specific heat capacity of CeGe. The solid line is calculated Schottky heat capacity. The dashed line indicates the magnetic part of the heat capacity with the Schottky heat capacity subtracted.

$$C_{\text{Sch}} = \left(\frac{R}{(k_{\text{B}}T)^2} \frac{e^{(\Delta_1 + \Delta_2)/k_{\text{B}}T}[-2\Delta_1\Delta_2 + \Delta_2^2(1 + e^{\Delta_1/k_{\text{B}}T}) + \Delta_1^2(1 + e^{\Delta_2/k_{\text{B}}T})]}{(e^{\Delta_1/k_{\text{B}}T} + e^{\Delta_2/k_{\text{B}}T} + e^{(\Delta_1 + \Delta_2)/k_{\text{B}}T})^2} \right)$$

$$(4.3)$$

where R is the universal gas constant and Δ_1 and Δ_2 are the crystal field split excited energy levels. The solid line in Fig. 4.11 shows the calculated Schottky heat capacity as given by equation 4.3. The experimentally observed Schottky anomaly is satisfactorily reproduced by the energy eigenvalues $\Delta_1 = 39$ K and $\Delta_2 = 111$ K, obtained from the CEF analysis of the magnetic susceptibility data which is discussed in the next section. It is worth mentioning here that the first excited state is close to the value at which the entropy reaches $R\ln 4$. The presence of a sizable background heat capacity due to the Schottky anomaly at the transition temperature T_{N} reduces the jump in the heat capacity at the magnetic transition from its mean field value of 12.5 J mol^{-1} K^{-1} (for $S = 1/2$). Here a heat capacity jump of 6.9 J mol^{-1} K^{-1} is observed. An analysis of the magnetic part of the heat capacity is made by using a model proposed by Blanco *et al.* [59], where they have derived the expressions for the equal moment (EM) and the amplitude modulated (AM) magnetic structures form the jump in the heat capacity. For the case of equal moment structure, the jump in the heat capacity at the ordering temperature is given by,

$$\Delta C_{\text{EM}} = 5\frac{J(J + 1)}{(2J^2 + 2J + 1)}R, \tag{4.4}$$

and for the amplitude modulated system,

$$\Delta C_{\text{AM}} = \frac{10}{3}\frac{J(J + 1)}{(2J^2 + 2J + 1)}R, \tag{4.5}$$

where J is the total angular momentum and R is the gas constant. For spin $S = 1/2$ system, the equal moment case ΔC_{EM} amounts to 12.47 J/K·mol and for the amplitude modulated case ΔC_{AM} amounts to 8.31 J/K·mol. It is evident from the dashed line in Fig. 4.11 that the jump in the Schottky subtracted magnetic part of the specific heat amounts to 8.26 J/K·mol which suggests an amplitude modulated magnetic structure for CeGe, which is in conformity with the neutron diffraction

results of polycrystalline CeGe.

4.4 Crystal field analysis

The high temperature (in the paramagnetic phase) magnetic anisotropy can be explained on the basis of CEF model. Here Ce atoms of orthorhombic CeGe occupy the $4c$ Wyckoff position and hence posses a monoclinic site symmetry. For Ce atoms in monoclinic site symmetry, the CEF would split the $J = 5/2$ multiplet into three doublets. In order to reduce the number of fitting parameters in the CEF analysis, the CEF Hamiltonian of an orthorhombic site symmetry has been used. For Ce atom in orthorhombic site symmetry, the CEF Hamiltonian is given by

$$\mathcal{H}_{\mathrm{CEF}} = B_2^0 O_2^0 + B_2^2 O_2^2 + B_4^0 O_4^0 + B_4^2 O_4^2 + B_4^4 O_4^4, \tag{4.6}$$

where B_ℓ^m and O_ℓ^m are the CEF parameters and the Stevens operators, respectively [24, 23].

Now including the molecular field contribution λ_i, the magnetic susceptibility is given by

$$\chi_i^{-1} = \chi_{\mathrm{CEF}i}^{-1} - \lambda_i, \tag{4.7}$$

where the expression for the CEF susceptibility is given in Chapter 1. Based on the above CEF model, the temperature dependence of inverse susceptibility is calculated for field along the three principal crystallographic directions. In this calculation, the [010] direction is defined as the quantization z-axis, the [100] direction as the y-axis and the [001] direction as the x-axis. The solid lines in Fig. 4.12 are the calculated susceptibility with the unique value of the crystal field parameters as given in table 4.1. The corresponding wave functions are also listed in the table.

Negative values for the exchange field constants λ_{x} and λ_{z} along [100] and [001] directions, indicate that the interaction between the Ce moments is antiferromagnetic in nature. However, along [010] direction, a positive exchange field constant is
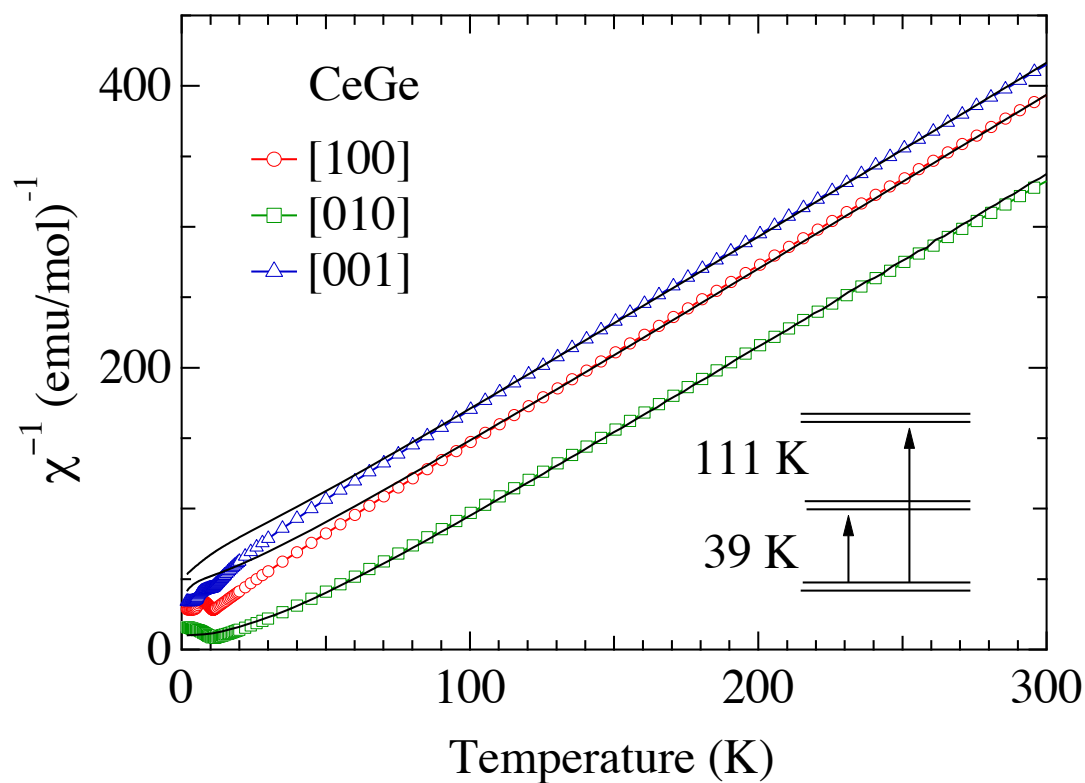
Figure 4.12: Temperature dependence of inverse magnetic susceptibility of CeGe. The solid line is the calculated susceptibility based on CEF model. The obtained energy levels are also shown.

Table 4.1: CEF parameters, energy levels and the corresponding wave functions for CeGe.

CEF parameters					
	B_2^0 (K)	B_2^2 (K)	B_4^0 (K)	B_4^2 (K)	B_4^4 (K)	λ_i (emu/mol)$^{-1}$
	3.0	0.86	0.01	-0.48	1.71	$\lambda_{[100]} = -34$
						$\lambda_{[010]} = 61$
						$\lambda_{[001]} = -50$
E(K)	$\lvert +5/2\rangle$	$\lvert +3/2\rangle$	$\lvert +1/2\rangle$	$\lvert -1/2\rangle$	$\lvert -3/2\rangle$	$\lvert -5/2\rangle$
111	0.834	0	-0.018	0	0.551	0
111	0	0.551	0	-0.018	0	0.834
39	0.011	0.463	-0.033	0.837	-0.018	-0.288
39	0.288	-0.018	-0.837	-0.033	-0.463	0.011
0	0.470	0	0.546	0	-0.694	0
0	0	0.694	0	-0.546	0	-0.470

obtained, signaling a ferromagnetic type of interaction of the moments along [010] direction. This is in accordance with the positive value of Weiss temperature θ_P obtained by the Curie-Weiss fitting of the high temperature susceptibility data. By diagonalizing the Hamiltonian given in equation 4.6 using the estimated crystal field parameters, the crystal field split energies $\Delta_1 = 39$ K and $\Delta_2 = 111$ K are obtained.

4.5 CeSi Results

CeSi also crystallizes in the orthorhombic crystal structure with the space group *Pnma* identical to CeGe, except that CeSi has slightly smaller unit cell volume in comparison to the CeGe, due to the smaller atomic radius of Si-atom. Noguchi *et al.* [65] have reported the basic anisotropic properties of CeSi single crystal. The present results on CeSi single crystal matches well with the the published data. In our work, we have performed the crystal field analysis of the magnetic susceptibility and the heat capacity data in addition to the anisotropic physical property studies. From the temperature dependence of isothermal magnetization, a magnetic phase diagram for CeSi has been constructed.

4.5.1 Structural properties

The single crystal of CeSi was grown by Czochralski pulling method, and the poly-crystalline sample of its non-magnetic analogue compound LaSi was prepared by arc-melting. From the powder x-ray diffraction, it was found that the samples are phase pure without any impurity peaks. It is to be mentioned here that the x-ray diffraction pattern is very similar to that of the iso-structural CeGe and the estimated lattice constants are $a = 8.300(2)$ Å, $b = 3.952(2)$ Å and $c = 5.952(0)$ Å. The until cell volume of CeSi is 195.2 Å^3 which is lower compared to that of CeGe which amounts to 205.2 Å^3. The reduction in the cell volume is mainly attributed to the smaller atomic radius of Si compared to that of Ge. The lattice constants match well with the previously reported values [76]. The single crystal was then oriented along the three principal crystallographic directions by back reflection Laue diffraction method. The oriented crystal was then cut to the desired shape and size by means of a spark erosion cutting machine for the anisotropic magnetic property measurements.

4.5.2 Magnetization

The temperature dependence of magnetic susceptibility for field parallel to the three principal crystallographic directions is shown in Fig 4.13(a). It is obvious from the figure that CeSi exhibits an antiferromagnetic ordering at $T_N = 6$ K. A very sharp drop in the magnetic susceptibility along the [010] direction is observed as shown in the inset of Fig. 4.13(a). The susceptibility is highly anisotropic in the ordered state although, the anisotropy along the [100] and [001] direction is not so high. Along the [100] and [001] direction, the susceptibility shows a very small change at the magnetic ordering temperature. From the sharp drop in the χ versus temperature plot in the [010]-direction, it can be concluded that [010] direction is the easy axis of magnetization, which is confirmed from the isothermal magnetization data to be discussed later. Fig 4.13(b) shows the inverse susceptibility plot along with the Curie-Weiss fitting. The effective magnetic moment μ_{eff} and the paramagnetic Weiss temperature θ_p thus obtained are 2.55 μ_B/Ce, -42 K for $H \parallel [100]$, 2.72 μ_B/Ce, 2.7 K for $H \parallel [010]$ and 2.57 μ_B/Ce, -25 K for $H \parallel [001]$. The effective magnetic moment is close to the theoretical value of 2.54 μ_B/Ce along all the three directions thus indicating that the
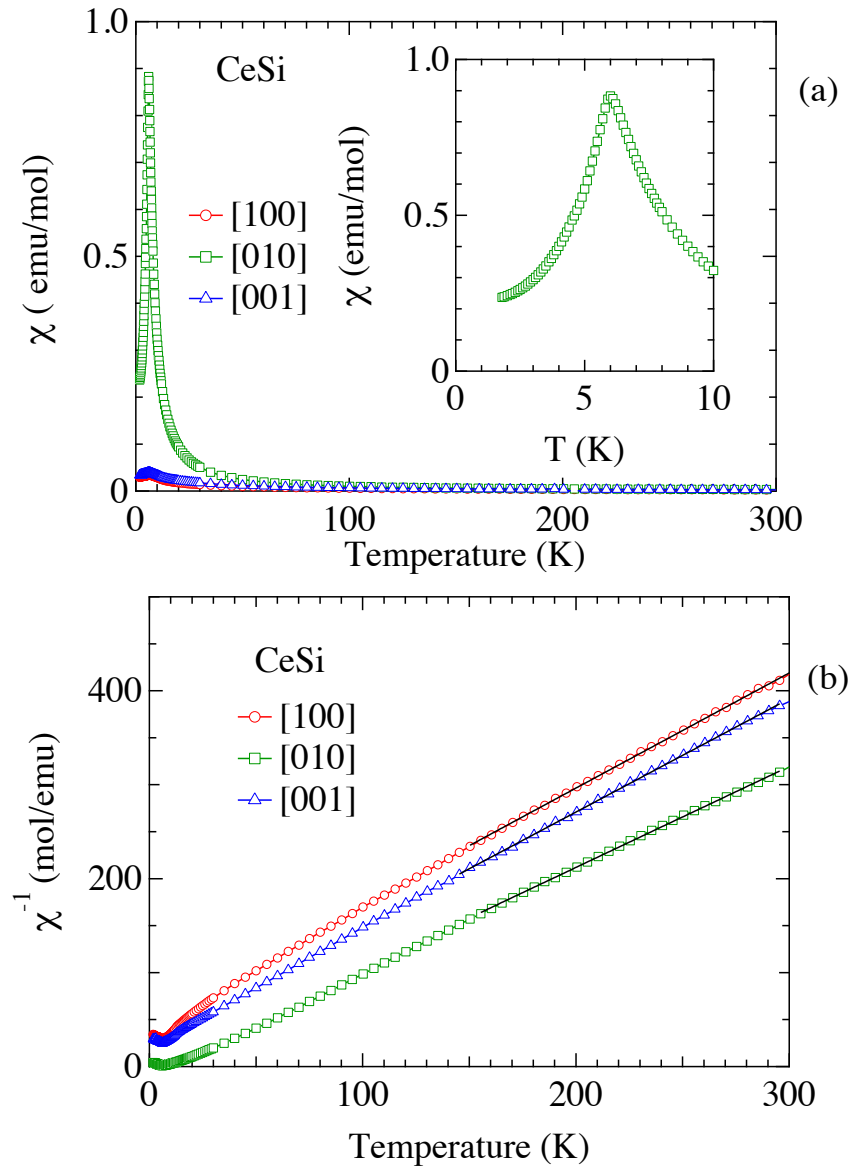
Figure 4.13: (a) Temperature dependence of magnetic susceptibility of CeSi along the three principal crystallographic directions in an applied field of 1 kOe. The inset shows the low temperature plot for $H \parallel$ [010], where antiferromagnetic ordering is clearly seen. (b) The inverse susceptibility plot of CeSi, the solid lines in the high temperature range are the Curie-Weiss fits

91
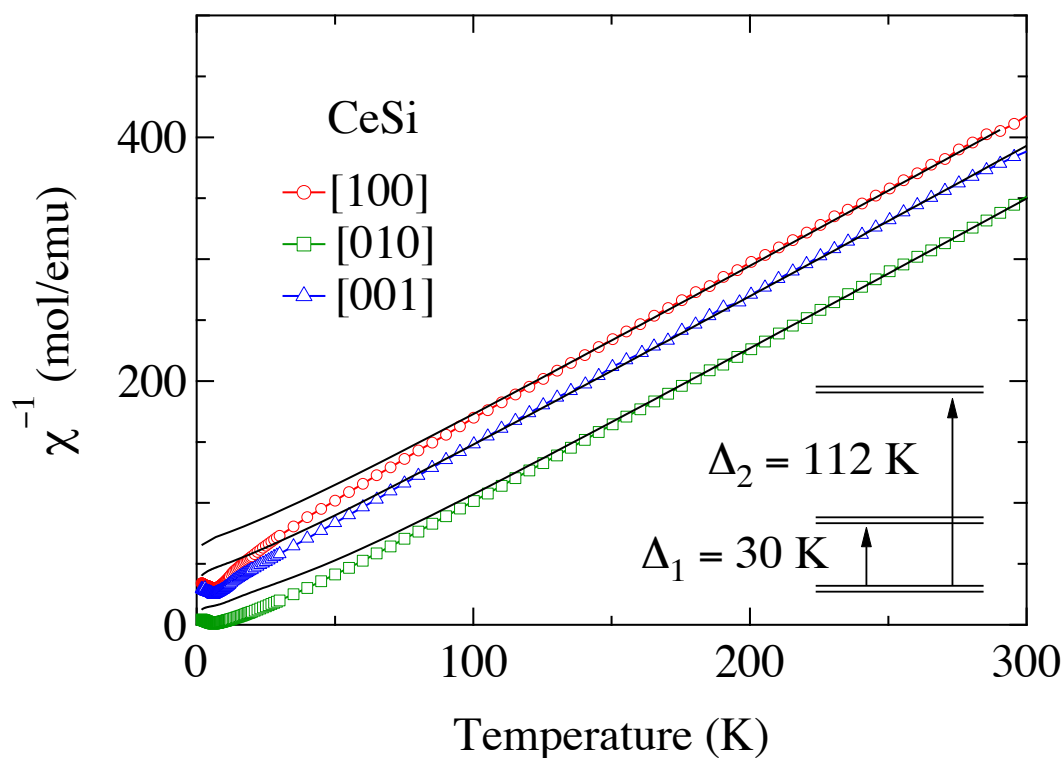
Figure 4.14: Temperature dependence of inverse susceptibility of CeSi. The solid lines are the calculated curves based on the CEF analysis. The obtained energy levels are also shown.

Ce-atom is in the trivalent state in this compound.

A large anisotropy in the magnetic susceptibility data in the paramagnetic state is mainly attributed to the crystal electric field effect. Hence the crystal field analysis on the inverse susceptibility data has been performed following the method described in Section 4.3.2. Figure 4.14 depicts the calculated CEF susceptibility shown by solid lines along with the experimental data. The calculated curve reasonably matches with the experimental data and an estimate of the splitting of $2J + 1$ level scheme is obtained. Owing to the low symmetry of the Ce-atom in the crystal structure, the CEF splits the ground state multiplet into three doublets and the calculated energy levels are 30 K and 112 K for the first and the second excited states. It is to be noted that the CEF level scheme obtained for CeSi are similar in magnitude to that
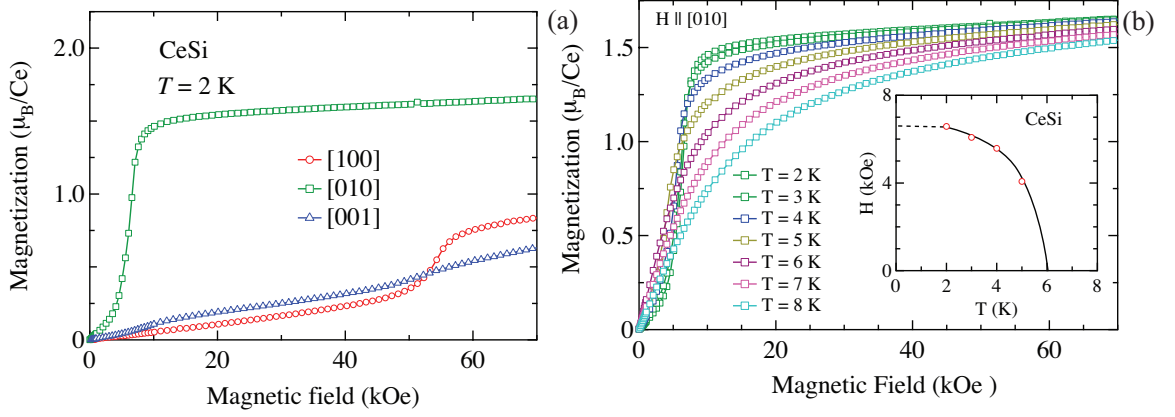
Figure 4.15: (a) Field dependence of isothermal magnetization of CeSi measured at 2 K along the three principal crystallographic directions. (b) Magnetization along the [010] direction at various fixed temperatures. The inset shows the magnetic phase diagram.

of CeGe.

The magnetic field dependences of the magnetization $M(H)$ measured at $T = 2$ K of CeSi single crystal in the magnetic fields up to 70 kOe along the three principal crystallographic directions are shown in Fig. 4.15. The plotted data are the results measured in the sequence of increasing magnetic field. There is a large anisotropy in the magnetization for field parallel to [010] and the other two directions namely [100] and [001]. The anisotropy between [100] and [001] direction is relatively small. There is a spin flip like metamagnetic transition at 6.5 kOe for $H \parallel$ to [010] direction, beyond which the magnetization attains a saturation value of 1.6 μ_{B}/Ce. The present result is consistent with the high field magnetization data on CeSi single crystal published by Noguchi *et al.* [65]. The magnetization for $H \parallel$ to [010] is close to the saturation value of the free ion Ce^{3+}, which amounts to 2.14 μ_{B}/Ce, thus indicating the easy axis of magnetization. A minor spin-reorientation is observed along the [100] direction at around 55 kOe, where as the magnetization along the [001] direction is linear and attains a value of 0.6 μ_{B}/Ce at 70 kOe indicating the hard axis of magnetization. The temperature dependence of isothermal magnetization of the *b*-axis magnetization is shown in Fig. 4.15(b). It is evident from the figure that as the temperature increases the spin-flip transition shifts towards lower field and eventually ceases at the magnetic ordering temperature *viz.*, $T_{\mathrm{N}} = 6$ K. A magnetic
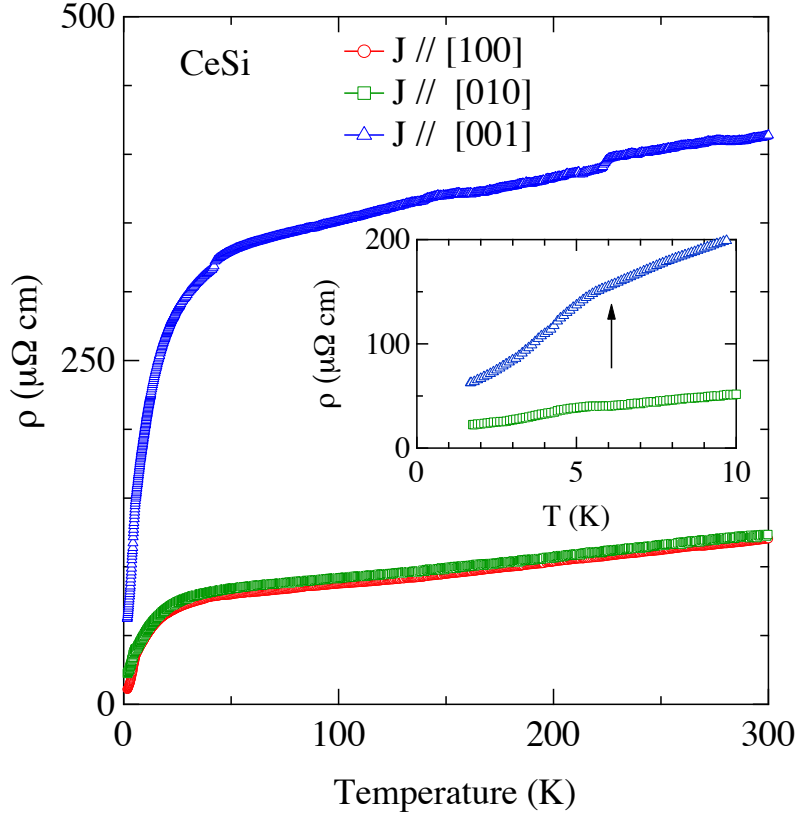
Figure 4.16: Temperature dependence of electrical resistivity for current parallel to the three principal crystallographic directions. The inset shows the low temperature part.

phase diagram has been constructed and is shown in the inset of Fig. 4.15(b).

4.5.3 Electrical resistivity

The temperature dependence of electrical resistivity of CeSi measured in the temperature range from 1.8 to 300 K, using standard four probe method, in a home made set up is shown in Fig. 4.16. The inset shows the low temperature part of the electrical resistivity. Over all, the resistivity shows a metallic behaviour by showing a decreasing trend as the temperature decreases. No signature of any Kondo effect is observed in the electrical resistivity. A change of slope is observed at $T_N = 6$ K due to reduction in spin disorder scattering of conduction electrons below magnetic

ordering. There is a large anisotropy in the electrical resistivity for current parallel to [001] direction and the other two perpendicular directions.

4.5.4 Heat capacity

The heat capacity of CeSi and its non-magnetic analogue compound LaSi measured in the temperature range form 1.8 to 100 K is shown in the main panel of Fig. 4.17(a). A sharp peak in the heat capacity at $T_N = 6$ K reveals the bulk magnetic ordering of CeSi. An estimate of the Sommerfeld coefficient γ was made from the low temperature part of C/T $vs.$ T^2 plot as shown in the bottom inset of Fig. 4.17(a) by extrapolating the data down to 0 K. The Sommerfeld coefficient thus obtained is 78 mJ/K^2 mol. The magnetic part of heat capacity is obtained by the usual method of subtracting the heat capacity values of LaSi from that of CeSi. Besides a peak at T_N the magnetic part of the heat capacity exhibits a broad peak centered around 30 K arising due to the Schottky contribution from the thermal variation of the population of the excited CEF levels. The magnetic entropy S_{mag} was estimated by integrating the C_{mag}/T vs. T curve and is shown in Fig. 4.17(b). The entropy at T_N is 4.2 J/K mol, which is close to the value of R $ln2$ and thus indicating that the ground state is a doublet. Having obtained the crystal field split energy levels from the analysis of the susceptibility data, we have used the energy levels 0, 30 and 112 K in the calculation of the Schottky heat capacity and found that the calculated curve matches closely the experimentally obtained Schottky heat capacity, thus justifying our crystal field calculations.

4.6   Conclusion

The single crystals of CeGe, LaGe, CeSi were grown by the Czochralski crystal pulling method in a tetra-arc furnace, while the polycrystalline sample of LaSi was prepared by arc-melting. The magnetic, transport and heat capacity data clearly indicate that CeGe orders antiferromagnetically below 10.5 K, while CeSi orders antiferromagnetically with $T_N = 6$ K. A strong magnetic anisotropy is observed in both the compounds in the magnetically ordered and paramagnetic states. The anisotropy in the para-
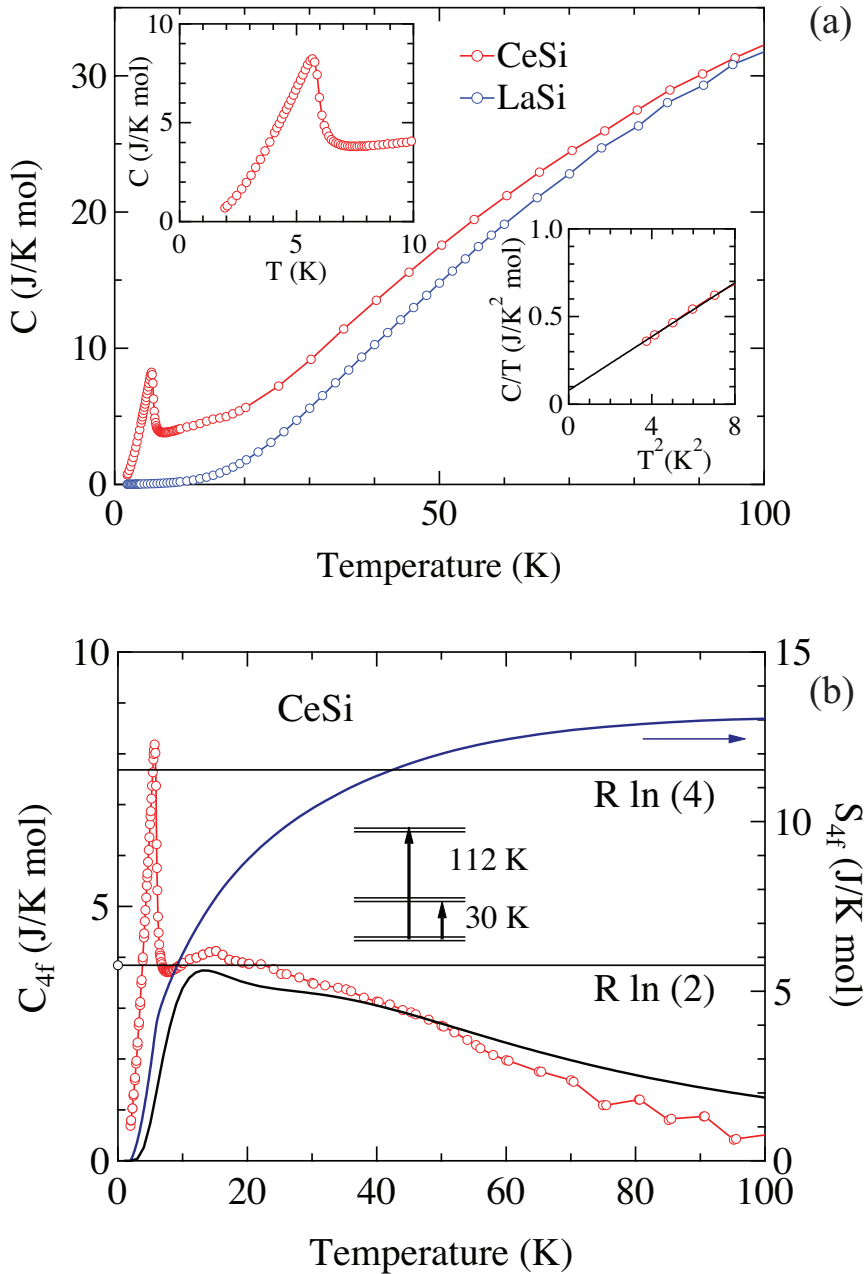
Figure 4.17: (a) Heat capacity of LaSi and CeSi measured in the temperature range from 1.8 to 100 K. The top inset shows the low temperature part of the heat capacity. The bottom inset shows the low temperature part of the C/T *vs* T^2 plot, the solid line is the linear extrapolation to estimate the Sommerfeld coefficient. (b) The temperature dependence of the magnetic part of the heat capacity, calculated entropy and the Schottky heat capacity of CeSi.

magnetic phase is explained on the basis of crystal electric field model. In case of CeGe, field induced magnetic transitions were observed along the [100] and [010] directions while no such transition was observed along [001] direction up to a field of 16 T, which is found to be the hard axis of magnetization. It is clearly evident from our measurements that [010] direction is the easy axis of magnetization. From the differential plot of isothermal magnetization measured at various fixed temperature a tentative magnetic phase diagram is constructed. The electrical resistivity of CeGe exhibits an upturn at T_{N}, which is attributed to the superzone gap formation below the magnetic transition temperature along all three principal crystallographic directions. The electrical resistivity data show a possible presence of Kondo interaction at high temperatures which weakens and vanishes at low temperatures. The crystal electric field analysis of the magnetic susceptibility and the heat capacity has revealed the splitting energies as 39 K and 111 K respectively for the first and second excited states from the ground state. The heat capacity analysis clearly indicates evidence of amplitude modulated magnetic structure of CeGe. We have performed similar crystal electric field analysis of magnetic susceptibility and heat capacity data on CeSi, and found that the crystal field splits the $J = 5/2$ multiplet of Ce^{3+} into three doublet states with energies 30 K and 112 K for first and second excited doublets from the ground state.

Chapter 5

Anisotropic magnetic properties of PrSi and PrGe single crystals

5.1 Introduction

It has been well documented in the literature that Ce compounds exhibit interesting magnetic properties owing to the close proximity of the $4f$-level to the Fermi energy. The preceding two chapters also reveal this. In this chapter, the magnetic properties exhibited by two Pr-based compounds viz., PrSi and PrGe are presented. The $4f$ electrons of the Pr-atoms are relatively more localized compared to that in Ce. Despite this, some Pr compounds also reveal interesting magnetic properties. For example, a heavy fermion behaviour is observed in $PrInAg_2$ with a large Sommerfeld coefficient reaching ≈ 6.5 J/(K^2 mol) [77]; an exotic heavy fermion nature is observed in $PrFe_4P_{12}$ compound with a cyclotron effective mass of 81 m_0, inferred from the de-Haas van Alphen experiment on a high quality single crystalline sample by Sugawara et $al.$ [78]. A dense Kondo behavior is observed in $PrSn_3$ single crystalline sample by Settai et $al.$ [79] where the magnetic part of the electrical resistivity increases with decreasing temperature, following a $-ln\ T$ dependence. The crystalline electric field effects also play an important role in the magnetic properties of Pr-compounds.

It has been already mentioned in the Introduction chapter that according to Kramer's theorem, the energy levels of the rare-earth atoms with odd number of

f-electrons remain at least doubly degenerate in the presence of crystal electric fields, while the degeneracy can be completely lifted for the rare earth atoms with even number of f-electrons; i.e., one can have singlet states. For Pr, there are two f electrons, and the total angular moment $J = 4$. The CEF splits the 9-fold $2J + 1$ degenerate multiplet of Pr^{3+}ions in such a way that a CEF-split singlet state is always present for all types of crystallographic site symmetry of the rare-earth atom [80]. The magnetic ordering in compounds having CEF-split non-magnetic singlet ground state depends very much on the relative strengths of the CEF and exchange interaction $\mathcal{J}_{ex}$ between the rare-earth ions. No magnetic ordering can occur in the singlet ground state systems unless the exchange interaction $\mathcal{J}_{ex}$ exceeds a certain critical value relative to the CEF splitting energy Δ between the ground state and the excited state [81]. In view of the effects of CEF on the magnetic properties of Pr-compounds, we have investigated the anisotropic magnetic properties of equiatomic PrX (X = Si and Ge) compounds.

As mentioned in the previous chapter, the equiatomic RX (where R = rare earth and X = Si, Ge, Ni or Pt) series of compounds crystallize in two closely related orthorhombic crystal structures, namely CrB type and FeB type structure, depending on the heat treatment during the crystal growth and the rare earth element present [48]. One of the earliest studies on the structural properties of RX series of compounds was done by Hohnke and Parthe [63] about five decades ago. They reported that RSi (with R = La-Er) compounds crystallize in the FeB-type structure while the higher rare earths from Dy to Er in this series exhibit polymorphism by crystallizing in both FeB and CrB type structures. On the other hand, most of the RGe (with R = Nd-Er) compounds crystallize in the CrB type structure. The RGe compounds of lighter rare earths, namely La and Ce, crystallize in the FeB-type structure. PrGe exhibits dimorphism by crystallizing in both CrB and FeB type structures, where the CrB type structure corresponds to the low temperature phase. This RX series of compounds exhibit not only interesting structural properties but also interesting magnetic properties [82, 83, 84]. Buschow and Fast [48] studied the magnetic properties of RGe (with R = La-Er) compounds on polycrystalline samples. They found that RGe (R = Ce, Sm, Gd, Tb, Dy, Ho and Er) compounds exhibit antiferromagnetic ordering at low temperature, while PrGe and NdGe have ferromagnetic ground state. In EuGe, Eu was found to have a divalent state with an antiferromagnetic ordering at 20 K

[85]. Like RGe compounds, most of the RSi compounds order antiferromagnetically upon cooling except PrSi and NdSi which exhibit ferromagnetic ground state [69].

The magnetic structure of PrSi and NdSi was studied by Nguyen *et al.*, by neutron diffraction on polycrystalline samples. They found that both compounds exhibit ferromagnetic ordering. NdSi possesses non-collinear structure, but in case of PrSi the antiferromagnetic component is too weak. Furthermore, they reported that the magnetic moments in PrSi lie in the $a - c$ plane, while in a recent study by Snyman *et al.* [86] it was found that PrSi has a collinear ferromagnetic structure with moments oriented along the crystallographic b-axis. In view of these intriguing results and considering the low symmetry crystal structure of PrSi and PrGe compounds, a detailed investigations on the anisotropic magnetic properties have been made.

5.2 Crystal growth

Both PrSi and PrGe phases melt congruently at 1657 °C and 1400 °C, respectively. The single crystals of these compounds have been grown by Czochralski pulling method in a tetra-arc furnace. We have obtained good quality single crystals. The details of crystal growth method are described in Chapter 2.

5.3 Results of PrSi

5.3.1 Structural properties

Powder x-ray diffraction measurement was performed on finely ground pieces of single crystal using PANalytical x-ray diffractometer with monochromatic Cu Kα radiation with wavelength 1.5406 Å. PrSi was found to crystallize in orthorhombic FeB-type crystal structure with space group $Pnma$ (no. 62). Both Pr and Si atoms occupy the crystallographic $4c$ site [87], which has a monoclinic site symmetry for the Pr atoms. A Rietveld analysis has been performed on the powder pattern using the FULLPROF software package [32]. The powder pattern is shown in Fig. 5.1. The lattice constants obtained from the Rietveld analysis, $a = 8.240(2)$ Å, $b = 3.942(1)$ Å,
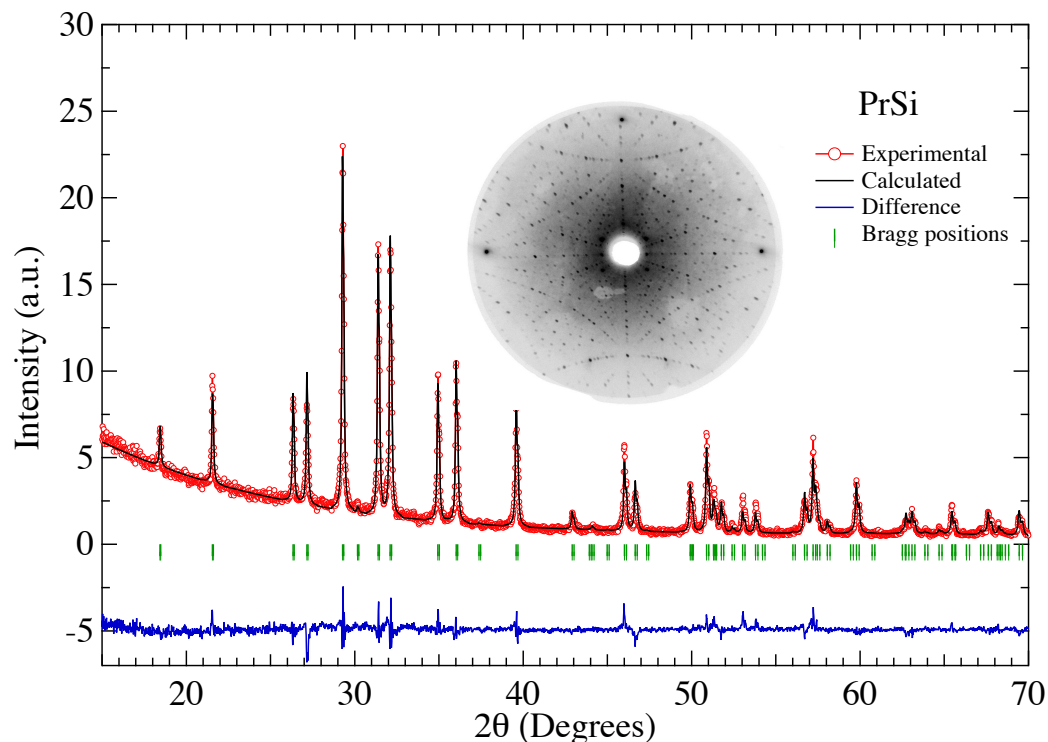
Figure 5.1: Powder x-ray diffraction pattern of PrSi along with the Rietveld refinement. The Bragg positions and the difference between the calculated and experimental pattern are also shown. A representative Laue pattern, corresponding to (010) plane is shown in the inset.

and $c = 5.921(1)$ Å, are in good agreement with the previous report [87]. The positions of the Pr and Si atoms at $4c$ site are found to be (0.179, 0.25, 0.612) and (0.040, 0.25, 0.120) for the Pr and Si atoms, respectively. The homogeneity of the single crystal was further confirmed from the energy dispersive analysis by x-ray (EDAX). The crystal was oriented along the three principal crystallographic directions by means of back reflection Laue diffraction method. We observed well defined Laue patterns for all three crystallographic directions. Clear Laue patterns along with sharp and rounded spots indicate a good quality of grown crystal. The symmetry of the Laue pattern also confirms the orthorhombic crystal structure of PrSi. A representative Laue pattern corresponding to the (010) plane is shown in the inset of Fig. 5.1.
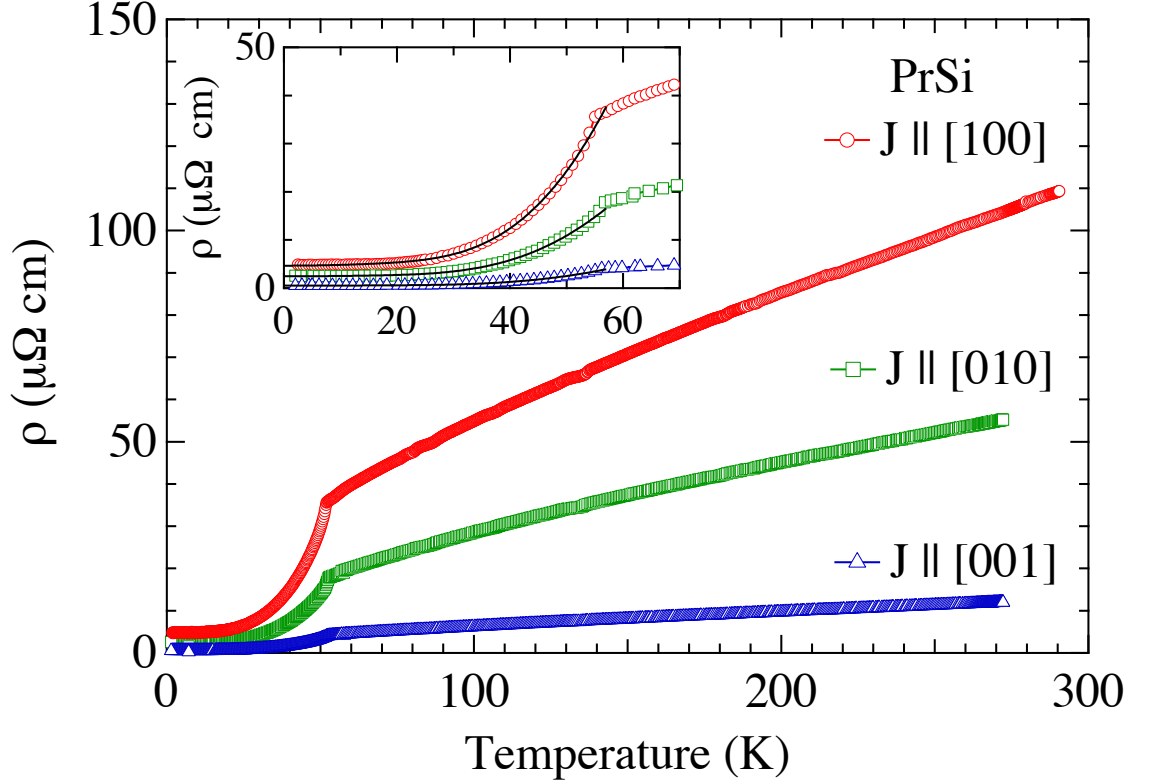
Figure 5.2: Temperature dependence of electrical resistivity of PrSi. The inset shows the low temperature part of the electrical resistivity, the solid lines are the fits to spin-wave gap model equation given in Eqn. 5.1.

5.3.2 Electrical transport

The electrical resistivity measured in the temperature range from 1.8 to 300 K for current parallel to the three principal crystallographic directions is shown in Fig. 5.2. The resistivity shows strong anisotropy reflecting the orthorhombic crystal structure. Close to room temperature the resistivity values are $\rho_{[100]} = 109\ \mu\Omega$cm, $\rho_{[010]} = 55\ \mu\Omega$cm and $\rho_{[001]} = 12\ \mu\Omega$cm. The electrical resistivity decreases with decreasing temperature with a broad curvature typical of rare earth intermetallic compounds. This broad curvature mainly arises due to the thermal depopulation of crystal electric field split levels as the temperature is reduced. The electrical resistivity falls off rapidly at 52 K, where the system undergoes a magnetic transition. This resistivity drop is due to the reduction in spin disorder scattering of conduction electrons below

	ρ_0 ($\mu\Omega$ cm)	a ($\mu\Omega$ cm/K^2)	b ($\mu\Omega$ cm/K^2)	Δ (K)
$\rho_{[100]}$	4.721	1.91×10^{-3}	2.88×10^{-2}	128
$\rho_{[010]}$	2.477	9.188×10^{-4}	9.53×10^{-3}	124
$\rho_{[001]}$	0.525	2.242×10^{-4}	2.58×10^{-3}	132

Table 5.1: Fitting parameters along the three principal directions derived from fitting Eqn. 5.1 to the resistivity data.

the magnetic ordering. It is evident from the magnetization data to be discussed later that PrSi undergoes a ferromagnetic ordering with $T_C = 52$ K. The low temperature resistivity data can be described by the spin-wave gap model. In the case of non-cubic (anisotropic) ferromagnets, the dispersion relation of the spin-wave spectrum is given by [88, 89] $\hbar\omega_m = \Delta + Dq_m^2$, where ω_m and q_m are the frequency and wave vector of magnons, respectively and D is the spin-wave stiffness and Δ is the gap in the spin-wave spectrum. The gapped magnons give rise to a temperature dependent resistivity for $k_B T \ll \Delta$, which takes the form,

$$\rho(T) = \rho_0 + aT^2 + bT\Delta \left(1 + \frac{2T}{\Delta}\right) \exp\left(\frac{-\Delta}{T}\right). \tag{5.1}$$

The second term in the above expression is the usual Fermi liquid term and the third term is the contribution from magnons. In Eqn. 5.1, ρ_0 is the residual resistivity, the coefficient a determines the degree of electron-electron scattering and b is a constant for the given material and depends on the spin wave stiffness D. The low temperature resistivity fits very well to the above expression as shown in the inset of Fig. 5.2. The parameters obtained from the fit are given in Table 5.1.

The residual resistivity ratio (RRR) amounts to 23, 22, and 23 for current parallel to [100], [010], and [001], respectively. The relatively small values of residual resistivity and the high values of RRR indicate the good quality of the single crystal.

5.3.3 Magnetization and crystal field analysis

The magnetization versus temperature measured in an applied field of 1 kOe along the three principal crystallographic directions in the temperature range from 1.8 to 300 K is shown in Fig. 5.3(a). A sharp increase of magnetization is observed below 52 K along the [010] direction, indicating the ferromagnetic nature of magnetic ordering. The magnetization exhibits an anomaly at 52 K for the H $\parallel$ [100] and H $\parallel$ [001] directions as well, however the magnetic behavior along these two directions is relatively complex. The magnetization is anisotropic, and is quite large along the [010] direction, thus signaling [010] direction as the easy axis of magnetization. The temperature dependence of reciprocal susceptibility is shown in Fig. 5.3(b). The inverse susceptibility varies linearly with temperature at high temperatures (100 - 300 K), and follows the Curie-Weiss law $\chi(T) = \mu_{\text{eff}}^2/(8(T - \theta_{\text{p}}))$, where μ_{eff} is the effective magnetic moment and θ_{p} is the paramagnetic Curie temperature. μ_{eff} and θ_{p} values were estimated to be 3.62(2) μ_{B}/Pr and $-10.3(2)$ K; 3.58(1) μ_{B}/Pr and 58.2(1) K; 3.654(3) μ_{B}/Pr and $-22.9(3)$ K for H $\parallel$ [100], [010], [001], respectively. The experimental value of μ_{eff} is close to the theoretical value of Pr^{3+} based on the Russell-Saunders $L - S$ coupling $(g_{\text{J}}\sqrt{J(J + 1)} = 3.58)$, where $g_{\text{J}} = 4/5$ and $J = 4$ are the Lande's g factor and the total angular momentum for the $4f^2$ configuration of Pr. This indicates the local moment behaviour of Pr^{3+} ion in this system. The Curie-Weiss temperature is found to be negative for the [100] and [001] directions, while it is positive along the [010] direction. However, the polycrystalline average is positive (8.3 K), which is in conformity with the ferromagnetic nature of magnetic ordering of this compound. It may be noted that the Curie temperature along the [010] direction is comparable to $T_{\text{C}} = 52$ K.

We have performed crystal electric field (CEF) analysis on the magnetic susceptibility data in order to understand the magnetocrystalline anisotropy and to estimate the CEF level splitting. The Pr atom in PrSi occupies the $4c$ Wyckoff position which has a monoclinic site symmetry. Hence the 9-fold degeneracy of the free Pr^{3+} will split into 9 singlets. In spite of the singlet ground state, PrSi exhibits a ferromagnetic ground state below $T_{\text{C}} = 52$ K. For a system having singlet ground state, there is a threshold value of the magnetic exchange interaction between the ground state and the first excited state above which only the system can order magnetically. Below
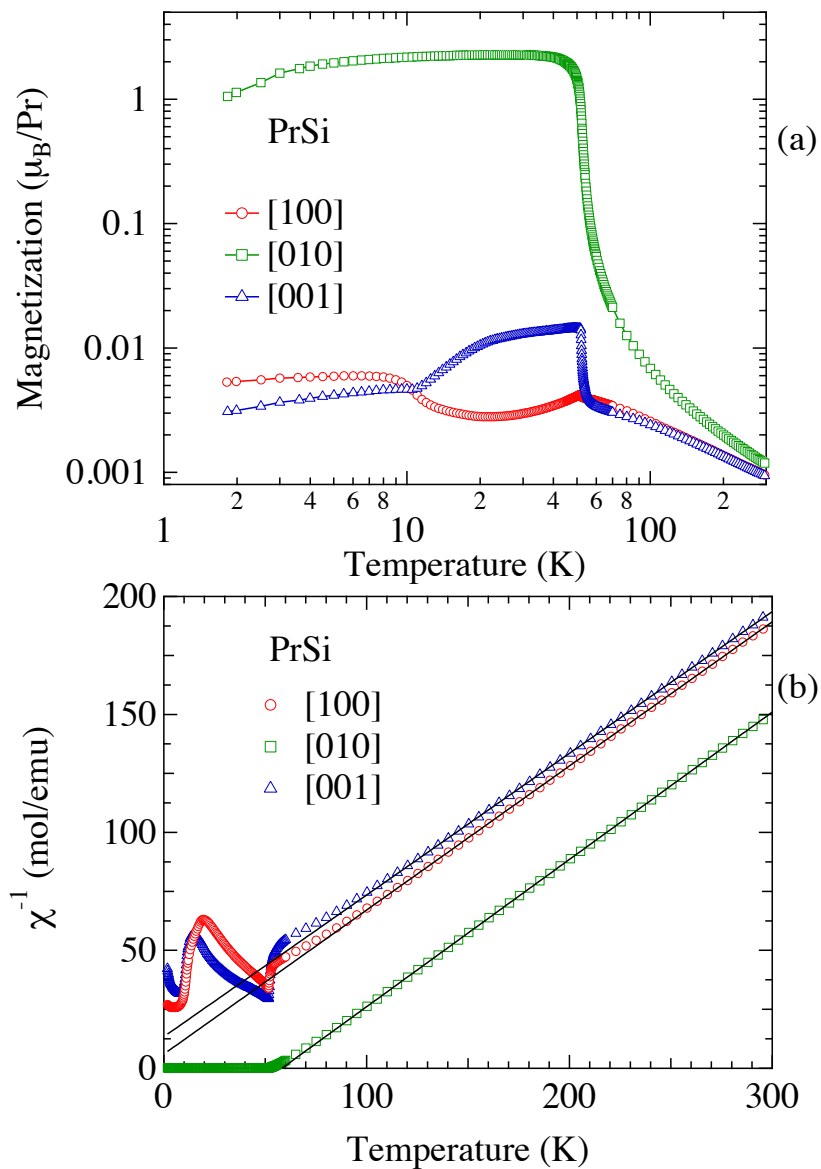
Figure 5.3: (a) Temperature dependence of magnetization of PrSi along [100], [001] and [010] in an applied field of 1 kOe plotted on a log-log scale, (b) shows the reciprocal magnetic susceptibility of PrSi. The solid lines represent the Curie-Weiss fit as mentioned in the text.

this threshold value the system is non-magnetic, and when the magnetic exchange interaction is strong enough the system transforms into a magnetically ordered state. The later is usually expected when the energy separation between the ground state and the first excited state is sufficiently low.

Although the Pr atoms in PrSi possesses monoclinic site symmetry, we have considered a CEF Hamiltonian for the orthorhombic site symmetry in order to reduce the number of fitting parameters. The Hamiltonian for the orthorhombic site symmetry is given by,

$$\mathcal{H}_{\text{CEF}} = B_2^0 O_2^0 + B_2^2 O_2^2 + B_4^0 O_4^0 + B_4^2 O_4^2 + B_4^4 O_4^4 + B_6^0 O_6^0 + B_6^2 O_6^2 + B_6^4 O_6^4 + B_6^6 O_6^6, \quad (5.2)$$

where B_l^m and O_l^m are the crystal field parameters and the Steven's operators [24, 23], respectively. Here the [010] direction has been considered as the quantization axis or the z-axis, [100] direction as the y-axis and [001] direction as the x-axis. Diagonalizing the above Hamiltonian gives the energy eigenvalues and the eigenfunctions.

The magnetic susceptibility including the molecular field contribution λ_i is given by

$$\chi_i^{-1} = \chi_{\text{CEF}i}^{-1} - \lambda_i (i = x, y, z). \quad (5.3)$$

The expression for the CEF magnetic susceptibility is given in the previous chapter. Based on above model, the magnetic susceptibility for three principal crystallographic directions is calculated and the crystal field parameters and the molecular field constants are obtained. Fig. 5.4 shows the temperature dependence of inverse susceptibility. The crystal field split energy level scheme is also shown in the figure. The high temperature anisotropy is well described by this model. The obtained crystal electric field parameters and the energy level values are listed in Table 5.2. Although the set of crystal field parameters calculated here may not be the unique set, these values have been chosen so that the energy levels reproduce the Schottky heat capacity that matches reasonably well with the experiment (to be discussed in the heat capacity section). A detailed inelastic neutron scattering experiment is nec-
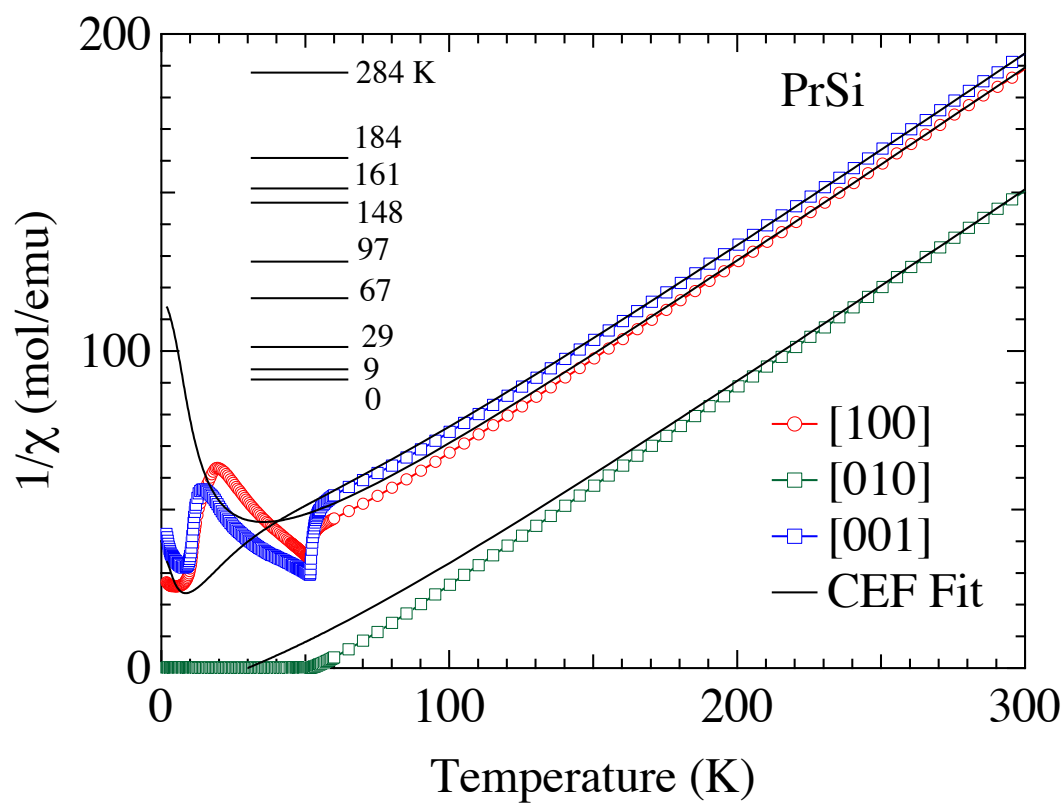
Figure 5.4: Inverse χ vs. T plot, the solid lines show the fit based on the crystalline electric field model. The crystal field energy levels are also shown.

Table 5.2: Crystal field parameters and the corresponding energy levels obtained from the CEF calculation of the reciprocal susceptibility of PrSi.

Crystal Field Parameters (K)									
B_2^0	B_2^2	B_4^0	B_4^2	B_4^4	B_6^0	B_6^2	B_6^4	B_6^6	$\lambda_i(i=x,y,z)$
-3.22	0.81	-0.021	-0.072	-0.215	0.002	-0.008	0.013	0.002	17 mol/emu
									13 mol/emu
									10 mol/emu
Energy levels (K)									
0	9	29	67	97	148	161	184	284	

essary to determine the unique crystal field level scheme. Here the crystal electric field splits the $(2J+1)$ nine-fold degenerate levels of Pr^{3+} ion into nine singlets with an overall splitting of 284 K. It is worth noting here that the ground state and the first excited state are separated by only 9 K. These two closely spaced singlet levels essentially form a quasi-doublet ground state, so that magnetic ordering occurs in PrSi, induced by a magnetic exchange which is apparently above the threshold value.

For an orthorhombic system, Bowden *et al.* [90] and Shohata [91] have shown that the paramagnetic Curie temperature θ_a, θ_b, and θ_c and the crystal electric field parameters B_2^0 and B_2^2 are related by the following expressions:

$$\theta_{\mathrm{a}} = \theta_\lambda + (2J-1)(2J+3)\frac{(B_2^0 + B_2^2)}{10k_{\mathrm{B}}} \tag{5.4}$$

$$\theta_{\mathrm{b}} = \theta_\lambda + (2J-1)(2J+3)\frac{B_2^0}{5k_{\mathrm{B}}} \tag{5.5}$$

$$\theta_{\mathrm{c}} = \theta_\lambda + (2J-1)(2J+3)\frac{(B_2^0 - B_2^2)}{10k_{\mathrm{B}}}, \tag{5.6}$$

where, θ_λ is the paramagnetic Curie temperature due to the molecular field and is given by the following expression,

$$\theta_\lambda = \lambda g_{\mathrm{J}}^2 \mu_{\mathrm{B}}^2 \frac{(J(J+1))}{3k_{\mathrm{B}}}. \tag{5.7}$$
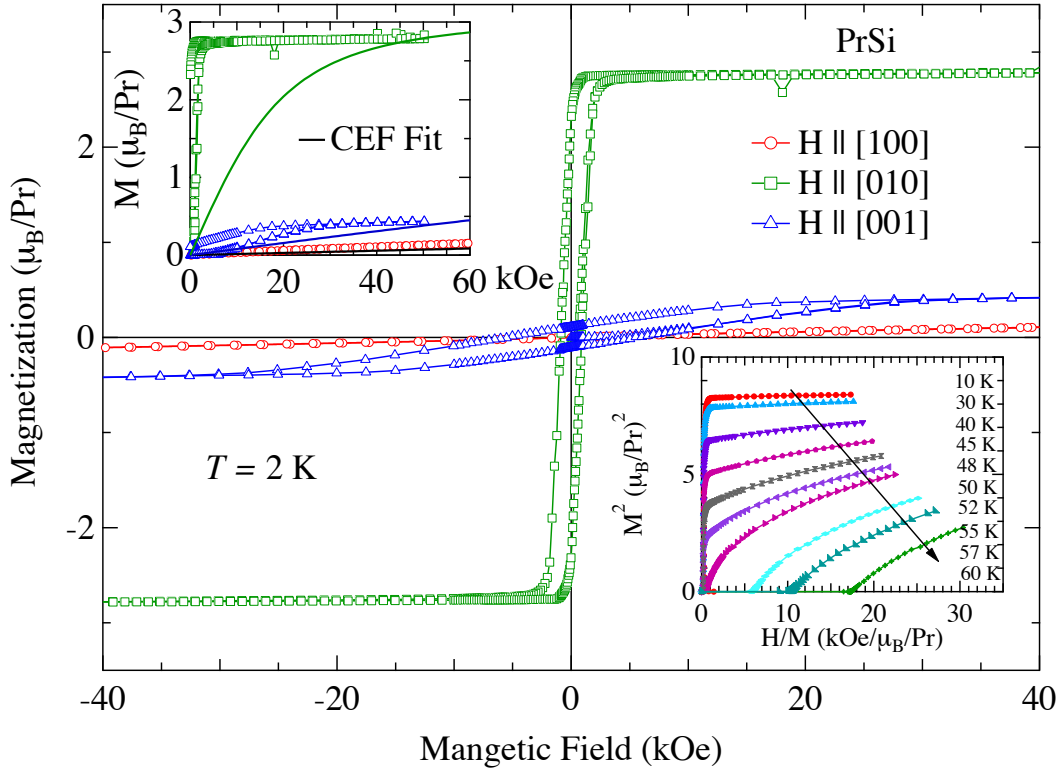
Figure 5.5: Isothermal magnetization of PrSi along the three principal crystallographic directions. The upper inset shows calculated magnetization based on the crystal field model and the lower inset shows the Arrott plot.

From the experimental values of the paramagnetic Curie-Weiss temperatures, for the three principal crystallographic directions, the B_2^0 and B_2^2 parameters were estimated to be -3.22 K and 0.81 K, respectively, which are in good agreement with the parameters obtained from our crystal field calculations.

The anisotropic magnetic properties of PrSi are further investigated by measuring the isothermal magnetization at $T = 2$ K well below the magnetic ordering temperature $T_C = 52$ K. The field dependence of magnetization is shown in Fig. 5.5. The magnetization measurements were performed in both increasing and decreasing fields. Hysteretic behavior is observed along all three principal crystallographic directions, confirming the ferromagnetic nature of magnetic ordering in PrSi. For field parallel to [010] direction, the magnetization increases very rapidly and saturates at fields greater than 3 kOe, thus confirming [010] as the easy axis of magnetization. The saturation

moment is 2.88 μ_B/Pr which is very close to the saturation value of the free Pr^{3+} ion, given by $g_J J = 3.2\ \mu_B/Pr$. On the other hand the magnetization along the [100] and [001] directions reaches only 0.13 μ_B/Pr and 0.43 μ_B/Pr, respectively, for an applied field of 40 kOe, indicating that they lie in the hard plane of magnetization. The lower inset of Fig. 5.5 shows the Arrott plots constructed in the temperature range from 10 to 60 K. The Arrot plots show S-shaped curvature which has been invoked in the literature as evidence of a first-order transition [92]. A similar type of behavior was observed in the PrGe single crystal [93].

The field dependence of magnetization has been analysed based on the CEF model given by the following Hamiltonian:

$$\mathcal{H} = \mathcal{H}_{\mathrm{CEF}} - g_J \mu_{\mathrm{B}} J_{\mathrm{i}}(H + \lambda_{\mathrm{i}} M_{\mathrm{i}}), \tag{5.8}$$

where $\mathcal{H}_{\mathrm{CEF}}$ is given by Eq. 5.2, the second term is the Zeeman term and the third is the molecular field term. The magnetization M_i is given by the following expression,

$$M_i = g_J \mu_{\mathrm{B}} \sum_n |\langle n|J_i|n\rangle| \frac{\exp(-\beta E_n)}{Z}, \quad (i = x, y, z) \tag{5.9}$$

With the set of crystal field parameters obtained from the analysis of the inverse susceptibility data, the diagonalisation of the CEF Hamiltonian was performed and the energy eigenvalues and eigenvectors were used in Eq. 5.9 to calculate the magnetization curve. The calculated magnetization based on this model is shown in the upper inset of Fig. 5.5. From the figure we see that the magnetocrystalline anisotropy is qualitatively explained by the set of crystal field parameters though the calculated magnetization curves do not match very well with the corresponding experimental plots.

The magnetization value of a singlet ground state ferromagnet at 0 K can be estimated from the energy separation between the ground state and first excited singlet state (Δ) and ferromagnetic Curie temperature T_{C} from the following expression[94, 95]:

$$m_{(T=0 \text{ K})} = 4g_J\mu_{\text{B}}\sqrt{1 - tanh^2\left(\frac{\Delta}{2k_{\text{B}}T_{\text{C}}}\right)}. \qquad (5.10)$$

Using $\Delta = 9$ K and $T_{\text{C}} = 52$ K, results in a theoretical value for the magnetization $(m) = 3.18$ μ_{B}/Pr in the zero temperature limit which is in close agreement with our experimental saturation value of 2.88 μ_{B}/Pr. The small discrepancy in the measured magnetization value may be attributed to the fact that the measurement was done at $T = 2$ K. Thus our crystal field calculation assuming an orthorhombic crystal potential is justified.

5.3.4   Heat capacity

The temperature dependence of specific heat was measured in the temperature range from 1.8 to 200 K. To find the magnetic part of heat capacity, the heat capacity of isostructural non-magnetic reference compound LaSi has also been measured in the same temperature range. Fig. 5.6 shows the temperature dependence of the heat capacity of LaSi, which is typical of a nonmagnetic metallic system. The low temperature part of C/T vs. T^2 plot is shown in the inset of Fig. 5.6. The Sommerfeld coefficient γ and the lattice contribution β is obtained by fitting the low temperature data to $C/T = \gamma + \beta T^2$. A best fit to the data was obtained for $\gamma = 5.341$ mJ/K^2 mol and $\beta = 1.2127 \times 10^{-4}$ mJ/K^4 mol. From the obtained value of β, we have calculated the Debye temperature (Θ_{D}) using the expression: $\Theta_D = (1943.7 \times n/\beta)^{1/3}$, where n corresponds to the number of atoms (for LaSi, $n = 2$). The Θ_{D} value thus obtained is 317 K. However, the simple Debye model only, does not explain the experimental data very well as shown by the dotted line in Fig. 5.6. This suggests that the higher energy optical modes should also be considered in LaSi and hence the heat capacity data were fitted to the following expression:

$$C_{\text{p}} = \gamma T + [mC_{\text{Debye}}(T) + (1-m)C_{\text{Einstein}}(T)], \qquad (5.11)$$

where the first term represents the electronic contribution and the second term represents the phononic contribution which includes the Debye plus the Einstein
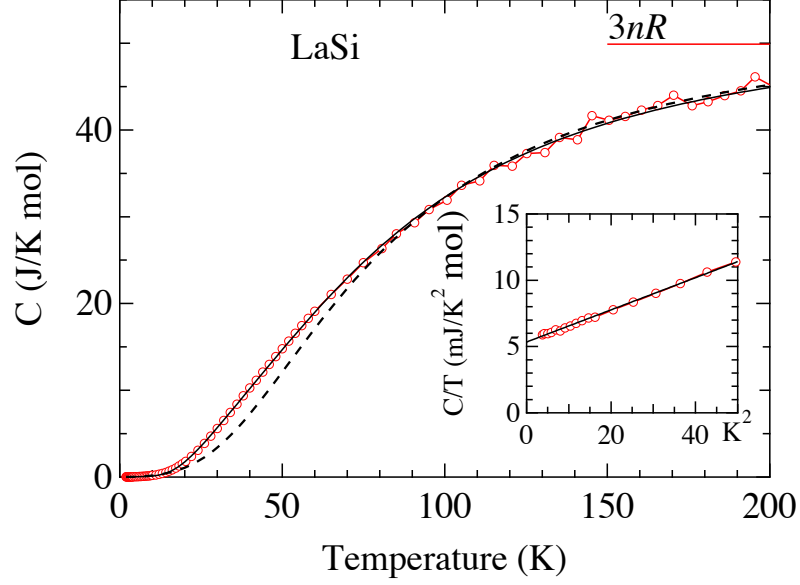
Figure 5.6: Temperature dependence of specific heat capacity of LaSi. The dashed line and the continuous line are fits to Debye model and Debye+Einstein model. The inset shows the low temperature part of C/T versus T^2 plot. The solid line in the inset is the fit to $C/T = \gamma + \beta T^2$ expression.

terms.

The Debye and Einstein terms are given by the following expressions,

$$C_{\mathrm{Debye}} = 9nR \left(\frac{T}{\Theta_{\mathrm{D}}} \right)^3 \int_0^{\Theta_{\mathrm{D}}/T} \frac{x^4 e^x}{(e^x - 1)^2} dx, \qquad (5.12)$$

and

$$C_{\mathrm{Einstein}} = 3nR \frac{y^2 e^y}{(e^y - 1)^2}, \qquad (5.13)$$

where $x = \Theta_{\mathrm{D}}/T$ and $y = \Theta_{\mathrm{E}}/T$. Equation 5.11 results in a best fit to the experimental data of LaSi with 74% of the weight to Debye term with $\Theta_{\mathrm{D}} = 373$ K and the remaining 26% to the Einstein mode with Einstein temperature $\Theta_{\mathrm{E}} = 120$ K as shown by the solid line. At 200 K, the experimental heat capacity reaches a value of about 45 J/K mol, which is close to the Dulong-Petit limiting value of $3nR = 49.884$ J/K mol.
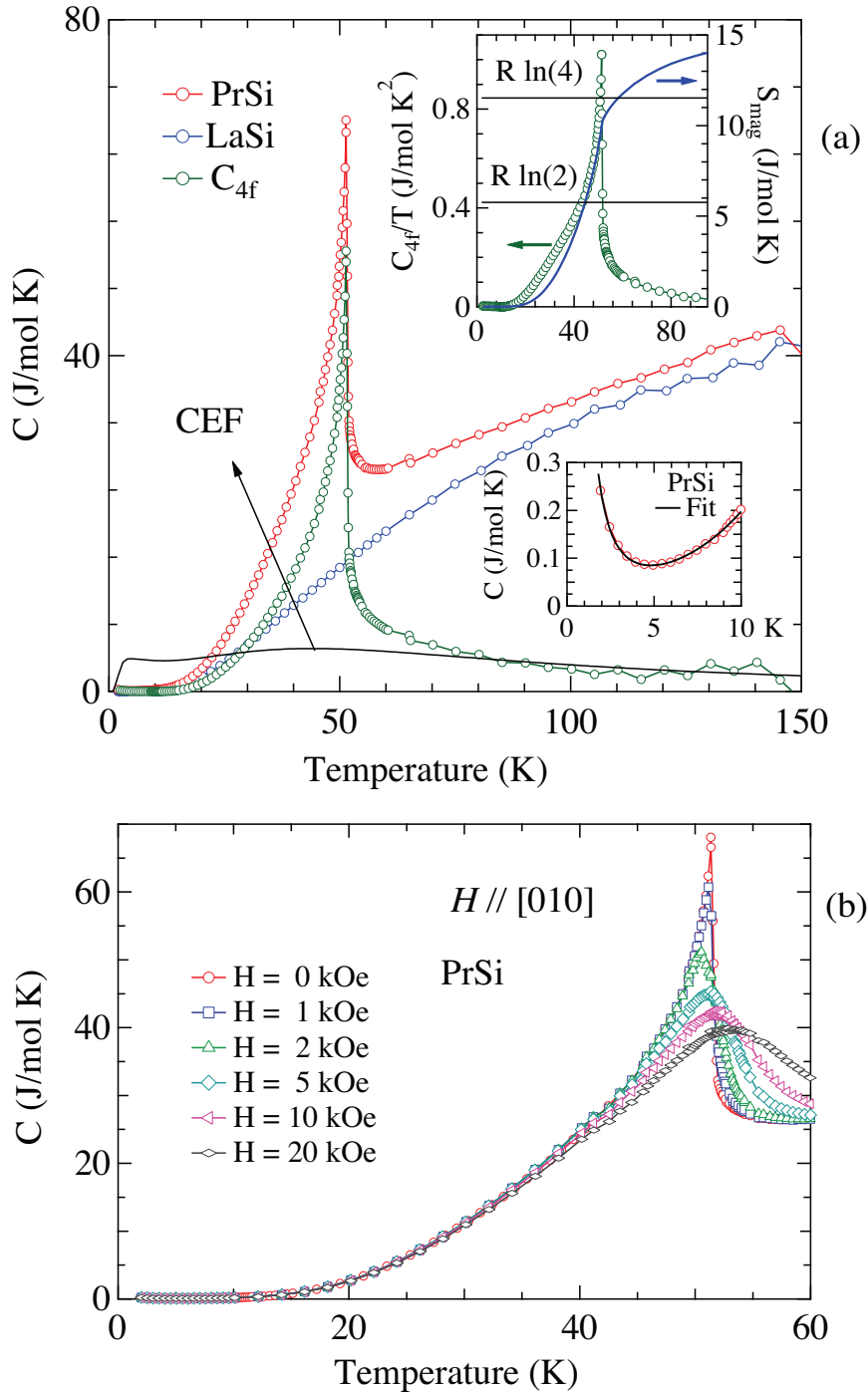
Figure 5.7: (a) Heat capacity of PrSi and LaSi, and the magnetic part of heat capacity, the top inset shows C_{4f}/T versus T plot and the entropy. The lower inset in (a) shows the low temperature part of heat capacity and a fit to the nuclear Schottky and (b) Magnetic field dependence of heat capacity in PrSi.

The temperature dependence of specific heat capacity of PrSi single crystal along with the magnetic part of heat capacity ($C_{4\mathrm{f}}$) is plotted in Fig. 5.7. Heat capacity decreases with temperature from 150 K down to 52 K smoothly, where a sudden jump in the heat capacity is observed signaling the bulk nature of the magnetic ordering. The jump in the heat capacity amounts to 40 J/mol K. Such a huge jump further indicates the first order nature of magnetic transition which was inferred earlier from the shape of Arrott's plot. It maybe noted here that the electrical resistivity of the sample near this transition temperature was measured very carefully by varying the temperature in very small steps. However, we did not observe a clear hysteresis in the electrical resistivity, which does not prima facie support the first-order nature of the ferromagnetic transition in PrSi.

At low temperature region, much below the Curie temperature T_{C}, for $T \leq 4$ K, we observed an upturn in the specific heat with decreasing temperature. This upturn is attributed to the nuclear Schottky contribution arising due to the interaction of the nuclear moments with $4f$ electrons. For $T \leq 4$ K, the heat capacity data was fitted to the following expression:

$$C_{\mathrm{p}} = \gamma T + \beta T^3 + \left(\frac{C_{\mathrm{N}}}{T^2}\right), \tag{5.14}$$

where the first term is the electronic contribution of heat capacity, second term is the lattice contribution, and third term is the nuclear Schottky term arising due to the level splitting of the hyperfine levels. Here the magnon term was not included while fitting the low temperature data, since the magnon gap is about an order of magnitude larger as estimated from the electrical resistivity data. The fitting parameters are found to be $\gamma = 7.378$ mJ/K^{2}mol, $\beta = 0.115$ mJ/K^4 mol and the nuclear Schottky term $C_{\mathrm{N}} = 850.2$ mJ K/mol. Here the coefficient C_{N} is related to the magnetic moment of Pr moment m_{4f} as given by the expression:

$$C_{\mathrm{N}} = R A_{\mathrm{hf}}^2 m_{4\mathrm{f}}^2 \frac{I(I+1)}{3g_J^2}, \tag{5.15}$$

where R is the gas constant, A_{hf} is the hyperfine coupling constant and I is the nuclear spin of Pr. For ^{141}Pr, the nuclear spin $I = 5/2$ and the value of A_{hf} is 0.052 K

as found in the literature. Using these values in Eqn. 5.15, the magnetic moment of Pr is obtained as 2.88 μ_B/Pr, which agrees well with our observed magnetization value along the easy axis of magnetization namely, [010] direction. This further supports that the low temperature increase in the heat capacity is due to the nuclear Schottky effect arising from the hyperfine splitting of the nuclear level, and not due to the presence of some magnetic impurities. The magnetic field dependence of the heat capacity of PrSi for $H \parallel [010]$ is shown in Fig. 5.7(b). There is a significant influence of the magnetic field on the specific heat. As the magnetic field is increased the jump in the heat capacity decreases and the peak position shifts to higher temperature, as the applied field aligns the moments ferromagnetically well above the zero field ordering temperature, which is typically observed in ferromagnetic compounds.

The magnetic part of heat capacity C_{4f} of PrSi is obtained by subtracting the nuclear Schottky part and the phonon part obtained from the LaSi heat capacity data. The magnetic entropy is obtained by the usual method of integrating the C_{4f}/T against temperature T. The entropy reaches $R\,ln4$ at 60 K, just above the magnetic transition temperature, which means that there are four CEF singlet levels below that temperature which is consistent with our CEF calculations discussed earlier. With further increase in temperature the entropy increases gradually due to the thermally induced occupation of the higher levels. Just below the magnetic transition the entropy falls off more rapidly down to the value $Rln2$ and then it falls off gradually at lower temperatures. The Schottky contribution to the heat capacity has been estimated using the expression given in the previous chapter. The energy levels obtained from the CEF calculation of susceptibility data have been used to calculate the Schottky heat capacity. The solid line in Fig. 5.7 shows the calculated heat capacity and it matches well with the heat capacity at high temperature above the magnetic ordering. This further justifies the validity of the crystal field parameters and the energy levels of nine singlets calculated from the magnetic susceptibility data.

5.4 Magnetocaloric effect

The huge jump in the heat capacity, a sharp drop in electrical resistivity at the magnetic transition and the shape of Arrott's plot revealed a first-order-like magnetic
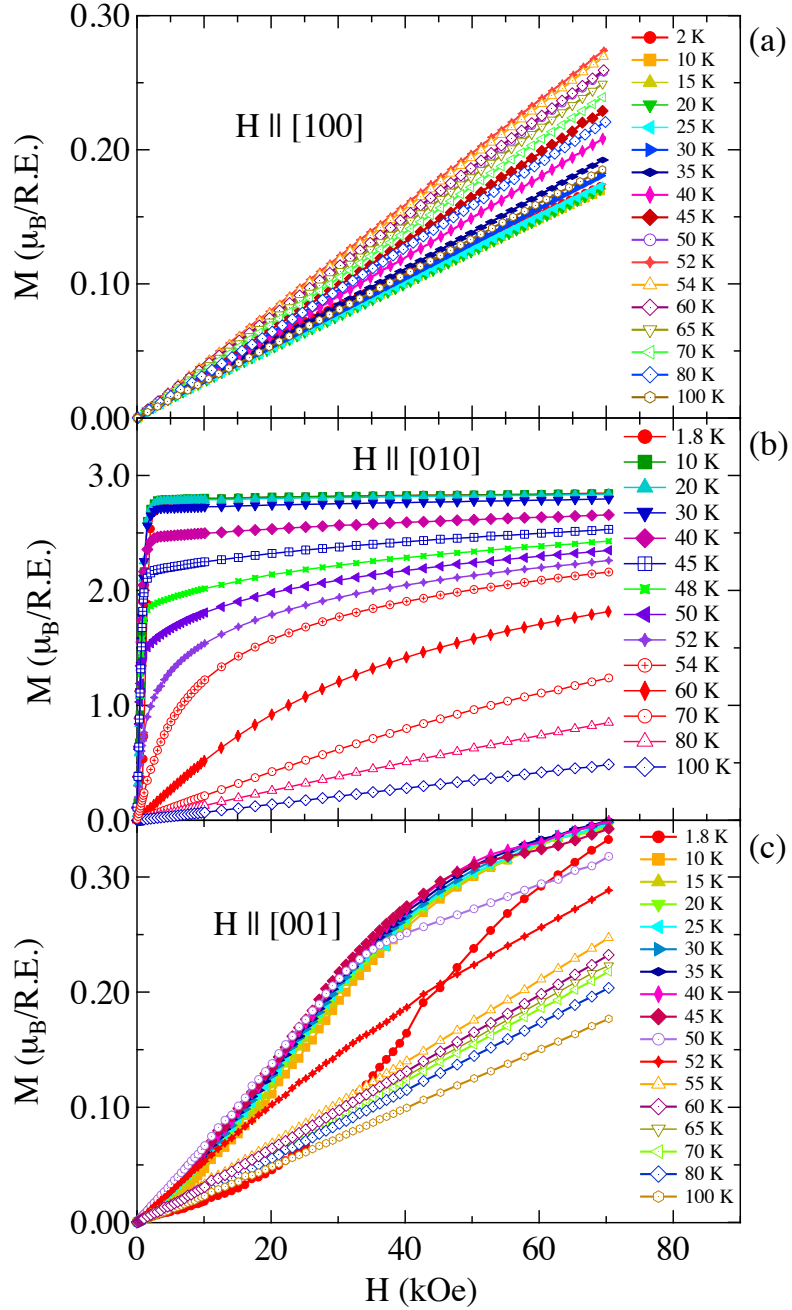
Figure 5.8: Representative magnetization isothermals at various selected temperatures along (a) the *a* axis, (b) the *b* axis and (c) the *c* axis of PrSi. Only field increasing measurement data are shown for each temperature.

Figure 5.9: (a), (b) and (c) represent the temperature variation of magnetic entropy change ($-\Delta S_M$, along the three principal crystallographic directions, at various constant temperatures around the magnetic transition of PrSi.

transition in this compound. Hence an attempt was made to study the magnetocaloric properties of PrSi single crystal. For this purpose, the magnetization of PrSi along the three principal crystallographic directions in the temperature range 2 K to 100 K at selected temperatures and for field ranging from 0 to 70 kOe, has been measured. The magnetization plots along the three directions are shown in Fig. 5.8. Along the easy axis [010] the variation of magnetization with temperature is relatively simple and along the expected lines and at temperature above the Curie temperature $T_C = 52$ K the paramagnetic behaviour is observed. On the other hand along the hard axes, [100] and [001], the magnetization showed some anomalous behaviour. Since there is a large magnetic anisotropy in PrSi, it is pertinent to calculate the individual magnetic entropy change (ΔS_M) for the three directions respectively. ΔS_M in PrSi was calculated from M *vs.* H isotherms using Maxwell's relation [96]:

$$\Delta S_M(0 \to H) = \int_0^H \frac{dM}{dT} dH \qquad (5.16)$$

Temperature dependence of the computed $-\Delta S_M$ at selected values of the magnetic field H, along the three principal directions are shown in Fig. 5.9. A low field is enough to induce complete saturation for $H \parallel [010]$ direction. Therefore, we observe giant negative magnetic entropy change along this direction around T_C. The maximum value of $-\Delta S_M$ is found to be 22.2 J/kg K for $\Delta H = 70$ kOe around T_C and it attains a value of 18.4 J/kg K for a field change of 50 kOe. These values of $-\Delta S_M$ are comparable to that of the well-known giant magnetocaloric compound $Gd_5Si_2Ge_2$ [97, 98]. The $-\Delta S_M$ value that we observe is larger than the value of PrSi polycrystalline sample [86]. Since the previous report was on polycrystalline sample they observed a lower MCE due to the large anisotropy. Along $H \parallel [001]$ axis the magnetization is much smaller even for fields up to 70 kOe. Besides the $M - H$ plot is non linear along this direction. Due to the lack of saturation here the value of $-\Delta S_M$ is almost 10 times smaller than $H \parallel [010]$ axis. On the other hand, for $H \parallel [100]$ direction the magnetic entropy is positive in the magnetically ordered state for fields as high as 70 kOe. By comparing $-\Delta S_M$ for the $H \parallel [010]$, and $H \parallel [100]$ directions, a giant anisotropy of $-\Delta S_M$ is observed in PrSi single crystal.

Relative cooling power (RCP) of a magnetic refrigerant is a measure of how much heat is transferred between the hot and cold sinks in one ideal refrigeration cycle
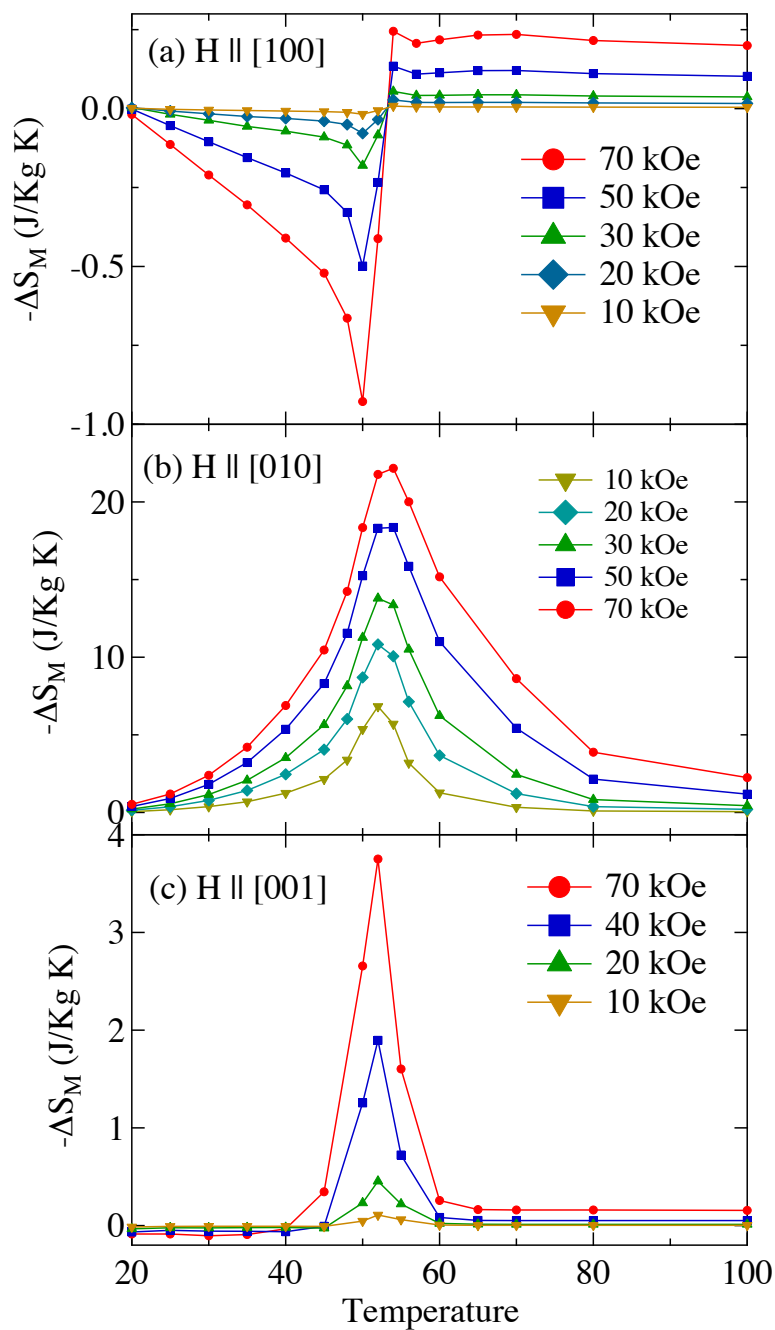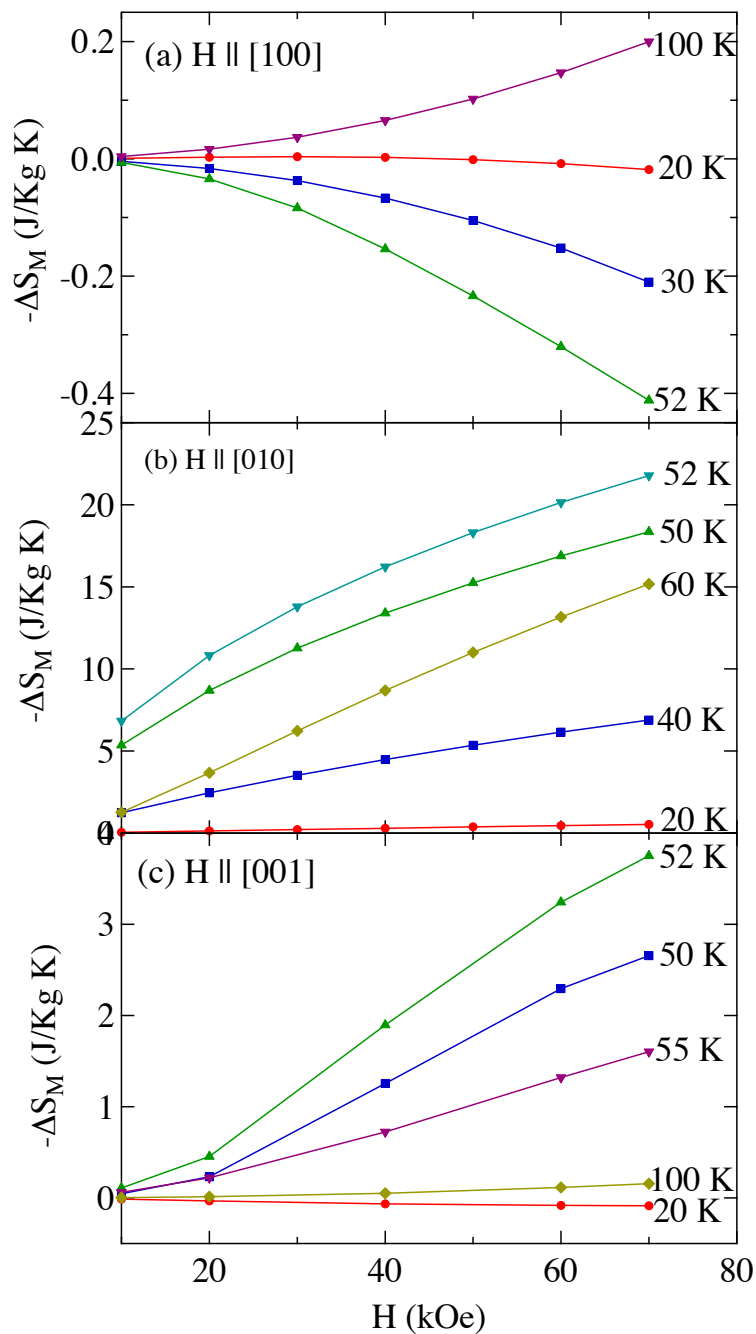
Figure 5.10: (a), (b) and (c) represents the field variation of magnetic entropy change $(-\Delta S_M$, along the three principal crystallographic directions, $H \parallel [010]$, $H \parallel [001]$ and $H \parallel [100]$) around the magnetic transition region at different constant temperatures of PrSi.
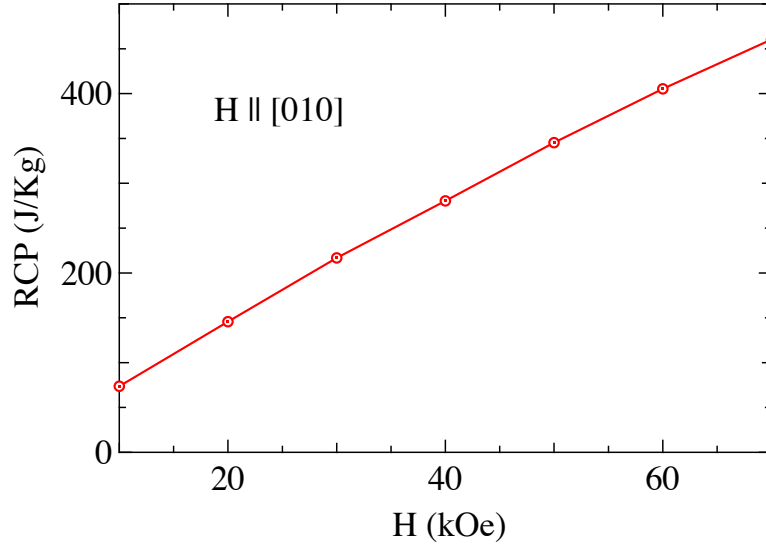
Figure 5.11: Magnetic field variation of relative cooling power for PrSi along the [010] direction.

and it is an important parameter as far as the magnetic cooling is concerned [96]. For a magnetocaloric material the magnetic cooling efficiency is evaluated by using the relation, RCP = $|\Delta S_M^{max}|\delta T_{FWHM}$ [99], where δT_{FWHM} is the full width at half maximum of the $-\Delta S_M$ vs. T curve and $|\Delta S_M^{max}|$ is the maximum value of the entropy change. Isothermal field dependence of RCP for PrSi is shown in Fig. 5.11. RCP varies linearly with H. RCP value is reasonably large, which is $\approx$ 470 J/K for a change of magnetic field H to 70 kOe. It is very interesting to note here that usually, this type of giant magnetocaloric effect and large RCP is observed for samples possessing heavier rare-earth elements whose magnetic moments are large [99, 98]. In spite of the Pr atom's low saturation moment value (3.2 μ_B) a large magnetocaloric effect is observed in PrSi. The large MCE in PrSi may tentatively be attributed to a magnetostructural transition at T_C such that the change in the configurational entropy adds to the magnetic entropy.

5.5   Results of PrGe

5.5.1   Structural properties of PrGe

PrGe single crystal was grown by the Czochralski pulling method. It has been reported in the literature [69] that the PrGe exhibits dimorphism by crystallizing in two different crystal structures, namely the CrB-type and FeB-type orthorhombic structures with space group $Cmcm$ (no. 63) and $Pnma$ (no. 62), respectively. As a first step to identify the crystal structure, a small portion of the crystal was subjected to powder x-ray diffraction at room temperature in a PANalytical x-ray diffractometer using monochromatic Cu Kα radiation with the wavelength 1.5406 Å. The powder x-ray diffraction pattern confirmed the crystal structure to be CrB-type, with the space group $Cmcm$. Fig. 5.12 shows the powder x-ray diffraction pattern along with the Rietveld analysis. The obtained lattice parameters are $a = 4.481(1)$ Å, $b = 11.087(2)$ Å, and $c = 4.050(1)$ Å with the reliability parameters $R_{\mathrm{B}} = 12.4\%$ and $R_{\mathrm{F}} = 6.5\%$. The lattice parameters are in excellent agreement with the previous reports [69]. In the $Cmcm$ orthorhombic space group both Pr and Ge atoms occupy the $4c$ Wyckoff position, with $y = 0.3608(3)$ and $0.0785(5)$, respectively. The stoichiometry of the grown crystal was further confirmed by EDAX measurement. Then, the crystal was oriented along the principal crystallographic directions by back reflection Laue method. The Laue pattern corresponding to the three principal crystallographic planes are shown in the bottom panel of Fig. 5.12. The well defined Laue diffraction pattern indicates a good quality of the single crystal, and also confirms the orthorhombic crystal structure. The crystal was cut in rectangular bar form by spark erosion cutting machine for anisotropic property measurements.

5.5.2   Electrical Resistivity

Figure 5.13(a) shows the temperature dependence of electrical resistivity of PrGe single crystal measured for current parallel to [100], [010] and [001] directions. The electrical resistivity decreases with decreasing temperature along the three directions and the magnetic ordering is clearly visible by the sharp drop of resistivity below the magnetic transition temperature due to the reduction in the spin disorder scattering
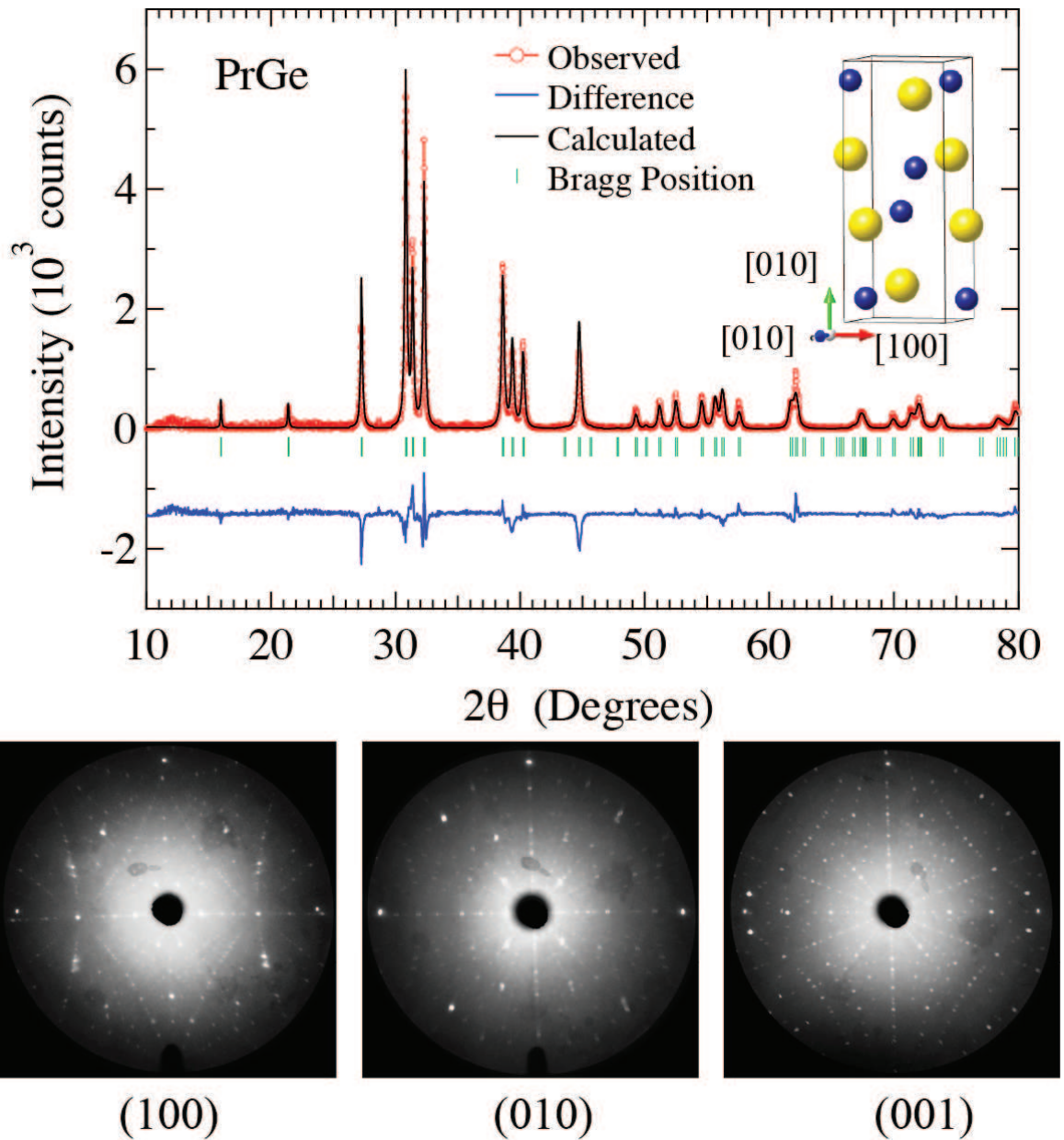
Figure 5.12: The top panel shows the powder x-ray diffraction pattern of PrGe together with the Rietveld refinement. The inset shows the crystal structure of PrGe. The Laue diffraction patterns corresponding to (100), (010) and (001) are shown in the bottom panel.
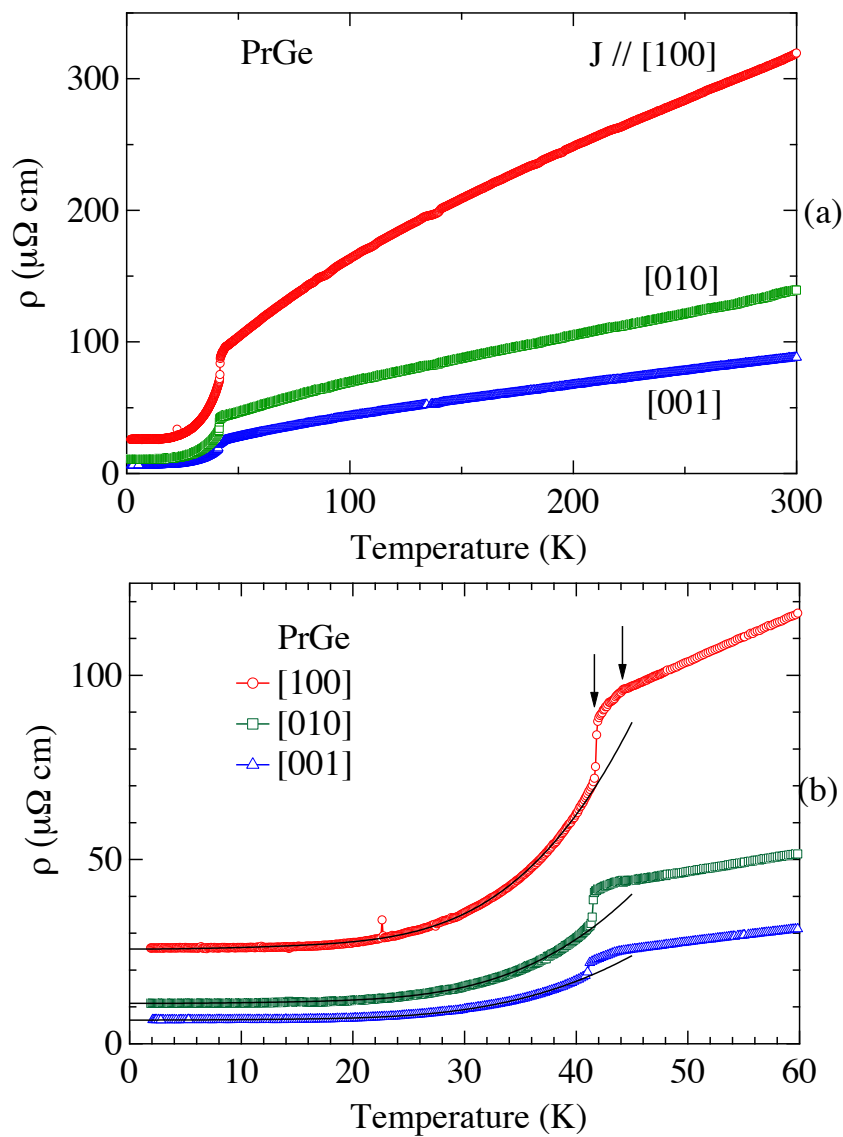
Figure 5.13: (a) Temperature dependence of electrical resistivity of PrGe for current parallel to the three principal crystallographic directions. (b) The low temperature part of the resistivity of PrGe. The solid lines are the fit to the spin-wave gap model.

	ρ_0	a	D	Δ
	$(\mu\Omega\ \text{cm})$	$(\mu\Omega\ \text{cm/K}^2)$	$(\mu\Omega\ \text{cm/K}^2)$	(K)
$\rho_{[100]}$	26	0.004	0.14	150
$\rho[010]$	10	0.002	0.07	154
$\rho[001]$	6.4	0.001	0.03	142

Table 5.3: Spin wave fitting parameters of the resistivity data along the three principal directions described in Eqn. 5.1.

of conduction electrons. There is a large anisotropy in the electrical resistivity with room temperature values of $\rho_{[100]}(300\ \text{K}) = 319\ \mu\Omega$cm, $\rho_{[010]}(300\ \text{K}) = 139\ \mu\Omega$cm and $\rho_{[001]}(300\ \text{K}) = 88\ \mu\Omega$cm for PrGe. Figure 5.13(b) shows the low temperature part of the electrical resistivity. There is a small change of slope at 44 K due to the antiferromagnetic transition at that temperature. The ferromagnetic ordering at $T_\text{C} = 41.4$ K results in a sharp drop in the electrical resistivity along all the three directions. At T_N there is a decrease in the resistivity. The resistivity drop is not so prominent between the temperatures T_N and T_C. Once the ferromagnetic ordering sets-in the electrical resistivity drops more rapidly due to the reduction in the spin-disorder scattering. This type of sharp drop in the electrical resistivity is attributed to the first order transition. The electrical resistivity of PrGe in the ferromagnetically ordered state can be fitted to the spin wave gap model as described by Eqn. 5.1 which involves, apart from the usual Fermi liquid term, the contribution from the energy gap in the magnon dispersion relation [100]. The solid lines in Fig. 5.13(b) represent the fit to the model and the parameters obtained from the fit are given in Table 5.3.

The obtained values of the spin wave gap is nearly equal for all the three directions even though there is a large anisotropy in the electrical resistivity. The residual resistivity ratio (RRR) amounts to 12.22, 12.52 and 13.54 for $J \parallel$ [100], [010] and [001] directions respectively thus indicating good quality of the single crystal.

5.5.3 Magnetic susceptibility and magnetization

Figure 5.14(a) shows the temperature dependence of magnetic susceptibility of PrGe measured in an applied magnetic field 1 kOe in the temperature range from 1.8 to 300 K for H $\parallel$ [100] and [010] directions. There is a large anisotropy in the magnetic

Figure 5.14: (a) Temperature dependence of magnetic susceptibility of PrGe along [100] and [010] directions, measured in an applied field of 1 kOe. (b) susceptibility of PrGe along [001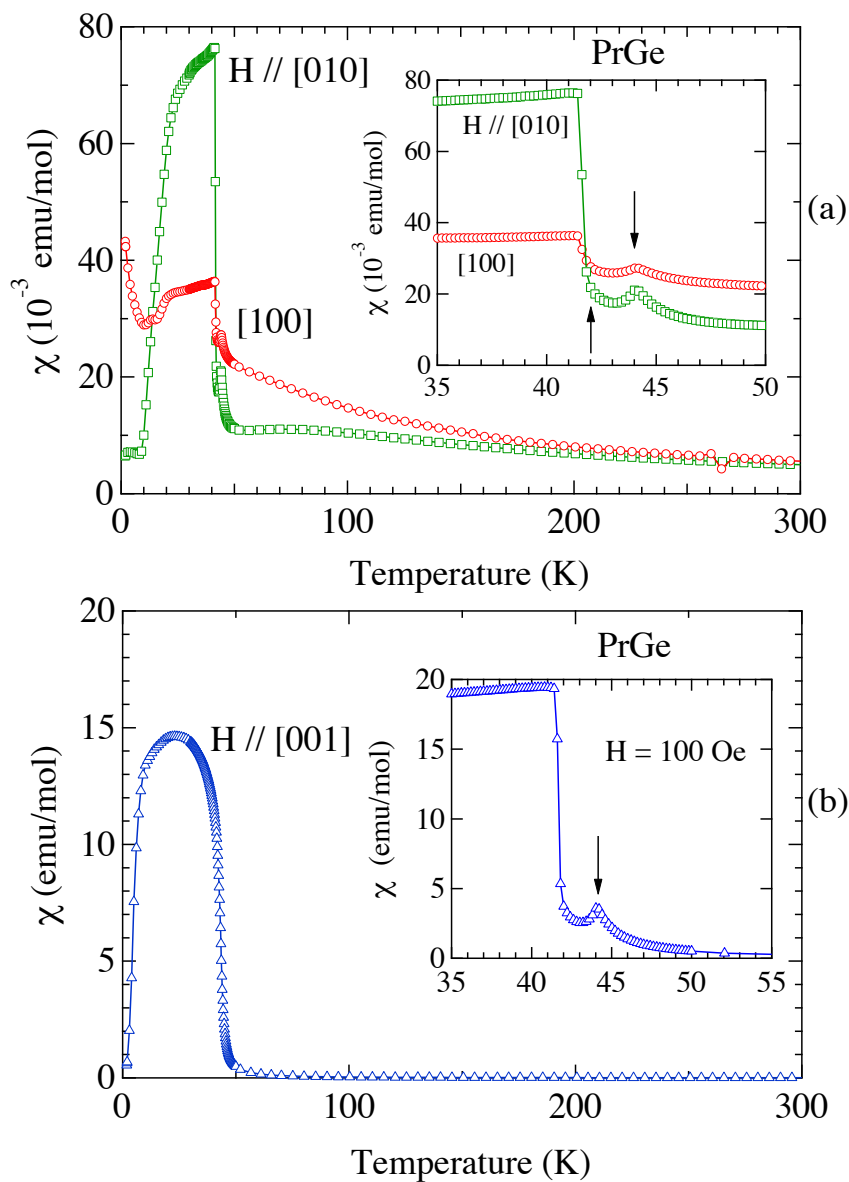] direction. The inset in both the figure shows the expanded scale susceptibility near the ordering temperature. The arrows indicate the magnetic transition. The inset in (b) shows data measured in a field of 100 Oe.

susceptibility between the two directions. Signatures of two magnetic transitions at 44 K and at 41.5 K are observed along the [100] and [010] directions. From the inset of Fig. 5.14(a) it is obvious that the high temperature transition at 44 K is anti-ferromagnetic indicated by the cusp like behavior of susceptibility usually observed for an antiferromagnetic transition. At 41.5 K the magnetic susceptibility shows an upturn signalling a ferromagnetic ordering. For $H \parallel [100]$ direction, below 10 K, the upturn of susceptibility is tentatively attributed to the canting of the ordered Pr moments along this hard axis. The magnetic susceptibility for H ∥ [001] direction is shown in Fig. 5.14(b). Unlike the other two directions, the susceptibility in a field of 1 kOe apparently exhibits only one transition at 44 K which is ferromagnetic like. However when the data are recorded in a lower field of 100 Oe (inset of Fig. 5.14(b)) the antiferromagnetic ordering at 44 K is clearly observed in the [001] direction as well, followed by a ferromagnetic like upturn at lower temperatures. The in-field, isothermal magnetization data to be discussed later further substantiate this claim.

The inverse magnetic susceptibility of PrGe is shown in Fig. 5.15. The anisotropy in the magnetic susceptibility along the three principal directions is clearly evident. The solid lines are fits to the modified Curie-Weiss law $\chi = \chi_0 + C/(T - \theta_p)$. It is observed that the Curie-Weiss law is obeyed from 300 K down to temperatures just above the magnetic transition and no deviation due to crystal electric field effect is observed. From the fitting, effective magnetic moment μ_{eff}, the paramagnetic Curie temperature θ_p and the temperature independent magnetic susceptibility χ_0 were found to be 3.78 μ_B, −24 K and 6.794 × 10^{-5} emu/mol; 3.90 μ_B, −70 K and 1.8166 × 10^{-4} emu/mol and 3.71 μ_B, 58 K and 2.5831 × 10^{-4} emu/mol, respectively for $H \parallel$ [100], [010] and [001] directions. The experimental value of the effective moment μ_{eff} is close to the free ion value of Pr^{3+}, 3.58 μ_B. The Weiss temperature θ_p is positive for $H \parallel$ [001], as expected for a ferromagnetic ordering compound.

The isothermal magnetization of PrGe measured at $T = 1.8$ K along the three principal crystallographic directions is shown in Fig. 5.16. Hysteretic behaviour is observed along all the three directions confirming the ferromagnetic ground state in PrGe, thus corroborating the previous neutron diffraction results on a polycrystalline sample of PrGe [69]. For $H \parallel$ [001] the magnetization increases more rapidly with field than along the other two directions thus indicating [001] direction as the easy axis of magnetization. At 1.8 K the magnetization saturates to 3.12 μ_B/Pr, very close
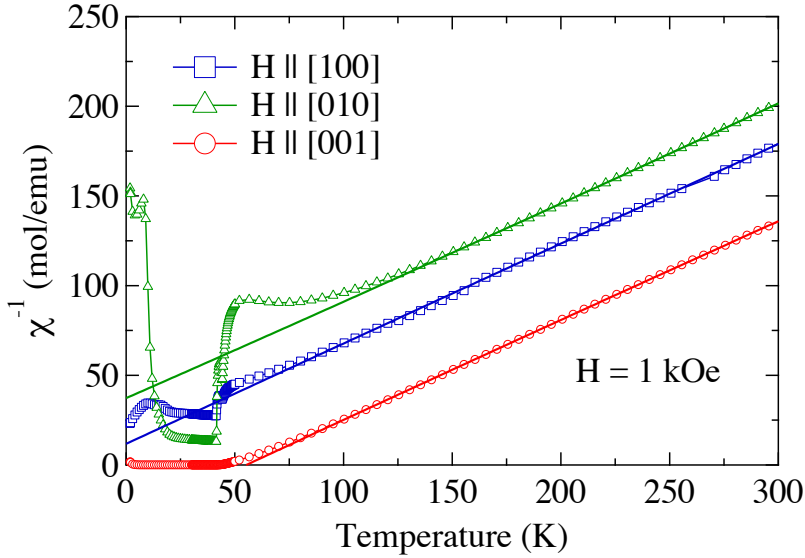
Figure 5.15: Inverse magnetic susceptibility of PrGe along the three principal crystallographic directions, the solid lines are fits to modified Curie-Weiss law.

to the saturation moment of free Pr^{3+} ion ($g_J J \mu_B = 3.20\ \mu_B$). The saturation value of the magnetic moment along [100] and [010] directions are much smaller indicating the hard axes of magnetization. The width of the hysteresis loop decreases as the temperature increases and above 42 K, where the sample enters into the antiferromagnetic state, there is no signature of hysteresis. A plot of coercive field versus temperature for $H \parallel$ [001] direction is shown in Fig. 5.16. For $H \parallel$ [001] direction the slope of the virgin curve is small which indicates the presence of narrow domain walls [101]. The impurities of atomic dimensions pin the domain wall as is evident from the flat virgin curve upto a field of 0.08 T (see inset of Fig. 5.16). At higher fields the magnetization increases, which means the external field is able to detach the pinned domain wall, the complete detaching of the pinned domain wall happens at 0.4 T and at higher fields the domain walls are completely removed. On reversing the field the reversed domain walls nucleate and only for the negative fields of about 0.4 T the domain walls are removed.
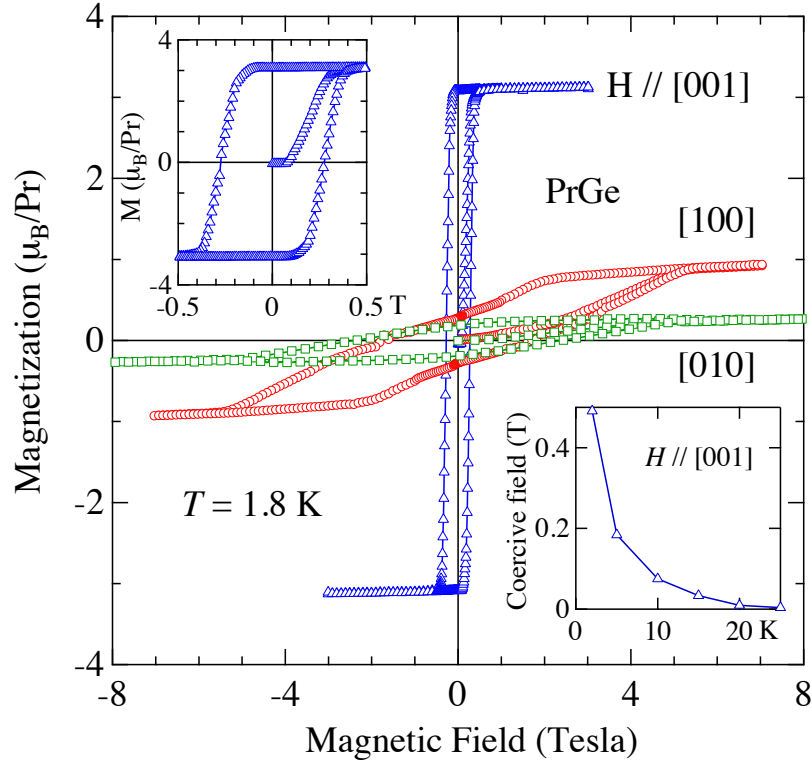
Figure 5.16: Isothermal magnetization of PrGe measured at 1.8 K for fields along the three principal crystallographic directions. The upper inset shows the low field part of the hysteresis loop for $H \parallel [001]$ direction. The lower inset shows the temperature dependence of the coercive field for $H \parallel [001]$ direction.
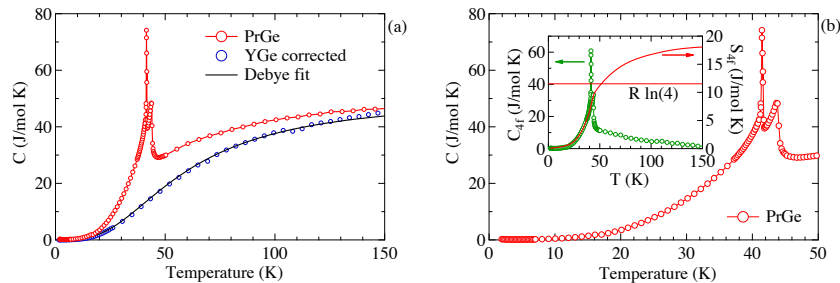
Figure 5.17: (a) Temperature dependence of the specific heat capacity in PrGe and YGe. The solid line through the data points of YGe is fit to the Debye model of heat capacity. (b) The main panel shows low temperature part of the specific heat of PrGe and the inset shows the magnetic part of heat capacity and the calculated entropy.

129
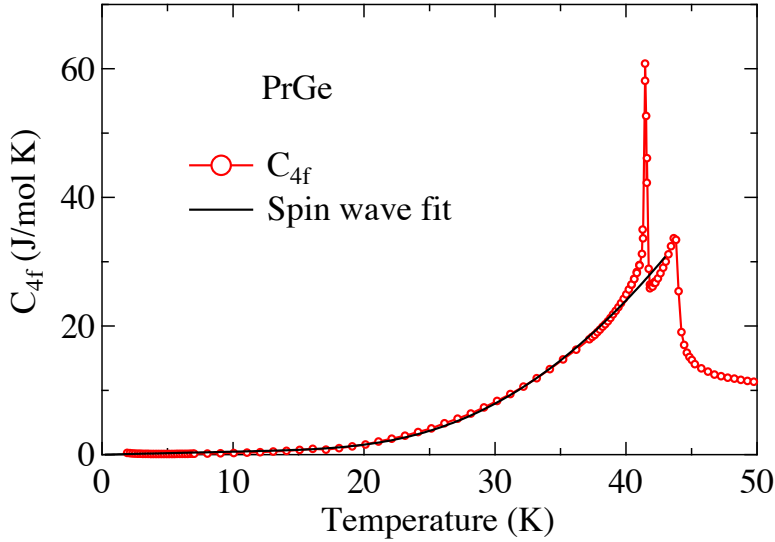
Figure 5.18: The magnetic part of the heat capacity (C_{4f}), the solid line is the fit to the spin-wave expression given in Eq. 5.18.

5.5.4 Heat capacity

The temperature dependence of the specific heat of PrGe single crystal and its non-magnetic reference compound YGe measured in the range of 1.8 to 150 K is shown in the main panel of Fig. 5.17(a). Since the crystal structure of LaGe is FeB-type which is different from the CrB-type structure of PrGe, a polycrystalline sample of YGe was prepared which has the same crystal structure as that of PrGe and it was used as the non-magnetic reference compound after taking into account the mass renormalization as mentioned in Ref. [102]. The heat capacity of YGe can be very well fitted to the Debye model as shown by the solid line through the data points of YGe and Θ_D was estimated to be 245 K. Furthermore, an estimation of γ was done from the low temperature heat capacity data of YGe and it was found to be 3.413 mJ/K^2·mol. The occurrence of two peaks in the heat capacity of PrGe exactly at the same temperatures as observed in magnetic susceptibility and electrical resistivity data, confirms the bulk magnetic transitions in the system. The low temperature part of heat capacity of PrGe is shown in Fig. 5.17(b). The heat capacity jump at the antiferromagnetic transition at 44 K amounts to 19.29 $J~K^{-1}~mol^{-1}$, while at 41.5 K where the system undergoes ferromagnetic transition, the heat capacity jump

amounts to 45.06 J K^{-1} mol^{-1}. Such a huge jump in the heat capacity along with the sharp drop in the electrical resistivity, as mentioned before, clearly indicates a first order nature of transition at 41.5 K. Further confirmation of first order nature of magnetic transition comes from the shape of Arrott's plot. The magnetic part of heat capacity C_{4f} was obtained by subtracting the heat capacity values YGe from that of PrGe and subsequently, the entropy (S_{4f}) was calculated by integrating C_{4f}/T data. The temperature dependence of S_{4f} is shown in the inset of Fig. 5.17(b). The heat capacity data of PrGe in the ferromagnetic state can be well described by the spin-wave gap model [103]. The magnetic part of heat capacity is given by

$$C_{4f} = \gamma T + C_{SW} \tag{5.17}$$

Where, γ is the electronic term of the heat capacity and the heat capacity due to ferromagnetic spin-wave is given by

$$C_{\text{SW}} = \alpha \left(\frac{\Delta^2}{\sqrt{T}} + 3\Delta\sqrt{T} + 5\sqrt{T^3} \right) e^{\frac{-\Delta}{T}} \tag{5.18}$$

Here, Δ is the gap in spin-wave spectrum, and α is a constant. The spin-wave fitting is shown in Fig. 5.18 by the solid line. It is evident that Eqn. 5.18 fits very well our data below 40 K. The obtained values of the fitting parameters are $\gamma = 45.9$ mJ K^{-2} mol^{-1}, $\alpha = 0.105$ J K$^{-5/2}$ mol^{-1} and $\Delta = 140$ K. The spin-wave gap Δ is in close agreement with the values obtained from the fitting of electrical resistivity data.

5.5.5 Magnetocaloric effect of PrGe

The magnetocaloric effect of PrGe has been investigated by the same procedure adopted for the PrSi single crystal. The isothermal magnetization was measured at various temperatures from 2 to 100 K at selected temperatures. The *M vs H* loops were measured for increasing field H from 0 to 70 kOe along the three principal crystallographic directions as shown in Fig. 5.19. The magnetic entropy change ΔS_{M} has been calculated from the *M vs H* isotherms using the Maxwell's relation 5.16.

131
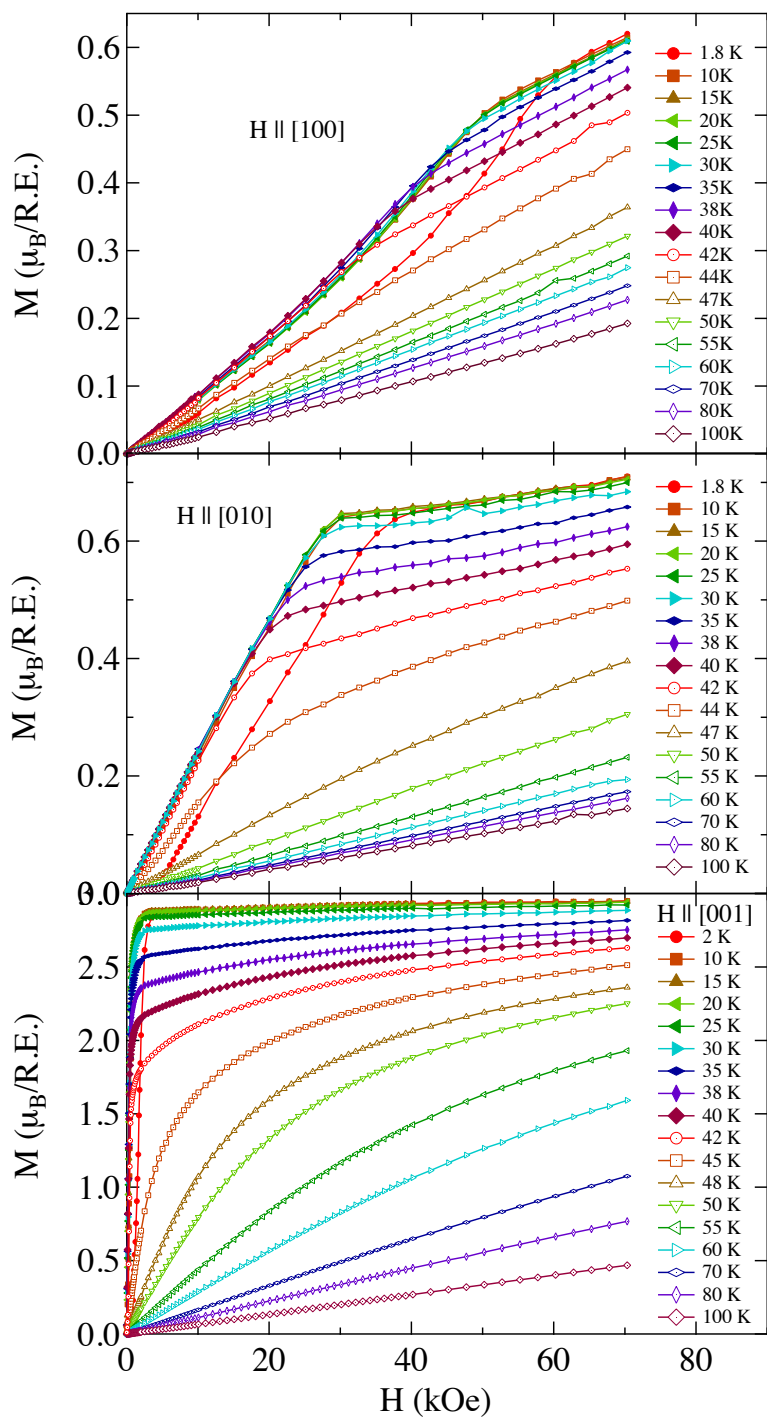
Figure 5.19: Representative magnetization isothermals at various temperatures along (a) the b axis ($H \parallel [010]$), (b) the c axis ($H \parallel [001]$) and (c) the a axis ($H \parallel [100]$). Only the data obtained while increasing the field are plotted for each temperature.
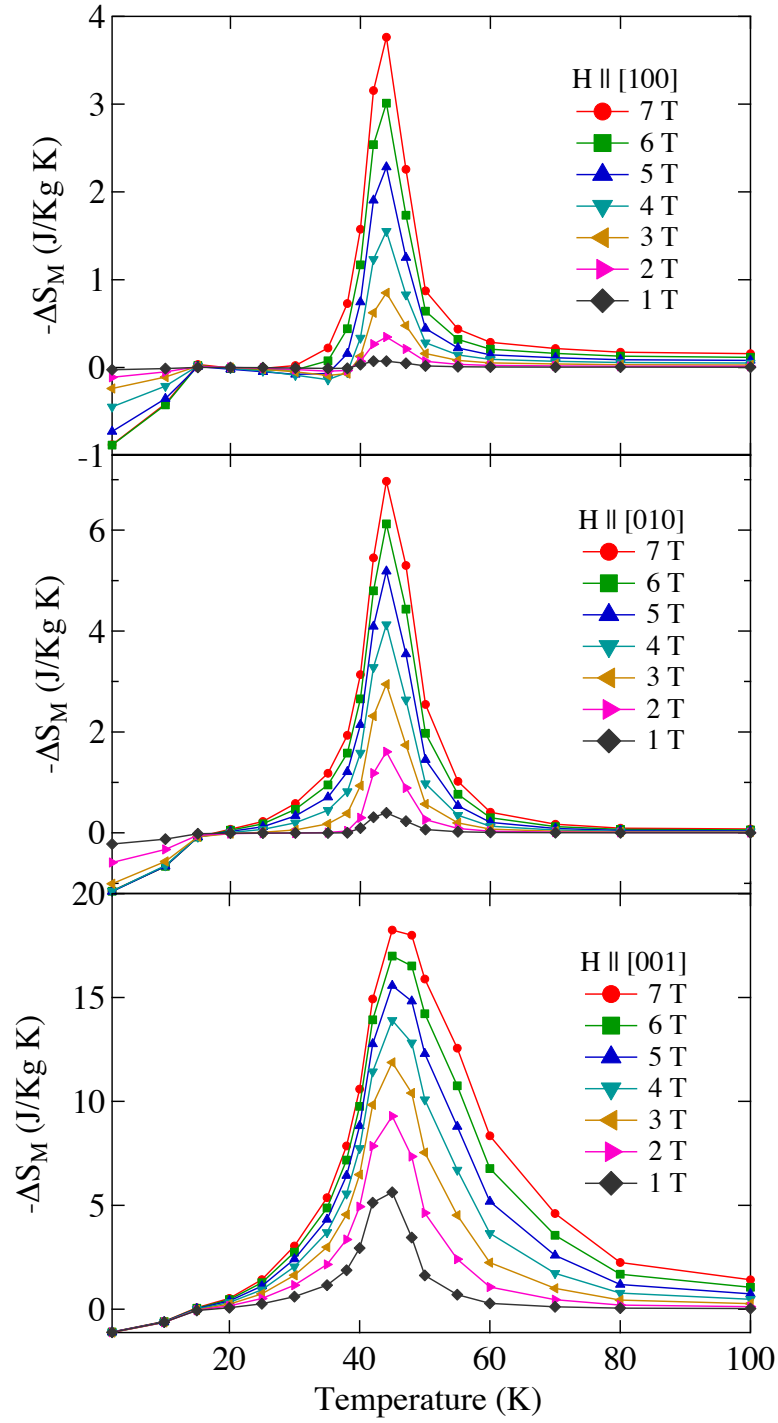
Figure 5.20: (a), (b), and (c) represents the temperature variation of magnetic entropy change ($-\Delta S_M$, along the three principal crystallographic directions, $H \parallel [010]$, $H \parallel [001]$ and $H \parallel [100]$ respectively) around the magnetic transition region of PrGe at various fields.
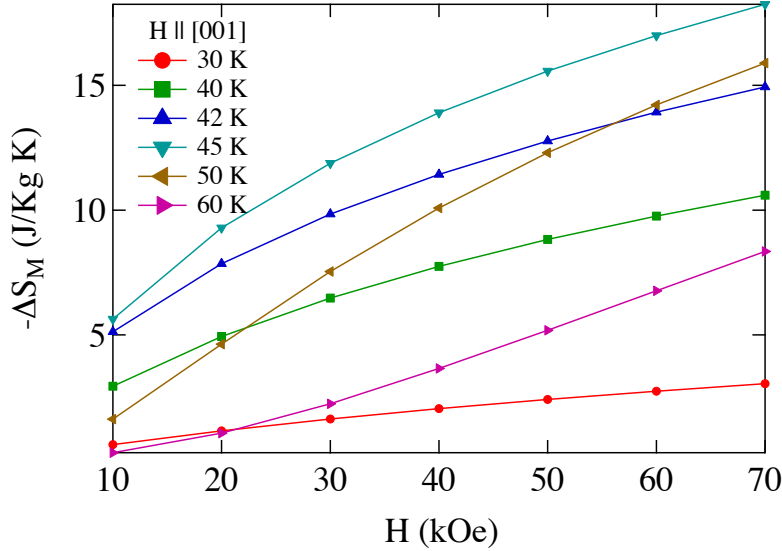
Figure 5.21: The field variation of magnetic entropy change in PrGe $(-\Delta S_M)$, along $H \parallel [001]$ around the magnetic transition region at different constant temperatures.

The temperature dependence of magnetic entropy change ΔS_{M} for different applied magnetic field H along the three crystallographic directions is shown in Fig. 5.20. Since [001] direction is the easy axis of magnetization, relatively low field is enough to induce complete saturation, hence a giant negative magnetic entropy change is observed in this direction around the magnetic ordering temperature. The maximum value of $-\Delta S_{\mathrm{M}}$ is found to be 18.2 J/Kg K for $\Delta H = 70$ kOe around 44 K. Along the other two crystallographic directions, a complete saturation is not observed up to a field 70 kOe. The $M vs. H$ data is nonlinear along these two directions. Due to lack of saturation here the value of $-\Delta S_{\mathrm{M}}$ along $H \parallel [100]$ and [010] directions is about three times smaller compared to the [001] direction.

Fig. 5.21 shows the isothermal field variation of magnetic entropy change along $H \parallel [001]$ crystallographic direction at various temperatures near its magnetic transition. Isothermal field dependence of RCP for PrGe is shown in Fig. 5.22. RCP varies linearly with H similar to that of PrSi. RCP value is reasonably large, which is 360 J/K for a change of magnetic field H to 70 kOe.

M versus H loops for each temperature were measured around the magnetic transitions from 2 K to 100 K at selected temperatures through increasing magnetic
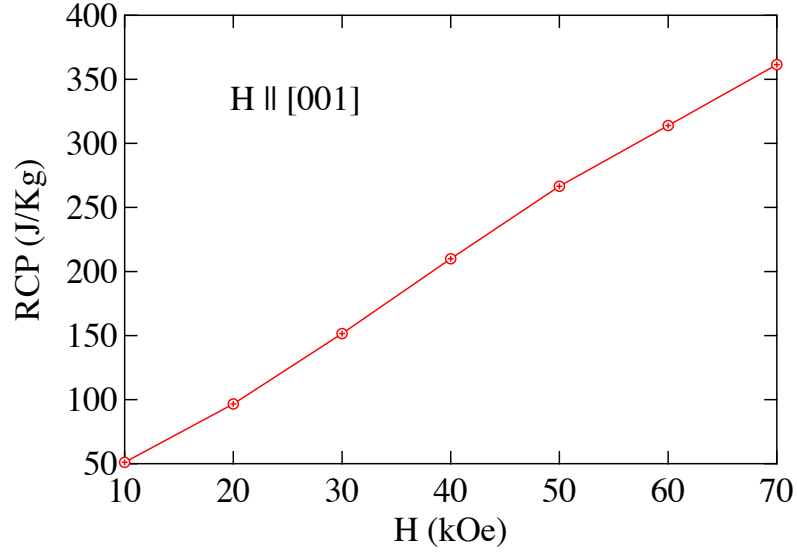
Figure 5.22: Magnetic field variation of relative cooling power for PrGe along the [001] direction.

field H from 0 to 70 kOe along three principal crystallographic directions to verify the anisotropic magnetization. The representative isothermal magnetization curves along the $H \parallel [100]$, $H \parallel [010]$ and $H \parallel [001]$ axes with a magnetic field up to 70 kOe were plotted in Fig. 5.19 (a), (b), and (c), respectively. Clear signature of magnetic anisotropy are observed in PrGe. At very low field ($\approx 2\ kOe$) we observed saturation magnetization along $H \parallel [001]$ axis. On the other hand $M - H$ curve does not show complete saturation behavior along the other two directions. The value of magnetization along $H \parallel [001]$ direction is almost five times larger than the other axes.

5.6 Discussion and conclusion

Single crystals of PrSi and PrGe have been grown by Czochralski pulling method and their anisotropic physical properties were studied in detail. Well defined Laue spots together with a low value of residual resistivity and high RRR, indicate the good quality of the grown single crystals. From the magnetic susceptibility, electrical transport and heat capacity data it is found that PrSi orders ferromagnetically below

$T_C = 52$ K, while PrGe first undergoes a paramagnetic to antiferromagnetic transition at 44 K and then antiferro to ferromagnetic transition at 41.5 K upon cooling. The magnetization measurements clearly showed that the magnetic moments are aligned along the crystallographic [010] direction in case of PrSi and along the [001] direction in the case of PrGe. Our result on PrSi does not support the previous neutron diffraction report where the magnetic moments were inferred to lie in the *ac* plane [87]. Along the hard axes of magnetization the magnetic behavior is anomalous, which may be attributed to the low lying CEF levels and/or to the complex nature of magnetic ordering in these compounds. A detailed neutron diffraction study is required on the single crystalline sample in order to better understand the complex magnetic structure of these systems. Crystal field analysis was performed on the magnetic susceptibility and heat capacity data of PrSi, and it was found that the CEF potential splits the $J = 4$ degenerate ground state of Pr^{3+} ion into nine singlet states with an overall splitting of 284 K. The ground state and the first excited states are separated by an energy difference of 9 K, such a small separation results in a quasi-doublet state, which leads to a magnetic ordering as the exchange interaction overcomes the energy gap Δ. A huge jump in the specific heat at the ferromagnetic transition and the shape of Arrott's plot, clearly suggests the ferromagnetic transition is first order like in both the systems. Hence there is a huge change in the magnetic entropy with applied magnetic field. A large magnetocaloric effect is observed along the easy axis of magnetization in both the systems and the MCE values are comparable to the values obtained in other popular magnetocaloric materials like $Gd_5Si_2Ge_2$. This suggests that both the compounds are potential candidates for magnetic refrigeration in the low temperature range. In case of PrSi, the low temperature heat capacity increases with decreasing temperature which is well explained by means of the nuclear Schottky effect arising due to the hyperfine splitting of ^{141}Pr nuclear levels. The Pr $4f$ moment estimated from the coefficient of nuclear Schottky effect matches very well with our experimental saturated magnetization value.

Chapter 6

Band structure study of PrGe by Angle resolved photoemmision

In the preceding chapters, various physical property studies by means of bulk measurement techniques; like magnetic susceptibility, isothermal magnetization, heat capacity, electrical transport, and the phenomenon like heavy fermion behavior in $CeMg_3$, level splitting due to crystal electric field, superzone gap formation in CeGe just below its antiferromagnetic ordering temperature, large magnetocrystalline anisotropy in PrGe and PrSi have been discussed. Many of these properties depend on the details of the electronic band structure of the compounds. The electronic structure of a system is the microscopic basis of all material properties including electrical and thermal conductivity, magnetism, optical properties.Thus the study of electronic structure of a material is important in order to understand the connection between the electronic, magnetic and structural properties exhibited by the systems. In this chapter we will discuss about Angle Resolved Photo Emission Spectroscopy (ARPES) study which is the best available technique to directly probe the electronic structure of a material. Unlike the techniques discussed in the preceding chapters, ARPES is a surface sensitive technique, meaning the method only probes the electronic states which are spatially localized near the surface of the sample. The PrGe binary exhibits a variety of magnetic phase transitions, and large magnetocrystalline anisotropy [104]. An investigation of electronic band structure of the PrGe maybe helpful in better understanding the complex magnetism of the system, and to explore further possible

interesting physical properties of this compound. Recently, the electronic structure of high-temperature superconductors [105], various electronic and magnetic phase transitions in heavy fermion systems [106, 107], valence fluctuations [108], topological insulators [109] have been successfully studied by ARPES. Various magnetic phase transitions of rare earth binary compound CeSb has been studied by ARPES [110], and the changes in volume of electron and hole pocket have been reported. A similar observation maybe expected in case of PrGe binary upon various magnetic phase transitions. Therefore a detailed study of the electronic structure, and their temperature evolution was studied by ARPES.

6.1   Motivation for present study

The primary goal of this study was to understand the complex magnetism, and large magnetocrystalline anisotropy of PrGe after experimentally determining the electronic band structure and Fermi surface topology of this compound, and their temperature evolution i.e., the changes upon various magnetic phase transitions. Along with this, PrGe is also a suitable compound to study the Rashba spin orbit interaction. Rashba-type spin-orbit interaction has attracted attention due to the possibility of spin control and manipulation by means of an electric field. The possibility of controlling the spin using a static electric field is of great interest since it can potentially lead to magnetic rand access memory (MRAM) devices. For a magnetic rare earth system, a large spin-orbit coupling is expected at the single crystal surface [111, 112]. The PrGe single crystal which exhibits large magnetic anisotropy and contains the high Z-element, is a natural choice for us to investigate the Rashba effect in this system [104]. In the present study we have experimentally determined the electronic band structure of (010) and (001) surfaces of PrGe along with its temperature dependence. We observed Rashba-type splitting of band on the (010) surface in the paramagnetic phase of PrGe.

6.2 Basic principle of ARPES

The basis of photoemission spectroscopy lies in the principle of photoelectric effect [113, 114]. The basic geometry of an ARPES setup is shown in Fig. 6.1. The material surface is illuminated by a monochromatic beam (either from a gas discharge lamp, or from a synchrotron source) of photons. The sample surface has to be a single crystal and properly aligned in order to perform the angle resolved or equivalently momentum-resolved photoemission measurement. If the energy of the photon is larger than the work function of the material and the binding energy of the electron, the electrons are emitted by photoelectric effect, and escape in vacuum in all directions. The kinetic energy (E_K) of the photoemitted electrons is measured by an electron energy analyzer for a given emission direction (θ, ϕ). Next step is to determine the electronic dispersion of the material. This is done by using the fact that the total energy and momentum component parallel to the sample surface is conserved by the photoemission process, while the perpendicular surface component of electrons is not conserved as it has to consume a portion of the kinetic energy to overcome the perpendicular surface potential before escaping into the vacuum. Thus it is not possible to extract the value of $k_\perp$ directly from experimental measurements [115]. However, by assuming the dispersion relation for the final electron states $E_f(\mathbf{k})$, it is possible to determine the perpendicular component $k_\perp$. This is particularly true when one uses results of band structure calculations, or assumes a nearly free electron description for the final bulk states [115]. Since the energy is conserved, the measured kinetic energy is directly related to the binding energy of electrons as:

$$h\nu = E_K + W_\phi + |E_B| \tag{6.1}$$

$$\mathbf{k}_{||,initial} = \mathbf{k}_{||,final} = \frac{1}{\hbar}\sqrt{2mE_{kin}}sin(\theta) \tag{6.2}$$

where $h\nu$ is the energy of incident photon, E_K is the kinetic energy of the photo electron, W_ϕ is the work function of the material, and E_B is the binding energy of the electron inside the solid. $\mathbf{k}_{||,initial}$ and $\mathbf{k}_{||,final}$ are the initial and final momentum of the electron parallel to the sample surface, respectively. Note that the momentum

of incident photon used in ARPES experiment (generally less than 100 eV), is much smaller than the typical Brillouin-zone dimension $2\pi/a$ of a solid, and thus maybe neglected.

Here the incident photon excite the electron from the initial occupied state $|\psi_i\rangle$ to a vacuum final state $|\psi_f\rangle$. The transition probability of the photo-excitation is given by the *Fermi's Golden rule*:

$$W = |\langle\psi_f|H'|\psi_i\rangle|^2\delta(E_f - E_i - h\nu) \tag{6.3}$$

where H' is the perturbation due to the photons.

The ARPES measurement maps the intensity of photoelectrons as a function of two angles (θ and ϕ) and the kinetic energy of the photo electron. The intensity is the function formed by a many body spectral wave function weighted by the Fermi Dirac distribution, and the probability function formed by the square of the matrix element of the interaction Hamiltonian with the many body initial and final states.

The cross section of the absorbed photons depends on the material and the energy of the incident photon. Another important thing to consider is the mean free path of the photoemitted electrons. The escape depths of the photoemitted electrons depend on the photon energy, and amounts to five to ten angstroms [116]. Thus we can consider ARPES as a surface sensitive technique which probes the electronic states that are in the spatial vicinity of the material surface.

The details of electronic structure study angle resolved photoemmision can be found in [115].

6.3   Spin orbit coupling

The spin orbit interaction is a well-known phenomenon which splits the spin-degenerate levels of one-electron energy level into levels with spin parallel and antiparallel to the orbit. Generally elements with high Z value have large spin orbit coupling strength. Therefore the spin orbit coupling is strong in rare earth elements, and their intermetal-
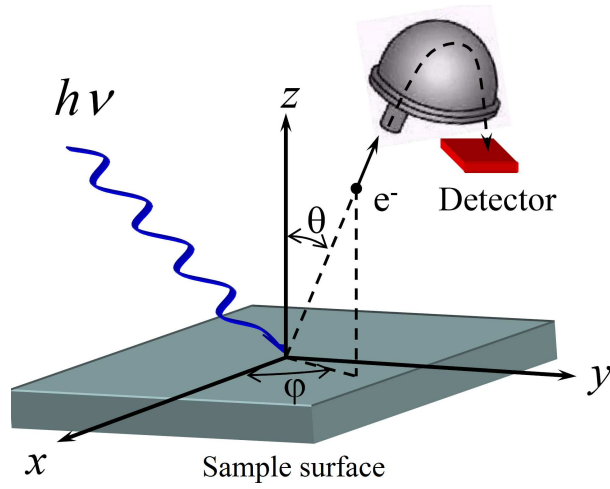
Figure 6.1: Geometric setup of an ARPES experiment. The emission direction of the photoelectrons is specified by the polar (θ) and azimuthal (ϕ) angles.
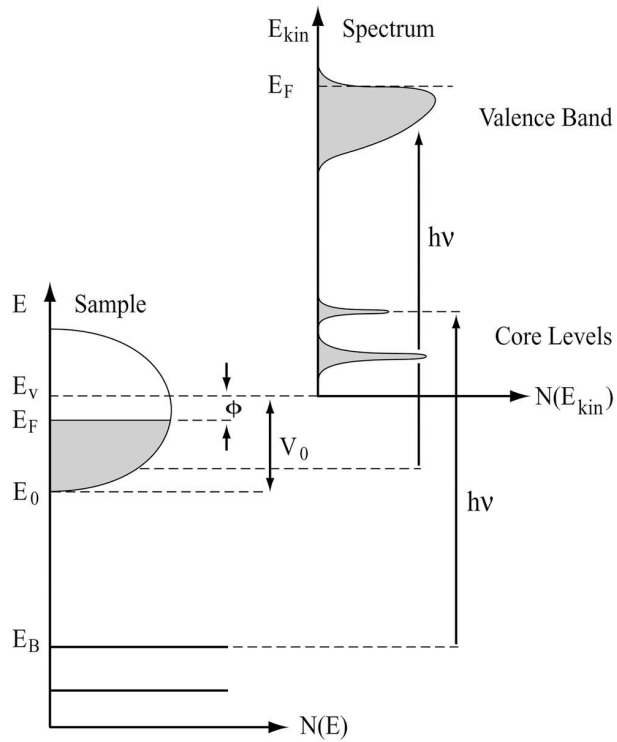

Figure 6.2: The schematic view of photoemission process, the diagram is taken from the Hufner's book. Energy distribution of photoemitted electrons produced by the incident photon measured as a function of E_K

lic compounds. However, in a solid such a splitting is forbidden due to the crystal symmetry. Is is easy to show that the time reversal symmetry leads to following restriction [117]:

$$E(\vec{k}, \uparrow) = E(-\vec{k}, \downarrow) \tag{6.4}$$

If the crystal posses inversion symmetry i.e., the operation $\vec{r} \to -\vec{r}$ does not change the crystal lattice, we have

$$E(\vec{k}, \uparrow) = E(-\vec{k}, \uparrow) \tag{6.5}$$

It is clear from above two equations 6.4 and 6.5 that if both time reversal and inversion symmetry are present,

$$E(\vec{k}, \uparrow) = E(\vec{k}, \downarrow) \tag{6.6}$$

i.e., the energy does not depend on the electronic spin. However in the surface of a crystal the 3-dimensional inversion symmetry is not present, thus opens up the possibility of spin degeneracy to be lifted. In the absence of magnetic fields, spin-orbit splitting is the only possible cause for a splitting of spin degenerate levels at the surface, and this interaction is described by the Rashba Hamiltonian [118]. The Pauli spin orbit Hamiltonian is given by:

$$H_{SOC} = -\frac{\hbar}{4m_0^2 c^2} \vec{\sigma} \cdot \vec{p} \times (\vec{\nabla} V) \tag{6.7}$$

where $\hbar$ is the Planck's constant, m_0 is the free electron mass, c is the velocity of light, $\mathbf{p}$ is the momentum operator, V is the Coulomb potential of the atomic core, and $\sigma = (\sigma_x, \sigma_y, \sigma_z)$ is the Pauli spin matrices. If we consider the free electron model, on the surface $\nabla V = dV/dZ \mathbf{e}_Z$, where Z direction is along the surface normal, and $\mathbf{e}_Z$ is unit vector along the Z-direction. Then the resulting spin-orbit Hamiltonian takes the following form:

$$H_{SOC} = \alpha_R(\mathbf{e}_Z \times \mathbf{p}) \cdot \sigma \tag{6.8}$$

the so-called Rashba term [118]. Here α_R is the strength parameter and proportional to the gradient of potential. The Hamiltonian $H = \frac{p^2}{2m} + H_{SOC}$ can be solved analytically [119], and it can be shown that the free electron parabolic dispersion will now be split in two parabolas, shifted in k-space corresponding to opposite (up or down) spin directions,

$$E_{\pm} = \frac{\hbar^2 k^2}{2m} \pm \alpha\hbar k \tag{6.9}$$

Though the above dispersion relation fits very well with the experimental data [119], the experimental splitting is much larger than would be estimated from the above calculation.

In a crystal having inversion symmetry, the splitting due to spin-orbit coupling (SOC) is not possible. However at surface, the 3-dimensional translation symmetry is broken, and thus opens the possibility of splitting of band due to SOC. The strength of the spin orbit coupling depends on the potential gradient near the core of the atoms, and therefore generally the heavier elements have stronger spin orbit coupling. We may see a spin split in the electronic states which are localized to the surface/interface. But the surface potential gradient itself is not strong enough to cause an observable spin split [119, 120]. The spin splitting becomes sizable when it couples to a large intra-atomic spin-orbit interaction of the system, which is case where the high Z elements are involved at the surface. In a magnetically ordered surface, the magnetic exchange interaction is usually much larger than the spin-orbit interaction. The spin polarization of electronic states in such system depends on the exchange interaction.

6.4 Sample surface preparation

In order to perform the ARPES measurements along the high symmetric directions, the PrGe crystallographic directions were determined by means of back reflection Laue diffraction method. The main practical challenge is to prepare a very good

quality sample surface. As we have already discussed that ARPES is surface sensitive technique, a small amount of oxidation of surface may lead to completely wrong information about the actual material. Also we need a surface which is atomically flat. Because one of the important information we measure in ARPES is the emission angle of photoemitted electrons, which is used to determine the in-plane crystal momentum of the electronic states inside the material. In order to get a very high quality atomically flat surface of our single crystal, we cleaved the single crystal inside UHV by using standard post-method, the crystal has nice cleavage plane along (010) and (001) directions. First the properly oriented piece of single crystalline sample is mounted on a copper plate using silver epoxy. The conductive glue was used in order to keep the sample electrically neutral under the photoemission process. Then a top-post was fixed at the top of the sample by using *Torr Seal*. Therefore the sample was sandwiched between the sample holder and the top-post. Conducting graphite paint was used to cover insulating *Torr Seal* and sample holder, in order to create contrast in the signal coming from the sample during the experiment. Once the sample was transferred to the manipulator in the measurement chamber, the top-post was mechanically removed using a screwdriver. We have obtained a clean mirror like surface for both PrGe (010) and (001).

6.5   Experiment

The measurements were performed at the APE beamline of Elettra Sincrotrone Trieste. Temperature as low as 20 K was achieved by means of liquid helium cooled cryostat. The measurements were performed at photon energy ranging from 20 - 76 eV. The data have been recorded in a Scienta SES 2002 electron energy analyzer. The energy resolution of our measurements was about 15-20 meV.

6.6   Results

The electronic band structure of PrGe (010) surface is experimentally determined, and shown in Fig. 6.3. The band structure is measured for both the paramagnetic

phase at 100 K and the ferromagnetic phase at 20 K. We observe that the band structure is symmetric with respect to Γ point. The most explicit feature is the Rashba-type band splitting at Γ. It is more prominent in the paramagnetic phase, and not so evident in the ferromagnetic phase. The changes in the band structure between the paramagnetic and ferromagnetic phases are observed near the Fermi energy; between E_F to 0.5 eV binding energy. The bands at deeper binding energy, below 1.5 eV, show similar behavior in both paramagnetic and ferromagnetic phases indicating that their characters are of bulk origin and localized in nature. In Fig. 6.3, we have observed that the two split bands show a strong photoemission intensity at 0.03 eV binding energy, and the maximum are shifted symmetrically with respect to Γ point by 0.08 Å^{-1}. The splitting can be compared on a wave number scale, where k_0 is the shift of the band maximum away from the Γ point, as well as on the energy scale where $E_R = \frac{\hbar^2 k_0}{m^*}$ is the Rashba energy. The coupling constant in the spin-orbit Hamiltonian is given by $\alpha_R = \frac{\hbar^2 k_0}{m^*}$. Here m^* represents the effective mass of the conduction electrons, and found to be about 18 m_0 from the heat capacity data described in Chapter 5, where m_0 is the free electron mass. Calculated value of E_R and α_R are 1.34 meV and 3.37 meVÅ, respectively. The values of E_R and α_R are comparable to the other Rashba systems [121, 122, 123, 124, 125].

We have also measured the temperature evolution of the electronic band structure across the magnetic phase transition, in the temperature interval from 20 to 100 K as shown in Fig. 6.4. We observed that a clear spin orbit splitting is present in the paramagnetic phase indicating the presence of Rashba effect of this system. The Rashba splitting in the paramagnetic phase from 100 K to 60 K does not change. The change in the band structure was observed below 50 K, which is the onset of antiferromagnetic ordering in this system. The splitting is considerably larger than the other magnetic systems [112]. Here the spin orbit splitting is observed in the paramagnetic phase, while in case of Gd and Tb rare earth metals, the splitting is observed in the ferromagnetic phase [111, 112]. In the antiferromagnetic phase the splitting in the hole-like bands disappears and becomes a single hole-band with the electron pockets appearing at the Γ point. This result is similar as observed in Bi/Ag (111) [125] surface alloy, where spin degenerate band with the maximum at high symmetry point is observed in the absence of splitting. The band structure clearly signifies that the spin polarization of PrGe (010) surface definitely plays important
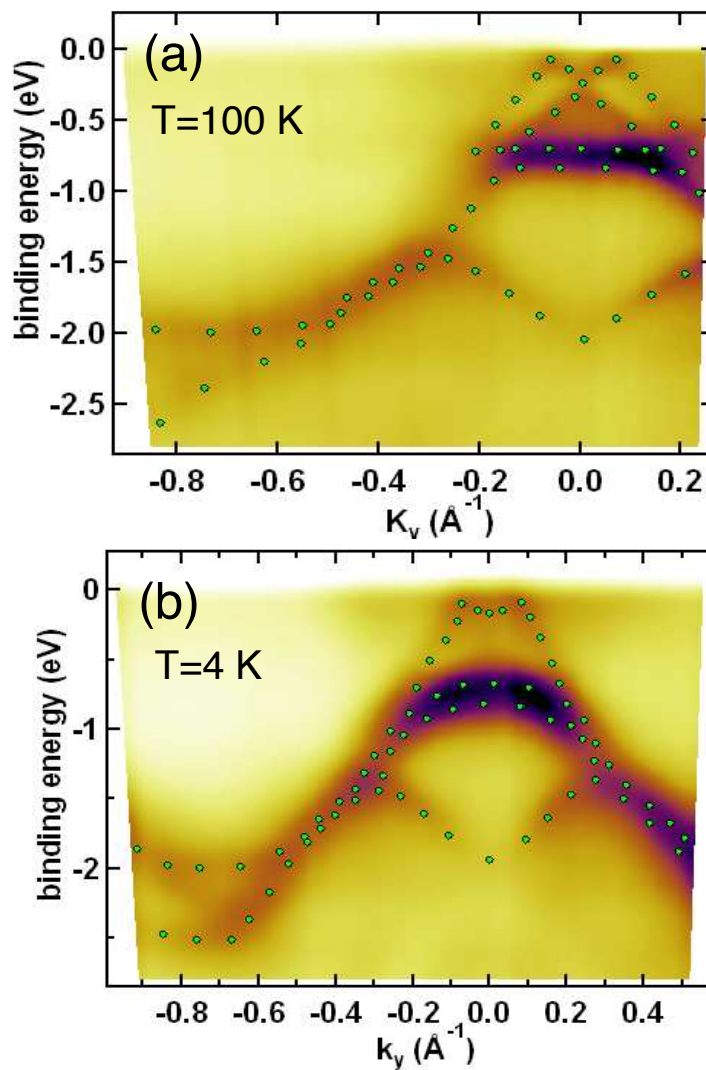
Figure 6.3: Electronic band structure of PrGe (010) surface measured at (a) 100 K in the paramagnetic phase showing clearly the splitting of bands near the Fermi surface at Γ point, and (b) ferromagnetic phase measured at 20 K, where the splitting is not so evident.

Figure 6.4: Temperature dependence of the band structure of PrGe across the magnetic transition measured at various temperatures.

Figure 6.5: Fermi surface and the cut along the Fermi surface in the (a) paramagnetic and (b) ferromagnetic phase.

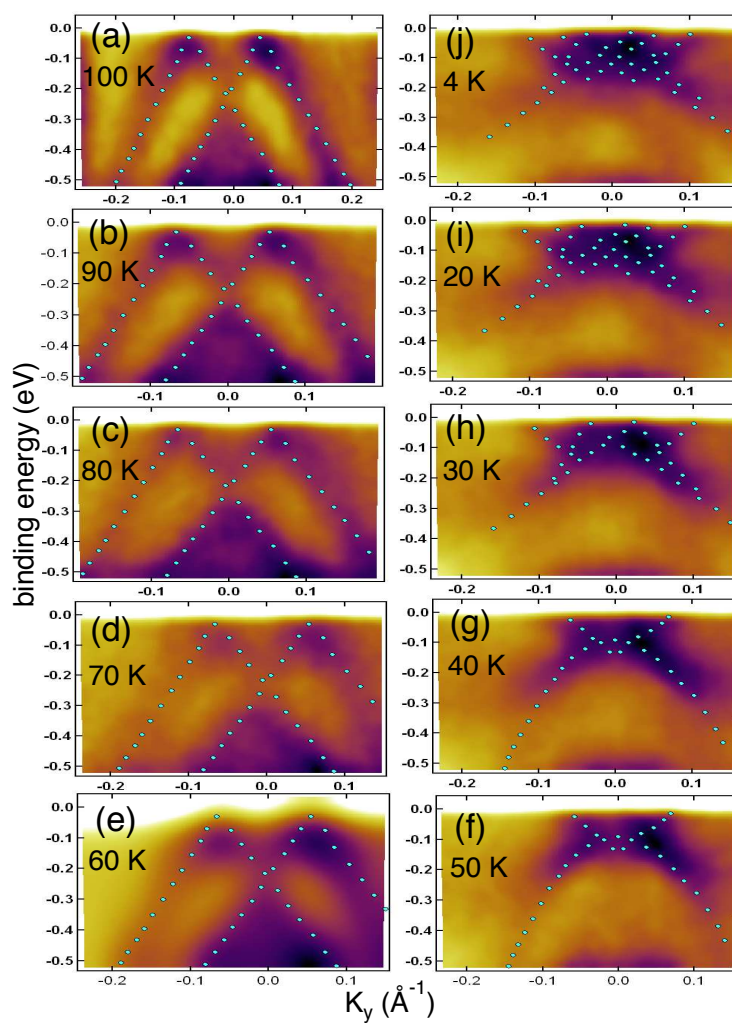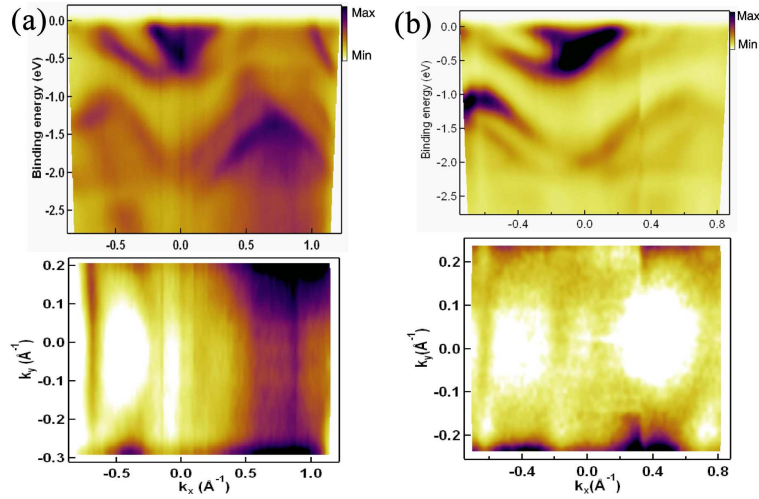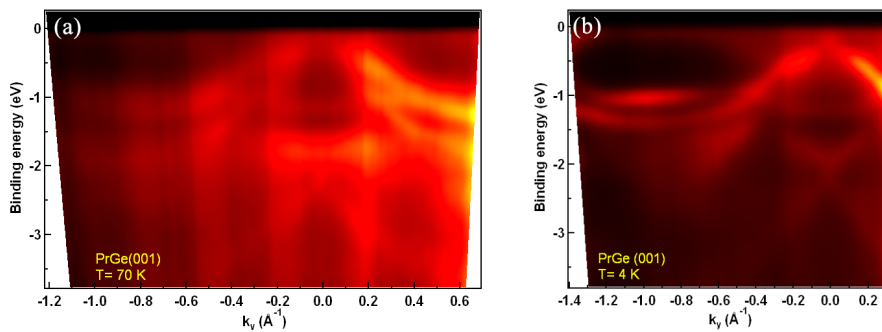Figure 6.6: The band structure of PrGe (001) surface measured in the paramagnetic and ferromagnetic phase. Unlike (010) surface, this surface does not show Rashba type splitting of bands.

role across the magnetic phase transition. Generally in case of ferromagnetic system, the magnetic exchange interaction is much larger than the spin-orbit interaction [126]. Thus the spin polarization of the electronic states is mainly defined by the exchange interaction, and the spins are aligned along a particular direction in the ferromagnetic state.

In Fig. 6.5 we show the Fermi surface and the cut along the Fermi surface marked by the arrow for both paramagnetic and ferromagnetic phases. The Fermi surface in the paramagnetic phase clearly shows the appearance of hole and electron pockets which are overlapping with each other. In the ferromagnetic phase we observe two hole pockets which are nested with the electron sheet in the k_x direction.

To further check the Rashba splitting depends on crystallographic directions, we have performed the band structure measurements on the (001) surface as well. The band structure of (001) surface is shown in Fig. 6.6 measured at the paramagnetic and ferromagnetic phases. Here we see the bands are symmetric with respect to the Γ point, as we observed in case of (010) direction. But we do not observe the splitting of bands, they are spin degenerate.This indicates that there are equal number of majority and minority spin bands on the surface and the net polarization is zero. This situation is similar to the observations on Bi/Al (111) surface [125]. To clearly see the changes in the band structure features we have, we have measured them in both paramagnetic and ferromagnetic phase. The hole pocket in the paramagnetic phase (Fig. 6.6) has been filled with the electron states in the ferromagnetic phase.

From the above observations we conclude that the presence of Rashba effect on the PrGe (010) direction is due to the alignment of spins of the itinerant electrons in the (010) direction and probably are canted in orientation. On the other hand in case of PrGe (001) surface the spins of the itinerant electrons are mostly parallel to the direction of momentum, and hence we do not see any spin-orbit slitting of bands. At present we do not have any theoretical band structure calculation for this system, which is planned for the future in order to compare with our experimental results.

Bibliography

[1] Ruderman, M. A. & Kittel, C. *Phys. Rev.* **96**, 99 (1954).

[2] Kasuya, T. *Prog. Theory Physics* **16**, 45 (1956).

[3] Yosida, K. *Phys. Rev.* **106**, 893 (1957).

[4] Kondo. *J. Progress of Theoretical Physics* **32**, 37 (1964).

[5] Ōnuki, Y., Shimizu, Y. & Komatsubara, T. *J. Phys. Soc. Japan* **53**, 1210 (1984).

[6] Ōnuki, Y., Goto, T. & Kasuya, T. *Materials Science and Technology*, volume 3A, Part I. VCH. Weinheim, (1991).

[7] Ōnuki, Y. & Hasegawa, A. *Handbook on the Physics and Chemistry of Rare Earths*, volume 20. Elsevier Science, Amsterdam, (1995).

[8] Ōnuki, Y. *et al. J. Phys. Soc. Jpn.* **73**, 769 (2004).

[9] Andres, K., Graebner, J. E. & Ott, H. R. *Phys. Rev. Lett.* **35**, 1779 (1975).

[10] Barbara, B. & et al, J. X. B. *Solid State Commun.* **24**, 481 (1977).

[11] Winzer, K. *Solid State Commun.* **16**, 521 (1975).

[12] Trovarelli, O. *et al. Phys. Rev. Lett.* **85**, 626 (2000).

[13] Okawa, M. *et al. Phys. Rev. Lett.* **104**, 247201 (2010).

[14] Stewart, G. R. *Rev. Mod. Phys.* **56**, 755 (1984).

[15] Stewart, G. R. *Rev. Mod. Phys.* **73**, 797 (2001).

BIBLIOGRAPHY

[16] Stewart, G. R. *Rev. Mod. Phys.* **78**, 743 (2006).

[17] Blundell, S. *Magnetism in Condensed Matter*. Oxford University Press, Oxford, (2006).

[18] Buschow, K. H. J. & van Daal, H. J. *Solid State Comm.* **8**, 363 (1970).

[19] Sumiyama, A. *et al. J. Phys. Soc. Jpn.* **55**, 1294 (1986).

[20] Brandt, N. B. & Moshchalkov, V. V. *Adv. in Phys.* **33**, 373 (1984).

[21] Doniach, S. *Physica B and C* **91 B**, 231 (1977).

[22] Settai, R., Takeuchi, T. & Ōnuki, Y. *J. Phys. Soc. Jpn.* **76**, 051003 (2007).

[23] Stevens, K. W. H. *Proc. Phys. Soc. London* **Sect. A 65**, 209 (1952).

[24] Hutchings, M. T. *Solid State Physics: Advances in Research and Applications*, volume 16. Academic Press, New York, (1965).

[25] Loidl, A. *et al. Phys. Rev. B* **46**, 9341 (1992).

[26] Maurya, A., Kulkarni, R., Dhar, S. K. & Thamizhavel, A. *J. Phys.: Condens. Matter* **25**, 435603 (2013).

[27] Runciman, W. A. *Phil. Mag. Ser. 8* **1**, 1075 (1956).

[28] Mackintosh, A. R. *Phys. Rev. Lett.* **9**, 90 (1962).

[29] Elliott, R. J. & Wedgwood, F. A. *Proc. Phys. Soc.* **81**, 846 (1963).

[30] Miwa, H. *Progress of Theoretical Physics* **29**, 477 (1963).

[31] Ellerby, M., McEwen, K. A. & Jensen, J. *Phys. Rev. B* **57**, 8416 (1998).

[32] Rodríguez-Carvajal, J. *Physica B* **192**, 55 (1993).

[33] Bridgman, P. W. *Proc. Am. Acad. Arts. Sci.* **60**, 305 (1925).

[34] Takeuchi, T. *et al. J. Phys.: Condens. Matter* **16**, L333 (2004).

[35] Honda, F. *et al. J. Phys. Soc. Jpn.* **77**, 043701 (2008).

[36] Nayeb-hashemi, B. & Clark, J. *Bull. Alloy Phase Diagrams* **9**, 916 (1988).

[37] Czochralski, J. *Z Phys Chem.* **92**, 219 (1918).

[38] Giffard, R. P., Webb, R. A. & Wheatley, J. C. Principles and methods of low-frequency electric and magnetic measurements using an rf-biased point-contact superconducting device. *J. Low Temp. Phys.* **6**, 533–610 (1972).

[39] Duzer, T. V. & Turner, C. W. *Principles of Superconductive Devices and Circuits.* New Your: Elsevier, (1981).

[40] Clarke, J. & Braginski, A. I. *The SQUID Handbook: Volume 1: Fundamentals and Technology of SQUIDs and SQUID Systems.* Wiley, (2004).

[41] Hwang, J. S., Lin, K. J. & Tein, C. *Rev. of Sci. Ins.* **68**, 94 (1997).

[42] Grosche, F. M. *et al. J. Phys. Condens. Matter* **13**, 2845 (2001).

[43] Jaccard, D., Behnia, K. & Sierro, J. *Phys. Lett. A* .

[44] Movshovich, R. *et al. Phys. Rev. B* **53**, 8241 (1996).

[45] Grosche, F., Julian, S., Mathur, N. & Lonzarich, G. *Physica B: Condens. Matt.* **223**, 50 (1996).

[46] Steglich, F. *et al. Phys. Rev. Lett.* **43** (1979).

[47] Knebel, G., Braithwaite, D., Canfield, P. C., Lapertot, G. & Flouquet, J. *Phys. Rev. B* **65**, 024425 (2001).

[48] Buschow, K. H. J. *J. Less-Common Met.* **44**, 301 (1976).

[49] Pierre, J., Murani, A. P. & Galera, R. M. *J. Phys. F: Et. Phys.* **11**, 679 (1981).

[50] Galera, R. M., Pierre, J. & Pannetier, J. *J. Phys. F: Met. Phys.* **12**, 993 (1982).

[51] Galera, R. M., Murani, A. P. & Pierre, J. *J. Magn. Magn. Mater* **23**, 317 (1981).

[52] Chatterji, T., Schneider, G. J. & Galera, R. M. *Phys. Rev. B* **78**, 012411 (2008).

[53] Tanida, H., Suzuki, H. S., Takagi, S., Onodera, H. & Tanigaki, K. *J. Phys. Soc. Jpn.* **75**, 073705 (2006).

[54] http://www.ill.eu/sites/fullprof/. .

[55] Rodrguez-Carvajal, J. *Physica B* **192**, 55 (1993).

[56] Cornut, B. & Coqblin, B. *Phys. Rev. B* **5**, 4541 (1972).

[57] Bredl, C. D., Stglich, F. & Schotte, K. D. *Z. PHys. B* **29**, 327 (1978).

[58] Besnus, M. J., Braghta, A., Hamdauoui, N. & Meyer, A. *J. Magn. Magn. Mater* **104-107**, 1385 (1992).

[59] Blanco, J. A. *et al. Phys. Rev. B* **49**, 15126 (1994).

[60] Desgranges, H. U. & Schotte, K. D. *Phys. Lett. A* **91**, 240 (1982).

[61] Gruner, G. & Zawadowski, A. *Rep. Prog. Phys.* **37**, 1497 (1974).

[62] Johnson, Q. C., Smith, G. S., Wood, D. H. & Cramer, E. M. *Nature* **204**, 600 (1964).

[63] Hohnke, D. & Parthé, E. *Act. Cryst.* **20**, 572 (1966).

[64] Shaheen, S. A. *Phys. Rev. B* **36**, 5472 (1987).

[65] Noguchi, S., Okuda, K., Nojiri, H. & Motokawa, M. *J. Magn. Magn. Mater* **177**, 403 (1998).

[66] Buschow, K. H. J. & Fast, J. F. *Phys. Stat. Solid* **16**, 467 (1966).

[67] Marcano, N., Espeso, J. I., Noakes, D. R., Kalvius, G. M. & Sal, J. C. G. *Physica B* **359**, 269 (2005).

[68] Marcano, N., Espeso, J. I. & Sal, J. C. G. *J. Magn. Magn. Mater* **310**, e35 (2007).

[69] Schobinger-Papamantellos, P. *et al. Physica B* **349**, 100 (2004).

[70] Gokhale, A. B. & Abbaschian, G. J. *Bull. Alloy Phase Diagr.* **10**, 142 (1989).

[71] Arrott, A. *Phys. Rev.* **108**, 1394 (1957).

[72] Meaden, G. T. *Contemp. Phys.* **12**, 313 (1971).

[73] Edwards, L. R. & Legvold, S. *Phys. Rev.* **176**, 753 (1968).

[74] Takabatake, T. *et al. J. Magn. Magn. Mater* **177-181**, 53 (1998).

[75] Onimaru, T. *et al. J. Phys. Soc. of Jpn.* **77**, 074708 (2008).

[76] Schobinger-Papamantellos, P. & Buschow, K.   **130**, 242 (1994).

[77] Yatskar, A., Beyermann, W. P., Movshovich, R. & Canfield, P. C. *Phys. Rev. Lett.* **77**, 3637 (1996).

[78] Sugawara, H. *et al. Phys. Rev. B* **66**, 134411 (2002).

[79] Settai, R. *et al. J. Phys. Soc. Jpn.* **69**, 3983 (2000).

[80] Walter, U. *J. Phys. Chem. Solids* **45**, 401 (1984).

[81] Bleaney, B. *Proc. Roy. Soc. Lond.* **276**, 39 (1963).

[82] Nguyen, V. N., Rossat-Mignod, J. & Tcheou, F. *Solid State Commn.* **17**, 101 (1975).

[83] Fillion, G., Gignoux, D., Givord, F. & Lemaire, R. *J. Magn. Magn. Mater* **44**, 173 (1984).

[84] sal, J. C. G., Fernandez, J. R., Sanchez, R. J. L. & Gignoux, D. *Solid State Commn.* **59**, 771 (1986).

[85] Buschow, K. H. J., Schobinger-Papamantellos, P. & Fischer, P. *J. Less Common Met.* **139**, 221 (1988).

[86] Snyman, J. L. & Strydom, A. M. *J. App. Phys.* **111**, 07A943 (2012).

[87] Nguyen, V. N., Tcheou, F. & Rossat-Mignod. *Solid State Commun.* **23**, 821 (1977).

[88] Andersen, N. H. & Smith, H. *Phys. Rev. B* **19**, 384 (1979).

BIBLIOGRAPHY

[89] Larrea, J. *et al. Phys. Rev. B* **72**, 035129 (2005).

[90] Bowden, G. J., Bunbury, D. S. P. & McClausland, M. A. H. *J. Phys.C* **4**, 1840 (1971).

[91] Shohata, N. *J. Phys. Soc. Jpn.* **42**, 1873 (1977).

[92] Banerjee, S. K. *Phys. Lett.* **12**, 16 (1964).

[93] Das, P. K., Kumar, K. R., Kulkarni, R., Dhar, S. K. & Thamizhavel, A. *J. Phys.: Condens. Matter* **24**, 476001 (2012).

[94] Yoshiuchi, S. *et al. J. Phys. Soc. Jpn.* **79**, 044601 (2010).

[95] Fazekas, P. *Lecture notes on Electron Correlation and Magnetism, Series in Modern Condensed Matter Physics*, volume 5. World Scientific, (1999).

[96] Gschneidner, K. A., Pecharsky, V. K. & Tsokol, A. O. *Rep. Prog. Phys.* **68**, 1479 (2005).

[97] Pecharsky, V. K. & Jr, K. A. G. *Phys, Rev. Lett.* **78**, 4494 (1997).

[98] Tishin, A. M. & Spichkin, Y. I. *The magneto caloric effect and its applications, publisher =.*

[99] Gschneidner, K. A. & Pecharsky, V. K. *Annu. Rev. Mater. Sci.* **30**, 387 (2000).

[100] Andersen, N. H. *Crystalline Field and Structural Effects in f-Electron Systems.* Plenum , New York, (1980).

[101] van den Broek, J. & Zijstra, H. *IEEE Trans. Magn. Mag.* **7**, 226 (1971).

[102] Bouvier, M., Lethuillier, P. & Schmitt, D. *Phys. Rev. B* **43**, 13137 (1991).

[103] Coqblin, B. *The Electronic Structure of Rare-Earth Metals and Alloys: The Magnetic Heavy Rare-Earths.* Academic, New York, (1977).

[104] Das, P. K., Kumar, K. R., Kulkarni, R., Dhar, S. K. & Thamizhavel, A. *J. Phys. Condens. Matt.* **24**, 476001 (2012).

[105] Damascelli, A., Hussain, Z. & Shen, Z. X. *Rev. Mod. Phys.* **75**, 473 (2003).

[106] Ito, T., Kumigashira, H., Kim, H.-D. & *et al*, T. T. *Phys. Rev. B* **59**, 8923 (1999).

[107] Raj, S., Iida, Y., Souma, S., Sato, T. & *et al*, T. T. *Phys. Rev. B* **71**, 224516 (2005).

[108] Matsunami, M., Hajiri, T., Miyazaki, H., Kosaka, M. & Kimura, S. *Phys. Rev. B* **87**, 165141 (2013).

[109] Hasan, M. & Kane, C. *Rev. Mod. Phys.* **82**, 3045 (2010).

[110] Kumigashira, H. *et al. Phys. Rev. B* **56**, 13654 (1997).

[111] Krupin, O. *et al. Phys Rev B* **71**, 201403 (2005).

[112] Krupin, O. *et al. New Journal of Physics* **11**, 013035 (2009).

[113] Hertz, H. *Ann. Phys.* **17**, 983 (1887).

[114] Einstein, A. *Ann. Physik* **31**, 132 (1905).

[115] Damascelli, A. *Physica Scripta* **T109**, 61 (2004).

[116] Hufner, S. *Photoelectron Spectroscopy.* Springer Verlag, (1995).

[117] Kittel, C. *Quantum Theory of Solids.* Wiley, New York, (1963).

[118] Rashba, E. I. *Sov. Phys. - Solid State* **2**, 1109 (1960).

[119] LaShell, S., McDougall, B. A. & Jensen, E. *Phys. Rev. Lett.* **77**, 3419 (1996).

[120] Petersen, L. & Hedegard, P. *Surf. Sci.* **459**, 49 (2000).

[121] Nitta, J., Akazaki, T., Takayanagi, H. & Enoki, T. *Phys. Rev. Lett.* **78**, 1335 (1997).

[122] Popovic, D. *et al. Phys. Rev. B* **72**, 045419 (2005).

[123] Cercellier, H. *et al. Phys. Rev. B* **73**, 195413 (2006).

[124] Koroteev, Y. M. *et al. Phys. Rev. Lett.* **93**, 046403 (2003).

[125] Ast, C. R. *et al.* **98**, 186807 (2007).

[126] Chikina, A., Hppner, M. & *et al*, S. S. *Nature Comm.* **5**, 3171 (2014).